論文 / 著書情報
Article / Book Information

題目(和文)	
Title(English)	Study on Performance of Steel Moment-Resisting Frames Subjected to Multiple Earthquakes
著者(和文)	TenderanRandy
Author(English)	Randy Tenderan
出典(和文)	学位:博士（工学）, 学位授与機関:東京工業大学, 報告番号:甲第12004号, 授与年月日:2021年3月26日, 学位の種別:課程博士, 審査員:吉敷 祥一,元結 正次郎,河野 進,佐藤 大樹,西村 康志郎,山田 哲
Citation(English)	Degree:Doctor (Engineering), Conferring organization: Tokyo Institute of Technology, Report number:甲第12004号, Conferred date:2021/3/26, Degree Type:Course doctor, Examiner:,,,,,
学位種別(和文)	博士論文
Type(English)	Doctoral Thesis

Study on Performance of Steel Moment-Resisting Frames Subjected to Multiple Earthquakes

by

Randy Tenderan

Graduate Major in Urban Design and Built Environment

Department of Architecture and Building Engineering

School of Environment and Society

Academic Supervisors:

Assoc. Prof. Shoichi Kishiki

Abstract

At an earthquake event, a number of ground shakings with various intensities usually occur within a certain period of time. In addition, in several earthquake events all around the world, it is found that more than one strong ground shaking with almost equal intensity could occur within a short period of time. For example, in the 2016 Kumamoto Earthquake, two strong shakings occurred within a time interval of only 28 hours. That shocking event leads structural engineers and researchers to ask how safe are the buildings designed using current seismic codes in response to seismic sequence events. Since under this seismic sequence event, no structural repair could be done so that the structure itself should utilize its available capacity to sustain all the strong shakings. Until now, the influence of the multiple shocks to the building damage has not been specifically considered in any seismic design codes. For example, the current Japanese seismic design code ensures that a building will be able to sustain one severe earthquake without collapse; however, its performance to sustain multiple severe earthquakes needs to be clarified further. The main objective of this study is to comprehensively evaluate the actual seismic performance of SMRFs under multiple earthquakes. To achieve the objective, extensive numerical analysis and experimental tests are conducted.

Firstly, in Chapter 2, a numerical analysis is conducted using a non-deteriorated model. In this model, any deterioration effect is not considered. Instead, the main focus is the ductile fracture of beams because the application of the strong column weak beam concept is resulting in the beam members weaker than the column members. Various non-deteriorated SMRF models are analyzed by conducting a series of inelastic time-history response analyses that simulate the occurrence of multiple earthquakes. The damage of the structure under multiple excitations is evaluated by the cumulative damage at the beam end. Overall, it is found that the structure could maintain stable behavior under multiple excitations. Although in a few cases, it is found that the ductile fracture might occur or the ultimate state might be reached when the input intensity is larger than the design level, the performance of the structure is satisfying. By adopting the criterion of over 90% uncollapsed cases, the structure can resist up to five excitations with an intensity of peak ground velocity (PGV) 0.75 m/s or three excitations with PGV 1.0 m/s. Moreover, the beam-to-column connection test is conducted to further verify the reliability of the cumulative damage evaluation method under random cyclic loading. The

loading history used in the test is created from the response analysis of the non-deteriorated model and simulating the occurrence of multiple earthquakes. By calculating the cumulative damage value of the test specimens, it can be verified that the reliability of the cumulative damage evaluation method is acceptable.

Secondly, in Chapter 3, the numerical analysis is conducted using a deteriorated model that considers the effect of strength deterioration due to local buckling of columns. Various deteriorated SMRF models are created for the analysis. These models are designed considering the combination of two main design parameters, i.e., the width-to-thickness ratio of the column member (D_c/t) and the column-to-beam moment capacity ratio ($_cM_p/_bM_p$). Then, an inelastic response analysis that simulates the occurrence of multiple shocks is carried out. Overall, it is found that the performance of SMRFs under multiple excitations is lower than that of the non-deteriorated model because the weak story collapse is more likely to occur. The behavior of the structure can be divided based on whether the structure reaches the deteriorated stage or not. If the structure stays in the non-deterioration stage, then stable behavior can be achieved. In general, it is found that in the cases where the structure is having a non-deterioration margin of over 50% at the 1st excitation, the stable behavior can be achieved under five excitations. Moreover, to achieve the same criterion of 90% uncollapsed cases, a lower D_c/t value or a higher $_cM_p/_bM_p$ value is necessary. The combination of D_c/t and $_cM_p/_bM_p$ that can achieve the criterion are provided.

Lastly, in Chapter 4, to further verify the analytical result, a full-scale steel frame test is conducted. To simulate the occurrence of multiple earthquakes, one typical set of loading history that corresponds to one earthquake is created. During the test, multiple loading sets with various levels of intensities are loaded to simulate the occurrence of multiple earthquakes. Two specimens are tested in the experiment. The specimens are single-floor, one-span substructures of an intermediate story of typical current Japanese middle- or low-rise steel buildings. In addition to the test, an inelastic response analysis is conducted by matching the maximum story drift angle range ($SDAR_{max}$) with those of the loading sets used in the test. It is found that by limiting the $SDAR_{max}$ under multiple earthquakes to 4%, an acceptable performance can be achieved. From the test result, until loading set with $SDAR_{max}$ of 4%, the strength and stiffness of the steel frames barely deteriorate and only a small crack and local buckling are found at the beam end. A similar result is obtained from the response analysis, until the $SDAR_{max}$ of 4%, the cumulative damage at the beam ends are all less than 25% and the column is still in an early stage of deterioration.

As a conclusion, in Chapter 5, all the findings found in the numerical analysis and experimental test are comprehensively summarized. Moreover, to ensure the performance of SMRFs under multiple earthquakes, the reserved strength and deformation limits are introduced for two levels of performance, namely, collapse prevention level and deterioration prevention level. The reserved strength limit is represented by the minimum non-deterioration margin at the 1st excitation (NM_1), while the deformation limit is represented by the $SDAR_{max}$ under multiple excitations. Both the reserved strength and deformation limits are provided for a various number of excitations and various input intensities. The performance of SMRFs under multiple earthquake excitation is ensured by designing the structure to fulfill both the reserved strength and deformation limits.

Acknowledgements

It is almost five years since I came to Japan to continue my study as a master's student in Yamada Laboratory. This five years' experience of studying and living in Japan is very valuable and precious for me. I realize that during these five years, I have learned a lot of new things and improved myself as a researcher and as a human being. Despite of all the ups and downs during my studies, I am finally able to complete this dissertation. I am fully aware that the completion of this dissertation will not happen without the help and contribution of many people. I would like to express my sincere gratitude to all of them.

First and foremost, I would like to express my sincere and huge gratitude to my supervisor, Prof. Satoshi Yamada. From the very first point when I was accepted as a student in his Lab to the very end when I am able to complete my study, all of the things will not go smoothly without his support and guidance. Spending five years as his student will be a very valuable part of my life. I learned many things from him either it is related or not related to the research, and I am able to improve myself a lot thanks to his guidance and teaching. It is an honor for me to be one of his students.

I would like to sincerely thank my second supervisor, Assoc. Prof. Shoichi Kishiki. All his critical comments and suggestions have contributed to the development and completion of this dissertation. Besides the technical guidance, by being part of the Yamada-Kishiki Lab, I am also able to learn a lot of good things from him as a researcher which help me improve myself even more.

I would like to express my sincere gratitude to Asst. Prof. Takanori Ishida. As a part of the research team, all his technical and non-technical guidance are very important and valuable for the completion of my study. Without all his support and contribution, I will not be able to complete this dissertation smoothly. I am very thankful to him.

I would like to sincerely thank Assoc. Prof. Yu Jiao for her technical contribution in the development of the research and experiment, not to mention for her non-technical support for me to complete my study. I would like to express my gratitude to Mr. Kohtaki Keita. As the person-in-charge of the steel frame experiment, the experiment and data processing will not go smoothly without his hard work and dedication. I sincerely appreciate his contribution.

I am grateful to all the members of Yamada-Kishiki Lab. To all the students, either my seniors or juniors, I would like to thank them for all their technical support in the research and experiment and their non-technical support during my stay in Japan for five years. Also, I would like to thank the secretary of Yamada and Kishiki Lab for their support, especially related to the administrative affairs. I am very thankful for all their help.

Last but not least important, a heartfelt thanks go to my family back at home, especially my parents, for their support during my study in Japan. I am able to complete my study smoothly thanks to their sincere and unrelenting support for me.

February 2021

Randy Tenderan

Contents

1. Introduction

1.1 Background

At an earthquake event, a number of ground shakings with various intensities usually occur within a certain period of time. The ground shakings are commonly classified as foreshocks, mainshocks, and aftershocks. The intensities of the foreshocks and aftershocks are generally considered much lower than those of the mainshocks; thus, the influences of foreshocks and aftershocks have been considered negligible in building design. However, in several earthquake events all around the world, it is found that more than one strong ground shaking with almost equal intensity could occur within a short period of time. Li and Ellingwood (2007) in their paper noted several past events worldwide in which the main shock was found to be followed by a considerably large aftershock, i.e., in Italy (Friuli, 1976; Umbria-Marche, 1997), Greece (1986, 1988), Turkey (1992), and Mexico (1993, 1994, 1995). In addition to that, within the last decade, there are also some notable earthquake events in which multiple strong shocks occurred in a short period of time, such as in the 2012 Sumatera earthquake in Indonesia (Earthquake Engineering Research Institute 2012), the 2016 Kumamoto earthquake in Japan (Kato et al 2016), the 2016 Central Italy earthquake in Italy (Stewart et al 2016), and the 2019 Ridgecrest earthquake in the United States (Brandenberg 2019). In the 2016 Kumamoto Earthquake, two strong shakings occurred within a time interval of only 28 hours, i.e., a strong foreshock at 21:26 JST on April 14 and the main shock on April 16 at 01:25 JST (Asano and Iwata 2016). Both shocks had a seismic intensity of 7 according to the Japan Meteorological Agency (JMA) scale (or approximately equivalent to intensity X-XII on the Mercalli scale) in the most damaged area, i.e., Mashiki Town. Japan Meteorological Agency (JMA) also noted that thousands of ground shakings occurred from April 14 until April 20 which 16 of them have seismic intensity larger than or equal to 5− (5 lower) according to the JMA seismic intensity scale.

That shocking event leads structural engineers and researchers to ask how safe are the buildings designed using current seismic codes in response to seismic sequence events. Since under this seismic sequence event which usually occurred in a short period of time, no structural repair could be done so that the structure itself should utilize its available capacity to sustain all the strong shakings. Until now, the influence of the multiple shocks to the building damage

has not been specifically considered in any seismic design codes. For example, the current Japanese seismic design code ensures that a building will be able to sustain one severe earthquake without collapse; however, its performance to sustain multiple severe earthquakes needs to be clarified in detail. Moreover, the current seismic design of steel moment-resisting frames under severe earthquakes commonly adopts the plastic design concept. This concept utilizes the inelastic deformation capacity of steel members to dissipate the seismic energy by damaging the designated members. As illustrated in Figure 1-1, theoretically, the structures with this design will undergo some damage (i.e., plastic deformation) if shaken by an earthquake with an intensity that is equal to or larger than the design intensity level. Consequently, as the number of strong shocks increases, the damage within the structure accumulates; thus, the structure becomes more vulnerable to collapse. In this situation, the number of strong shocks that can be resisted by the structure before collapsing has become a growing concern in recent years.

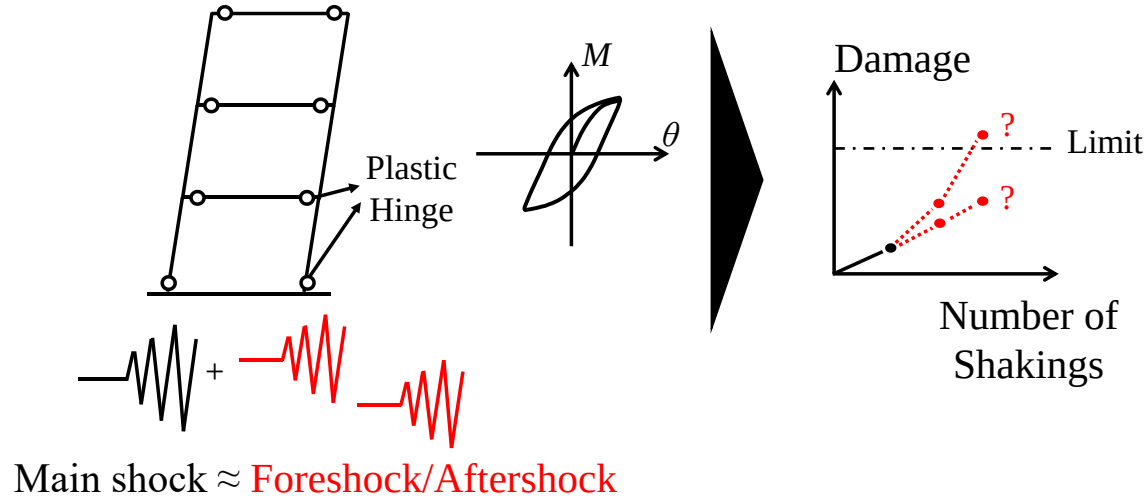

Figure 1-1 Accumulation of damage under multiple earthquakes

1.2 Previous Studies on Performance of SMRFs Subjected to Seismic Sequence

In the past, some researchers have analyzed the influence of seismic sequence on structural performance (Fragiacomo et al. 2004, Lee and Foutch 2004, Li and Ellingwood 2007, Iancovici and Ionică 2007, Hatzigeorgiou and Beskos 2009, Hatzigeorgiou 2010, Ruiz-García and Negrete-Manriquez 2011, Loulelis et al. 2012, Zhai et al. 2013, Li et al. 2014, Zhai et al. 2014, Ruiz-García and Aguilar 2015, Zhai et al. 2016, Abdollahzadeh et al. 2019). Fragiacomo et al.

(2004) evaluates the reduction in behavior factor (q) under the repeated seismic sequence. They found that some reduction of q should be considered in the earthquake-prone regions where the seismic sequences are highly possible to occur. Lee and Foutch (2004) evaluates the safety of a damaged building using the brittle fracture of connections as the main safety criterion. They mainly aim to provide an analytical tool to evaluate damaged buildings due to the mainshock. Li and Ellingwood (2007) evaluates the damage ratio (number of brittle fractured connections) under mainshock-aftershock sequences. They found that the probability of an aftershock causing large additional damage is small if the initial damage from the mainshock is small. Ruiz-García and Negrete-Manriquez (2011) evaluates the drift demands under as-recorded mainshock-aftershock sequence. They found that the as-recorded seismic sequences do not increase the drift demands as significant as those of artificial sequences. Loulelis et al. (2012) evaluates the maximum horizontal displacement and inter-story drift ratio (IDR) under mainshock-aftershock sequences and found that a higher displacement demand is required under the seismic sequences. Li et al. (2014) evaluates the collapse probability of SMRFs under mainshock-aftershock sequences and found that the structural collapse capacity may reduce significantly when the building is subjected to a high intensity mainshock; thus, the structural collapse is likely to occur even if only a small aftershock follows the mainshock. Ruiz-García and Aguilar (2015) conducted an incremental dynamic analysis to evaluate the collapse capacity under aftershock taking into account the postmainshock residual drift. They mainly found that the aftershock collapse capacity decreases as the postmainshock residual drift increases. Abdollahzadeh et al. (2019) compares the drift increment under mainshock-aftershock sequences of SMRFs designed by elastic design method and performance-based plastic design method and found that the performance of SMRFs designed by performance-based plastic design method is better than that of design by elastic design method. Overall, those past studies mainly consider "main shock–aftershock sequences" in which the intensity of the aftershock is smaller than that of the main shock. The past studies are mainly focused on analyzing the design demand under main shock only compared to that of under main shock–aftershock sequences. However, in the 2016 Kumamoto Earthquake, two strong shakings with an almost equal intensity occurred in a short period of time which shows the necessity to not only consider the main shock–aftershock sequences, but also multiple strong earthquake sequences.

In addition, most of the studies on the influence of seismic sequence are using the simple single-degree-of-freedom (SDOF) models as found in the study of Iancovici and Ionică (2007),

Hatzigeorgiou and Beskos (2009), Hatzigeorgiou (2010), Zhai et al. (2013, 2014, 2016), and Kojima and Takewaki (2016). As an example, Zhai et al. (2014) conducted an inelastic analysis of SDOF system considering various vibration period (T), strength reduction factor (R), and hysteresis model. The vibration period is taken between 0.1 s and 5.0 s. The reduction factor (R) is taken to equal to 2, 3, 4, 5, and 6. And the hysteresis model uses four different models, i.e., elastic-perfectly-plastic (EPP) model, modified clough (MC) model, pinching model, and stiffness strength degradation (SSD) model. The ductility demand (μ), normalized hysteretic energy, and modified Park-Ang damage index are used to evaluate the damage of the structure. Zhai et al. found that the influence of aftershock to the damage of the structure strongly depends on the reduction factor (R) and the ratio of the intensity of the aftershock to the intensity of the main shock, but in general, they found that the damage of structure due to main shock-aftershock sequence is larger than the damage due to single main shock. A similar study by Hatzigeorgiou and Beskos (2009) also found that the inelastic displacement ratio of SDOF structure under seismic sequence is larger than that of under single main shock. Those simple studies using the SDOF model have shown us the importance of considering the seismic sequence. However, a more realistic response analysis using the multi-degree-of-freedom (MDOF) model is necessary to understand not only the damage state or ductility demand but also the seismic behavior of the structure under multiple earthquakes.

Up until these days, only a few researchers have analyzed a multi-degree-of-freedom (MDOF) model of steel moment-resisting frames (SMRFs) such as Fragiacomo et al. (2004), Lee and Foutch (2004), Li and Ellingwood (2007), Ruiz-García and Negrete-Manriquez (2011), Loulelis et al. (2012), Li et al. (2014), Ruiz-García and Aguilar (2015), Abdollahzadeh et al. (2019). However, most of those researchers mentioned above used the inelastic ductility demand (μ), behavior factor (q), force reduction factor (R), maximum roof displacement, or maximum inter-story drift ratio (IDR) to measure the seismic performance. Those parameters are mostly related to design and do not directly represent the actual damage state of the structure. In addition, none of these researchers have focused on identifying the seismic behavior of SMRFs under multiple earthquakes.

The seismic design of SMRFs commonly adopts a plastic design concept, especially for the ultimate state. In other words, during severe earthquakes, damages are allowed to occur, and the seismic energy will be dissipated by damaging the designated members. In the case of multiple strong shakings, more seismic energy must certainly be dissipated, which in turn further damages the structural members. Loulelis et al. (2012) have attempted to quantify the

damage index using the Park and Ang (1985) and Krawinkler and Zohrei (1983) equations. The Park and Ang (1985) damage index is defined by considering the combination of the maximum displacement and the total energy dissipated; however, that equation is originally defined for a reinforced concrete structure; thus, it might not be suitable for a steel structure. Meanwhile, the Krawinkler and Zohrei (1983) damage index considers the low-cycle fatigue phenomenon that occurs in a steel member. However, this criterion is outdated because as we know a bunch of improvement in the quality of steel material, steel connection, and welding has been made in the past decades following the occurrence of 1994 Northridge and 1995 Kobe Earthquake to prevent the premature brittle fracture and develop a ductile fracture failure mode. Therefore, the actual structural damage of SMRFs under multiple earthquake excitations needs to be evaluated using the recent evaluation criterion that considers the ductile fracture failure mode.

Moreover, most prior studies do not take into account the deterioration effect of the damaged structural member, especially on the columns, and they mainly employ a bilinear or trilinear model that considers only the material strain hardening without strength deterioration. However, in the current seismic design practice, even under the sway mechanism, the formation of a plastic hinge at the 1st story column base is allowed (Mazzolani and Piluso 1996, Goel et al. 2010); thus, there is a possibility that the column may undergo a deterioration after this plastification, and the limitation of the seismic performance of SMRFs are determined by the deteriorated column members (Yamada and Akiyama 1994). If the strength and stiffness deterioration of the column members are simulated in the analysis, how the structure behaves and the damage accumulates under multiple strong ground motion excitations currently remain unclear.

Li et al. (2014) and Ruiz-Garcia and Aguilar (2015) consider strength and stiffness deterioration in their analytical model using a hysteretic model proposed by Ibarra et al. (2005) and Lignos and Krawinkler (2011). Both of these studies focus on evaluating the collapse capacity of a 4-story SMRF building model under main shock-aftershock sequences by conducting the incremental dynamic analysis (IDA). They found that the collapse probability of the SMRF model under main shock-aftershock sequences is higher than that under the main shock only. This finding proves that a structure is more vulnerable to collapse under multiple strong shocks; however, in both of those studies, the effect of strength deterioration of the behavior and performance of SMRFs subjected to multiple strong motions has not been analyzed in detail. In addition, the effect of column strength deterioration may vary depending

on the structural design parameters of the models; however, in both of those studies, a wide variety of SMRF models with various structural design parameters, such as the width-to-thickness ratio and column-to-beam moment capacity ratio, have not been considered in the analysis.

Furthermore, the effects of multiple earthquakes on the steel moment-resisting frames (SMRFs) have been evaluated by several researchers through numerical analyses. All of these numerical analysis results are valuable resources used to study the effects of multiple earthquakes. However, the need to conduct experimental tests to further clarify the effects of multiple earthquakes is inevitable because the experimental test provides an actual verification by considering all the complex interactions within the structure that in some cases cannot be captured by the analytical model. However, up until now, there is no experimental investigation that specifically simulating the occurrence of multiple earthquakes.

The experimental investigation of beam-to-column connection mostly employed an incremental loading protocol (Building Research Institute and Japan Iron and Steel Federation 2002, Krawinkler et al. 2000, American Institute of Steel Construction 2005) to measure the plastic deformation capacity or a constant loading history to measure the low-cycle fatigue performance of the connection (Kishiki et al. 2019). Meanwhile, in terms of an experimental investigation on full-scale SMRFs, a number of experimental tests have been conducted (Nakashima et al. 2006, Nakashima et al. 2007, Yamada et al. 2008, Suita et al. 2008). Nakashima et al. (2006) conducted a cyclic-loading test of a full-scale, three-story SMRF to acquire real information about the damage and strength deterioration of the structure and to study the interactions between the structural and nonstructural components. In addition, Nakashima et al. (2007) conducted another cyclic loading test of full-scale, two-story SMRF to study the interaction (composite action) between the steel beam and the reinforced concrete (RC) floor slab. Moreover, Yamada et al. (2008) and Suita et al. (2008) conducted a shaking table test of a full-scale, four-story SMRF to evaluate the performance of the building against the various levels of ground motion. However, an experimental test of full-scale SMRFs that aims to specifically investigate the effect of multiple earthquakes has not been conducted.

1.3 Objectives and Research Scheme

The main objective of this research is to comprehensively evaluate the actual seismic performance of SMRFs under multiple earthquakes. The seismic performance is evaluated in

multiple factors, such as the behavior of SMRFs under multiple earthquakes, the actual damage state and the accumulation of damage under multiple earthquakes, and the collapse fragility under multiple earthquakes. To achieve the objective, extensive numerical analysis and experimental verifications are conducted.

Figure 1-2 shows the overall research scheme of this research. The numerical analysis is mainly divided into two parts considering the non-deteriorated model and deteriorated model. The non-deteriorated model represents the steel moment-resisting frames with high ductility. In this model, the deterioration effect caused by local buckling of column members is not considered. Instead, the main focus is the ductile fracture of beam members because the application of the strong column weak beam concept makes the beam members are generally weaker than the column members. In the analysis using the non-deteriorated model, the structure is expected to have high seismic performance under multiple strong ground motion excitations. This kind of building model represents the upper-limit or the strongest structure that could be provided by the current seismic design code.

Meanwhile, the counterpart deteriorated model considers the effect of strength and stiffness deterioration due to local buckling of column members. This model is also important to be considered because under strong shakings of the earthquake, in general, the occurrence of local buckling on the column members is unavoidable. By considering such deterioration to possibly occur between the excitations, the strength of the structure is expected to be weaker when the number of earthquake excitations increases. Thus, the seismic performance is also expected to be lower than that of the non-deteriorated model.

Moreover, to verify the analytical result, an experimental test of beam-to-column connections and full-scale steel frames is conducted. The loading histories used in the experimental test are created using the numerical analysis results. These loading histories simulate the occurrence of multiple earthquakes. The beam-to-column connection test mainly considers the ductile fracture failure mode of the beam connections. Through the beam-to-column test, the reliability of the cumulative damage evaluation method used in the numerical analysis will be verified. Meanwhile, in the full-scale steel frame test, not only the ductile fracture but also other factors such as local buckling, the existence of concrete slab (composite steel beam), and the nonstructural components are all accompanied in the test. The result obtained from the steel frames test will be compared with those obtained from the numerical

analysis. Through the comparison and verification, the overall seismic performance of SMRFs subjected to multiple earthquakes will be comprehensively summarized and concluded.

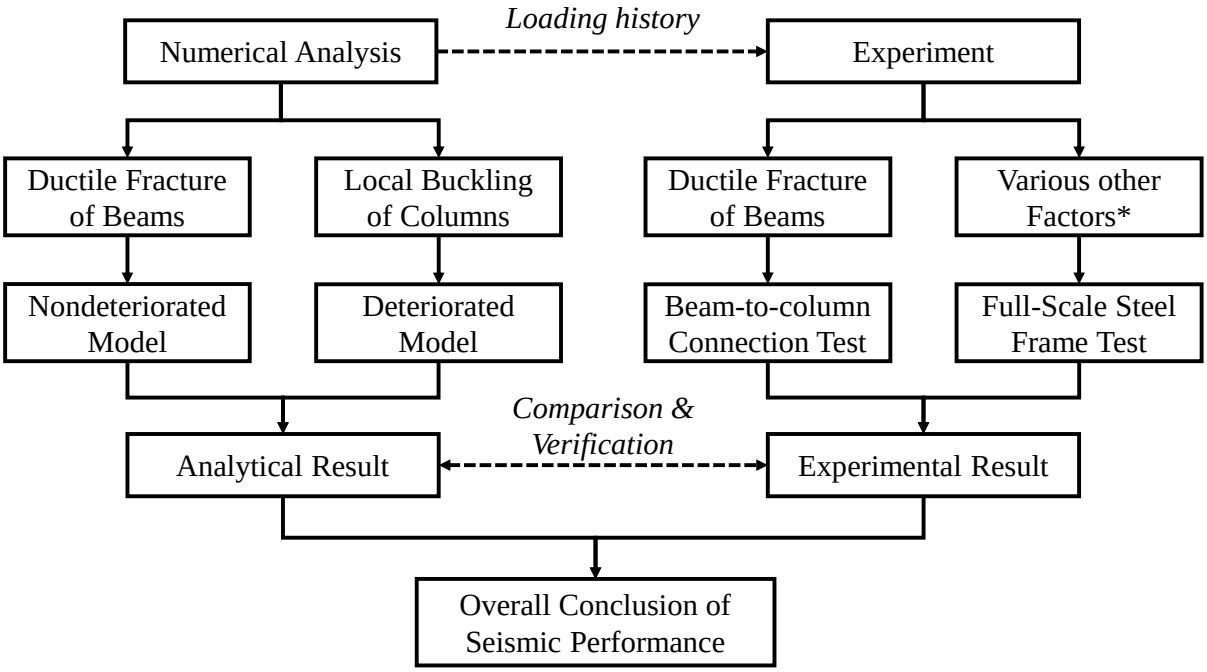

*) Such as local buckling, concrete slab, and nonstructural components

Figure 1-2 Research scheme

1.4 Systematics of Thesis

The organization of this thesis is mainly divided into five chapters. **Chapter 1** covers the introduction to the research to give an overview and the idea of the study. This chapter consists of the background, statement of problems, objectives, research scheme, and systematics of the thesis.

In **Chapter 2**, the response analysis using the non-deteriorated model is presented. Through this chapter, the seismic performance of SMRFs under multiple earthquakes is evaluated using the non-deteriorated model. The behavior of the structure, the actual damage state, the accumulation of damage, and the collapse fragility is comprehensively evaluated. In addition, the beam-to-column connection test is conducted. The loading history used in the test is created from the response analysis of the non-deteriorated model. Through this experimental

test, the reliability of the cumulative damage evaluation method used in the numerical analysis is verified.

In **Chapter 3**, the response analysis using the deteriorated model is presented. Similar with that of Chapter 2, in this chapter, the seismic performance of SMRFs under multiple earthquakes is evaluated by considering the effect of strength and stiffness deteriorated caused by local buckling of column members. The behavior of the structure, the actual damage state, the accumulation of damage, and the collapse fragility is comprehensively evaluated and compared with those of the non-deteriorated model.

In **Chapter 4**, the full-scale steel frame test is presented. The loading history used in the experiment is created from the numerical analysis result and simulating the occurrence of multiple earthquakes. Through this experiment, the performance of SMRFs is realistically evaluated. The result obtained from the experiment is compared with the numerical analysis result to further verify the performance of SMRFs under multiple earthquakes.

As a summary of all the obtained results, either through numerical analysis or experimental test, a simple design recommendation and the overall conclusion of the seismic performance of SMRFs subjected to multiple earthquakes is presented in **Chapter 5**.

2. Response Analysis of Non-deteriorated SMRF Model Subjected to Multiple Earthquakes

2.1 Introduction

In this chapter, the seismic performance of SMRFs subjected to multiple earthquakes is evaluated using the non-deteriorated models. In this non-deteriorated model, the effect of strength deterioration of any structural members, e.g., due to local buckling, is not considered. Six non-deteriorated SMRF models are analyzed by conducting a series of inelastic time-history response analyses that simulate the case of multiple earthquakes. The models consist of two parameters, i.e., the number of stories and the strength of the column base. The number of stories is taken as one of the parameters because models with a different number of stories are expected to have different natural periods and characteristic dissipated energy distributions. In addition, the variation in the strength of the column base mainly determines whether slip behavior occurs. The effect of the slip of the column base on the performance of SMRFs under multiple earthquakes, in particular, has not yet been discussed by any researchers. Through the inelastic response analysis, the behavior of the structure, the actual damage state, the accumulation of damage, and the collapse fragility are evaluated. In this chapter, the damage index of the member is represented by the cumulative damage at the beam end since the application of the strong-column–weak-beam concept in the design results in the beams becoming the weakest member of the SMRF. In addition, the influence of random and incremental-decremental seismic sequence are also investigated. Moreover, the beam-to-column connection test is conducted. The loading history used in the test was created from the response analysis of the non-deteriorated model. Through this experimental test, the reliability of the cumulative damage evaluation method used in the numerical analysis is verified.

2.2 Analytical Procedure

2.2.1 Outline of Model

The infinite uniform plane frame model (Yamada et al. 1996) is used as the analytical model with a typical story height of 3.5 m and span of 7 m, as illustrated in Figure 2-1(a). This plane frame model assumes that an infinite number of SMRFs with uniform size exist

throughout the plane so that simply taking one bay of the frame could represent the whole response of the frame because the response will be uniform in every bay. For the numerical modeling, the components are modeled as a rigid beam with elasto-plastic hinges at both ends while the joints (panels and column bases) are modeled as an elasto-plastic hinge as illustrated in Figure 2-1(b). The weight per story per span is assumed to be 400 kN. Columns and panel zones have square hollow sections (SHSs) with BCR295 grade steel (nominal yield strength of 295 N/mm^2 and nominal tensile strength of 400 N/mm^2), beams have wide-flange sections with SN400 grade steel (nominal yield strength of 235 N/mm^2 and nominal tensile strength of 400 N/mm^2), and the column base is an exposed-type of column base (with the bolt configuration as shown in Figure 2-2). A more detail explanation about the infinite uniform plane frame model is included in Appendix A. In the time history response analysis, the average acceleration method is used for the numerical integration with a time step of 1/2000 s. In addition, the 2% Rayleigh damping for the 1^{st} and 2^{nd} natural periods and the *P-Δ* effect are considered in this analysis.

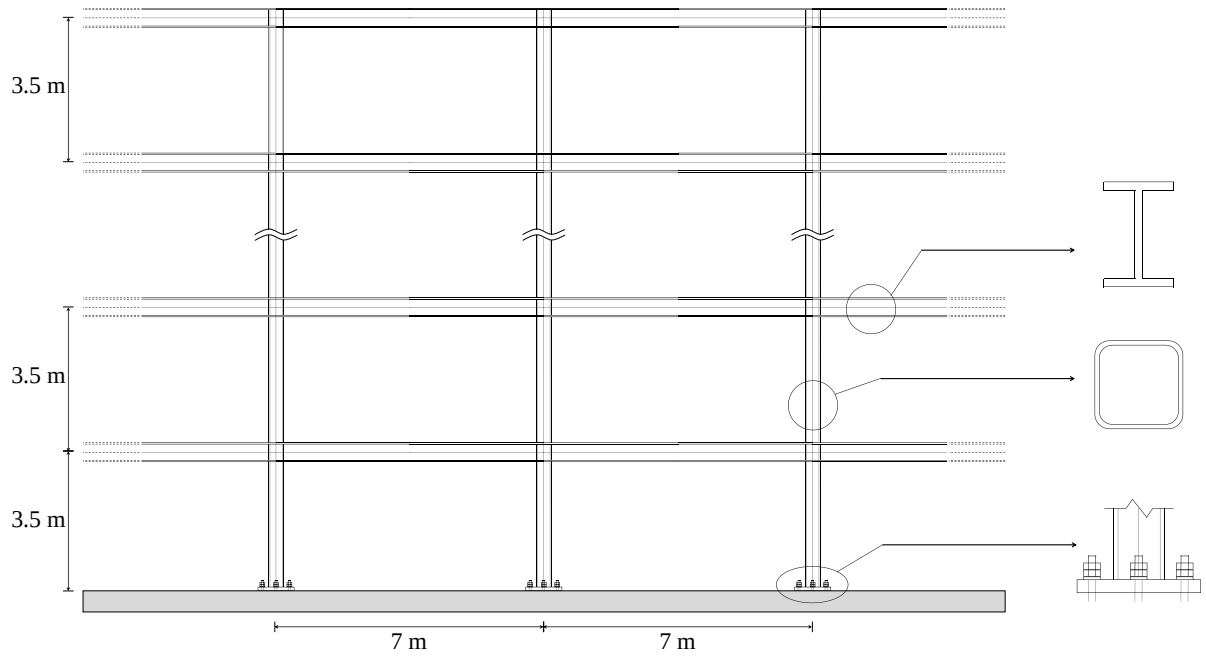

(a) Infinite plane SMRFs

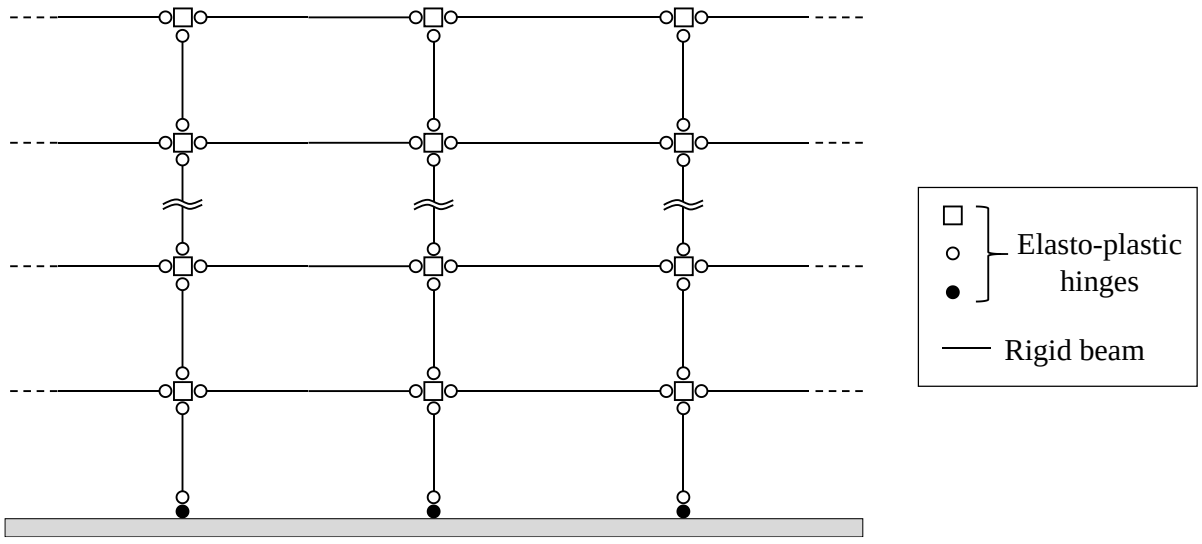

(b) Numerical model

Figure 2-1 Infinite uniform plane frame model

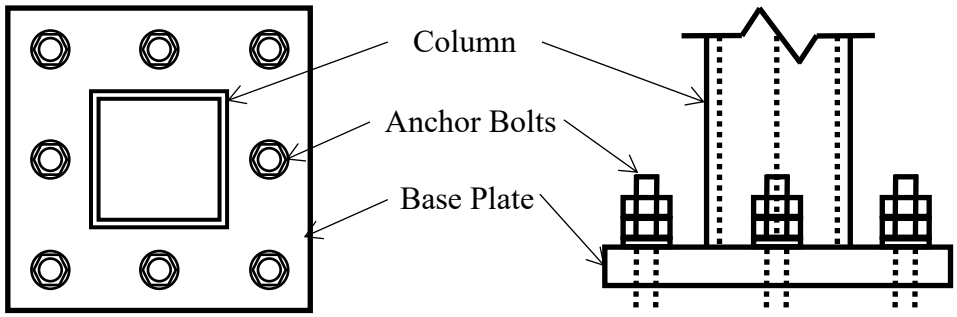

Figure 2-2 Configuration of exposed-type column base

2.2.2 Parameter and Building Model

Six types of SMRFs, named 3-13, 6-13, 9-13, 3-07, 6-07, and 9-07, are analyzed. These frames consist of two main parameters, i.e., the number of stories and the ratio of the moment capacities of the column base and the 1st story column. The first index of the models' names represents the number of stories. The last two indices indicate the moment capacity ratio of column base to 1st story column, which is equal to 1.3 in the case of strong-type column base and 0.7 in the case of the weak-type column base. The models are designed using a plastic design method for severe earthquakes based on the Japanese seismic design code. In the code, a severe earthquake approximately corresponds to PGV (peak ground velocity) = 0.5 m/s. Some important assumptions and concepts used during the design are highlighted and summarized as follows.

- The same size of beam and column are used in every three stories.
- The strong-column–weak-beam concept is applied and, according to the Building Standard Law of Japan (2013a), the column-to-beam moment ratio ($_cM_p/_bM_p$) should be greater than or equal to 1.5.
- The cross-section of columns and beams are designed to be in FA rank; thus, the *Ds* value to calculate the required lateral strength is equal to 0.25 (Building Center of Japan 2013b).
- The width-to-thickness ratio is taken as the limit value of the FA rank structural members. For example, the width-to-flange thickness ratio of SN400 wide-flange section should be less than or equal to 9.0 to be classified as FA rank. Then, during the design, the width-to-flange thickness ratio is set as close to that value.
- For wide-flange section, the flange thickness is taken as 1.5 times the web thickness.

- The yield strength of all members is assumed to be 1.1 times of the nominal yield strength.
- Plastic hinges are assumed to be formed at the beams' end, 1st story column lower end, and top story column upper end.
- The total beams' strength at one story is assumed to be distributed half each to the upper and lower story.

The details of members' cross section, ultimate lateral strength capacity (Q_{ui}), required ultimate lateral strength (Q_{uni}), column-to-beam strength ratio ($_cM_p/_bM_p$), diameter and ultimate strength of anchor bolts, and 1st and 2nd mode natural period of each model are shown in Appendix B. In addition, a pushover analysis is performed to check the capacity of the models against the required ultimate lateral strength (Q_{uni}). The pushover analysis is conducted using the force control method assuming that the force distribution at each story follows the A_i distribution (Building Center of Japan 2013c). The pushover analysis results are also shown in Appendix B.

2.2.3 Hysteresis Characteristics of Structural Member

The hysteresis loop characteristic of the members is based on the decomposition of the skeleton part, the Bauschinger part, and the elastic unloading part, as illustrated in Figure 2-3 (Kato et al. 1973, Akiyama and Takahashi 1990). The skeleton part corresponds with the load-deformation relationship under monotonic loading (Kato et al. 1973, Akiyama and Takahashi 1990). Moreover, the Bauschinger part is modeled using the simplified model proposed by Akiyama and Takahashi (1990). Last, the elastic unloading part is the unloading part of the loops that are characterized by the same stiffness as the original elastic stiffness of the member. The skeleton curve models of the columns and beams are shown in Figure 2-4, i.e., a tri-linear model considering the strain hardening effect of the members. Note that even though local buckling is likely to occur in the column section, in the present analysis, that type of deterioration effect is not considered, and the column is assumed to be strong enough to maintain its restoring force without any deterioration. For the exposed-type column base, the hysteresis model is shown in Figure 2-5. The model uses a form of the slip-type model that considers the effect of the moment resistance due to axial force (M_n) and strain hardening of the anchor bolt (K_p) (Yamada et al. 1997).

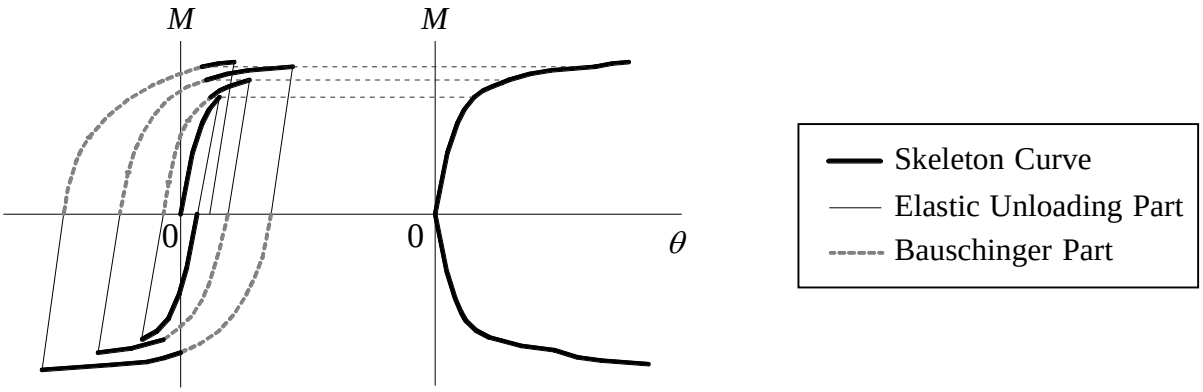

Figure 2-3 Decomposition of hysteresis loops

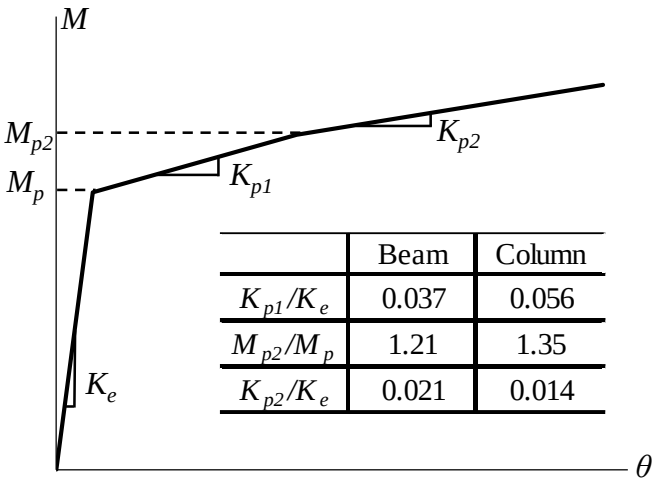

	Beam	Column
K_{p1}/K_e	0.037	0.056
M_{p2}/M_p	1.21	1.35
K_{p2}/K_e	0.021	0.014

Figure 2-4 Tri-linear model of the beam and column

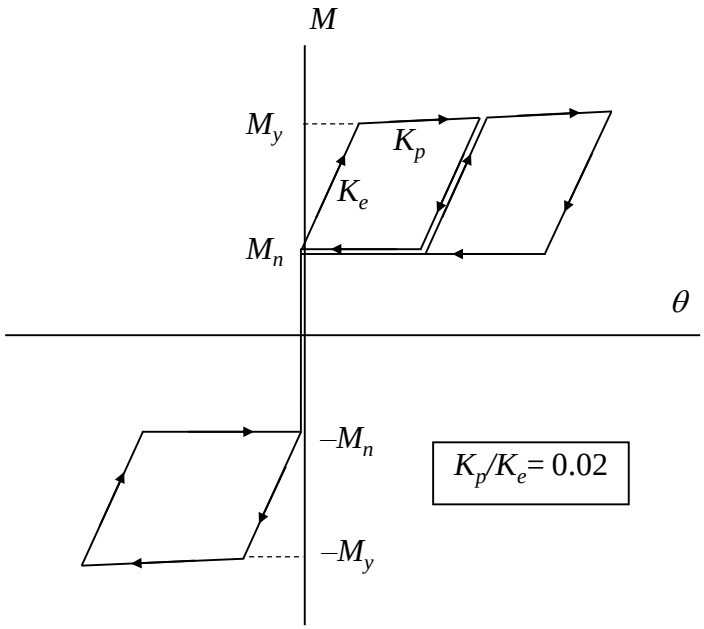

Figure 2-5 Slip-type model of the exposed-type column base

2.2.4 Input Ground Motion

For the input ground motion in the inelastic analysis, ten ground motion records are used, as listed in Table 2-1. All the records are scaled based on the PGV value to control their input energy. Three intensities are considered, i.e., PGV = 0.5 m/s (design level), 0.75 m/s, and 1.0 m/s. The velocity response spectra of all records at the design level and the 1st mode natural period of all models are plotted together in Figure 2-6. In every analysis, five repeated excitations of the same input wave and the same intensity are considered to simulate multiple earthquake sequences. The reason for using the same records and the same intensity is for the simplicity in presenting the analytical result because the trend can be clearly shown. Meanwhile, the limitation of the number of excitations to five excitations is because the occurrence of more than five strong ground motions in a short period of time is considered as an extremely rare case. To simulate the real condition of the seismic sequences, between excitations, 30 seconds of zero acceleration was added to the original input ground acceleration. In other words, during that 30 seconds, the structure will be freely vibrated until its response become constant (i.e., the structure has stopped vibrating).

Table 2-1 Ground motion records used in the analysis

No.	Earthquake	M_w	Seismic Record	Component	PGA (m/s^2)	PGV (m/s)
1	1940 Imperial Valley	6.95	El Centro	North-South	3.42	0.38
2	1952 Kern County	7.36	Taft	East-West	1.76	0.18
3	1968 Tokachi-oki	8.2	Hachinohe	East-West	1.81	0.37
4	1989 Loma Prieta	6.93	Gilroy Array #3	90 deg.	3.61	0.45
5	1994 Northridge	6.69	Newhall	North-South	5.78	0.97
6			Olive View	North-South	8.26	1.29
7	1995 Kobe	6.9	JMA Kobe	North-South	8.21	0.89
8	1999 Chi Chi	7.6-7.7	TCU129	East-West	9.81	0.55
9	2011 Tohoku	9	JMA Sendai	North-South	4.10	0.54
10	2016 Kumamoto (Apr. 16)	7.3	Kik-net Mashiki	East-West	11.57	1.42

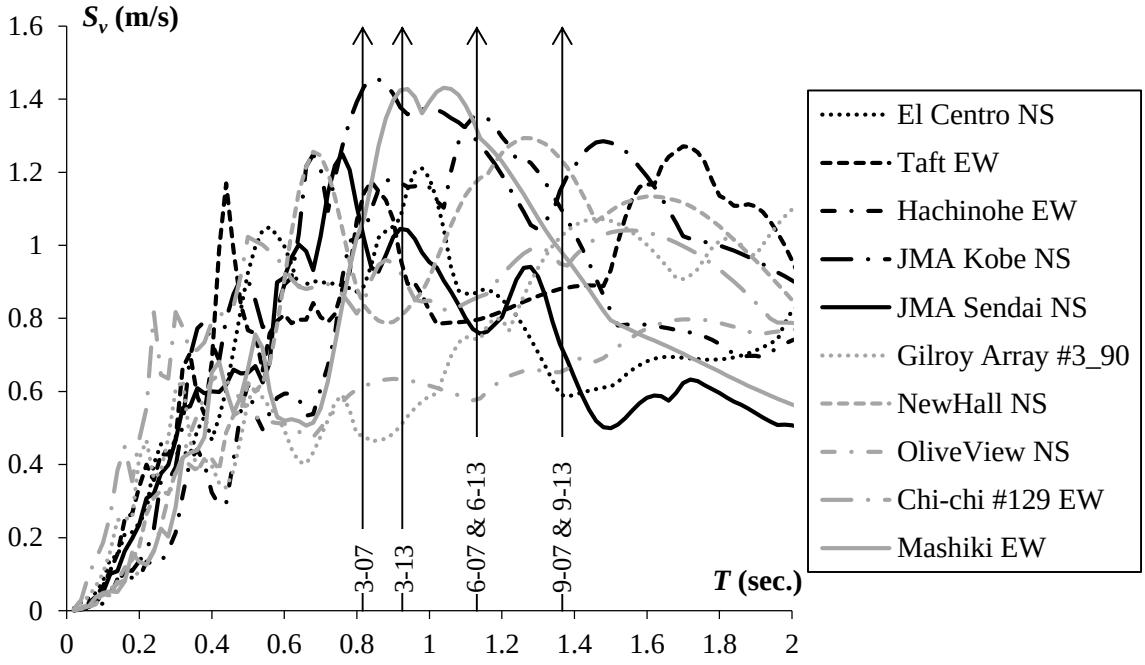

Figure 2-6 Velocity response spectra of the input ground motion at the design level (h = 5%)

2.2.5 Cumulative Damage Evaluation Method

The damage index of the structure is represented by the cumulative damage at the beam end since the application of the strong-column-weak-beam concept in the design is resulting in the beams are becoming the weakest member of the steel moment-resisting frames. To

calculate the cumulative damage of the beams, a new cumulative damage evaluation formula proposed by Kishiki et al. (2019) is used. The formula evaluates the low-cycle fatigue performance of steel beam-to-column connections that have a ductile fracture failure mode by considering the effects of decreasing the moment transfer efficiency at the beam web-to-column connection due to the slip behavior of the bolts, the out-of-plane deformation of the column flange, and the loss of web section due to the weld access hole. The proposed formula is shown in Equation (1). Here, N_f is the number of cycles to failure; $\Delta\theta_b$ is the peak-to-peak amplitude rotation angle of the beam; and J_b is the ratio of the effective yield moment at the beam web-to-column connection and the yield moment of the beam flange to the yield moment of the beam member. J_b is a factor that depends on the cross-section of the column and beam, as well as the connection detail. In calculating J_b, all the beam-to-column connection of the models is assumed to have a fully welded connection with weld access hole detail of R35+10R that conform to JASS 6 (Architectural Institute of Japan 1996).

$$N_f = 2.6 \times 10^{-3} J_b^{27.23} \times \Delta\theta_b^{6.06J_b - 8.89} \tag{1}$$

By combining $N_f - \Delta\theta_b$ relationship with Miner's Rule (Equation (2)), the cumulative damage of beam to fracture can be computed. In Equation (2), D expresses cumulative damage, and when the value of D equals 1.0, the beam is estimated to be fractured; n_i is the number of cycles with peak-to-peak amplitude rotation angle-i ($\Delta\theta_{b\text{-}i}$); and N_{fi} is calculated using Equation (1). In the case of the random loading, the number of cycles (n_i) and the corresponding peak-to-peak amplitude rotation angle ($\Delta\theta_{b\text{-}i}$) are counted using the rainflow counting method (Endo et al. 1974).

$$D = \sum_i \frac{n_i}{N_{fi}} \tag{2}$$

2.3 Analytical Result

The inelastic response is analyzed using the six models and ten input ground motions with three different ground motion intensities, as mentioned in the previous sections, thus resulting in a total of 180 cases. The damage index of the structure is represented by the cumulative

damage of the critical beam (*D*), which was calculated by the previously described method. The critical beam is the beam element that has the largest cumulative damage; this beam also commonly has the largest amount of dissipated energy. The analytical result is mainly presented in two major parts, i.e., the response of the structure caused by ground motion excitations with an intensity equal to the design level (PGV of 0.5 m/s) and greater than the design level (PGV of 0.75 m/s and 1.0 m/s).

2.3.1 Ground Motion Intensity of PGV 0.5 m/s

Under design-level excitations (PGV of 0.5 m/s), the structures show a stable behavior, even after five repeated strong ground shakings. Figure 2-7 shows one of the examples of the response of the non-deteriorated SMRFs excited by multiple ground accelerations; it is a 6-13 model that is excited by the design level of the JMA Sendai North-South (NS) record. In Figure 2-7(a), the increment in both the maximum and residual story drift angle (SDA) is relatively small, so the structure can still maintain its stability. Moreover, Figure 2-7(b) shows the cumulative damage of the critical beam (*D*) vs. the number of excitations (No. Exc.) and the hysteresis response of the critical beam in some stages of excitation. Clearly, the cumulative damage increases almost constant, i.e., the relation between *D* and the number of excitations is approximately linear. In terms of the hysteresis response of the beam, at the 1st excitation, the skeleton part can be observed, i.e., the beam's rotation increases from the elastic to the inelastic condition. However, usually starting from the 3rd excitation, the skeleton could hardly be observed, and the energy was predominantly dissipated by the Bauschinger part; thus, the beam's rotation is almost constant, as is the increment in the cumulative damage. Note that the constant increment in the cumulative damage is also related to the usage of the same input records of the five excitations.

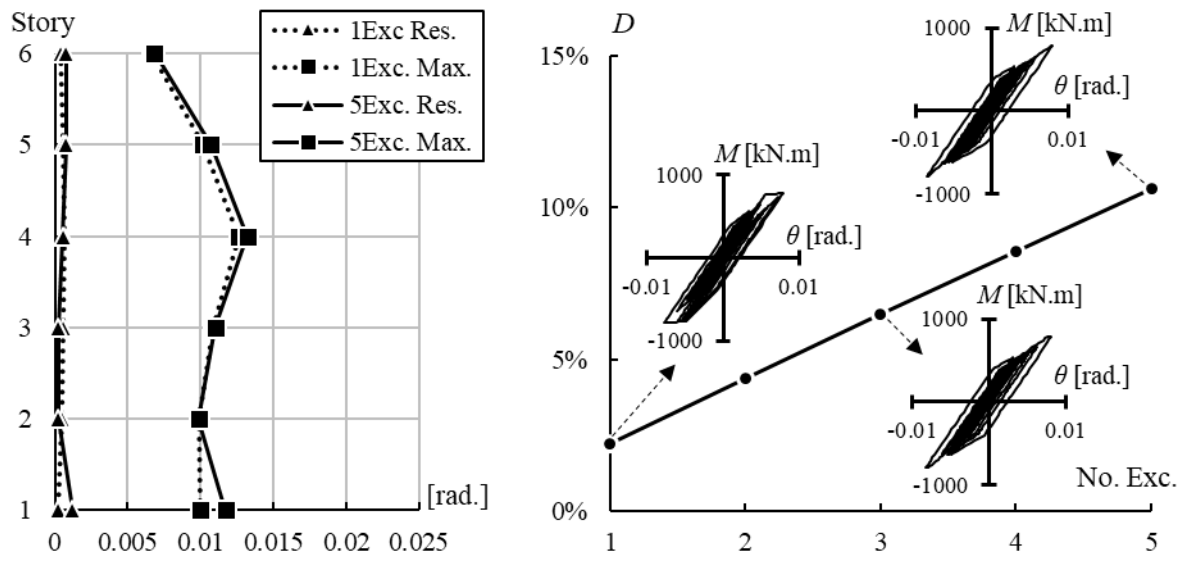

(a) story drift angle (b) critical beam's cumulative damage

Figure 2-7 PGV 0.5 m/s JMA Sendai NS excitation of the 6-13 model

In summary, the increment in maximum SDA is relatively small on average, i.e., approximately 0.005 rad, 0.0035 rad, and 0.003 rad for the 3-, 6-, and 9-story model, respectively. Moreover, the residual SDA is less than 0.01 at the 5th excitation for all cases. Regarding cumulative damage of the critical beam, it constantly increases in every excitation. At the 5th excitation, the cumulative damage of all cases ranges from 1.5% to 43.2%, and, on average, the cumulative damages for 3-, 6-, and 9-story models are 16.0%, 6.9%, and 5.7%, respectively.

Figure 2-8 shows a comparison of the critical beam's cumulative damage for different input ground motions. The cumulative damage results of the strong column base model excited by various input ground motions are shown as examples (the other results are all included in Appendix C, Figure C-1). It could be seen that the cumulative damage of the model with the same natural period is varied depending on the characteristic of the input ground motion. However, the increment in the cumulative damage still shows the same linear trend and stable behavior, regardless of the input ground motion.

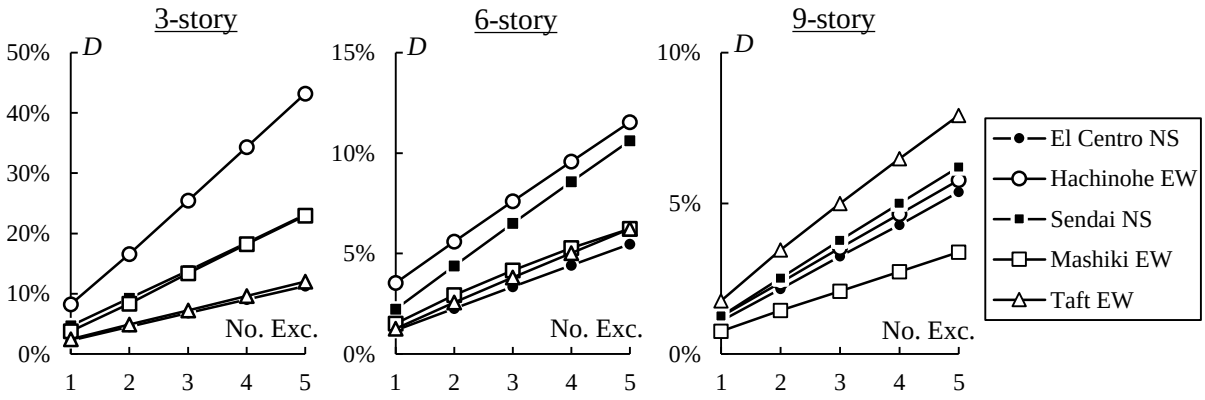

Figure 2-8 Comparison of the cumulative damage of the strong column base model for different input ground motions

A comparison of the critical beam's cumulative damage related to the two parameters of the models is shown in Figure 2-9. Figure 2-9(a) shows the comparison regarding the number of stories, one of the examples of the analytical result, i.e., the strong column base model excited by design level of JMA Sendai NS record, is shown. The 3-story building clearly has the largest cumulative damage, followed by 6-story and then 9-story; the main reason for this result is the concentration of dissipated energy. As shown in Figure 2-10, in the 3-story building, the energy is mostly dissipated by the 1st story; however, for 6- and 9-story buildings, the middle stories also absorbed a fair amount of energy. The influence of the type of column base on the cumulative damage of the critical beam is shown in Figure 2-9(b), illustrating the response of a 3-story model excited by JMA Kobe NS record as an example. In the weak column base model, the column base is expected to slip, thus increasing the beam's rotation in every excitation. However, Figure 2-9(b) shows that the cumulative damages of the model using strong and weak column bases are almost equal, and in almost all the cases, the difference between the cumulative damage at the 5th excitation of those two types is less than 8.4%, which is relatively small. However, no definite trend is observed that indicates, e.g., whether the weak column base model always suffered more damage or vice versa; the damage differs for each combination of ground motion records and the number of stories. Figure 2-11 shows the hysteresis response of the critical beam and the column base of the same case shown in Figure 2-9(b). At the 1st excitation, slip occurs; however, at the next excitation, the column base's maximum rotation angle does not significantly increase. In other words, even though a weak column base is used, as long as the upper structure is ductile, a similar stable behavior could be achieved.

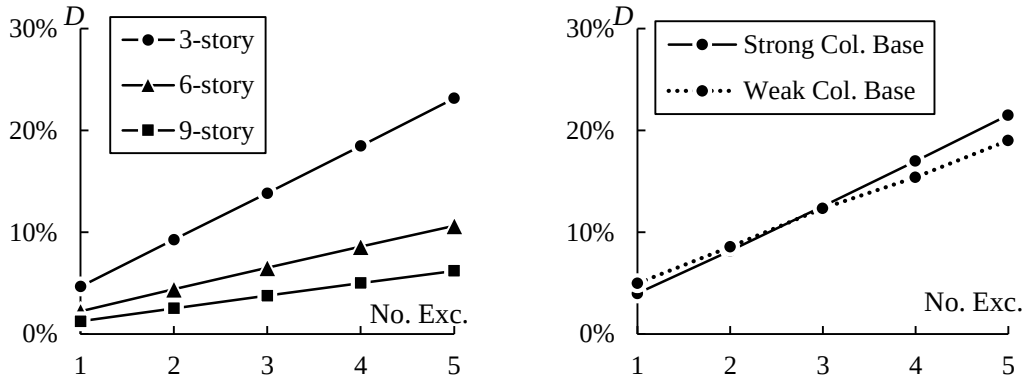

(a) PGV 0.5 m/s JMA Sendai NS excitation of the strong column base model

(b) PGV 0.5 m/s JMA Kobe NS excitation of the 3-story model

Figure 2-9 Comparison of the cumulative damage by the number of stories and the column base type

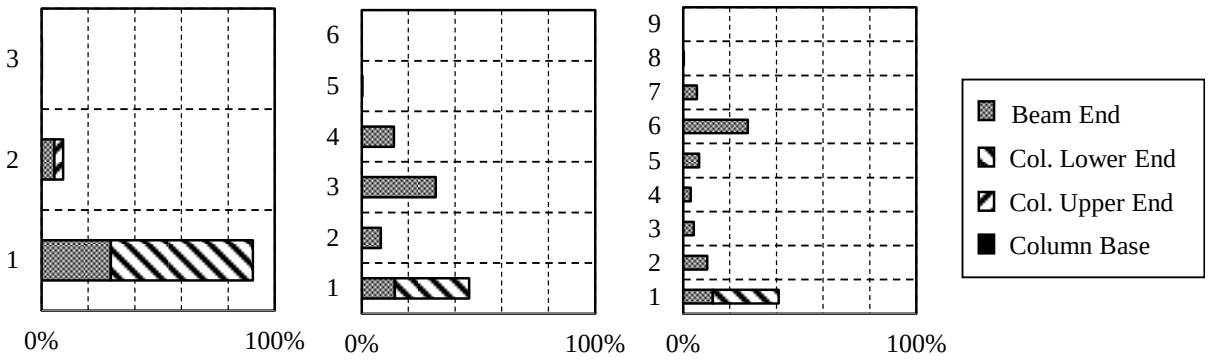

(a) 3-story (b) 6-story (c) 9-story

Figure 2-10 Distribution of dissipated energy of PGV 0.5 m/s JMA Sendai NS exc. of the strong column base type model

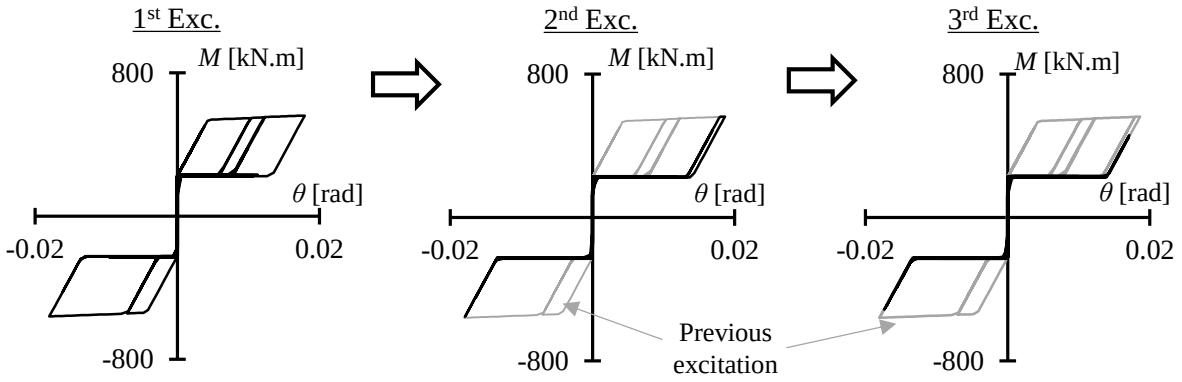

(a) column base

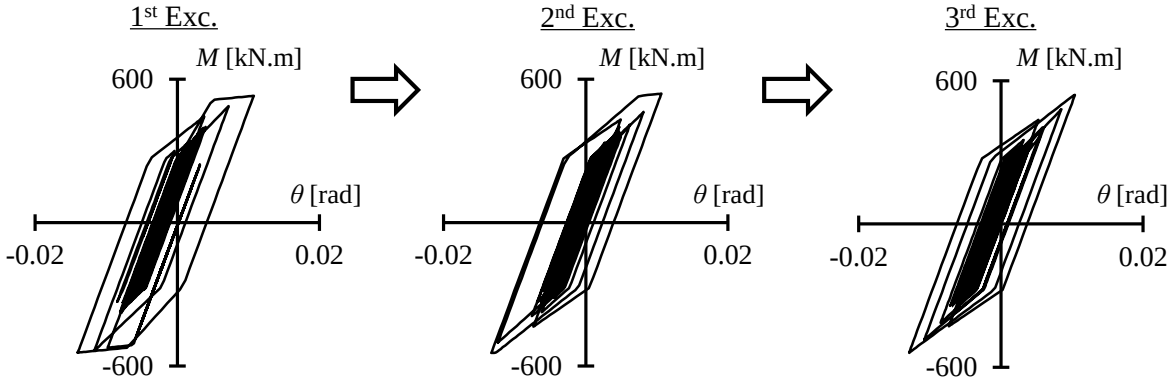

(b) critical beam

Figure 2-11 Hysteresis response of PGV 0.5 m/s JMA Kobe NS exc. of 3-07 model

2.3.2 Ground Motion Intensity of PGV 0.75 m/s and 1.0 m/s

Under multiple excitations with the PGV of 0.75 m/s and 1.0 m/s, stable behavior (Figure 2-7) is still observed in most cases. However, in several cases, a collapse occurred within the five repeated excitations. The collapse cases can be divided into two categories, i.e., local collapse via fracture of the critical beam and a collapse due to reaching the ultimate state. The critical beam is estimated to fracture when the cumulative damage (D) is equal to or greater than 1.0. Moreover, the structure is assumed to reach the ultimate state when the maximum SDA is 10% or higher. At the PGV of 0.75 m/s, the collapse occurred in 3 out of a total of 60 cases, i.e., Hachinohe EW excitation of the 3-07 and TCU129 EW and Hachinohe EW excitations of the 3-13 models. Moreover, at the PGV of 1.0 m/s, the collapse occurred in 17 of a total of 60 cases, i.e., Gilroy Array #3 90 deg., Hachinohe EW, JMA Sendai NS, and Kik-net Mashiki EW excitations of 3-07 model; TCU129 EW, Gilroy Array #3 90 deg., Hachinohe EW, JMA Kobe NS, JMA Sendai NS, Kik-net Mashiki EW, Newhall NS, and Taft EW

excitations of 3-13 model; Gilroy Array #3 90 deg. and Hachinohe EW excitations of 6-07 model; Hachinohe EW excitation of 6-13 model; Taft EW excitation of 9-07 model; and Taft EW excitation of 9-13 model. The cumulative damage of the critical beam under PGV of 0.75 m/s and 1.0 m/s are included in Appendix C, Figures C-2 and C-3, respectively. The average cumulative damages of the critical beam of the uncollapsed cases at 5^{th} excitation are 44.5%, 19.8%, and 15.2% for the 3-, 6-, and 9-story models with a PGV of 0.75 m/s, respectively, and 69.5%, 39.6%, and 30.4% for the 3-, 6-, and 9-story models with a PGV of 1.0 m/s, respectively.

Figure 2-12 shows an example where the critical beam is estimated to be fractured, i.e., 6-13 model excited by Hachinohe EW record with the PGV of 1.0 m/s. Figure 2-12(a) shows that the maximum and residual SDA of the building continue to increase significantly as the number of excitations increases until the structure starts to lose its stability. This result is demonstrated by the relationship between *D* vs. No. Exc. shown in Figure 2-12(b), which is no longer linear; for comparison, the corresponding results with the PGV of 0.5 m/s are shown in the same graph. Figure 2-12(c) shows the hysteresis response of the critical beam at several stages of excitation, revealing that the skeleton part is observed at every stage. In other words, in every stage of excitation, the beam's rotation angle becomes increasingly large, so the cumulative damage increases exponentially instead of constantly.

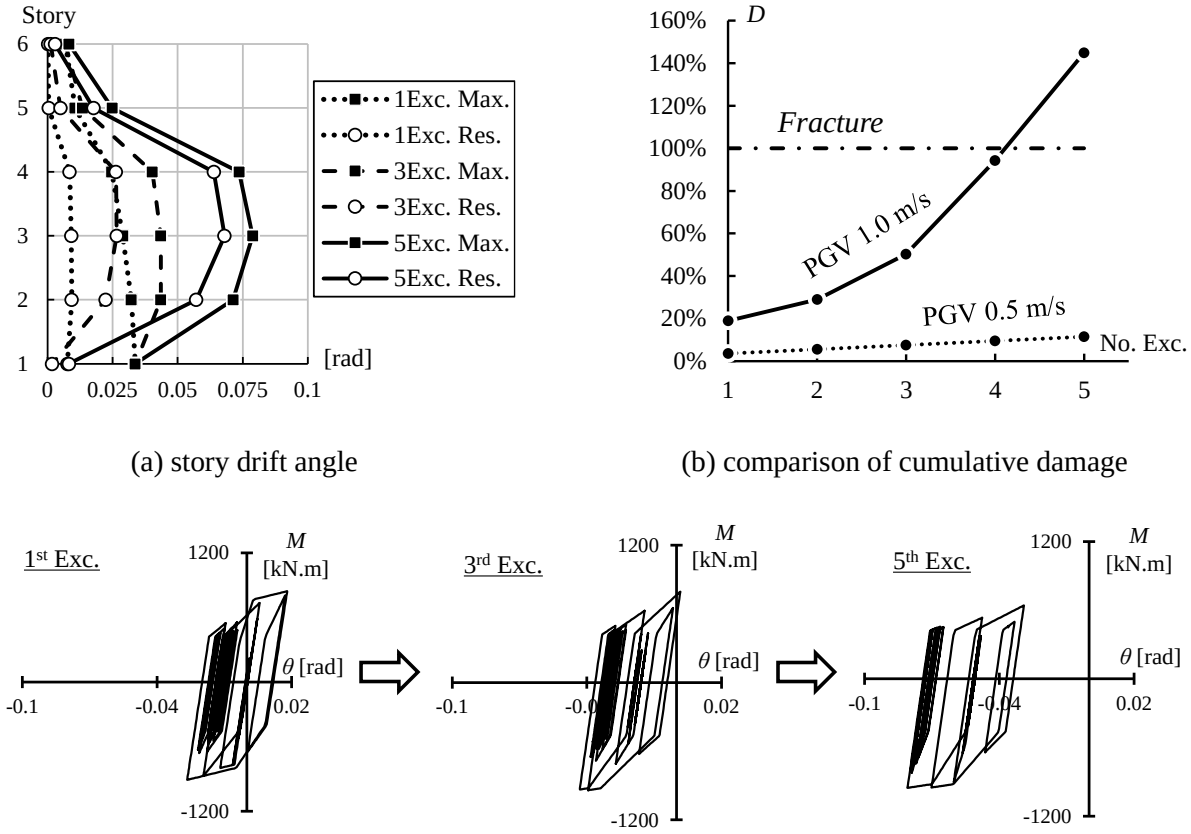

(a) story drift angle

(b) comparison of cumulative damage

(c) critical beam's hysteresis response

Figure 2-12 PGV 1.0 m/s Hachinohe EW excitation of the 6-13 model

Figure 2-13 shows an example where the structure reaches the ultimate state, i.e., 3-07 model excited by Hachinohe EW record with the PGV of 0.75 m/s. Figure 2-13(a) illustrates the weak story mechanism that occurred at the 1st story as the structure reaches the ultimate state. At the 1st excitation, the building remains stable, and plastic hinges are formed at the beam end and column upper end of the 1st story. However, at the 2nd excitation, the structure suffers large residual SDA, as shown in Figure 2-13(b). Finally, at the 3rd excitation, the maximum SDA reaches over 10%, causing the story to completely lose its stability and reach the ultimate state. Figure 2-13(c) shows the story shear vs. story drift relationship of the 1st story at the three stages of excitation; the black circle indicates the peak story shear, which is located at the 2nd excitation. This figure shows that somewhere during the 2nd excitation, the 1st story reaches the maximum capacity (indicated by the black circle in the graph) and starts to suffer large deformation until it finishes at approximately 0.05 rad of residual SDA at the end of 2nd excitation. Because the deterioration effect caused by the local buckling of members is not considered in this case, the story shear capacity is almost constant, and only a small

decrease occurs via the *P–Δ* effect. Figure 2-13(d) shows the cumulative damage of the critical beam, which exhibits a trend similar with that of the cumulative damage of beam fractured case (Figure 2-12(b)).

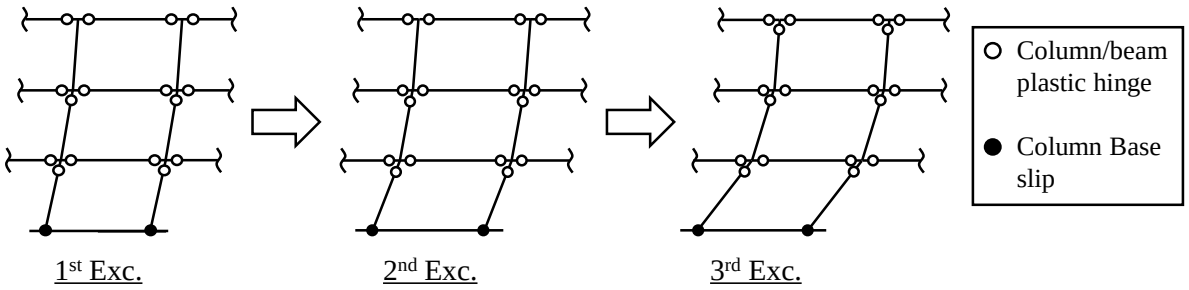

(a) weak story mechanism

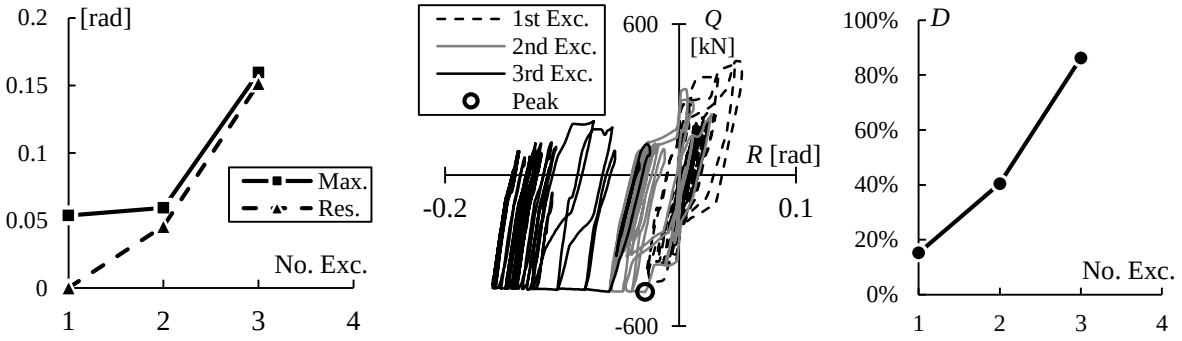

(b) 1st story drift angle (c) 1st story shear vs. story drift (d) cumulative damage

Figure 2-13 PGV 0.75 m/s Hachinohe EW excitation of the 3-07 model

2.3.3 Collapse Fragility

The collapse fragility of the non-deteriorated SMRF models under multiple earthquake excitations is investigated in this section. Figure 2-14 shows the percentage of uncollapsed cases by the number of excitations for various intensities. As shown in the figure, under the one excitation, almost all cases do not collapse. However, as the number of excitations increase, the percentage of uncollapsed cases decreases. In this study, the simple and uniform criterion of more than or equal to 90% (≥ 90%) of uncollapsed cases is used. 90% is considered to be high enough since the occurrence of multiple strong ground motions in a short period of time is not very common. By using that simple criterion, it can be seen that in the case of the non-deteriorated SMRF models, the number of excitations that could be resisted by the structure

before collapsing is five excitations of PGV intensity of 0.75 m/s or three excitations of PGV intensity of 1.0 m/s.

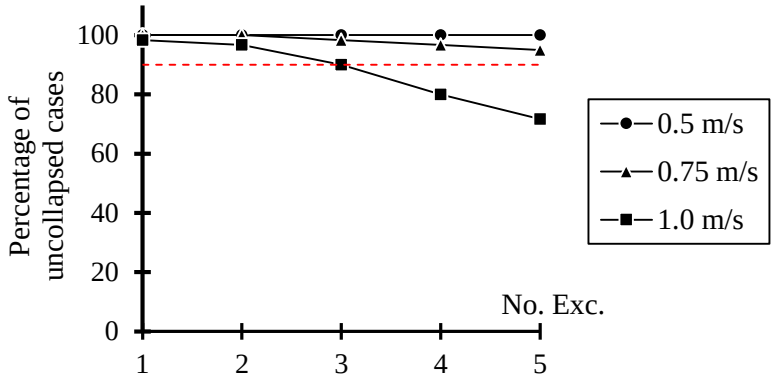

Figure 2-14 Percentage of uncollapsed cases by number of excitations and input ground motion intensity

2.4 Random and Incremental-Decremental Sequences

In the previous section, the inelastic time-history response analysis was conducted using the simple repeated input ground motion with the same intensity to simulate the occurrence of multiple earthquakes. However, the real earthquake sequences might occur with different wave characteristics and different intensities. Thus, in this section, the effect of random sequences (different input records but same intensity) and incremental-decremental sequences (same input records but different intensity) will be investigated.

2.4.1 Random Sequences

To investigate the effect of random sequences, two groups that consist of ten different random sequences are created. The records for the 1st, 2nd, until 5th excitations are chosen randomly among the ten input ground motion records listed in Table 2-5 by assuming the uniform probability density function (each record has the same chance to be chosen). The list of records for random sequences group 1 (G1) and group 2 (G2) are shown in Table 2-2 and Table 2-3, respectively. Same with the previous analysis, three different intensities are used, i.e., PGV of 0.5 m/s, 0.75 m/s, and 1.0 m/s. Then, the inelastic response analysis is conducted using the random sequence input ground motions on the six non-deteriorated SMRF models.

Table 2-2 List of random sequences group 1 (G1)

Case	1st Exc.	2nd Exc.	3rd Exc.	4th Exc.	5th Exc.
1	Kik-net Mashiki	El Centro	JMA Sendai	Gilroy Array #3	JMA Sendai
2	Newhall	JMA Sendai	Hachinohe	JMA Kobe	Olive View
3	JMA Sendai	JMA Sendai	Gilroy Array #3	El Centro	Taft
4	Olive View	Kik-net Mashiki	Newhall	Gilroy Array #3	Gilroy Array #3
5	El Centro	JMA Kobe	El Centro	JMA Sendai	El Centro
6	El Centro	Hachinohe	Newhall	JMA Kobe	JMA Kobe
7	Newhall	El Centro	Kik-net Mashiki	Newhall	Gilroy Array #3
8	Gilroy Array #3	JMA Kobe	Gilroy Array #3	Olive View	Newhall
9	Hachinohe	Newhall	Hachinohe	TCU129	JMA Sendai
10	JMA Kobe	JMA Sendai	Olive View	JMA Sendai	TCU129

Table 2-3 List of random sequences group 2 (G2)

Case	1st Exc.	2nd Exc.	3rd Exc.	4th Exc.	5th Exc.
11	JMA Kobe	Olive View	Newhall	Kik-net Mashiki	Taft
12	JMA Sendai	El Centro	Taft	El Centro	Hachinohe
13	Olive View	Olive View	Taft	Gilroy Array #3	Kik-net Mashiki
14	Hachinohe	Olive View	TCU129	Taft	Newhall
15	Gilroy Array #3	Hachinohe	Gilroy Array #3	JMA Kobe	Olive View
16	Hachinohe	JMA Sendai	Taft	TCU129	Newhall
17	Olive View	Newhall	Newhall	Hachinohe	Taft
18	Olive View	El Centro	Hachinohe	JMA Sendai	TCU129
19	Kik-net Mashiki	JMA Sendai	TCU129	JMA Kobe	TCU129
20	El Centro	JMA Sendai	Taft	Newhall	Kik-net Mashiki

The cumulative damage of the critical beam under the random input sequences is computed using the same damage evaluation method used in the previous section. Figure 2-15 shows the comparison of average cumulative damage for PGV intensity of 0.5 m/s. The complete results of the cumulative damage under random sequences are included in Figures C-4 to C-6 and Figures C-7 to C-9 (Appendix C) for random sequence group 1 and group 2, respectively. As shown in Figure 2-15, the average cumulative damage under the repeated or random sequence is almost the same, especially in cases where the structure stays stable, and

as found in the previous section, the structure can maintain its stable behavior under PGV intensity of 0.5 m/s. To compare the result in cases where collapse might occur (under PGV intensity of 0.75 m/s and 1.0 m/s), the comparison of collapse fragility is investigated, as shown in Figure 2-16. As shown in the figure, the percentage of uncollapsed cases under repeated and random sequences are almost the same. The largest difference of percentage is between repeated and random sequence group 2 under PGV intensity of 1.0 m/s at the 3rd excitation which is around 8.3% difference or 5 cases of the total of 60 cases. Overall, the results found by using the repeated and random sequences are not shown a significant difference in terms of average cumulative damage and collapse fragility. Thus, using the simple repeated sequence could be more favorable considering the easiness in analysis and presenting the result.

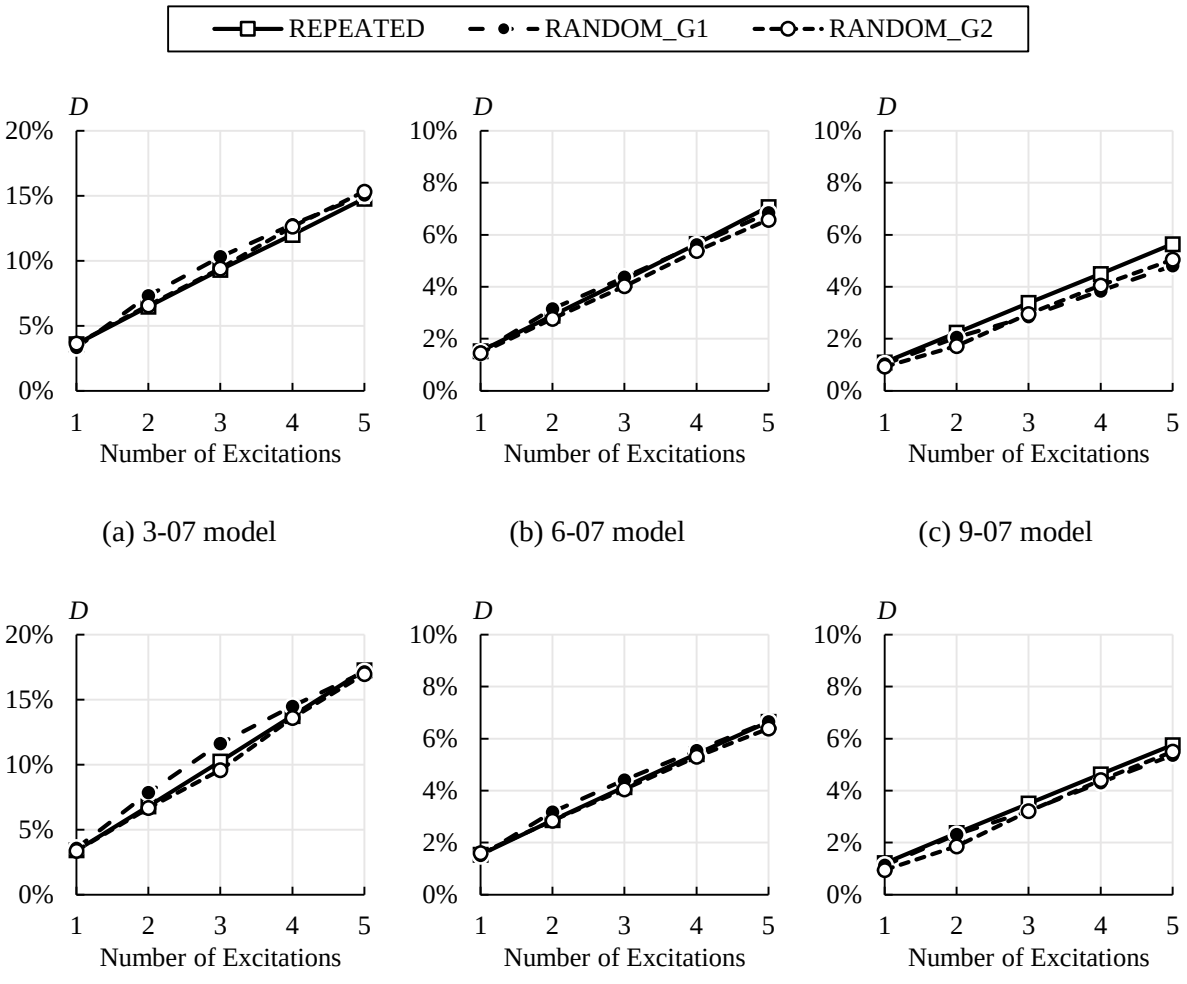

(a) 3-07 model (b) 6-07 model (c) 9-07 model

(d) 3-13 model (e) 6-13 model (f) 9-13 model

Figure 2-15 Comparison of average cumulative damage under input ground motion intensity of PGV 0.5 m/s by sequence types

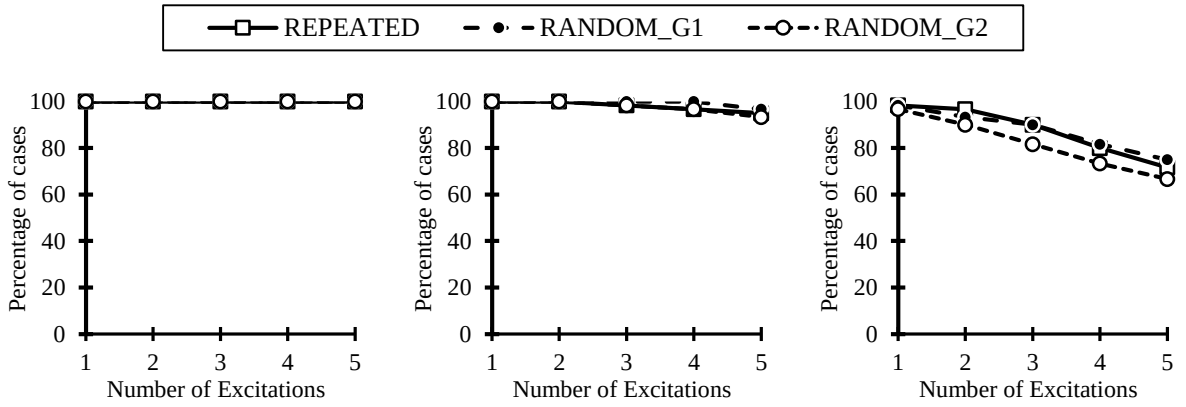

(a) PGV 0.5 m/s (b) PGV 0.75 m/s (c) PGV 1.0 m/s

Figure 2-16 Comparison of collapse fragility by sequence types

2.4.2 Incremental-Decremental Sequences

In this section, the effect of variation in the intensity is specifically investigated. Two types of sequences called the incremental and decremental sequences, are created. For the incremental sequence, the intensity of the 1st, 2nd, and 3rd excitations are 0.5, 0.75, and 1.0 m/s, respectively, while for the decremental sequence, the intensities are being reversed (1.0, 0.75, and 0.5 m/s for the 1st, 2nd, and 3rd excitations, respectively). The incremental and decremental sequences can also be seen as the representative of the foreshock-main shock and main shock-aftershock type of sequences, respectively. For the 1st, 2nd, and 3rd excitations, the same records are used. Then, the inelastic response analysis is conducted on the six non-deteriorated SMRF models and the cumulative damage is computed. The complete results of the calculated cumulative damage of the critical beam are shown in Figure C-10 of Appendix C. Figure 2-17 shows the comparison of cumulative damage under incremental and decremental sequences at the 3rd or the last excitation. All cases are plotted in the figure except for the case of 3-13 model excited by Hachinohe EW records because the cumulative damage under the decremental sequence has reached over 100% at the 1st excitation. As shown in the figure, the cumulative damage at the last excitation is almost the same except for two cases in the gray dashed line circle in which the cumulative damage under incremental sequences is much higher than that of decremental sequences. This is caused by excessive deformation under the incremental sequence. As found in the previous section, the structure generally starts to lose its stability when the residual story drift is around 4% or larger. In those two cases, the residual story drift angle under the incremental sequence is 5.8% and 6.16%, which indicates that the structure no longer stable. Aside from those two cases, in all the other cases where the structure is still able

to maintain its stability, the difference of cumulative damage under incremental and decremental sequences is shown in Figure 2-18. As shown in the figure, the difference of cumulative damage for all cases is less than 10% which is relatively small. Thus, it could be concluded that as long as the structure can maintain the stable behavior, the influence of incremental type or decremental type of input intensity is not significant. However, even though only two cases are found in the current analysis, the incremental type of sequence might result in higher cumulative damage in cases where the structure loses its stability.

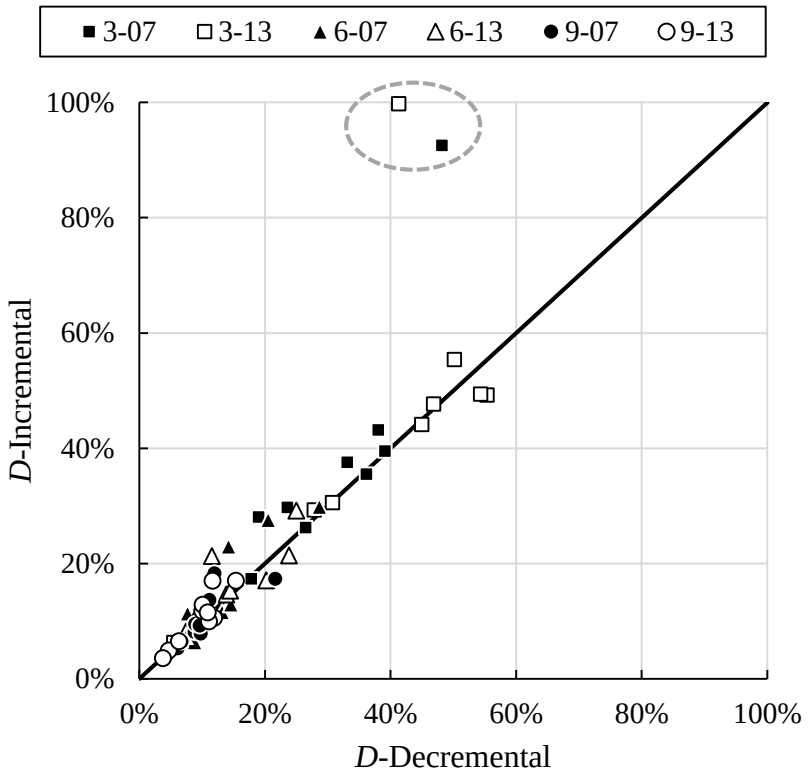

Figure 2-17 Comparison of cumulative damage at the 3rd (last) excitation under incremental and decremental sequences

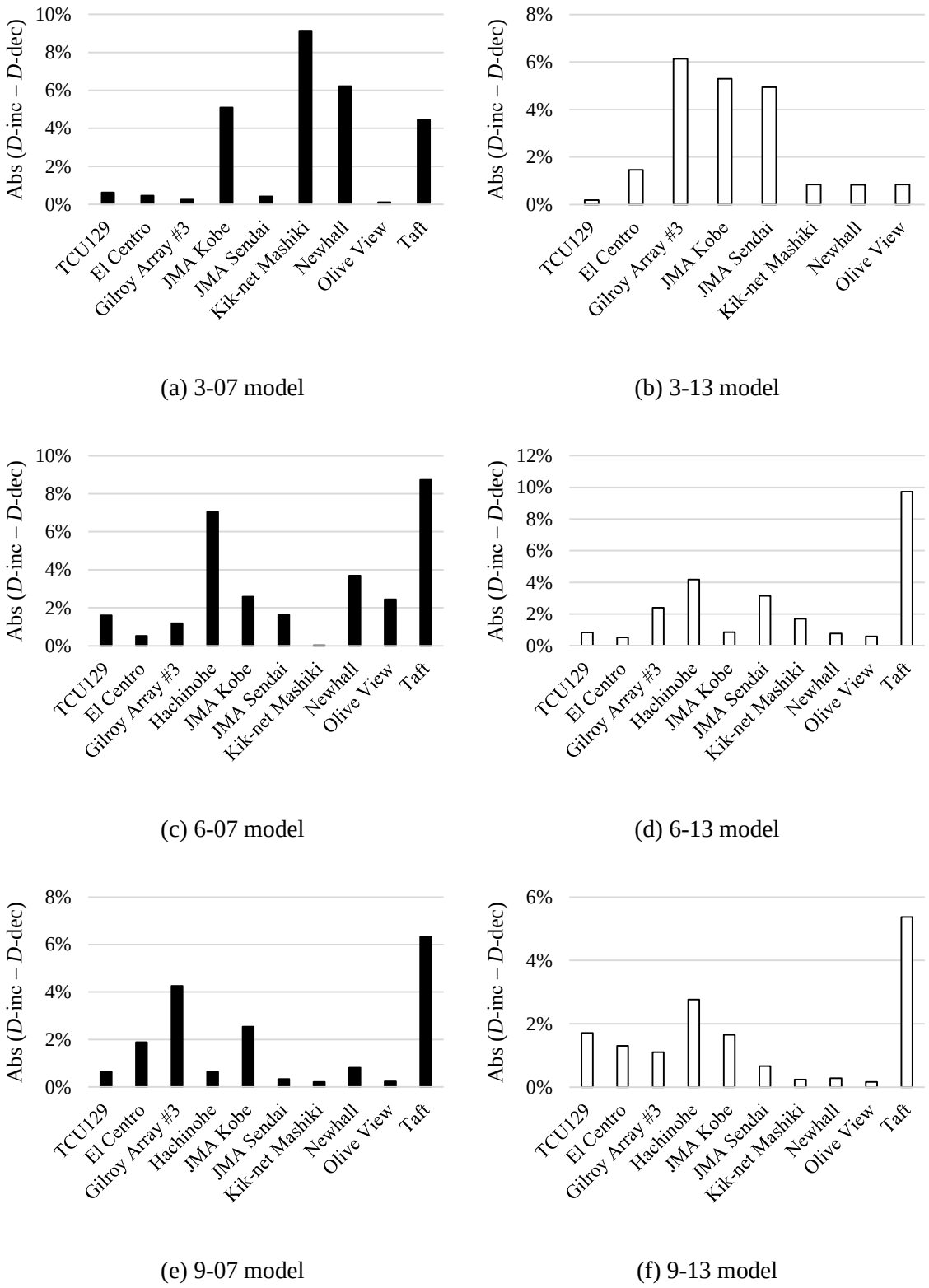

Figure 2-18 Difference of cumulative damage (absolute value) under incremental and decremental sequences

2.5 Steel Beam-to-Column Connection Test Simulating Multiple Earthquakes

To further verify the reliability of estimation of cumulative damage on beam end under random cyclic loading that is the basis of the evaluation of the performance of non-deteriorated SMRFs under multiple earthquakes, an experimental test of the subassembly of a beam-to-column connection is conducted. The beam-to-column connection is designed to fail via ductile fracture which is the same as the failure mode considered in evaluating the performance of the non-deteriorated SMRF models. During the test, multiple sets of cyclic loading are conducted to simulate the occurrence of multiple earthquakes. The one typical loading set is created using the response analysis result of the non-deteriorated models.

2.5.1 Test Setup and Specimens

Two beam-to-column connection specimens with the same structural and connection details are tested in this test. The test specimen and connection details are shown in Figure 2-19. The beam is a wide-flange section of 500 mm (depth) × 200 mm (width) × 10 mm (web thickness) × 16 mm (flange thickness) SN400B steel grade (nominal yield strength is 235 N/mm^2, and nominal tensile strength is 400 N/mm^2), while the column is a rectangular hollow section of 400 mm (depth) × 400 mm (width) × 12 mm (thickness) BCR295 steel grade (nominal yield strength is 295 N/mm^2, and nominal tensile strength is 400 N/mm^2). The beam is connected to the column using through diaphragms with weld access hole details of 35R+10R that conform to JASS 6 (Architectural Institute of Japan 2018). Stiffeners are attached 120, 220, and 320 mm from the column face to prevent local buckling. Thus, the failure will be controlled by the ductile fracture. Tensile coupon tests of the flange and the web are conducted using JIS-1A testing samples (Japanese Industrial Standard Committee 2011), and the material test results are shown in Table 2-4.

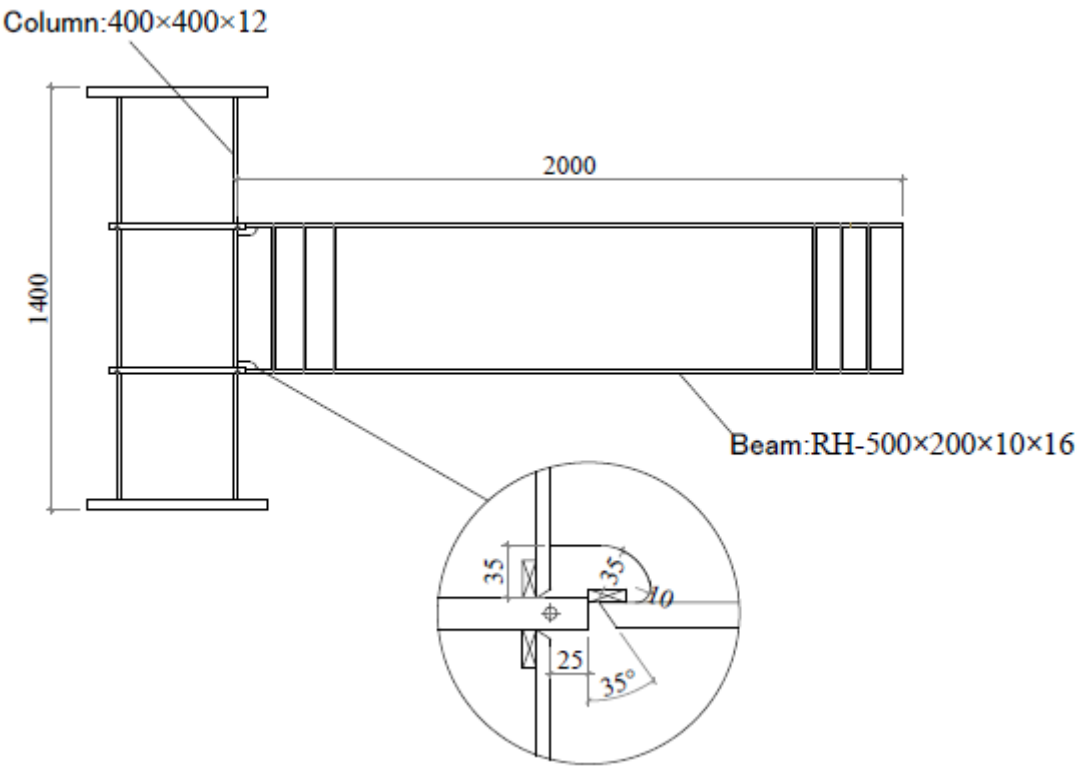

Figure 2-19 Test specimen

Table 2-4 Material test result

Section	Yield Strength [N/mm^2]	Tensile Strength [N/mm^2]
Flange	278	447
Web	318	463

The test setup is shown in Figure 2-20. A half-span beam with cantilever loading is used to represent the double curvature bending characteristic of the beam under lateral/seismic loading. The specimen was rotated 90° so that the beam is standing vertically and the column lying horizontally. An oil jack is attached at the beam's free end to load it, and a screw jack is attached at the other end to receive the reaction force. To prevent out-of-plane and torsional deformation of the beam, lateral supports are attached at two positions, i.e., near the loading point and near the beam-to-column connection.

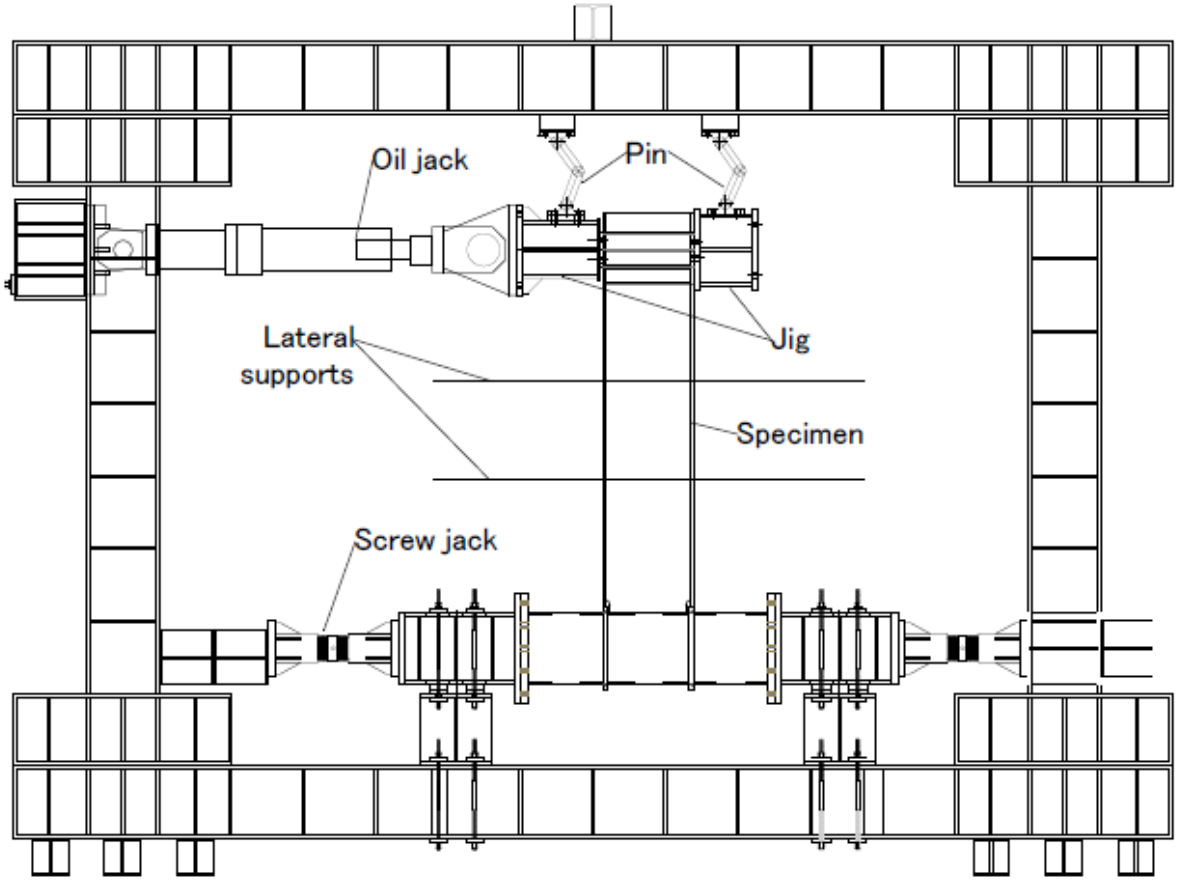

Figure 2-20 Test setup

2.5.2 Loading History

The loading history used in the test is created from the response analysis result using the non-deteriorated model. The 3-story non-deteriorated model (with the strong-type column base) is used because from the previous result, it shows the largest amount of cumulative damage. The story height of the model is 3.5 m which is the same as the original story height; however, the span is adjusted to match the total span of the specimen. Since the half-span of the specimen is equal to 2 m, the total span used in the analytical model is 4 m. The section of the column and the beam is also adjusted to be the same as that of the specimen. For the input ground motion sequences, two real sequences obtained from the 2016 Kumamoto earthquake and 2011 Tohoku earthquake is used. The sequences are shown in Table 2-5. For the 1st specimen, the input sequence is the records measured at the Kik-net Kumamoto station (NS direction) due to foreshock on April 14, main shock on April 16, and aftershock on April 16. Meanwhile, for the 2nd specimen, the input sequence is the records measured at Kik-net Sendai station (NS direction) due to main shock on March 11 and aftershock on April 7. Since the real sequences

have a high intensity, they were scaled down to PGV of 0.9 m/s and 0.5 m/s for the Kumamoto and Sendai records, respectively.

Table 2-5 Input ground motion used to create loading histories

Input Seq.	Foreshock	Main shock	Aftershock	Scaled PGV
1st (Kik-net Kumamoto NS)	2016/04/14-M6.5	2016/04/16-M7.3	2016/04/16-M5.9	0.9 m/s
2nd (Kik-net Sendai NS)		2011/03/11-M9.0	2011/04/07-M7.1	0.5 m/s

The inelastic time-history response analysis is conducted using the adjusted 3-story non-deteriorated model with the two scaled input sequences. Then, the rotation response history of the critical beam (beam at the 1st story) is extracted. Considering the time limitation in executing the experiment, most of the elastic cycles are sorted out. Those elastic cycles are considered to have a relatively small contribution to the cumulative damage. After sorting out most of the elastic cycles, the loading set, as shown in Figure 2-21, is obtained for the 1st and 2nd specimen. Both loading sets consist of eight peak points.

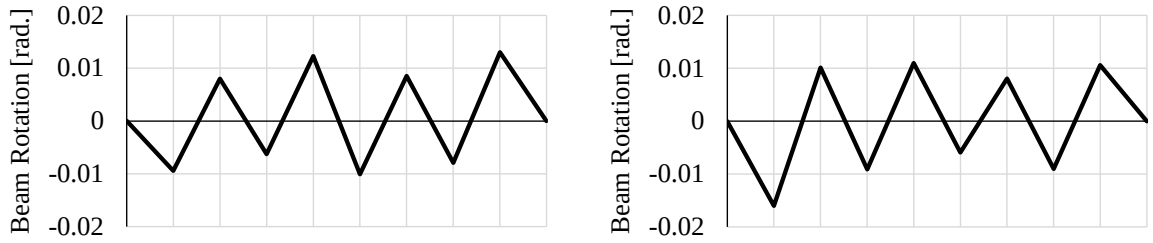

(a) 1st specimen (Kumamoto seq.) (b) 2nd specimen (Sendai seq.)

Figure 2-21 Loading history

2.5.3 Test Result

During the test, the typical loading set shown in the previous section is performed multiple times until one side of the flange is fully fractured. Figure 2-22 shows the crack progression as the number of loading sets performed increases. For both specimens, the crack was initiated at

the bottom of the weld access hole. For the 1st specimen the crack was first found at the 16th set; at the 23rd set, the crack almost penetrated through the flange thickness; and the flange was fully fractured at the 28th set before reaching the 5th peak point. Meanwhile, for the 2nd specimen, the crack was first found at the 10th set; it almost penetrated through the flange thickness at the 17th set; and finally, the flange was fully fractured at the 19th set before reaching the 2nd peak point.

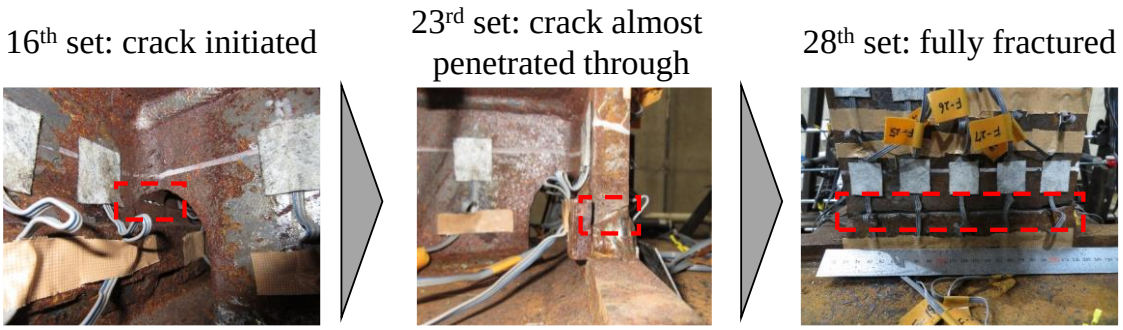

(a) 1st specimen

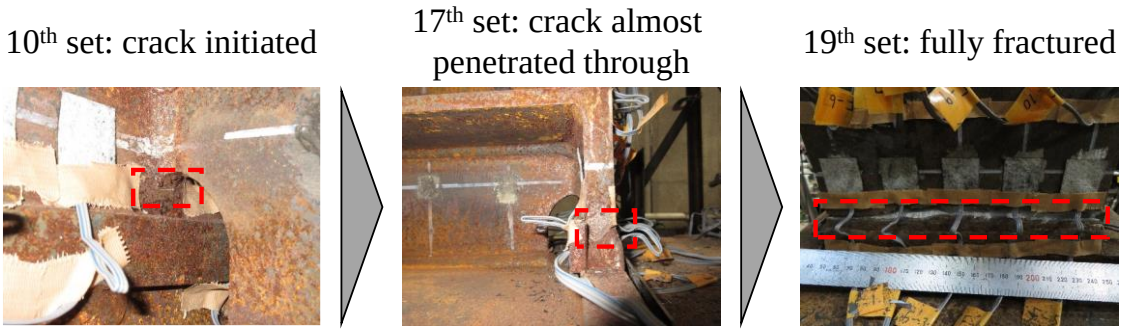

(b) 2nd specimen

Figure 2-22 Crack progression to ductile fracture

The load-deformation relationships obtained from the experiment are shown in Figure 2-23. The calculated plastic moment (M_p) is also plotted in the graphs. The graphs are divided based on crack progression. The left graphs contain the load-deformation relationship from the 1st set until the set where the crack is firstly initiated; the middle graphs contain the sets where the crack is first initiated until the crack almost penetrates through the flange thickness; and the right graphs contain the sets where the crack almost penetrates through until the flange is fully fractured. Moreover, Figure 2-24 and Figure 2-25 shows the strength and elastic stiffness

transition under multiple sets, respectively. In Figure 2-24, the strength of each set is taken as the maximum strength within the set (absolute value of positive and negative side); then, the strength value is normalized by the strength at the 1st set. Meanwhile, in Figure 2-25, the elastic stiffness of each set is calculated by averaging the unloading stiffness within the set (the unloading stiffness is calculated from the start point of the unloading (θ_{unload}) until it reaches $\theta_{unload} + \theta_p$ for unloading to the positive side or $\theta_{unload} - \theta_p$ for the unloading to the negative direction; where θ_p is the rotation that corresponds to M_p; then, the elastic stiffness value is normalized by the elastic stiffness at the 1st set. It can be seen from the graphs that the strength and stiffness of the beam-to-column connection are very stable until it reached the set where the crack almost penetrates through the flange thickness. In all sets before the crack almost penetrates through, the normalized strength and normalized elastic stiffness value are more than 0.95, while at the last set where the flange is fully fractured, the normalized strength and elastic stiffness decrease until the minimum value of 0.82 and 0.91, respectively.

To verify the reliability of the cumulative damage evaluation method used in the analysis, the cumulative damage of both specimens until fracture is computed. The rainflow counting method is performed to the load-deformation (M-θ) relationship of both specimens; then, the cumulative damage is calculated using the miner's rule and the low-cycle fatigue cumulative damage evaluation formula as described in Section 2.2.5. It is found that the cumulative damage (D) of the 1st and 2nd specimens are around 99.1% and 87.6%, respectively. The D value is very close to 100% for the 1st specimen. Although the value is a little bit lower for the 2nd specimen, the D value is close to 90%. Overall, these results verify the reliability of the cumulative damage evaluation method even under the random cyclic loading.

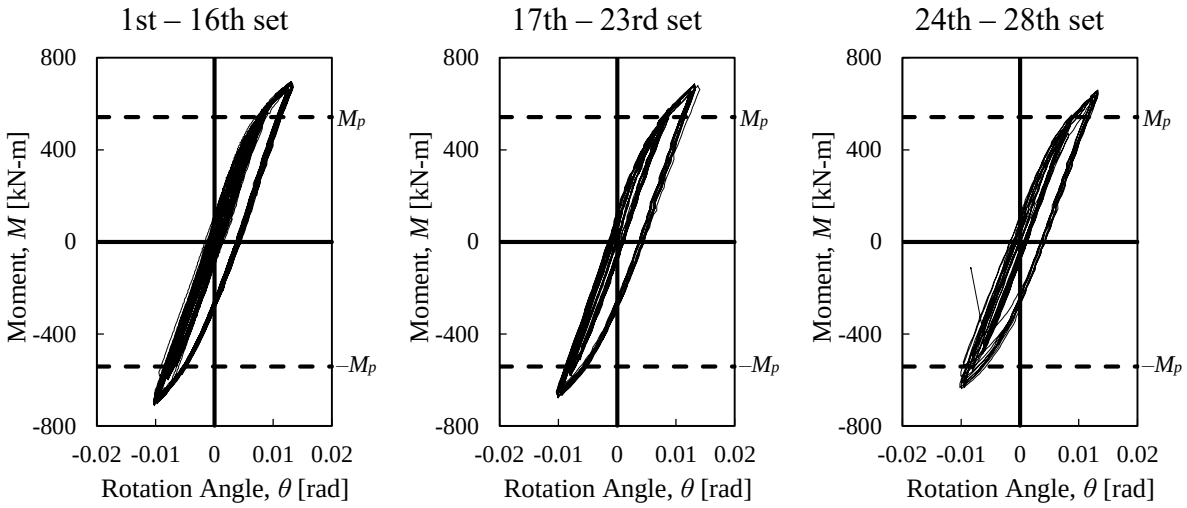

(a) 1st specimen

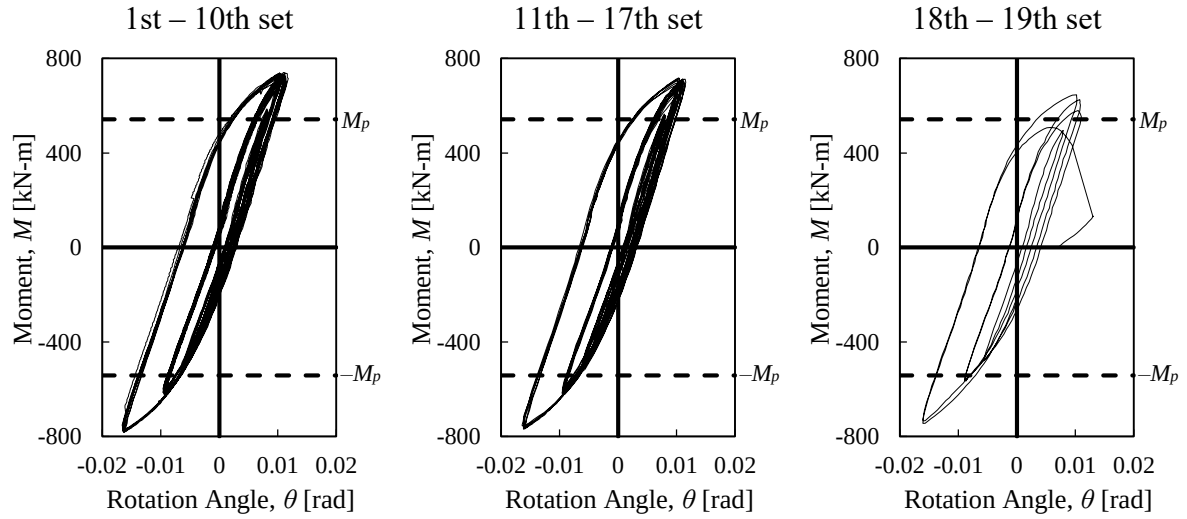

(b) 2nd specimen

Figure 2-23 Load-deformation relationship

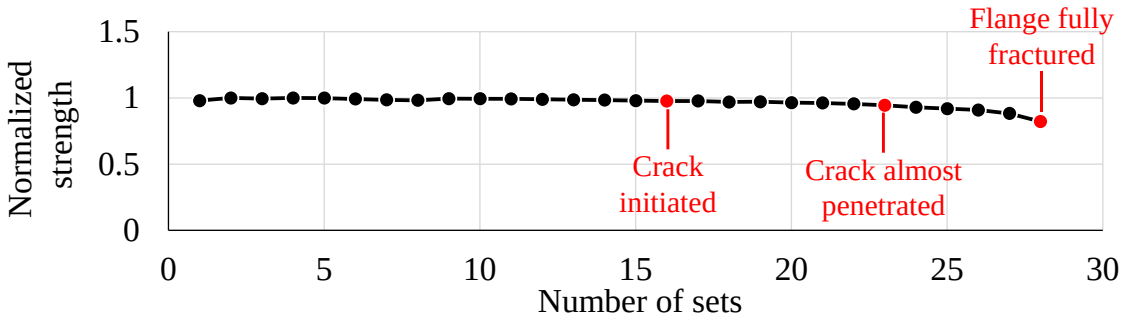

(a) 1st specimen

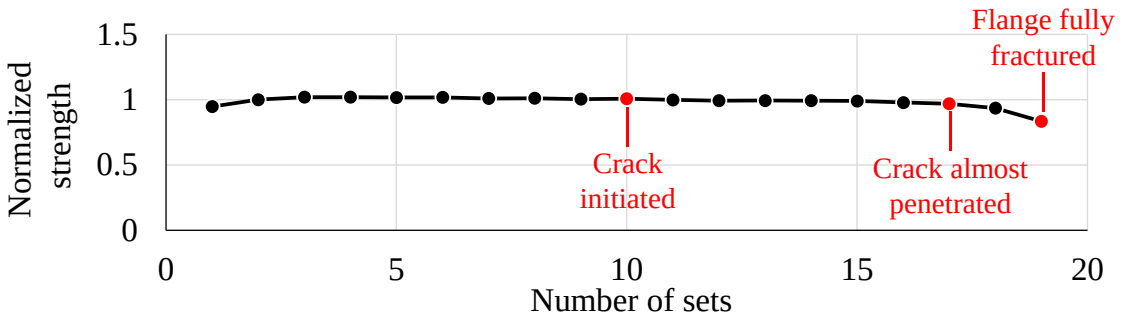

(b) 2nd specimen

Figure 2-24 Strength transition by number of sets

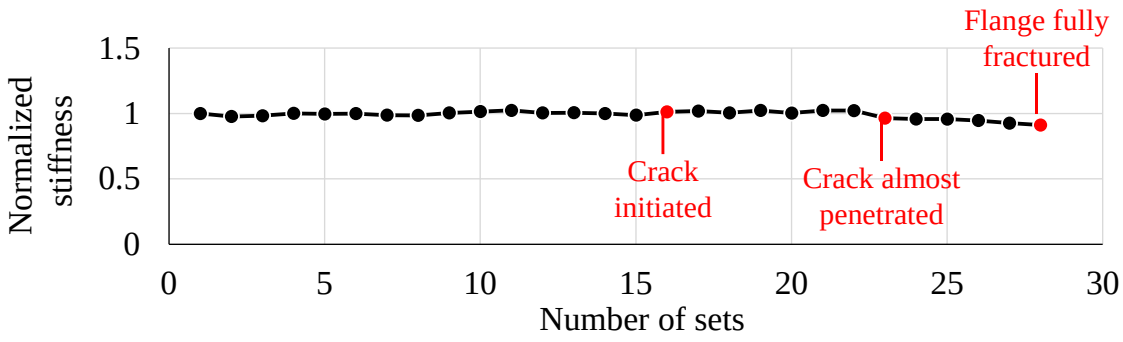

(a) 1st specimen

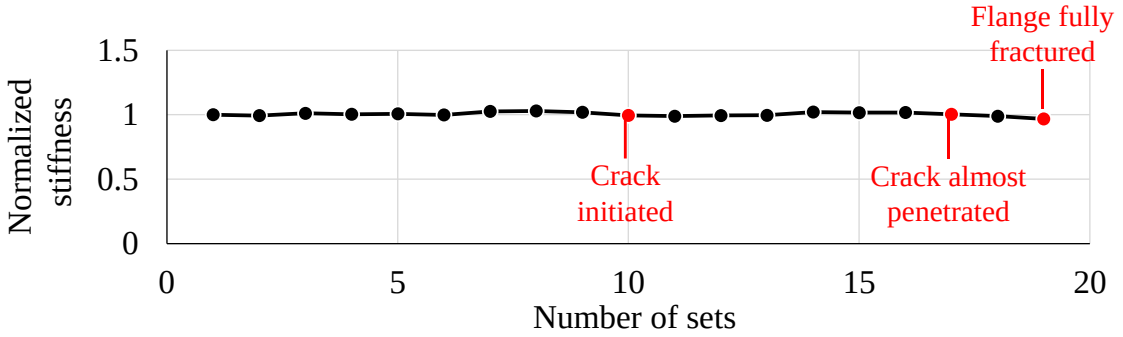

(b) 2nd specimen

Figure 2-25 Elastic stiffness transition by number of sets

2.6 Summary

The seismic performance of non-deteriorated steel moment-resisting frames under multiple earthquakes is evaluated in this chapter by considering the cumulative damage to fracture of the beam as the main damage index. Six non-deteriorated SMRF models are created considering two parameters, i.e., the number of stories and the strength of the column base. The building models are designed using a plastic design method for severe earthquakes based on the Japanese seismic design code. Then, an inelastic time-history response analysis simulating the occurrence of multiple earthquakes is conducted to the six SMRF models considering three different input ground motion intensities (i.e., PGV of 0.5 m/s, 0.75 m/s, and 1.0 m/s), and the seismic performance of those SMRF models is evaluated using the beam cumulative damage evaluation method proposed by Kishiki et al (2019). The findings of the analysis are summarized below.

- In most of the cases, the structures are found to be able to dissipate the energy with stable behavior under multiple earthquakes which is indicated by the linear increment in cumulative damage, particularly in the case in which the ground motion intensity is equal to the design level (PGV of 0.5 m/s). However, when the ground motion intensities are larger than the design level (PGV of 0.75 m/s and 1.0 m/s), collapse might occur in several cases.
- The collapse can be a local collapse caused by the fracture of a critical beam or a collapse due to reaching the ultimate state, both of which are related to the occurrence of large residual story drift angle.
- The influence of the two model parameters (i.e., the number of stories and the column base type) is identified. The 3-story building is found to experience the largest cumulative damage at the critical beam, followed by the 6-story and then the 9-story buildings due to the concentration of dissipated energy in a certain story. Moreover, the influence of using either a weak or a strong column base on the cumulative damage is not significant; as long as the upper structure is ductile, similar stable behavior can be achieved.
- By adopting the simple criterion of $\geq 90\%$ uncollapsed cases, the number of excitations that can be resisted by the structure before collapsing is obtained which is five excitations under PGV intensity of 0.75 m/s or three excitations under PGV intensity of 1.0 m/s.
- The effect of sequence with different input records (random sequences) and different input intensity (incremental-decremental sequences) are also investigated. By comparing the average cumulative damage and collapse fragility, it is found that the result of analysis

using repeated and random sequences do not differ significantly. In addition, from the comparison of cumulative damage under incremental and decremental sequences, it is found that as long as the structure can maintain its stable behavior, the difference of cumulative damage at the last excitation is less than 10%.

- The reliability of the cumulative damage evaluation method is further verified by conducting a steel beam-to-column connection test considering the ductile fracture failure mode. By calculating the cumulative damage value until fracture of the test specimens, it can be confirmed that the reliability of the method under random cyclic loading is acceptable.

3. Response Analysis of Deteriorated SMRF Model Subjected to Multiple Earthquakes

3.1 Introduction

In this chapter, the seismic performance of SMRFs subjected to multiple earthquakes is evaluated using the deteriorated models. In this deteriorated model, the effect of strength deterioration of column members due to local buckling is considered. To simulate the strength deterioration due to column local buckling, the hysteretic model proposed by Yamada et al. (2018) is employed in the response analysis model. This hysteretic model specifically simulates the hysteretic behavior of a square hollow section (SHS) column. The hysteretic model includes a non-deterioration range and a deterioration range. The deterioration range simulates the hysteretic behavior of the SHS column undergoing strength deterioration caused by local buckling. This model is chosen because the accuracy of this model has been verified by comparing it with the experimental test results of SHS columns subjected to various loading histories, including a random cyclic loading history.

To evaluate the seismic performance of SMRFs under multiple strong ground motions, various SMRF models are created for analysis. These models are designed considering the combination of two main design parameters that may affect the strength of the column, i.e., the width-to-thickness ratio of the column member and the column-to-beam moment capacity ratio. In addition to those two main parameters, three variations of the number of stories are also considered to cover a wider range of low-rise to mid-rise buildings. Then, an inelastic time-history response analysis that simulates the occurrence of multiple shocks is carried out for each model. The effect of the column strength deterioration on the behavior of SMRFs under multiple excitations is investigated. Moreover, the state of deterioration, cumulative damage, and collapse fragility are computed considering a various number of excitations and input intensities. In addition, the influence of random and incremental-decremental seismic sequence are also investigated.

3.2 Analytical Procedure

3.2.1 Parameter and Building Model

The analytical model is an infinite uniform plane frame model (Yamada et al. 1996), the same type of model that is used in Chapter 2, Figure 2-1. The analytical frame has a typical height of 3.5 m, typical span of 7 m, and typical weight per story per span of 400 kN; the column section and panel zone are SHSs with BCR295 steel grade (nominal yield strength of 295 N/mm^2 and nominal tensile strength of 400 N/mm^2); the beam section is a wide-flange section with SN400 steel grade (nominal yield strength of 235 N/mm^2 and nominal tensile strength of 400 N/mm^2); and the column base is an exposed-type column base. The sizes of the columns, beams, and column bases are designed according to the parameters of the model. Three variations of the number of stories are investigated: 3, 6, and 9 stories. For the column width-to-thickness ratio (D_c/t), three variations are investigated: D_c/t = 29.45, 25, and 20. D_c/t = 29.45 is the limit value of the ductile SHS column (called the FA rank column in the code) with BCR295 steel grade according to the Japanese Building Code (Building Center of Japan 2013b). Meanwhile, for the column-to-beam moment capacity ratio ($_cM_p/_bM_p$), five variations are investigated: $_cM_p/_bM_p \geq$ 1.1, 1.25, 1.5, 1.75, and 2.0. $_cM_p/_bM_p \geq 1.5$ is the recommended value in the Japanese Building Code (Building Center of Japan 2013a). Combining all the variations of the three parameters, a total of 45 SMRF models are analyzed in this study.

The models are named according to the three design parameters with the format A-XX-YYY. The first index (A) indicates the number of stories (3, 6, or 9); the second index (XX) indicate the D_c/t (29 (for 29.45), 25, or 20); and the last index (YYY) indicates the $_cM_p/_bM_p$ (1.1, 1.25, 1.5, 1.75, or 2.0). All the models are designed to comply with the Japanese seismic design code. The assumptions and concepts used in the design are the same with those used to design the non-deteriorated models (as described in Section 2.2.2), except for the D_c/t and $_cM_p/_bM_p$ which follow the values for each model. In addition, the same exposed-type column base model used for the non-deteriorated model is also employed in the analytical model. However, since the deterioration of the column is the main focus in the analysis, the column base is designed to be stronger than the 1st story column to prevent the column base from slipping; thus, the damage is concentrated in the column. During the analysis, the column base remained elastic, and the elastic stiffness of the column base is considered in the analytical model. The details of members' cross section, ultimate lateral strength capacity (Q_{ui}), required ultimate lateral strength (Q_{uni}), column-to-beam strength ratio ($_cM_p/_bM_p$), and 1st and 2nd mode natural period of each model are shown in Appendix D. In addition, a pushover analysis is

performed to check the capacity of the models against the required ultimate lateral strength (Q_{uni}). The pushover analysis is conducted using the force control method assuming that the force distribution at each story follows the A_i distribution (Building Center of Japan 2013c). The pushover analysis results are also shown in Appendix D.

In the time history response analysis, the average acceleration method is used for the numerical integration with a time step of 1/2000 s. In addition, the 2% Rayleigh damping for the 1st and 2nd natural periods and the *P-Δ* effect are considered in this analysis.

3.2.2 Hysteretic Model of Structural Members

For the beam members, the same hysteretic model that is used in Chapter 2, Figure 2-4, is employed in the analytical model which is based on the decomposition of hysteretic loops into the skeleton part, the Bauschinger part, and the elastic unloading part (Figure 2-3). Meanwhile, for the column members, the deteriorated hysteretic model proposed by Yamada et al. (2018) is employed. This model also adopts the same concept of hysteretic loop decomposition (Kato et al. 1973, Akiyama and Takahashi 1990). However, the model is divided into two ranges: the non-deteriorating range and deteriorating range as shown in Figure 3-1. The non-deteriorating range is the range before reaching the maximum strength (${}_cM_u$); the hysteretic behavior in this range is the same as that in the hysteretic model of the beam (Figure 3-2(a)). Additionally, the deteriorating range is the range after reaching the maximum strength. In this deteriorating range, the Bauschinger part no longer exists; instead, this part is replaced by the strength increasing part. Every progression of plastic deformation associated with the strength increasing part corresponds to the progression in the skeleton curve (Figure 3-2(b)). Thus, once the column enters the deteriorating range, every progression of plastic deformation contributes to the strength deterioration. The comparison of skeleton curves of the 1st story column by D_c/t and ${}_cM_p/{}_bM_p$ are shown in Figure 3-3. As shown in the figure, models with larger ${}_cM_p/{}_bM_p$ have stronger capacity due to having a larger cross-section, while models with lower D_c/t have higher ductility (in both non-deteriorating and deteriorating range) and slightly higher maximum strength (peak moment before deterioration).

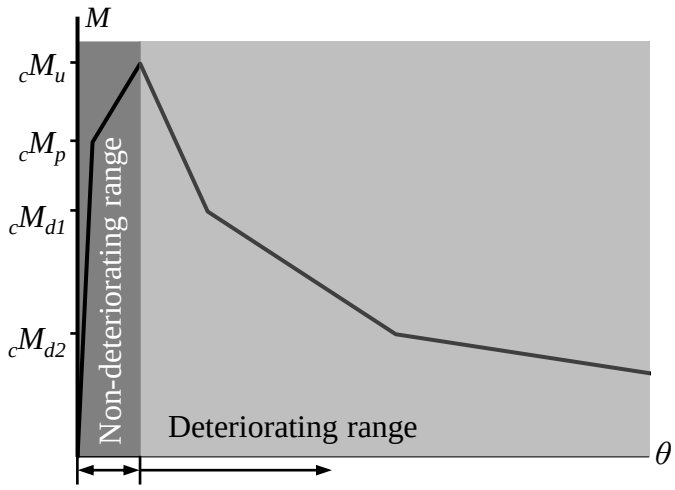

Figure 3-1 Idealized skeleton curve model of column members

3.2.3 Input Ground Motions

The same ten earthquake records listed in Table 2-5 of Chapter 2 are used as the input ground motion. To standardize the input energy, all the input ground motions are scaled based on the peak ground velocity (PGV). Three different intensity levels are chosen, PGV = 0.5 m/s, 0.75 m/s, and 1.0 m/s which is the same with those used in Chapter 2. The intensity of PGV = 0.5 m/s is also known as the design level in Japan because the time history analysis for building design is conducted with the intensity of PGV = 0.5 m/s. To simulate the occurrence of multiple strong earthquakes, an earthquake sequence is created by repeating the same ground motion with the same intensity for five excitations, and 30 s of zero acceleration is inserted between two consecutive excitations to allow the structure to stop vibrating before responding to the next excitation. The repeated sequence consisting of the same ground motion is chosen because it is useful to simply evaluate the effect of column strength deterioration on the structural behavior of SMRFs, while the same intensity within the sequence is applied to consider the extreme condition where multiple strong shocks with almost equal intensity occur in a short period of time during an earthquake event. In addition, the limitation of a maximum of five excitations is used to standardize the number of excitations performed during the analysis, and five excitations are considered to be appropriate because the occurrence of more than five strong excitations in a short period of time is extremely rare.

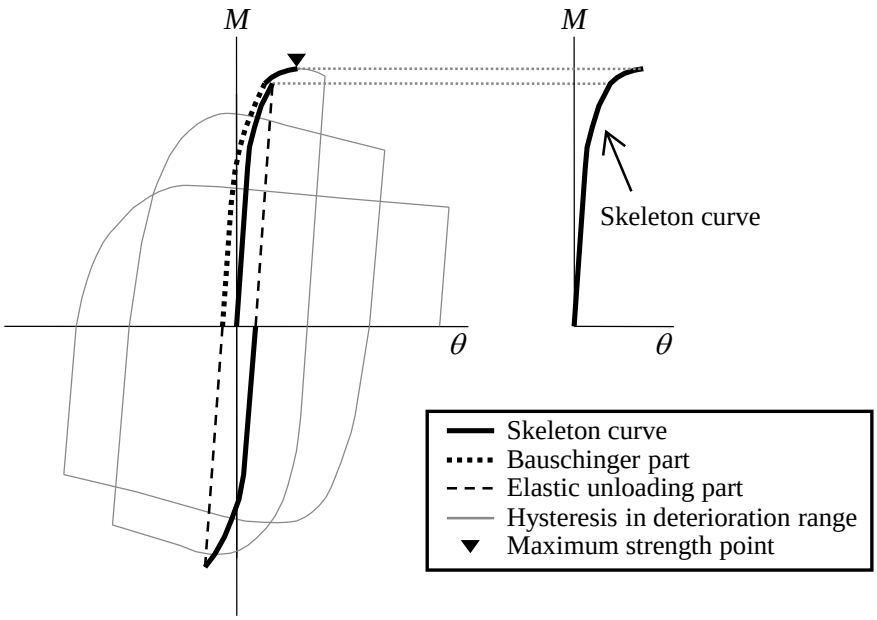

(a) In the non-deteriorating range

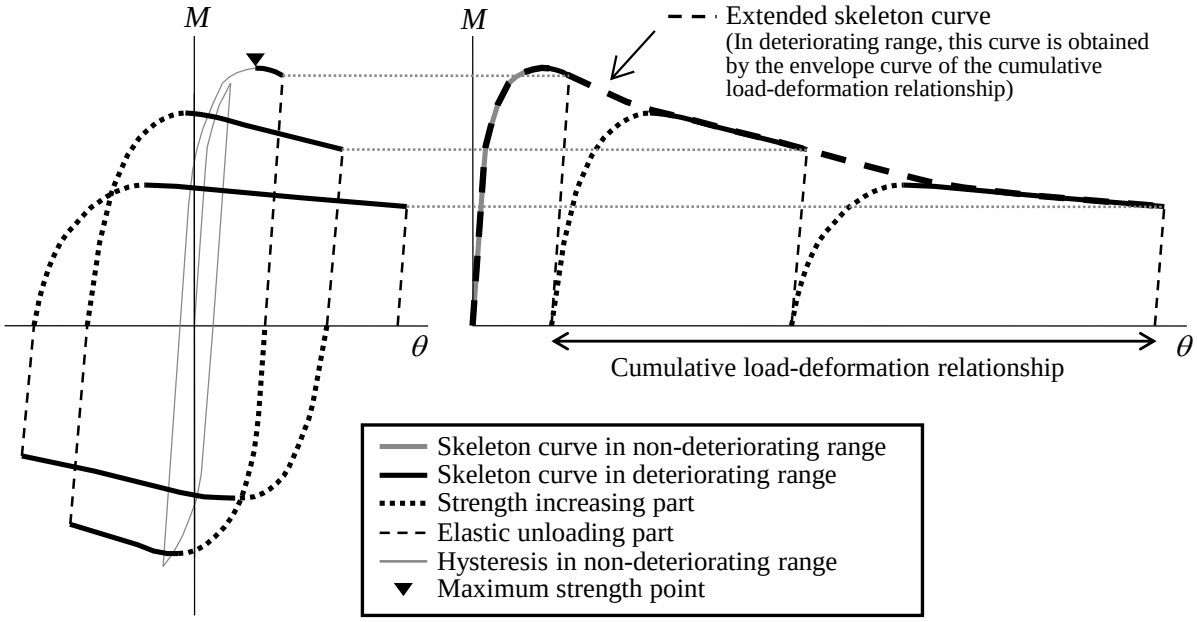

(b) In the deteriorating range

Figure 3-2 Decomposition of hysteretic loops of column hysteretic model

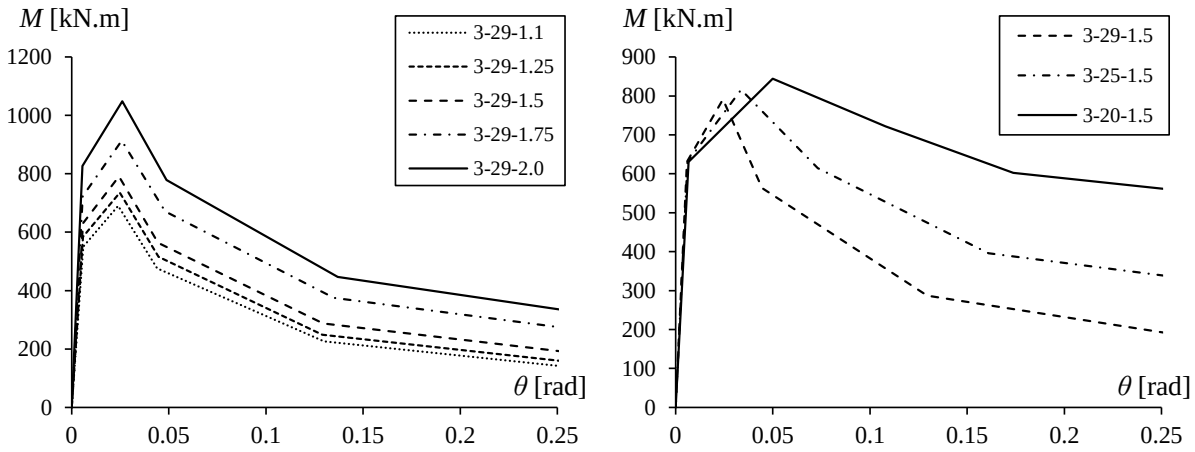

(a) by ${}_cM_p/{}_bM_p$ (b) by D_c/t

Figure 3-3 Comparison of skeleton curves of the 1st story columns

3.3 Analytical Results

3.3.1 Typical Structural Behavior

Inelastic earthquake response analysis is conducted on the aforementioned 45 SMRF models using ten different input ground motions with three different intensities; thus, this analysis includes a total of 1350 cases. Regardless of the model, input ground motion, and input intensity, the analytical result can be divided into two typical cases: (i) column strength deterioration does not occur within five excitations, and (ii) column strength deterioration occurs within five excitations. For case (ii), in many cases, story collapse might occur due to the significant column strength deterioration. Story collapse is defined to occur when the story stiffness is negative and the story shear (Q) becomes zero.

Figure 3-4 shows the analytical results of model 6-29-1.5 excited by the El Centro NS record with a PGV intensity of 0.5 m/s; this case corresponds to the typical case (i). From the moment-rotation (M-θ) relationship between the 1st story beam end and column lower end, the energy is mainly dissipated by the Bauschinger part. During the 1st and 2nd excitations, a small portion of the skeleton part can be observed; however, starting from the 3rd excitation, the hysteresis response is completely dominated by the Bauschinger part which means that there is no significant increment in terms of maximum deformation of the 1st story column and beam. This response tends to become stable during the 4th and 5th excitations. A similar trend can also be observed from the story drift angle and the distribution of dissipated energy. As shown in the figure, the maximum story drift angle hardly increases from the 1st to 5th excitations, and

the residual story drift angle is relatively small. In addition, the distribution of dissipated energy barely changes from the 1st to 5th excitations. In this case, the structure can maintain the sway mechanism throughout the five excitations of strong ground motion. This behavior agrees with the stable behavior observed in the analytical results of SMRFs under multiple strong ground motions using a non-deteriorated hysteretic model (Chapter 2).

Figure 3-5 shows the analytical results of model 6-29-1.5 excited by the El Centro NS record with a PGV intensity of 1.0 m/s. In this case, which corresponds to the typical case (ii), both column strength deterioration and story collapse occurred within five excitations. As shown in the figure, during the 1st and 2nd excitations, no deterioration occurs at the 1st story column lower end hinge, and the 1st story column upper end hinge remains elastic. However, during the 3rd excitation, strength deterioration occurs at the 1st story column lower end, and during the 4th excitation, the deterioration proceeds until the 1st story upper end hinge is formed. Additionally, during the 4th excitation, the distribution of dissipated energy changes drastically and result in the concentration of damage to the 1st story. Finally, during the 5th excitation, the 1st story column lower end hinge completely loses its restoring force and behave like a pin joint; this effect causes moment redistribution to the upper end of the 1st story column. Hence, the 1st story column upper end hinge also deteriorates, which causes a shift from the sway mechanism to the weak story mechanism. This deterioration continues until the 1st story completely lost its resistance, as shown by the story shear of the 1st story becoming less than zero. Note that the story shear can become less than zero even before both column end hinges completely lose their strength because of the *P-Δ* effect.

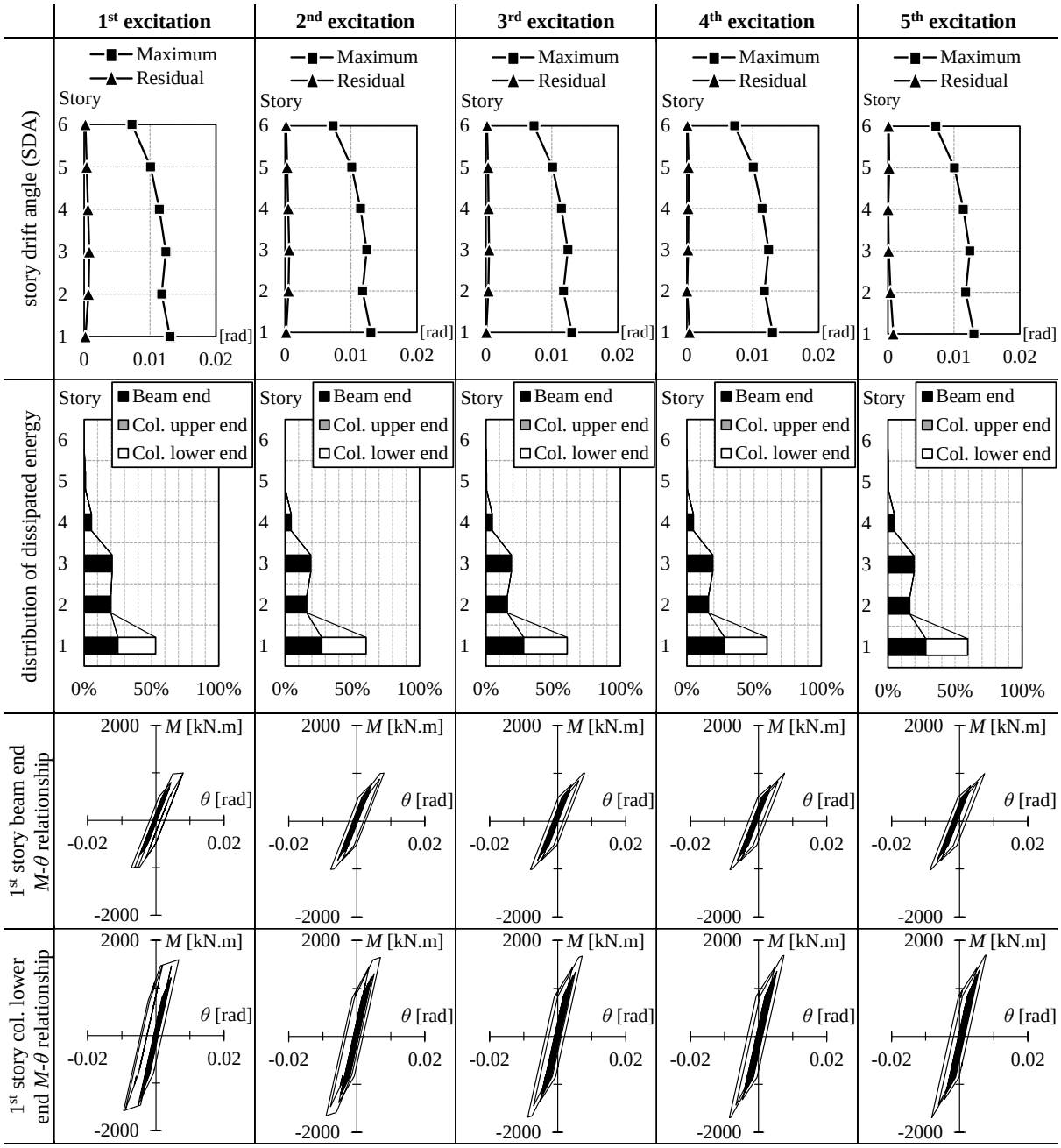

Figure 3-4 Analytical results for a case in which column strength deterioration does not occur (model 6-29-1.5 excited by El Centro NS record with PGV of 0.5 m/s)

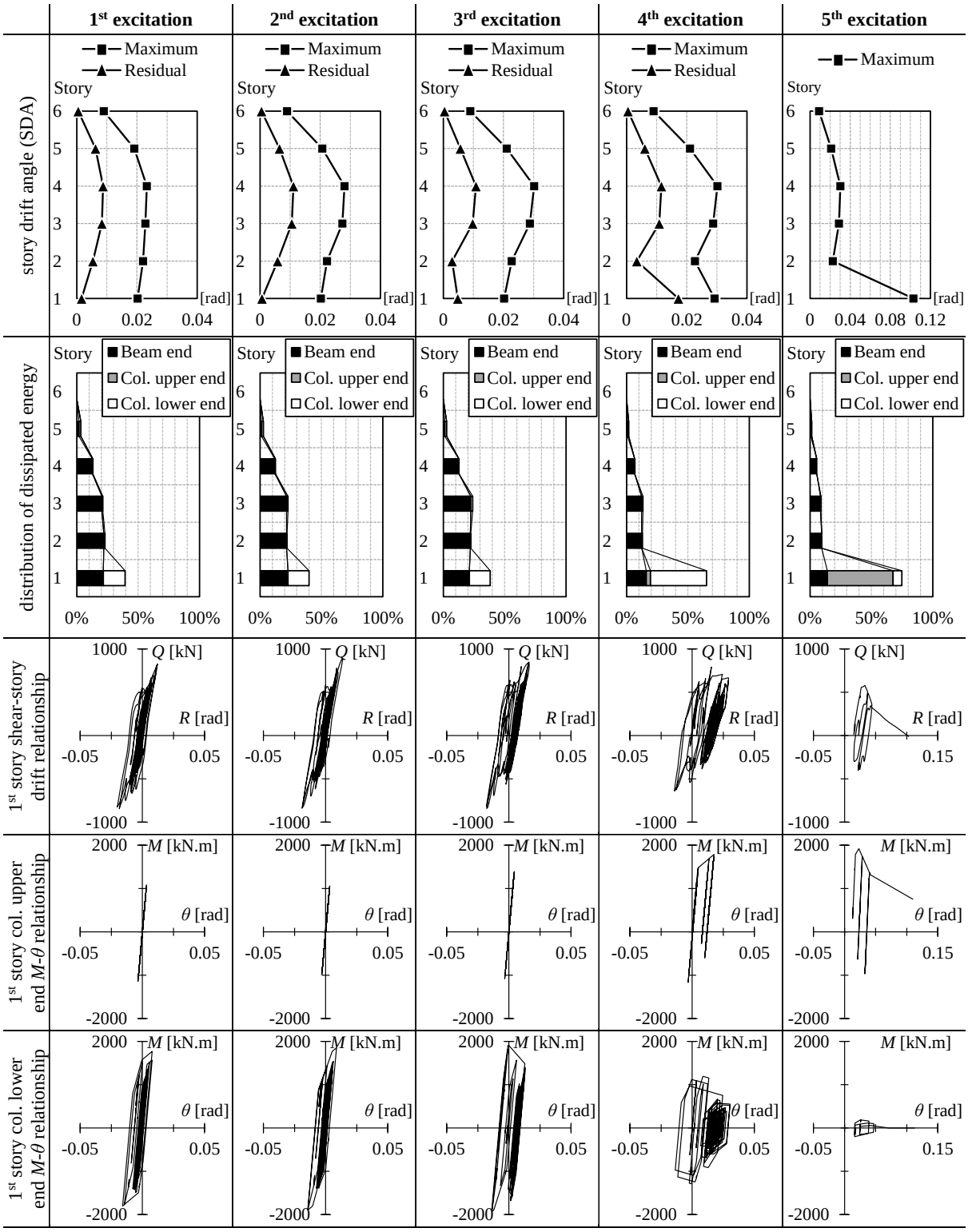

Figure 3-5 Analytical results for a case in which column strength deterioration and collapse occur (model 6-29-1.5 excited by El Centro NS record with PGV of 1.0 m/s)

3.3.2 Stages to Collapse under Multiple Strong Ground Motions

Based on the explanation provided in the previous section, the stage to collapse for a deteriorated model of SMRFs under multiple strong ground motion excitations can be summarized as illustrated in Figure 3-6. There are three main stages. In stage 1, plastic hinges are formed at the beam end, and the 1st story column lower end without strength deterioration. In this stage, the structure has a stable behavior and can maintain its sway mechanism. However, in stage 2, strength deterioration occurs at the 1st story column lower end hinge and causes moment redistribution to the 1st story column upper end. Additionally, in this stage, because the 1st story shear resistance continues to decrease, the story drift continues to increase and causes damage to concentrate at the 1st story. In stage 3, both column end hinges deteriorate, which causes the mechanism to shift to a weak story mechanism, and 1st story collapse might occur when both column end hinges lose a considerable amount of strength.

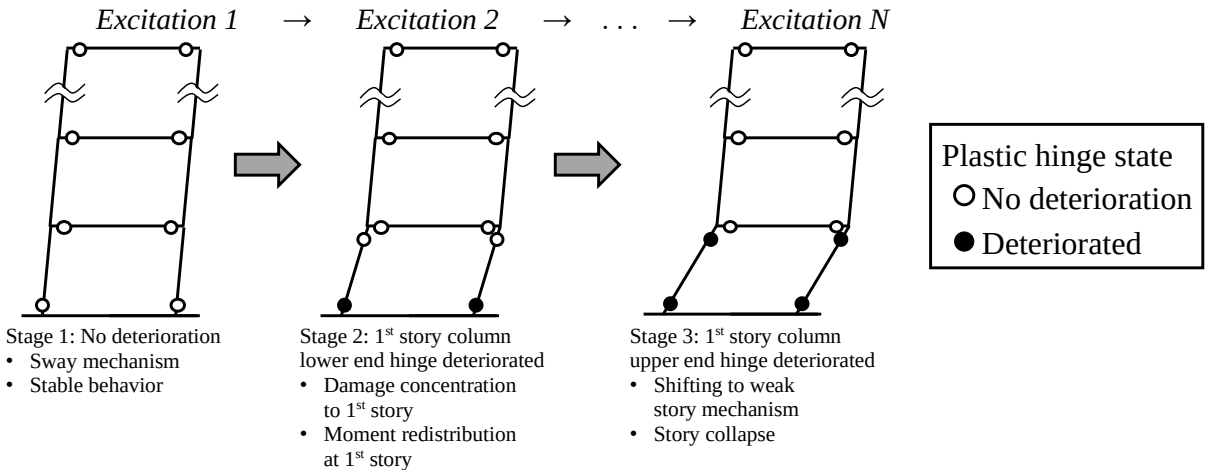

Figure 3-6 Stages to collapse under multiple strong ground motion excitations

As an example, Figure 3-7 shows the stages to collapse for the A-29-1.5 series models under various ground motion intensities. Comparing the model results in terms of the number of stories, Figure 3-7 shows that the 3-story model is the most vulnerable, followed by the 6-story model and then the 9-story model. The main cause of this difference is the differences in the patterns of the dissipated energy distribution. Figure 3-8 shows the dissipated energy distribution at the 1st excitation of models with a different number of stories. As shown in the figure, for the 3-story model, the dissipated energy concentrates at the 1st story. Meanwhile, for the 6-story and 9-story models, the amounts of energy dissipated by the 1st story are much

smaller than that of the 3-story model; the rest of the energy is dissipated by the beam end hinges at the middle or upper-middle stories. This characteristic shows the vulnerability of the 3-story model to weak story collapse; the process of damage concentration at the 1st story in stage 2 naturally occurs from the 1st excitation.

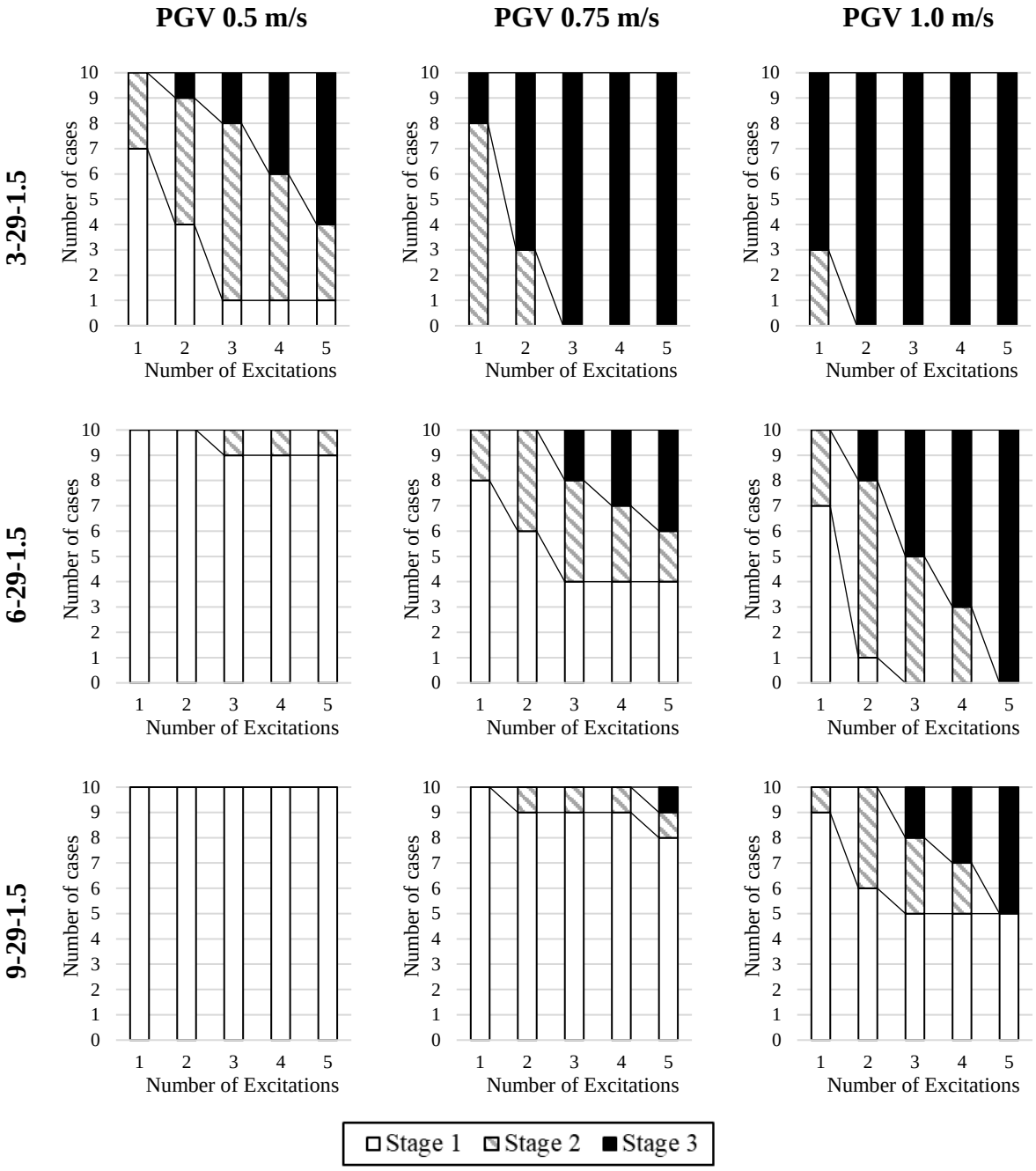

Figure 3-7 Stages to collapse of A-29-1.5 series models under various intensities

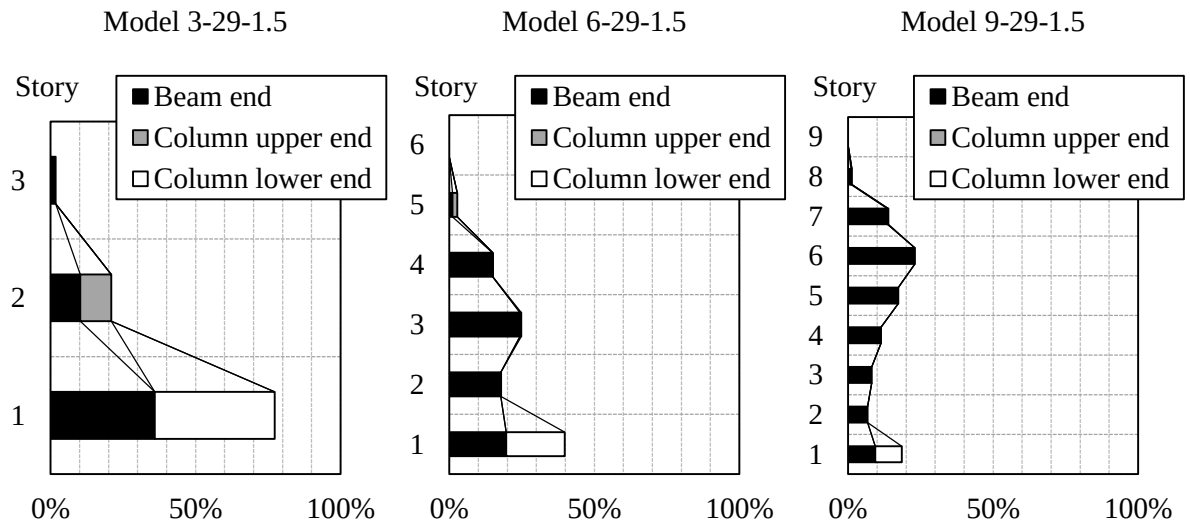

(a) Distribution of dissipated energy (excited by the JMA Kobe NS record with a PGV of 0.5 m/s)

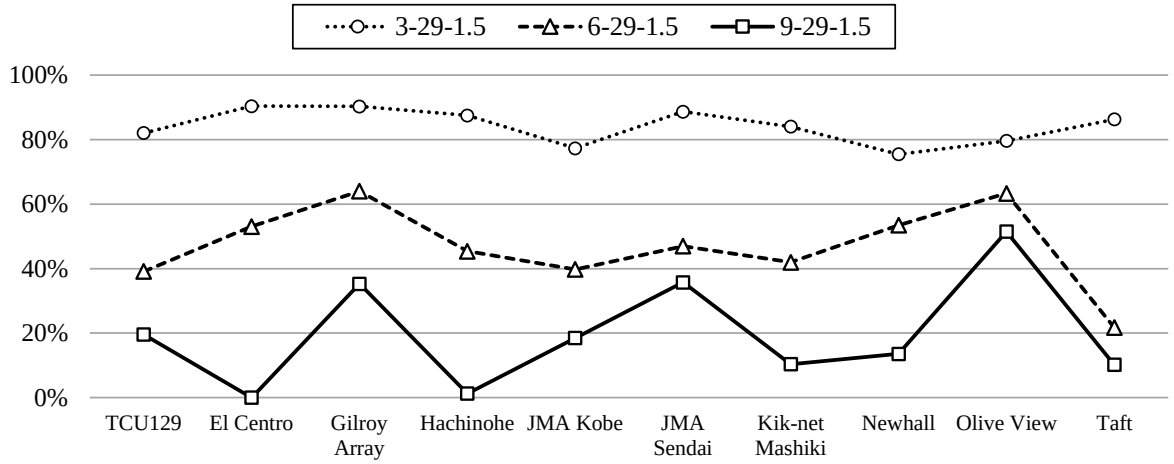

(b) Distribution of dissipated energy at the 1st story of A-29-1.5 series models (excited by various records with a PGV of 0.5 m/s)

Figure 3-8 Comparisons of the distribution of dissipated energy at the 1st excitation by the number of stories

By grouping all the cases based on the ${}_cM_p/{}_bM_p$ and D_c/t, the comparison of the percentage of cases reaching stages 2 and 3 are shown in Figure 3-9 and Figure 3-10, respectively. In general, either increasing the ${}_cM_p/{}_bM_p$ or lowering the D_c/t, both can improve the performance of SMRFs under multiple excitations. In addition, as shown in the figure, the improvement is more significant under the higher intensity ground motions. Increasing the ${}_cM_p/{}_bM_p$ by one step (1.1→1.25; 1.25→1.5; 1.5→1.75; 1.75→2.0) is averagely decreasing the percentage of cases reaching stage 2 by 5.8%, 10.6%, and 10.5% for the PGV of 0.5, 0.75, and 1.0 m/s, respectively,

and the percentage of cases reaching stage 3 by 4.2%, 10.6%, and 13.7% for the PGV of 0.5, 0.75, and 1.0 m/s, respectively. Moreover, lowering the D_c/t by one step (29→25; 25→20) is averagely decreasing the percentage of cases reaching stage 2 by 14.8%, 19%, and 17.7% for the PGV of 0.5, 0.75, and 1.0 m/s, respectively, and the percentage of cases reaching stage 3 by 7.1%, 17.3%, and 21.7% for the PGV of 0.5, 0.75, and 1.0 m/s, respectively. From those comparisons, to achieve the same percentage reduction, lowering D_c/t by one step almost equals to increasing ${}_cM_p/{}_bM_p$ by two steps.

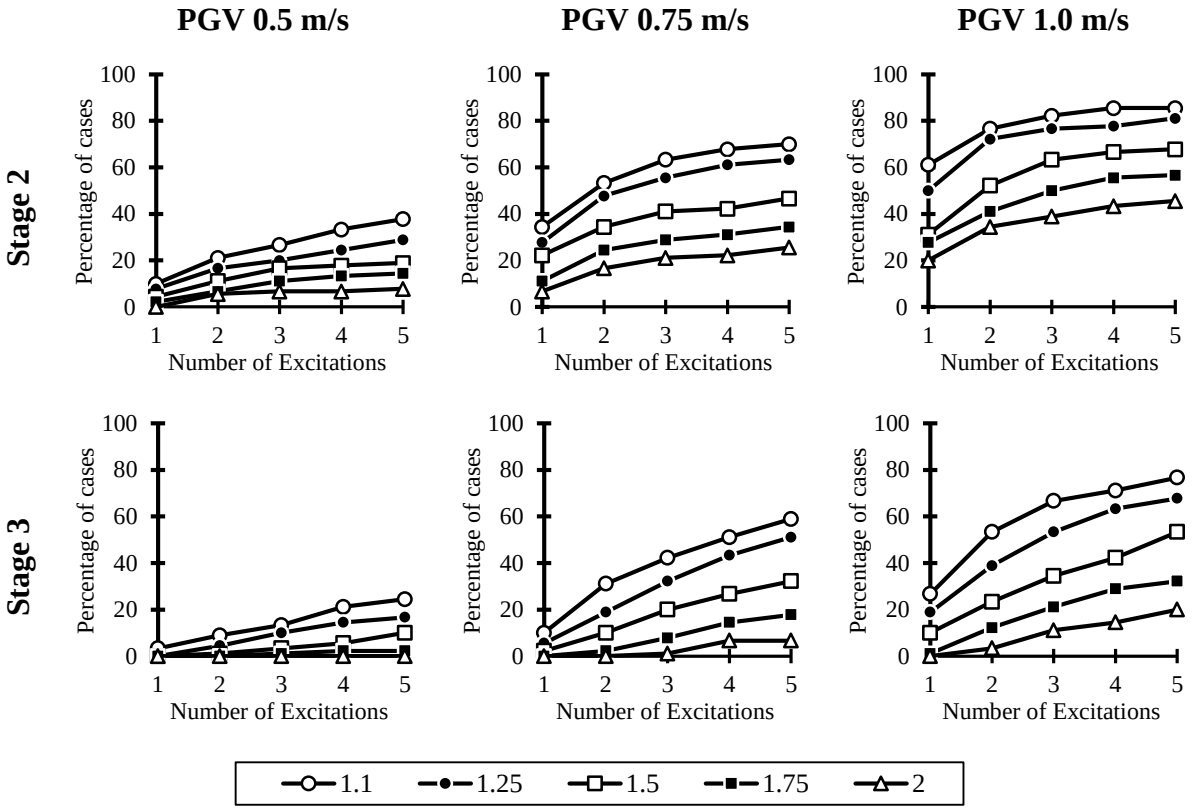

Figure 3-9 Comparison of percentage of cases reaching stages 2 and 3 by ${}_cM_p/{}_bM_p$

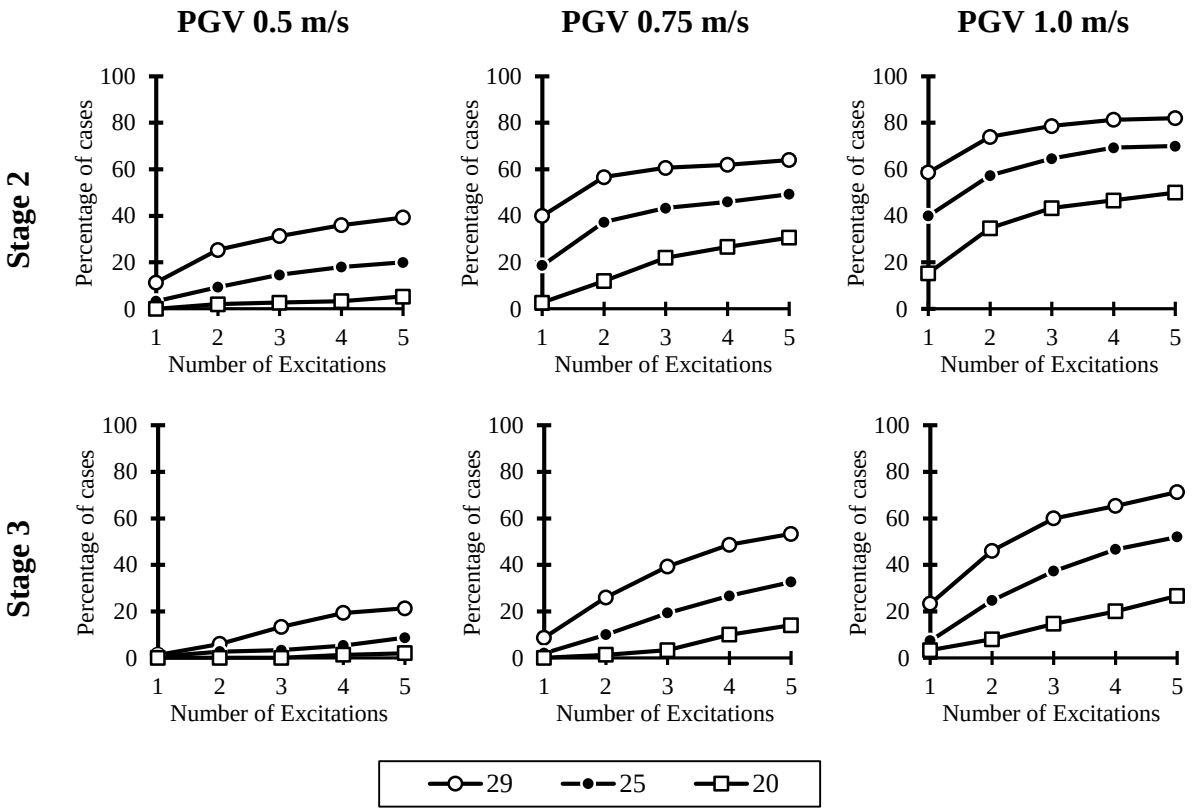

Figure 3-10 Comparison of percentage of cases reaching stages 2 and 3 by D_o/t

3.3.3 Cumulative Damage Under Multiple Excitations

The stage to collapse shown in the previous section indicates that the hinge state of the 1st story column can be a good index to represent the whole condition of the structure to collapse because the changing of 1st story column hinge state greatly affects the response of the whole structure. Thus, the 1st story column hinge state is used as the main cumulative damage index. This index ranges from –100% to 100% and is the combination of two values called the non-deterioration margin (*NM*) and deterioration index (*DI*), which are computed using the method explained in Figure 3-11. *NM* ranges from 100% to 0% and indicates when the margin reaches the maximum moment ($_cM_u$) or starts to deteriorate. A value of 100% means that the 1st story column end hinges remain elastic. Meanwhile, *DI* ranges from 0% to –100% and indicates how much the strength of the 1st story column has deteriorated. Since both end hinges of the column contribute to the strength, *DI* is calculated by averaging the *DI* values of the 1st story column lower end and upper end hinges. A value of –100% means that the 1st story column has completely lost its strength. However, as explained in the previous section, 1st story collapse may occur even before all the column strength deteriorates because of the *P-Δ* effect.

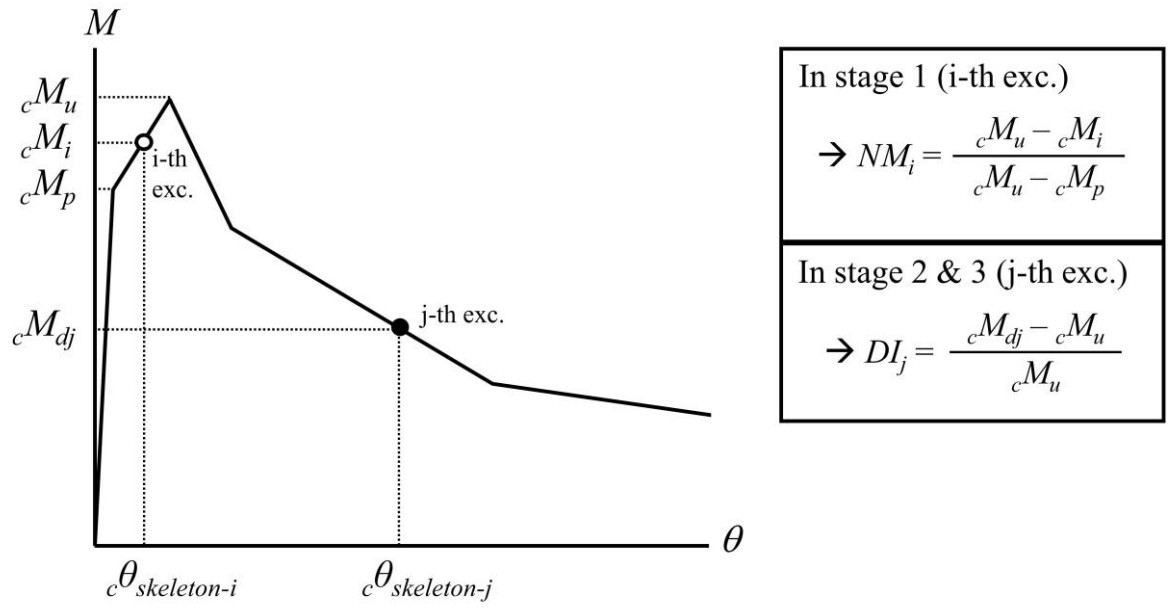

Figure 3-11 Definitions of the non-deterioration margin (*NM*) and deterioration index (*DI*)

Figure 3-12 shows the comparison of cumulative damage of several selected cases (all the other cases are shown in Figures E-1 to E-15 of Appendix E). As shown in the figure, the progression of column strength deterioration can typically be identified according to the stage to collapse. In stage 1, no strength deterioration, the progression of *NM* tends to be asymptotic. At this stage, if *NM* at the 1st excitation is approximately higher than 50%, generally, the structure can maintain its stable behavior within five excitations (no deterioration). In stages 2 and 3, the progression of *DI* can be differentiated by the degree of decrement. In stage 2, *DI* tends to decrease slowly, but when the mechanism shifts (stage 3), *DI* decreases more sharply than before. Increasing the ${}_cM_p/{}_bM_p$ is generally increasing the *NM* value at the 1st excitation and slowing down the transition to stage 3 because, as shown in Figure 3-3(a), increasing the ${}_cM_p/{}_bM_p$ mainly improves the maximum strength (peak moment) of the column at both ends (lower end and upper end). Meanwhile, lowering the D_c/t is increasing the *NM* value at the 1st excitation and slowing down the rate of deterioration (decrease in *DI*) because, as shown in Figure 3-3(b), lowering the D_c/t improves the ductility of the column (in both non-deteriorating and deteriorating range) significantly and the strength slightly. Thus, both improvements can contribute to decreasing the cumulative damage under multiple excitations.

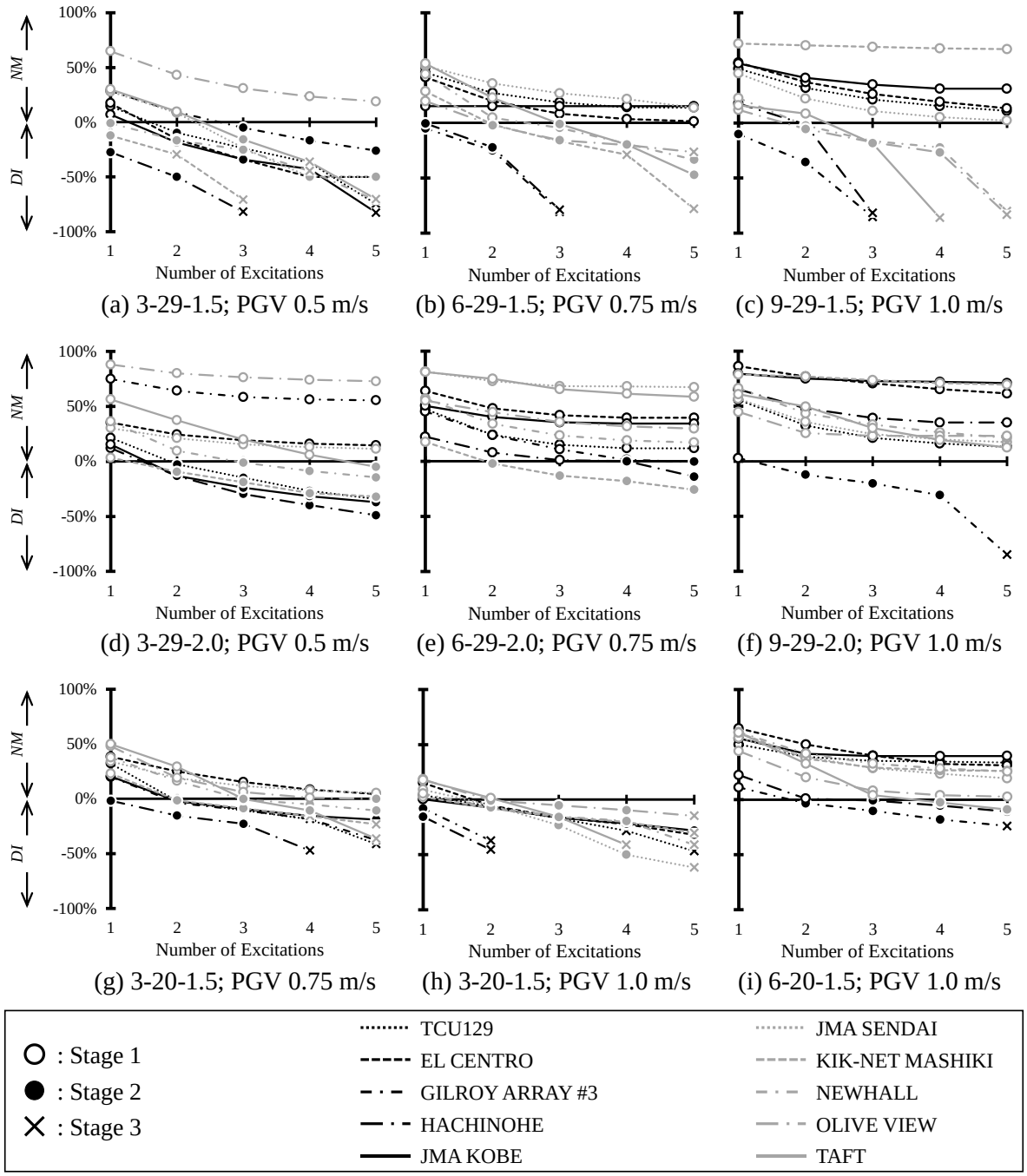

Figure 3-12 Comparison of *NM* and *DI* under multiple excitations

3.3.4 Collapse Fragility

In Chapter 2, the seismic performance of non-deteriorated SMRF models excited by multiple strong ground motions has been evaluated. In the non-deteriorated model, the effect of column strength deterioration is not considered. Thus, the damage is concentrated on the beam members because the beam is weaker than the column. In Chapter 2, it is found that when the intensity of the input ground motion is larger than the design level (> 0.5 m/s), in a few

cases, collapse might occur. The collapse might be a local collapse due to the ductile fracture at the beam end or a collapse due to reaching the ultimate state of maximum SDA of 10%. All the ductile SMRF models analyzed in Chapter 2 are designed with D_c/t = 29.45 and ${}_cM_p/{}_bM_p \geq$ 1.5. In this chapter, the collapse is evaluated using similar criteria, i.e., ductile fracture at the beam end and the weak story collapse due to strength deterioration of columns. The story collapse occurs when the story stiffness is negative and the story shear has deteriorated until less than zero as shown in Figure 3-5. Meanwhile, the ductile fracture is evaluated using the same cumulative damage evaluation method in Chapter 2, Section 2.2.5.

Figure 3-13 shows the comparison of the percentage of uncollapsed cases of the non-deteriorated models (Chapter 2) and the deteriorated models analyzed in this chapter under various intensities. A-29-1.5 series models (Figure 3-13(a)) have the same design parameters as the ductile models. However, since the weak story collapse is more likely to occur in the deteriorated models due to the column strength deterioration, the percentage of the uncollapsed cases is lower than that of ductile models. To cope with the effect of the column strength deterioration under multiple strong ground motion excitations, the design parameters need to be improved, either by increasing the ${}_cM_p/{}_bM_p$ or lowering the D_c/t. For example, as shown in Figure 3-13, A-29-2.0, A-25-2.0, and A-20-1.75 series models have similar performance (in terms of percentage of uncollapsed cases) with those of non-deteriorated models under the intensity of PGV 0.5, 0.75, and 1.0 m/s, respectively.

Table 3-1 shows the combination of D_c/t and minimum ${}_cM_p/{}_bM_p$ to achieve the acceptance criterion. The acceptance criterion is the same as that used in Chapter 2 which is more than or equal to 90% (≥ 90%) of uncollapsed cases. For every D_c/t value, Table 3-1 shows the minimum ${}_cM_p/{}_bM_p$ needed to achieve the acceptance criterion under various intensities and number of excitations. "–" mark means that none of the ${}_cM_p/{}_bM_p$ used in this study can fulfill the acceptance criterion for the specific D_c/t value. The lower the D_c/t, the lower the minimum ${}_cM_p/{}_bM_p$ requirement. With the D_c/t = 29.45, the standard value of ${}_cM_p/{}_bM_p \geq 1.5$ can only resist up to four excitations of intensity of PGV 0.5 m/s. However, with the D_c/t = 20, the standard value of ${}_cM_p/{}_bM_p \geq 1.5$ can resist up to five excitations of PGV 0.5 m/s, five excitations of PGV 0.75 m/s, or four excitations of PGV 1.0 m/s.

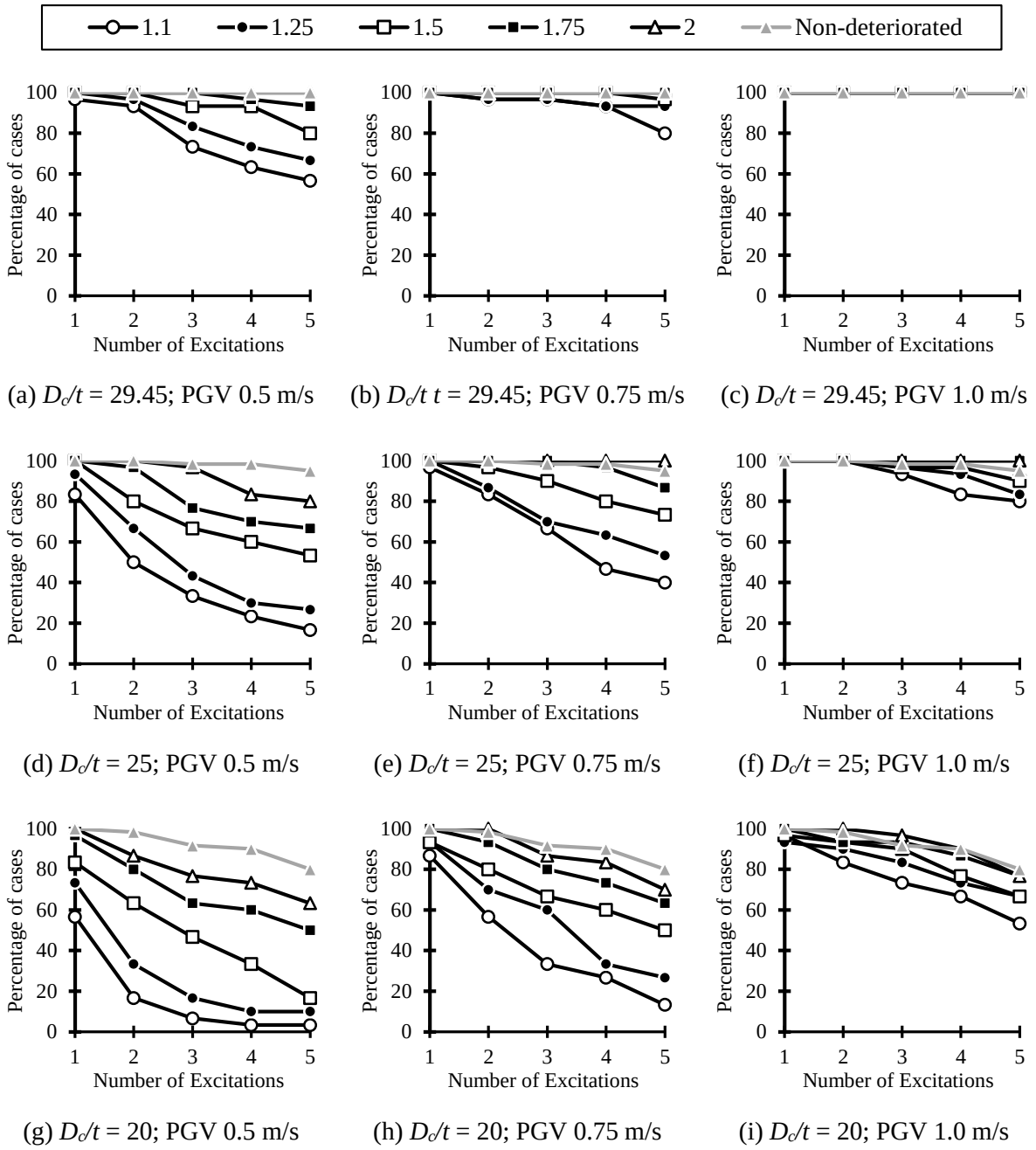

(a) D_c/t = 29.45; PGV 0.5 m/s (b) D_c/t t = 29.45; PGV 0.75 m/s (c) D_c/t = 29.45; PGV 1.0 m/s

(d) D_c/t = 25; PGV 0.5 m/s (e) D_c/t = 25; PGV 0.75 m/s (f) D_c/t = 25; PGV 1.0 m/s

(g) D_c/t = 20; PGV 0.5 m/s (h) D_c/t = 20; PGV 0.75 m/s (i) D_c/t = 20; PGV 1.0 m/s

Figure 3-13 Comparison of percentage of uncollapsed cases of ductile and deteriorated models

Table 3-1 Combination of ${}_cM_p/{}_bM_p$ and D_c/t to achieve ≥ 90% uncollapsed cases

Intensity (PGV)	0.5 m/s				0.75 m/s				1.0 m/s			
Number of Exc.	2	3	4	5	2	3	4	5	2	3	4	5
D_c/t = 29.45	1.1	1.5	1.5	1.75	1.75	2.0	–	–	–	–	–	–
D_c/t = 25	1.1	1.1	1.1	1.25	1.5	1.5	1.75	2.0	1.75	–	–	–
D_c/t = 20	1.1	1.1	1.1	1.1	1.1	1.1	1.25	1.5	1.25	1.5	2.0	–

3.4 Random and Incremental-Decremental Sequences

The same investigation with that of Chapter 2 is conducted for the deteriorated SMRF models. The effect of different input records is investigated by considering the random input sequences, while the effect of different input intensity is investigated by considering the incremental and decremental type of sequences.

3.4.1 Random Sequences

The same groups of random sequences used in Chapter 2 (Table 2-6 and Table 2-7) are used in this section. Then, the inelastic response analysis is conducted on the A-29-1.5 series models (models with the less ductile column) and A-20-1.5 series models (models with the more ductile column). Figure 3-14 shows the comparison of *NM* and *DI* of several selected cases under the repeated and random sequences (all the other results are included in Figures E-16 to E-17 and Figures E-18 to E-19 (Appendix E) for random sequence group 1 and group 2, respectively). As shown in the figure, the *NM* and *DI* under repeated and random sequences, either for models with a less ductile or more ductile column, do not differ significantly. As a summary of all the cases, Figure 3-15 shows the comparison of the percentage of cases reaching stages 2 and 3, while Figure 3-16 shows the comparison of the percentage of uncollapsed cases. As shown in both figures, the percentage of cases reaching stages 2 and 3 as well as the percentage of uncollapsed cases under repeated and random sequences do not differ significantly. Similar with the conclusion found in Chapter 2 for the non-deteriorated SMRF models, the effect of the sequence type (repeated or random) is also not significant in the deteriorated SMRF models. Thus, considering the easiness in analyzing and presenting the result, using the simple repeated sequences are more favorable than using the random input sequences.

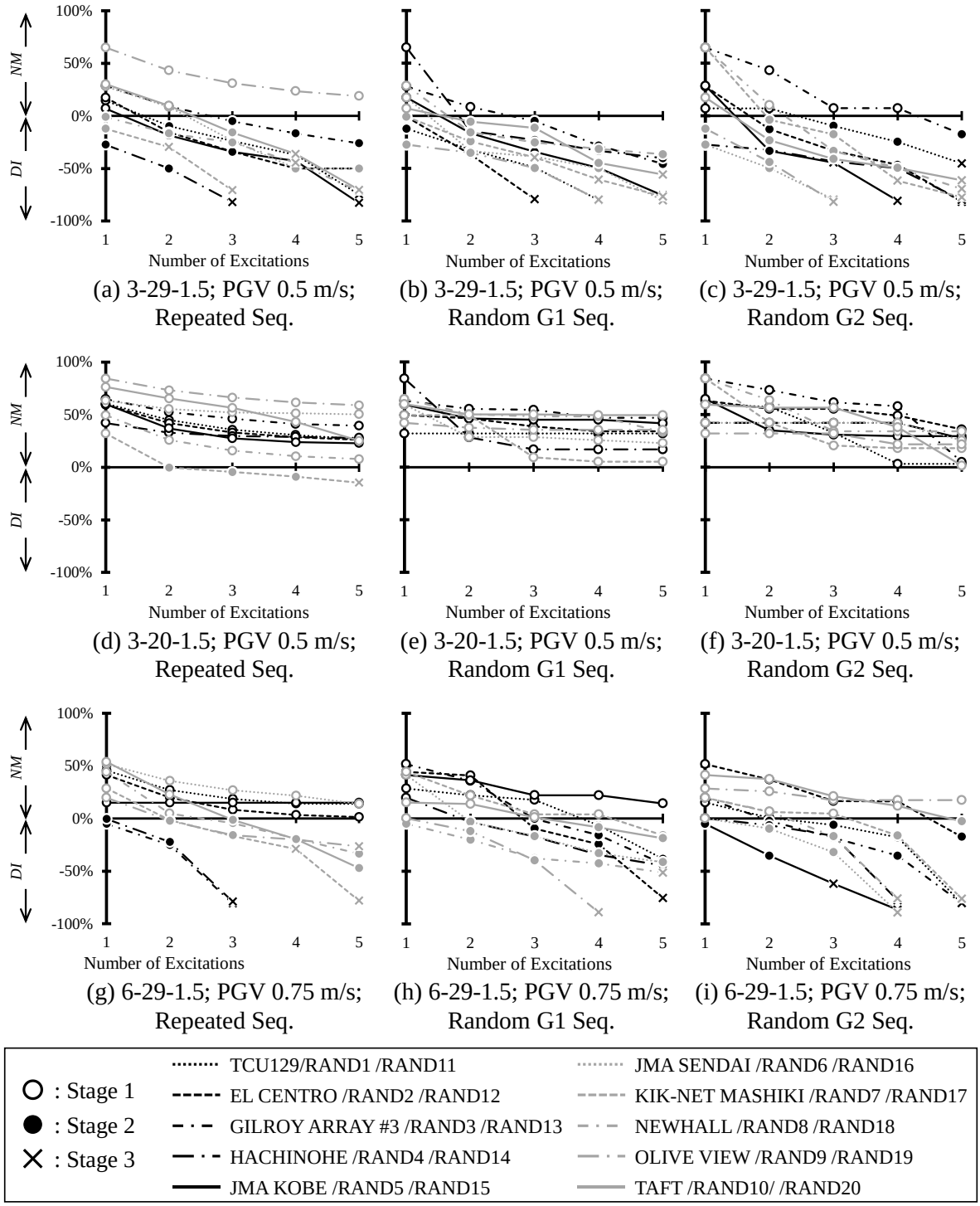

Figure 3-14 Comparison of *NM* and *DI* under multiple excitations by sequence types

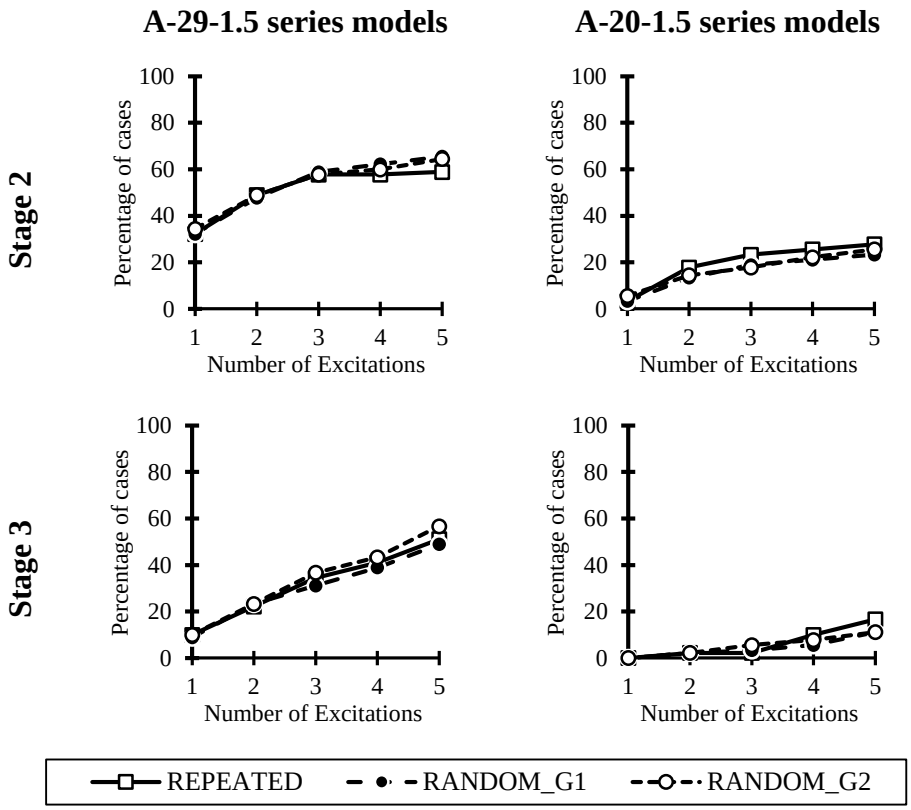

Figure 3-15 Comparison of percentage of cases reaching stages 2 and 3 by sequence types

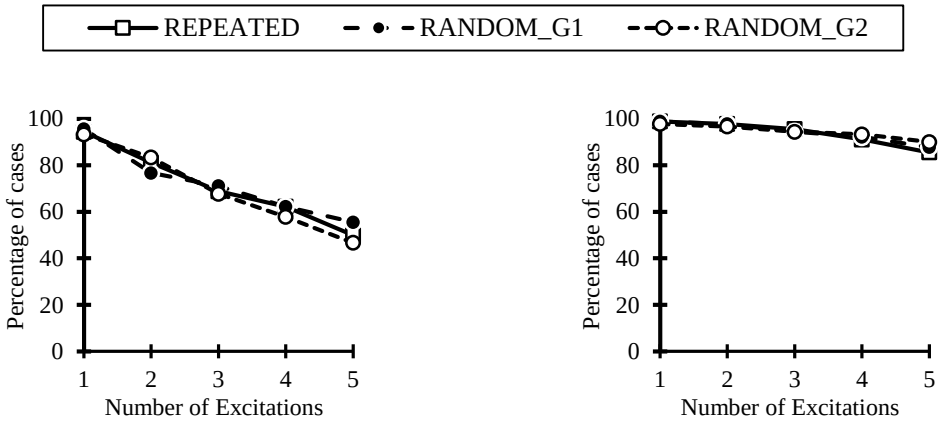

(a) A-29-1.5 series models (b) A-20-1.5 series models

Figure 3-16 Comparison of percentage of uncollapsed cases by sequence types

3.4.2 Incremental-Decremental Sequences

In this section, the incremental and decremental sequences are the same as those used in Chapter 2. Each sequence consists of three excitations with the same records but different

intensities. For the incremental sequences, the intensities are 0.5, 0.75, and 1.0 m/s for the 1st, 2nd, and 3rd excitations; and the intensities are reversed for the decremental sequences. Same with the previous section, the inelastic response analysis is only conducted on the A-29-1.5 series models (models with the less ductile column) and A-20-1.5 series models (models with the more ductile column). The results are shown in Figure 3-17 in terms of the percentage of cases reaching stages 2 and 3 and in Figure 3-18 in terms of comparison of *NM* and *DI* (the detail results of *NM* and *DI* under incremental-decremental sequences are included in Figures E-20 and E-21 (Appendix E) for A-29-1.5 and A-20-1.5 series models, respectively). The percentage of cases reaching stage 3 at the 3rd (last) excitation is very close and even equal either for the models with a less ductile or more ductile column. However, the percentage of cases reaching stage 2 at the last excitation is larger in the case of incremental sequences. This might be caused by the existence of residual deformation. Under the incremental sequences, before the occurrence of the higher intensity, the structure generally has a certain residual SDA (residual SDA caused by excitation with PGV of 0.5 m/s before the excitation with PGV of 0.75 m/s; and residual SDA caused by excitations with PGV of 0.5 and 0.75 m/s before the excitation with PGV of 1.0 m/s). Because of that effect, the excitation with higher intensity might have more impact under the incremental sequence than the decremental sequences. This effect seems to be more apparent in the deteriorated models than the non-deteriorated models because the large SDA has a direct impact on deteriorating the strength of the structure. A similar trend is also found from the comparison of the *NM* and *DI* at the last excitation where, in most of the cases, the *NM* or *DI* of the incremental sequences is larger than that of decremental sequences. From those two comparisons, it could be recommended that in case the variation of input intensity needs to be considered in the analysis, using the incremental type of input ground motions might be better because it is resulting in a more conservative prediction.

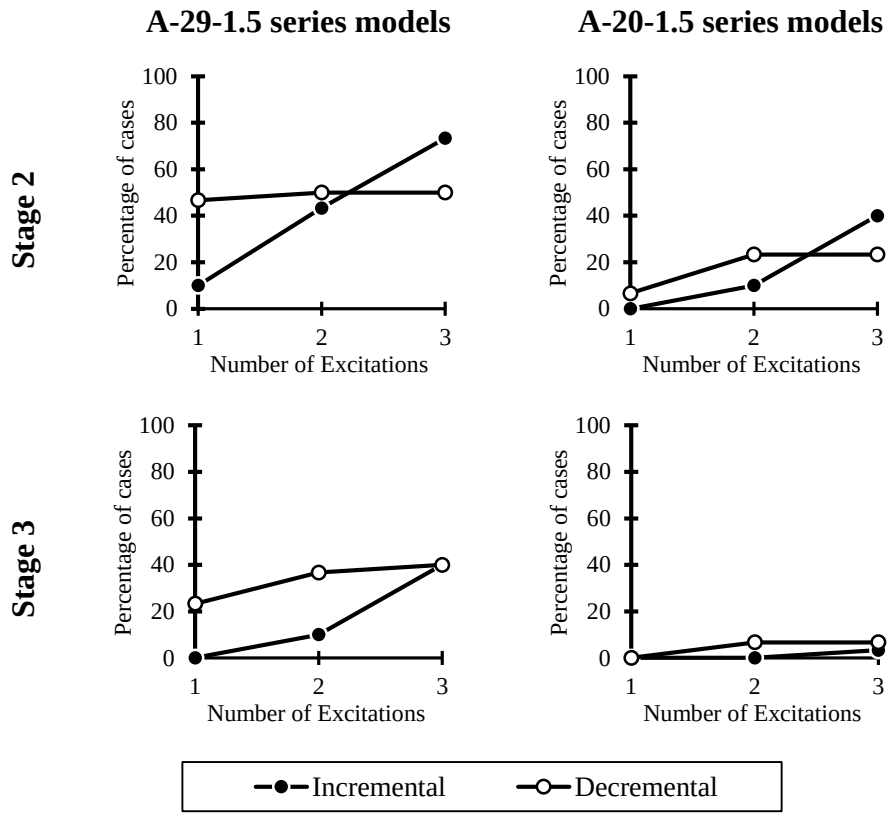

Figure 3-17 Comparison of percentage of cases reaching stages 2 and 3 by incremental and decremental sequences

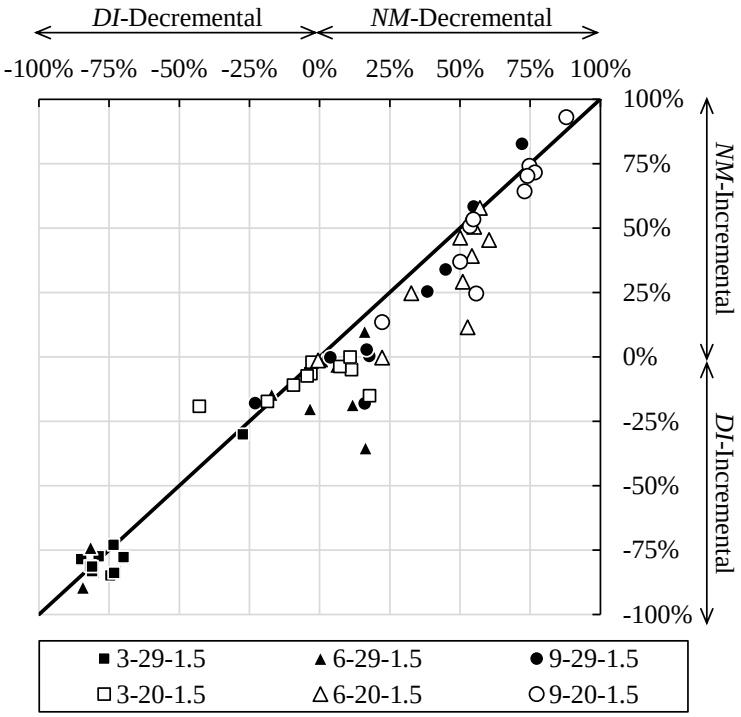

Figure 3-18 Comparison of *NM* and *DI* at the last excitation under incremental and decremental sequences

3.5 Summary

The effect of column strength deterioration on the seismic performance of SMRFs under multiple strong ground motion excitations is evaluated in this chapter. The SHS column hysteretic model considering strength deterioration due to local buckling is employed in the analytical model. To evaluate the seismic performance, 45 analytical models are created to consider three parameters: the number of stories (3, 6, and 9 stories), the column-to-beam moment capacity ratio ($_cM_p/_bM_p \geq$ 1.1, 1.25, 1.5, 1.75, and 2.0), and the column width-to-thickness ratio (D_c/t = 29.45, 25, and 20). The building models are designed using a plastic design method for severe earthquakes based on the Japanese seismic design code. Then, an inelastic earthquake response analysis is conducted for these models using ten different input ground motion records that are scaled to the PGV intensities of 0.5 m/s, 0.75 m/s, and 1.0 m/s to control the input energy. A summary of the findings from the analytical results is listed below.

- The typical structural behavior can be divided into groups depending on whether strength deterioration occurs on the 1st story column lower end hinge. If this strength deterioration does not occur, the structure generally achieves a stable behavior in which the seismic energy is dominantly dissipated by the Bauschinger part which means that there is no significant increment in terms of maximum deformation of the members. Additionally, moment redistribution occurs in a case in which the strength deterioration occurs; thus, this effect causes plastification on the 1st story column upper end as well, and when both end hinges lose a considerable amount of strength, 1st story collapse may occur.
- Three stages to story collapse under multiple strong ground motion excitations are defined. In stage 1, no deterioration occurs in the column. In this stage, the structure dissipates energy by the sway mechanism and maintains its stable behavior. Stage 2 is marked by deterioration at the 1st story column lower end. In this stage, the damage concentration and moment redistribution occur in the 1st story. The last stage, stage 3, is marked by the deterioration at the 1st story column upper end. In this stage, the structural mechanism shifts to a weak story mechanism, and when both end hinges lose a considerable amount of strength, 1st story collapse may occur.
- In terms of the number of stories, the 3-story model is the most vulnerable to excitation of multiple strong ground motions, followed by the 6-story model and the 9-story model. The main reason for this difference is the concentration of dissipated energy at the 1st story in the 3-story model, even before the 1st story column lower end hinge deteriorates. In

contrast, in the 6- and 9-story models, most of the energy is dissipated by the beam end hinges at the middle stories. This characteristic accelerates the progress of story collapse in the 3-story model due to the naturally occurring concentration of damage at the 1st story (stage 2).

- Comparing the percentage of cases reaching stages 2 and 3, it is found that increasing the ${}_cM_p/{}_bM_p$ or lowering the D_c/t can improve the performance of SMRFs under multiple excitations. The improvement is more significant under the higher intensity ground motions. In addition, lowering D_c/t by one step (29→25; 25→20) is found to be more effective to reduce the percentage of cases reaching stages 2 and 3 than increasing the ${}_cM_p/{}_bM_p$ by one step (1.1→1.25; 1.25→1.5; 1.5→1.75; 1.75→2.0).
- The progression of cumulative damage at every excitation which represents by the hinge state of the 1st story column can be identified according to the stages to collapse. In stage 1 (no deterioration), the decrease in the safety margin to deterioration is asymptotic as the structure reaches stable behavior. Meanwhile, in stage 2 (deterioration), the column strength deteriorated at a slower rate. Moreover, in stage 3, as the mechanism shifts to a weak story mechanism, the column strength deteriorates significantly until the 1st story collapse occurs. Increasing the ${}_cM_p/{}_bM_p$ can increase the safety margin at stage 1 and slowing down the transition from stage 2 to stage 3 while lowering the D_c/t can increase the safety margin at stage 1 and slowing down the rate of deterioration at stages 2 and 3.
- The column strength deterioration causes the deteriorated SMRF models to be more fragile to weak story collapse than the non-deteriorated SMRF models. Thus, the improvement in the design parameter (${}_cM_p/{}_bM_p$ and D_c/t) is needed to prevent more story collapse. The combination of ${}_cM_p/{}_bM_p$ and D_c/t to achieve the acceptance criterion of more than 90% uncollapsed cases is investigated.
- The effect of variation in input records and input intensity is investigated by conducting the analysis using random sequences and incremental-decremental sequences. From the comparison between the repeated and random sequences, it is found that the overall result in terms of percentage of cases reaching stages 2 and 3 as well as the percentage of uncollapsed cases do not differ significantly; thus, using the simple repeated sequence is more recommended considering the easiness in analyzing and presenting the results. In addition, from the comparison of the incremental and decremental sequences in terms of the percentage of cases reaching stage 2 and the *NM* and *DI* at the last excitation, in case the variation of input intensity needs to be considered in the analysis, it is recommended

to use the incremental type of input sequences because it is resulting in a more conservative prediction.

4. Full-Scale Steel Frame Test Simulating Multiple Earthquakes

4.1 Introduction

In this chapter, the effects of multiple earthquakes on the seismic performance of SMRFs is evaluated by conducting a cyclic-loading test on full-scale SMRFs with nonstructural components. Two specimens are tested in the experiment. The specimens are single-floor, one-span substructures of an intermediate story of typical current Japanese middle- or low-rise steel buildings. The structural systems of these two specimens are the same, but the attached nonstructural components are different. The light gauge steel (LGS) partition wall and autoclaved lightweight concrete (ALC) exterior wall are used as nonstructural components for each specimen. To simulate the occurrence of multiple earthquakes, one typical set of loading history that corresponded to one earthquake is created from the inelastic time-history response analysis results. During the test, multiple loading sets with various levels of intensities are loaded to simulate the occurrence of multiple earthquakes. From the test result, the damage progression as well as the change of strength and stiffness under multiple loading set is evaluated. In this study, the main focus of the test is to evaluate the structural performance of the SMRFs under multiple earthquakes. The attachment of the nonstructural component is for an additional consideration to evaluate building performance in terms of functionality related to the structural performance. In addition to the test result, further verification of the full structure through the numerical analysis result using both the non-deteriorated and deteriorated models is also presented.

4.2 Experimental Program

4.2.1 Specimen

In this experiment, two full-scale SMRF specimens are tested. Figure 4-1 shows the setup and geometry of the specimen. The specimen represents a single-story, one-span of the intermediate story of middle- or low-rise steel buildings. The floor areas of the specimens are 6 m × 2.5 m and the heights were 3.5 m. In this test, the focus of the experiment is on the north-south (NS) direction of the steel frames (6 m × 3.5 m). Thus, two oil jacks are attached at the

top corner of the two steel frames in the NS direction. The oil jacks are connected to the strong wall, while the specimen is connected to the strong floor with the use of the pin joint at the four corners.

Both specimens have the same structural components. The column members use the square hollow section (SHS) with BCR295 steel (nominal yield strength ≥ 295 N/mm^2; nominal tensile strength ≥ 400 N/mm^2), while the beam members use the wide flange section with SN400B steel (nominal yield strength ≥ 235 N/mm^2, nominal tensile strength ≥ 400 N/mm^2). The cross-sections and actual material properties (obtained from the material test) are shown in Table 4-1. The section of beams and columns are designed so that the ratio of the nominal yield moment of the column to the nominal full plastic moment of the beam is more than or equal to 1.5 to ensure that the strong-column weak-beam mechanism is reliably formed.

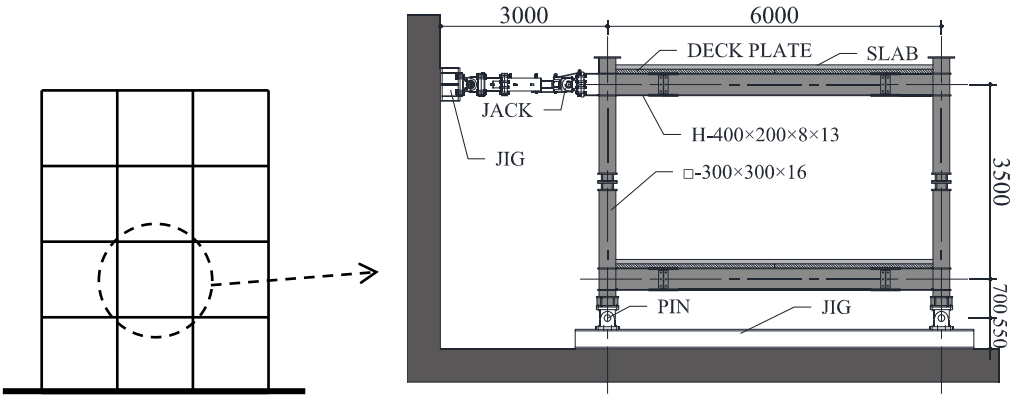

(a) Elevation view

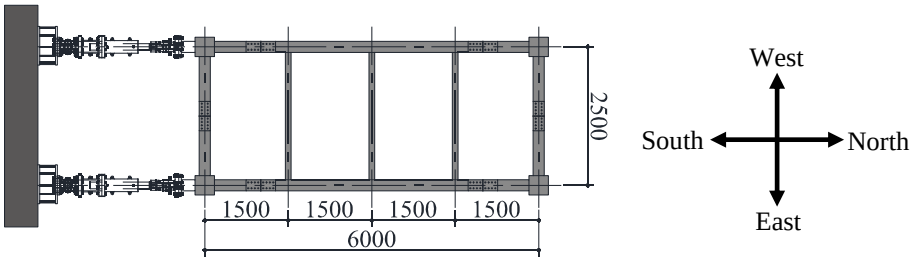

(b) Plan view

Figure 4-1 Geometry and setup of specimen

Table 4-1 Cross-sections and material properties

Member		Steel grade	Section [a)]	σ_y [b)] [N/mm^2]	σ_u [b)] [N/mm^2]
Column		BCR295	□–300×16	363	402
Beam	Flange	SN400B	H–400×200×8×13	277	410
	Web			377	458

a) □ – width × thickness, H – depth × width × web thickness × flange thickness (unit: mm), Symbol "□" and "H" denote square hollow section and wide flange section, respectively.

b) σ_y : yield strength, σ_u : tensile strength

In the east-west direction, in addition to the main beam, secondary beams (H-200×100×5.5×8) are attached every 1.5 m to provide lateral support to the main beams in the NS direction (Figure 4-1(b)). At the upper and lower floors, reinforced concrete slabs are cast on the deck plate; the height of the deck plate rib is 75 mm, while the thickness of the concrete slab above the rib is 80 mm (Figure 4-2). The slabs are connected to the steel beam by the shear stud. The spacing of the shear stud is determined in accordance with the Architectural Institute of Japan (AIJ) Design Recommendations for Composite Constructions (Architectural Institute of Japan 2010) to ensure full composite action between the steel beam and the concrete slab.

As shown in Figure 4-1, within one specimen, there are two typical steel frames in the NS direction, i.e., E- and W-frames (Figure 4-1(b)). The main difference between these two steel frames is the detail of the beam-to-column connection. As shown in Figure 4-2, the beam end connections of the E-frame have a weld access hole that conforms to Japanese Architectural Standard Specification 6 (Architectural Institute of Japan 2018), while those of the W-frame have no weld access hole. These two types of beam-to-column connection details are the new enhanced types of details that have been improved after the 1995 Kobe earthquake to prevent early fractures due to a stress concentration at the toe of the weld access hole.

In both types of connections, the wide flange section beams are shop-welded to the SHS column through the diaphragms. For the sake of easiness of transportation of the specimen to the experimental site, beam and column splices are provided as shown in Figure 4-1(a). The beam splices are located at a distance of 1 m from the centerline of the column, while the column splices are located at the middle of the column height.

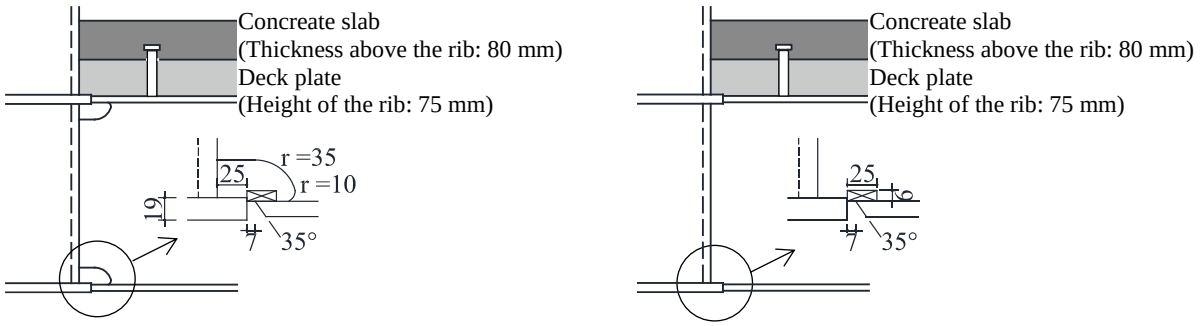

(a) With weld access hole, E-frame (b) Without weld access hole, W-frame

Figure 4-2 Beam-end connection detail for each specimen

While the structural components of both specimens are the same, the nonstructural component attached to the 1st and 2nd specimens are different. For the first specimen, the LGS partition wall type, which is one of the typical interior wall types, is installed on the steel frames. The LGS partition wall mainly consists of two layers of gypsum board and the LGS foundation frame to support the boards. Meanwhile, in the second specimen, the ALC wall type, which is one of the typical exterior wall types, is attached to the steel frames. The ALC wall is attached to the outer parts of the steel frame with a vertical rocking installation system and is mainly composed of the ALC panel and supporting angles that are attached around the door and window openings to support the panels. Hereafter, the first and second specimens will be referred to as "LGS frame" and "ALC frame," respectively.

Figure 4-3 shows the configuration of the LGS wall. As shown in the figure, the configuration of the LGS wall in the E- and W-frames are different. In the E-frame, all of the partition walls are installed aligned with the steel frame (flat part). Meanwhile, in the W-frame, some parts of the partition wall are not installed/aligned with the steel frame (eccentric part), and an opening is provided in the partition wall (opening part). These three types of configuration are commonly used for the interior partition wall in real buildings.

Figure 4-4 shows the configuration of the ALC wall. Similar with the LGS frame, the configuration of the ALC wall is designed to be different in both frames to consider some typical configurations for the exterior wall type. As shown in the figures, the E-frame wall has no openings, while the W-frame wall has two openings for a door and a window.

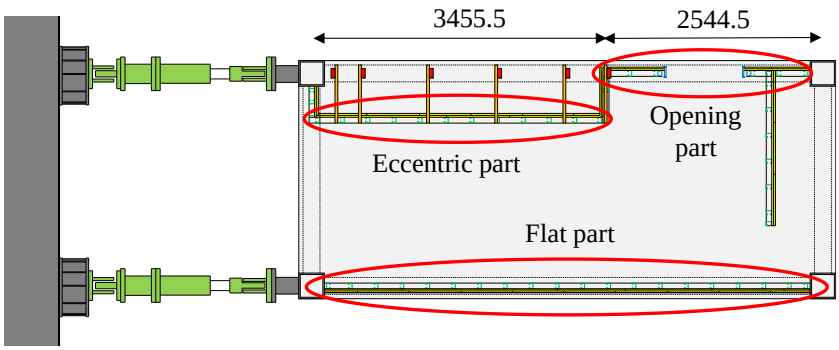

(a) Plan view

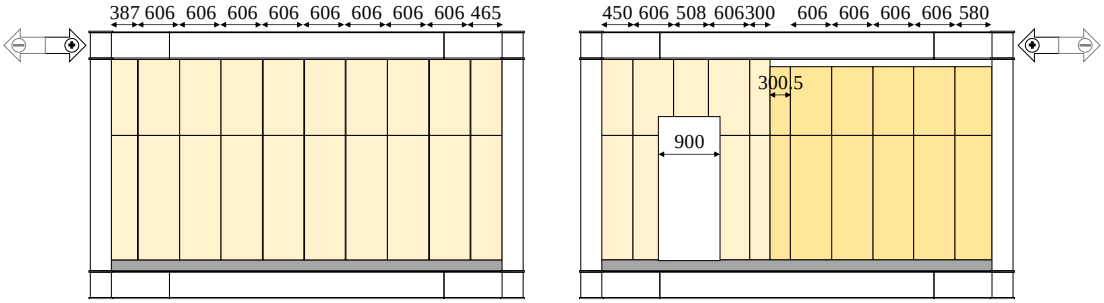

(b) E-frame (c) W-frame

Figure 4-3 Configuration of light gauge steel (LGS) wall

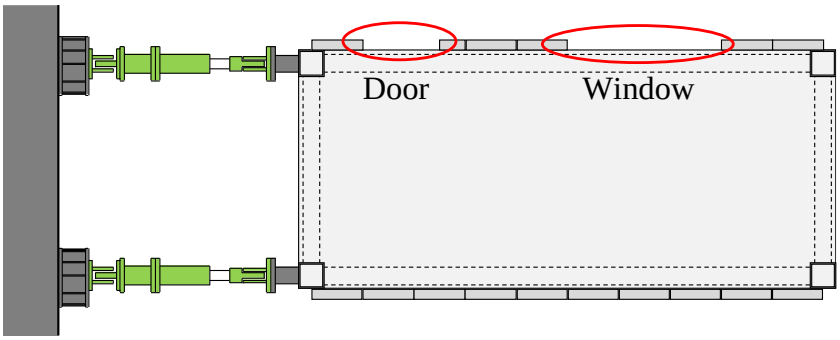

(a) Plan view

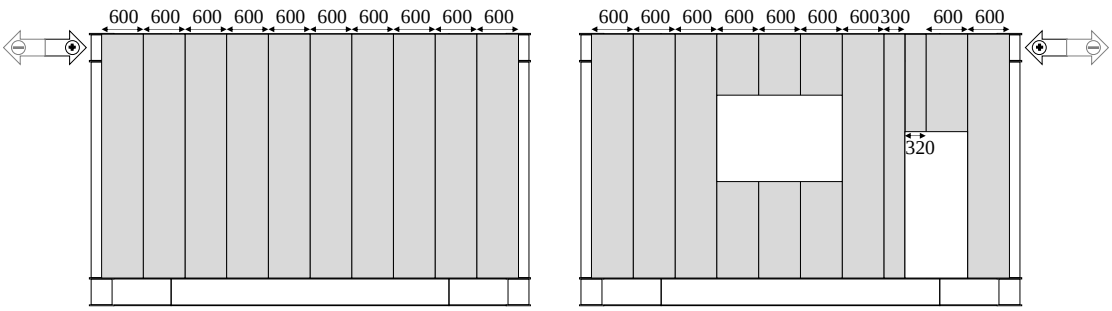

(b) E-frame (c) W-frame

Figure 4-4 Configuration of autoclave lightweight concrete (ALC) wall

4.2.2 Loading History

As explained in the previous section, two oil jacks are attached at the top corner of the E- and W-frames. During the loading, the static lateral force is generated from the jacks to the specimen in the NS direction. The loading is controlled by the lateral displacement of the frames, and the same displacement is induced to both frames at the same time.

To simulate the occurrence of multiple earthquakes, a special type of loading history is created from an inelastic time-history response analysis. The three-story model of non-deteriorated SMRF models with a strong-type column base (3-13 model of Chapter 2) is used to create the loading history. The same ten input ground motions are used in the analysis. All of the ground motions are scaled to the intensity of the peak ground velocity of 0.5 m/s to standardize the intensity.

From the response analysis, the story drift angle (R) time–history response at the 2nd story is extracted, and the rainflow counting algorithm (Endo et al. 1974) is performed to obtain the number of cycles of each amplitude. The amplitudes of each case are then grouped into five groups based on the ratio of their values to their maximum amplitudes (R_{max}). Table 4-2 lists the number of cycles in each group for each case of input ground motion. The average values shown in Table 4-2 are calculated after the exclusion of the maximum and minimum values in each group. One set of loading history is then created according to the average values shown in Table 4-2. Thus, one set of loading history consists of 0.4 R_{max} × 4 cycles, 0.6 R_{max} × 2 cycles, 0.8 R_{max} × 2 cycles, and 1.0 R_{max} × 1 cycle. It is also noted that the group of 0.1–0.3 R_{max} is neglected and the number of cycles of the group 0.3–0.5 R_{max} is reduced to half because of the time constraints regarding the execution of the experiment. These groups are chosen because the effects of the small-amplitude cycles on the specimen are considered to be negligible. The typical single set of loading history is shown in Figure 4-5. The cycles are symmetrically arranged by positioning the maximum amplitude cycle at the center. This set of loading history is considered to correspond to one earthquake.

Table 4-2 Number of cycles of each group

Case no.	Earthquake	0.1–0.3 R_{max}	0.3–0.5 R_{max}	0.5–0.7 R_{max}	0.7–0.9 R_{max}	0.9–1.0 R_{max}
1	El Centro	35	8	5	2	1
2	Taft	31	11	6	4	1
3	Hachinohe	65	8	2	3	1
4	Gilroy Array Number 3	27	12	1	2	2
5	Newhall	13	4	0	1	1
6	Olive View	12	1	2	1	1
7	JMA Kobe	16	9	1	1	1
8	TCU 129	28	7	3	1	1
9	JMA Sendai	101	45	4	2	1
10	Kik-net Mashiki	12	2	1	0	1
	Average	28	8	2	2	1

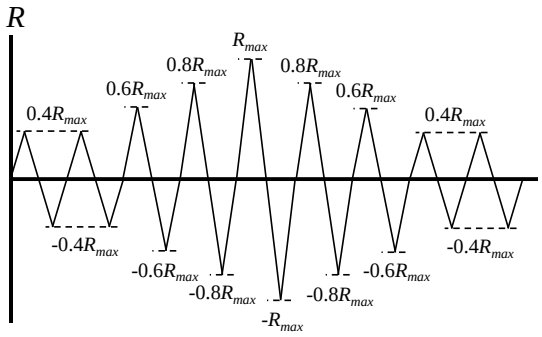

Figure 4-5 Typical single set of loading history

Set No.	R_{max}
1	1/400
2	1/200
3	1/100
4	1/200
5	1/75
6	1/100
7	1/50
8	1/75
9	1/33

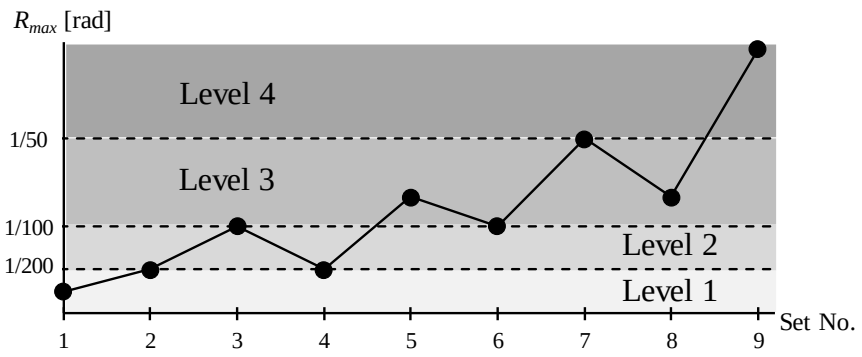

Figure 4-6 Maximum story drift angle (SDA) of each set and the corresponding earthquake level

During the test, multiple sets of loadings are performed with the incremental and decremental variations of the maximum amplitude (R_{max}) to simulate the occurrence of multiple earthquakes. The magnitude of the loading set is adjusted by changing the R_{max} value. Figure 4-6 shows the variation of R_{max}. In total, nine sets of loadings are planned to be conducted for each specimen. The loading sets are grouped in four different groups based on the R_{max}. Each level corresponded to an earthquake with a certain intensity. Level 1 is the lowest level with the limit of R_{max} of 1/200. At this level, the structure is expected to remain in the elastic range. For level 2, the limit of R_{max} is considered to be twice the limit of level 1 because 1/100 is commonly used as the targeted maximum story drift angle (SDA) in the design to guarantee the performance of SMRF and a certain type of nonstructural components, such as the ALC wall. The next two levels, namely, levels 3 and 4, are considered to be the over-design levels. For level 3, the limit of R_{max} is considered to be twice that of level 2 (1/50), while level 4 includes all the levels with R_{max} above the limit of level 3.

4.2.3 Measurements

The measurements and method used to obtain the actual value of SDA and the shear force that acted on each frame (E- and W-frames of both specimens) are described in this section. In this test, the SDA is defined as the ratio of the relative horizontal displacement of the centerline of the upper and lower beams to the story height that corresponds to the vertical distance between the centerline of the upper and lower beams. The SDA is obtained from the measured displacement at each node (δ). Figure 4-7 shows the positions of displacement transducers. In turn, δ is obtained by averaging the two displacement transducers that measured the absolute displacements at the upper and lower diaphragms. The SDA (R) is then calculated by the equation shown in Figure 4-9.

To measure the shear force that acted on the steel frames ($_cQ$), strain gauges are glued to the columns. Figure 4-8 shows the position of the strain gauges which are two sections of each column (CA and CB section). Four strain gauges are used for each section. The bending moments that acted on the sections CA and CB (M_{CA} and M_{CB}) are calculated using the measured strain based on the assumption that the plane section remains plane and the stress-strain curve is bilinear (see Appendix F). By assuming the linear moment distribution along the column, the shear force that acted on the column can be obtained by dividing the sum of M_{CA} and M_{CB} by the distance between the CA and CB sections. Accordingly, the value of $_cQ$

can then be obtained by summing the shear forces that acted on both columns as shown in Figure 4-9. Lastly, the shear force that acted on the nonstructural component can be calculated by subtracting the shear force that acted on the entire frame (Q) by ${}_cQ$. Q is measured by the load cell in the oil jacks in this test.

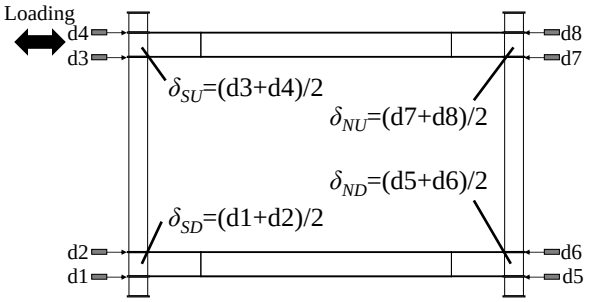

Figure 4-7 Position of displacement transducers used to obtain δ

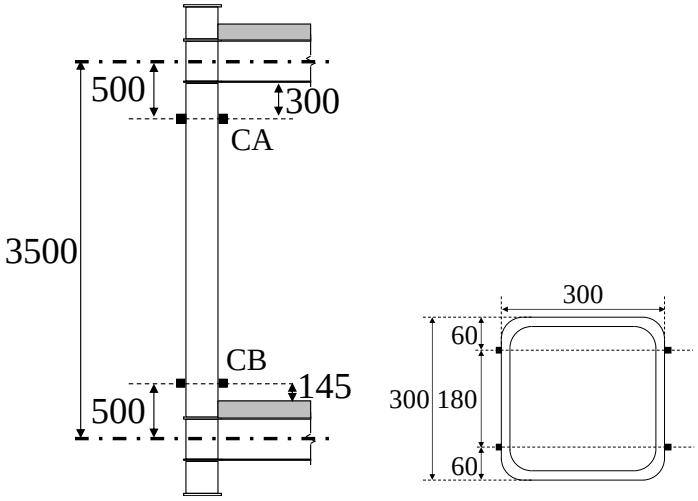

(a) Location of section (b) Glued position

Figure 4-8 Position of strain gauges used to obtain ${}_cQ$

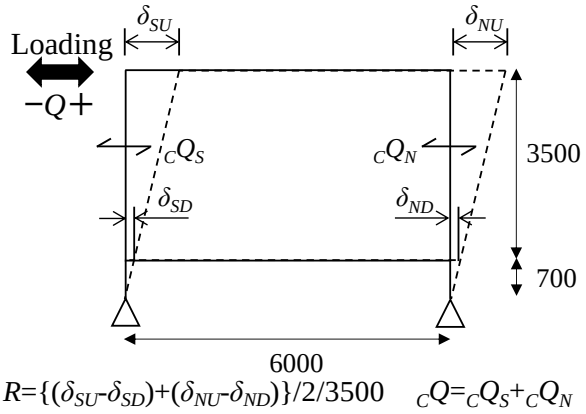

Figure 4-9 Calculation method used to obtain R and ${}_cQ$

4.3 Test Results

4.3.1 Damage Progression of LGS Frame

The first specimen that was tested during the experiment is the LGS frame. During the experiment, an observation was conducted regularly to check the visible damage generated within the structural and nonstructural components. The summary of the damages found in the structural and nonstructural components are shown in Table 4-3, and some of the observation photographs are shown in Figure 4-10.

Table 4-3 Damage progression of LGS frame

Set no. (R_{max}) [Intensity level]	The number of repetitions of each intensity level before reaching current set no.	Progression of damage	
		Structural component	Nonstructural component
1 (1/400) [Level 1]	–	–	Crack of the paint of gypsum board at the corner of the opening (Figure 10a)
2 (1/200) [Level 1]	Level 1 × 1	Crack of concrete slab due to negative bending moment above the beam splice	Previous crack deepened and reached the gypsum board
3 (1/100) [Level 2]	Level 1 × 2	Steel frame yielded	–
4 (1/200) [Level 1]	Level 1 × 2 Level 2 × 1	–	–
5 (1/75) [Level 3]	Level 1 × 3 Level 2 × 1	Crack of concrete slab due to positive bending moment close to the column	LGS foundation frame of eccentric part was detached (Figure 10b)
6 (1/100) [Level 2]	Level 1 × 3 Level 2 × 1 Level 3 × 1	Slab crack was slightly extended	–
7 (1/50) [Level 3]	Level 1 × 3 Level 2 × 2 Level 3 × 1	Local buckling at lower flange of E-frame and W-frame's lower beam (Figure 10c) Crack at the toe of the weld access hole of E-frame's lower beam	Gypsum board of flat part was deformed out-of-plane
8 (1/75) [Level 3]	Level 1 × 3 Level 2 × 2 Level 3 × 2	Slab crack was extended	–
9 (1/33) [Level 4]	Level 1 × 3 Level 2 × 2 Level 3 × 3	Crack at the toe of the weld access hole of E-frame's lower beam almost penetrated through flange (Figure 10e) Crack at the weld toe of the lower beam of the W-frame Crack at the web of E-frame's lower beam	Gypsum board of flat part was largely deformed out-of-plane, and the outside layer of the gypsum board fell off (Figure 10d)
Constant (1/33)	Level 1 × 3 Level 2 × 2 Level 3 × 3 Level 4 × 1	Crack at the lower flange of the E-frame's lower beam penetrated through the flange, and the flange section was fully fractured (Figure 10f)	–

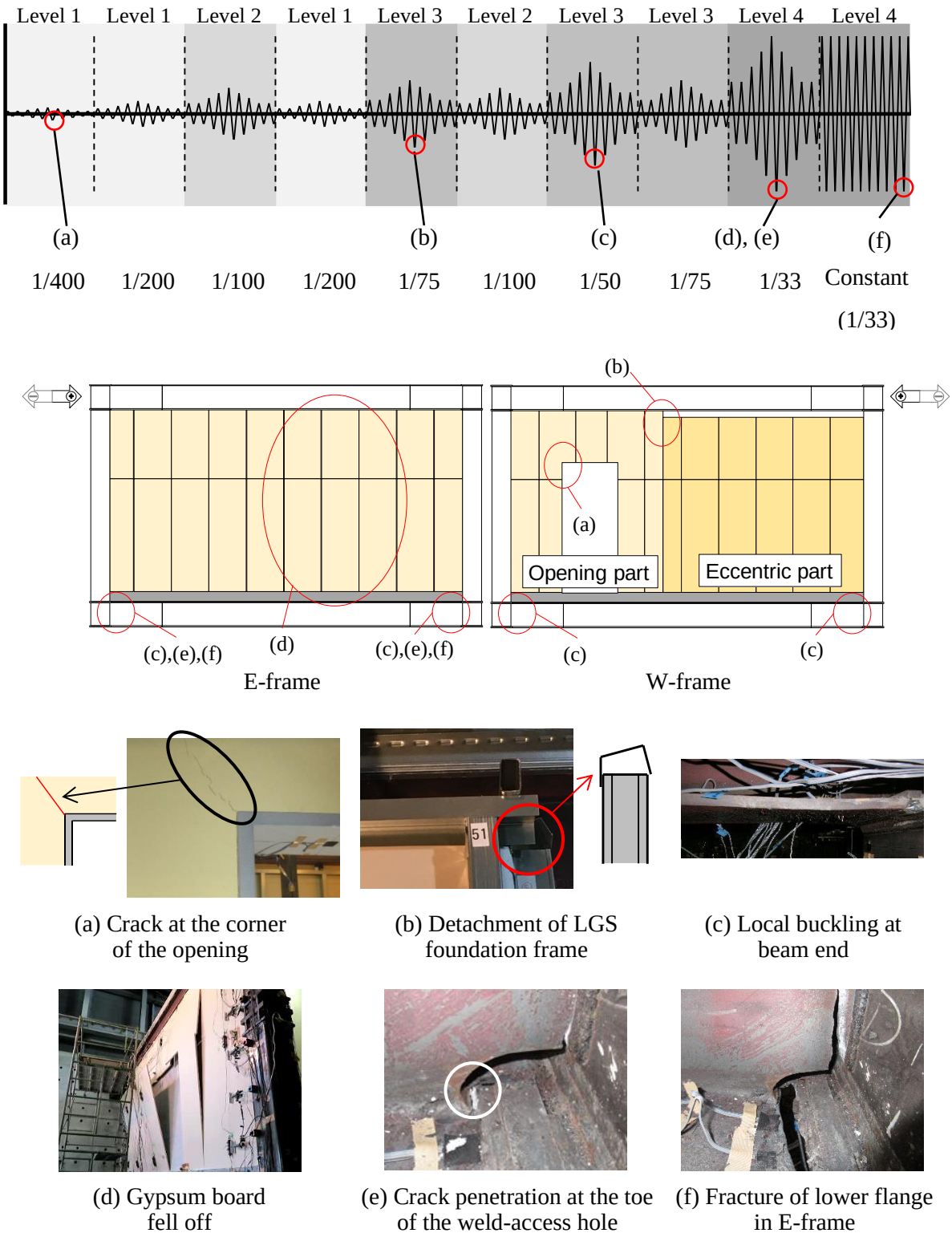

Figure 4-10 Damage progression of LGS frame

Until set no. 2 (level 1 × 2), a crack was generated on the gypsum board at the corner of the door opening (Figure 4-10(a)) and on the concrete slab above the beam splice. However,

structural members (columns and beams) remained in the elastic range. The lower beam of the steel frame started to yield at set no. 3 (level 2). At set no. 5 (level 3), the LGS foundation frame of the eccentric part was detached (Figure 4-10(b)), and another crack was generated on the concrete slab close to the column edge. The crack at the toe of the weld access hole and local buckling of the lower flange at the lower beam end were first observed at set no. 7. The crack was generated only in the E-frame (connection detail with weld access hole), while local buckling was observed in both frames (Figure 4-10(c)). At the same set, the gypsum boards in the flat part were deformed outside the plane owing to the large deformation. Lastly, at set no. 9 (level 4), the outside layer of the gypsum board was largely deformed outside the plane and fell off (Figure 4-10(d)). Furthermore, at this last set, the crack initiated from the toe of the weld access hole was almost penetrated through the flange thickness, and another crack was generated on the web (Figure 4-10(e)), while in the beam end of the W-frame, a small crack was generated at the weld toe of the beam lower flange. After completing all the nine sets of loading, the test was continued by applying the constant amplitude of R = 1/33. The loading was stopped after ten and a half cycles of constant amplitude because the lower flange and over half of the web depth of the lower beam in the E-frame had been fully fractured (Figure 4-10(f)).

4.3.2 Damage Progression of ALC Frame

The second specimen in the test was the ALC frame. Similar with the first specimen, an observation was conducted regularly to check the visible damage generated within the structural and nonstructural components. Table 4-4 summarizes the damages generated within the specimen, and Figure 4-11 shows some of the observation photographs.

The ALC wall remained undamaged until set no. 7. At set no. 7, the crack of the ALC panel was found around the opening, as shown in Figure 4-11(a). Meanwhile, until the end of the loading, there was no significant damage in the ALC wall of the E-frame. Conversely, the damage found in the structural component was similar with that of the LGS frame. The crack was first generated at set no. 7 at the toe of the weld access hole of the lower flange at the lower beam end, and the crack penetrated through the entire flange thickness at set no. 9, as shown in Figure 4-11(b). After completing all the sets, the loading was continued by applying a constant amplitude R = 1/50. After five cycles of constant amplitude loading, the loading was

stopped because the lower flange of the lower beam in the E-frame was fully fractured, as shown in Figure 4-11(c).

Table 4-4 Damage progression of ALC frame

Set no. (R_{max}) [Intensity level]	The number of repetitions of each intensity level before reaching current set no.	Progression of damage	
		Structural component	Nonstructural component
2 (1/200) [Level 1]	–	Crack of concrete slab due to negative bending moment above the beam splice	–
3 (1/100) [Level 2]	Level 1 × 1	Steel frame yielded Crack of concrete slab due to positive bending moment close to the column	–
4 (1/200) [Level 1]	Level 1 × 1 Level 2 × 1	–	–
5 (1/75) [Level 3]	Level 1 × 2 Level 2 × 1	Local buckling at lower flange of E-frame and W-frame's lower beam	–
6 (1/100) [Level 2]	Level 1 × 2 Level 2 × 1 Level 3 × 1	Slab crack was slightly extended	–
7 (1/50) [Level 3]	Level 1 × 2 Level 2 × 2 Level 3 × 1	Crack at the toe of the weld access hole of the lower beam of the E-frame	Crack of the ALC panel around the opening in the W-frame (above the window) (Figure 11a)
8 (1/75) [Level 3]	Level 1 × 2 Level 2 × 2 Level 3 × 2	Slab crack was extended	–
9 (1/33) [Level 4]	Level 1 × 2 Level 2 × 2 Level 3 × 3	The crack at the toe of the weld access hole of E-frame's lower beam penetrated through the flange (Figure 11b)	–
Constant (1/50)	Level 1 × 2 Level 2 × 2 Level 3 × 3 Level 4 × 1	Lower flange of the E-frame's lower beam was fractured (Figure 11c)	Until the loading was completed, no considerable damage was found on the ALC panel in the E-frame (without openings)

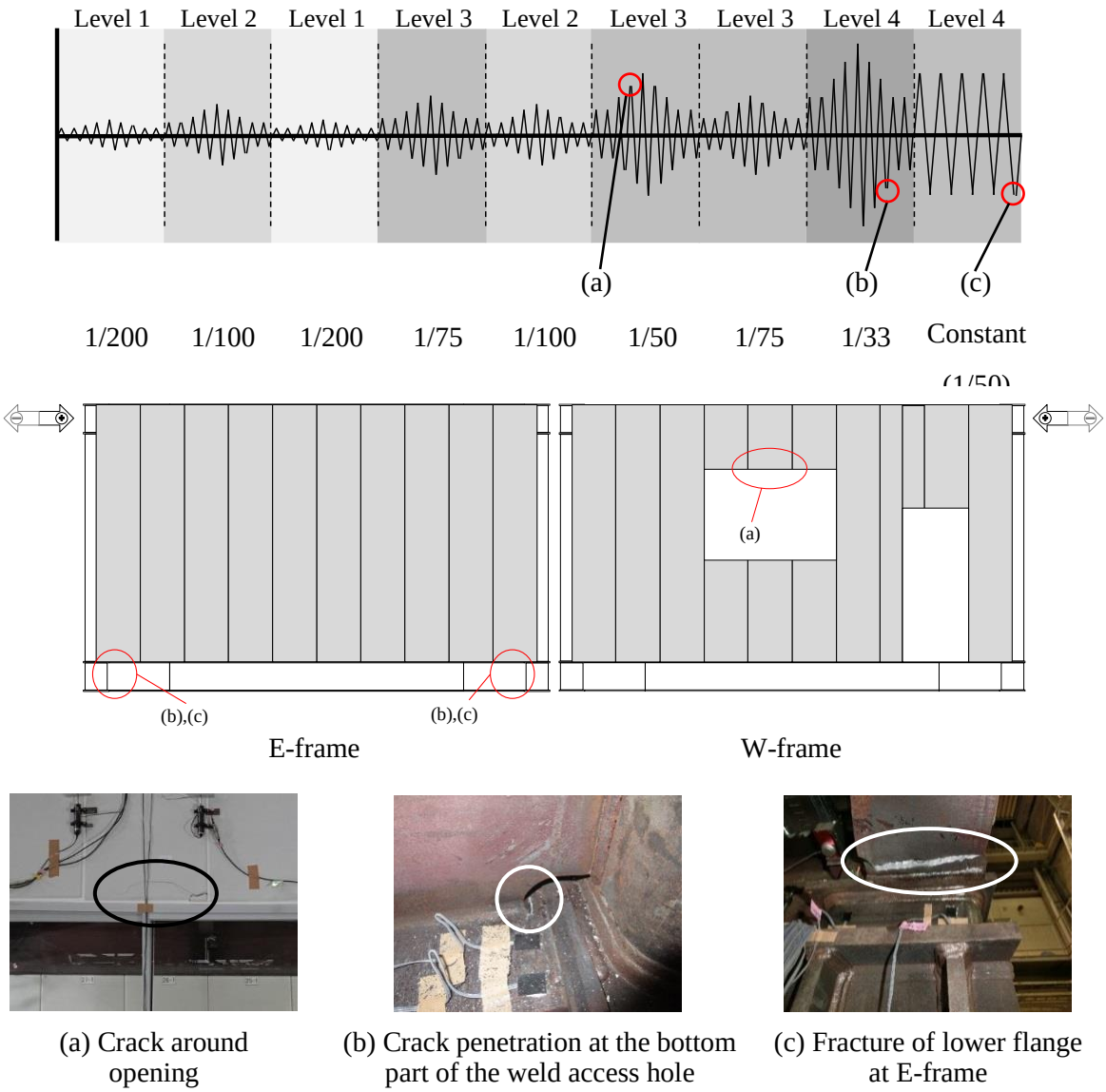

(a) Crack around opening

(b) Crack penetration at the bottom part of the weld access hole

(c) Fracture of lower flange at E-frame

Figure 4-11 Damage progression of ALC frame

4.3.3 Comparison of Performance Based on Damage Progression

In general, the steel frames performed well when subjected to multiple earthquakes. From set no. 2 to 6 (R_{max} < 1/50), no heavy damage is found on the structure other than cracks on the slab and local buckling. Cracks on the beam-to-column connections are initiated at set no. 7 (R_{max} = 1/50) and extended at set no. 9 (R_{max} = 1/33), and a considerable crack is found on the E-frame (connection with weld access hole). This means that based on the observation of visible damage, the connection without the weld access hole performs better when it is subjected to multiple earthquakes.

In the case of the nonstructural component, the ALC wall performs better than the LGS wall. This may be related to the attachment position of the wall. The LGS wall is attached inside the steel frame. Thus, the LGS wall and the structure came into contact when the structure is deformed and the LGS wall resists a considerably large amount of shear force that typically causes its damage. Meanwhile, the ALC wall is attached outside of the steel frame. Thus, the contact between the ALC wall and the structure do not occur even when the structure deforms. The shear force is only generated by the friction or contact caused by rocking between the ALC panel which is relatively small compared with the direct contact in the case of the LGS wall. The opening and eccentric parts also affect the performance. In both specimens, the walls without openings performs better. The damage on the LGS wall with an opening is first found at set no. 1 (R_{max} = 1/400), while the damages on the LGS wall without an opening and ALC wall with openings are first found at set no. 7 (R_{max} = 1/50). Furthermore, the ALC wall without openings is relatively undamaged until the last set. In addition, the new visible damages on the nonstructural component are only found at the set when the R_{max} is increasing (set nos. 2, 5, 7, and 9). This shows the capacity of the nonstructural components to resist lower-level earthquakes after the occurrence of a higher level earthquake.

4.3.4 Load–Deformation Relationship

Figure 4-12 shows the load-deformation relationship of LGS frame at set 7 as an example, while all the other load-deformation relationship obtained in this experiment are included in Appendix G. In the figure, three types of load-deformation relationship are shown, i.e., whole frame (left), structural component only (middle), and nonstructural component only (right). As explained in section 5.2.3, the shear force that acted on the entire frame (Q) is obtained from the load cell inside the oil jack, while the force that acted on the steel frame only ($_cQ$) is obtained from the strain gauges attached on the columns, and the force that acted on the nonstructural component is the difference of Q and $_cQ$. Moreover, the values on the graph showed the absolute value of the shear force (in kN) at the R_{max} of the loading set.

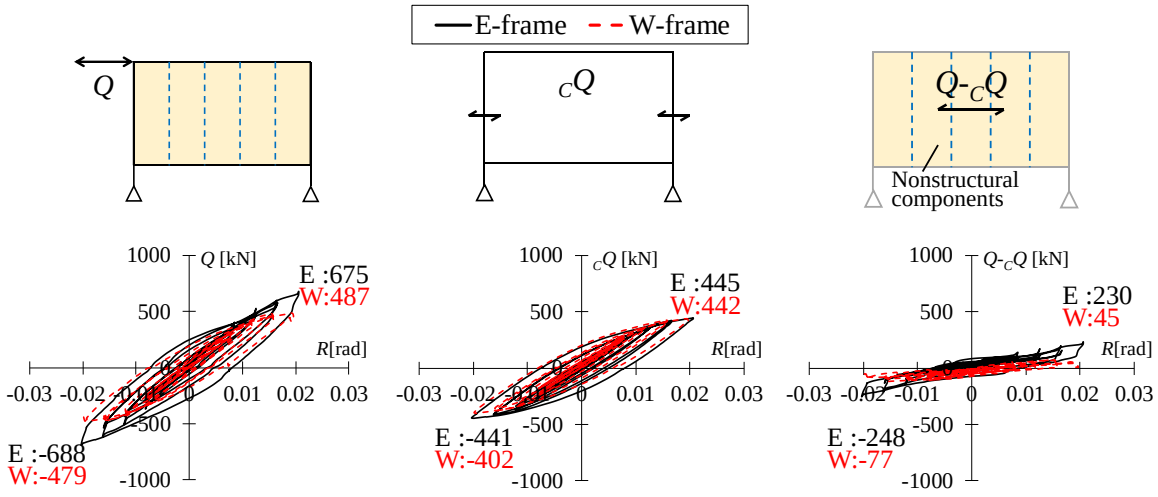

Figure 4-12 Three types of load–deformation relationship (set 7, level 3, R_{max} = 1/50, LGS frame)

4.3.5 Comparison of Two Sets with the Same R_{max} Values

Among the nine sets of loading, there are three pairs of sets with the same R_{max} values, i.e., set nos. 2 and 4 (R_{max} = 1/200), set nos. 3 and 6 (R_{max} = 1/100), and set nos. 5 and 8 (R_{max} = 1/75). Between the two sets with the same R_{max} values, there is a set with a larger R_{max} value, e.g., between set nos. 5 and 8, there is set no. 7 with R_{max} = 1/50. The effect of this larger level set on the structural and nonstructural components is evaluated by comparing the load-deformation relationship of two sets with the same R_{max}. Figure 4-13 shows the comparison for the structural component. The load-deformation relationships of the structural component of the W-frame in the LGS frame and the E-frame in the ALC frame are shown as examples. As shown in the figure, the trends for all levels (level 1: R_{max} = 1/200, level 2: R_{max} = 1/100, and level 3: R_{max} = 1/75) are the same. The strength at the story level is slightly decreased, however, the stiffness is mostly constant.

Figure 4-14 shows the comparison of nonstructural components. The load-deformation relationship of the LGS wall of the E-frame (without an opening) and the ALC wall of the W-frame (with openings) are shown as examples. The trend for the nonstructural components depends on the wall type (LGS or ALC) and the existence of opening and eccentric parts. For the LGS wall in the E-frame, as shown in Figure 4-14(a), both the strength and stiffness are decreased, and the tendency becomes clearer at the higher level. Conversely, for the ALC wall of the W-frame, as shown in Figure 4-14(b), the strength is only slightly decreased, while the stiffness is almost the same.

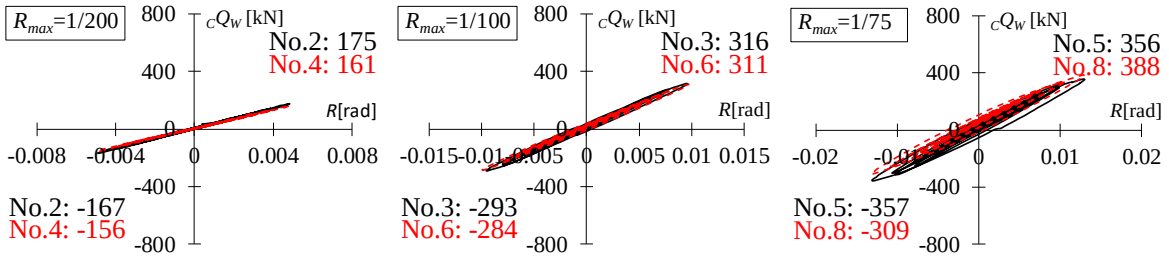

(a) W-frame in the LGS frame

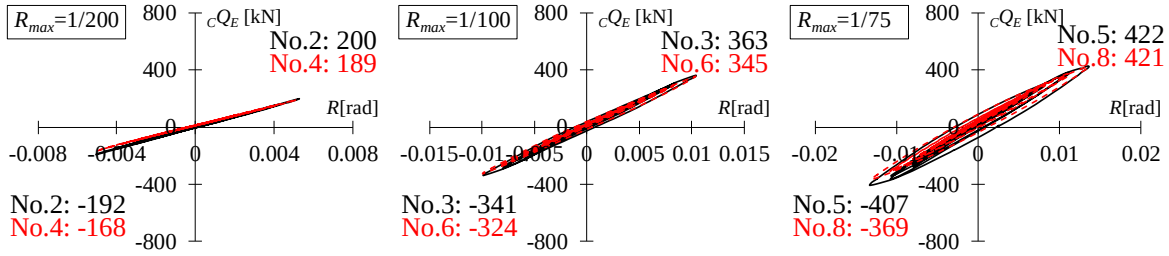

(b) E-frame in the ALC frame

Figure 4-13 Comparison of the load-deformation relationships of the structural components for two sets with the same R_{max} values

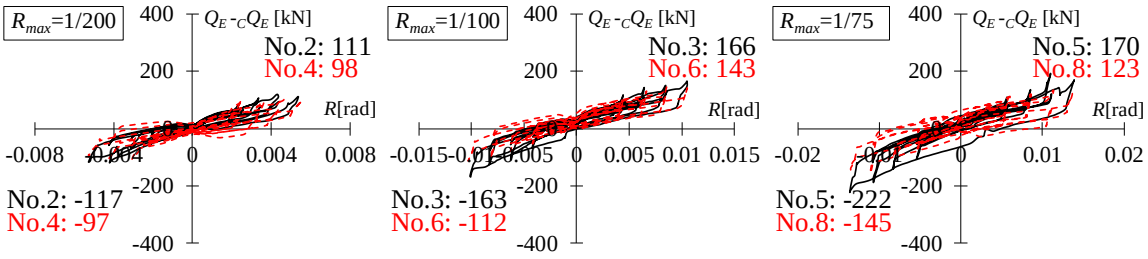

(a) LGS wall of the E-frame (Without an opening)

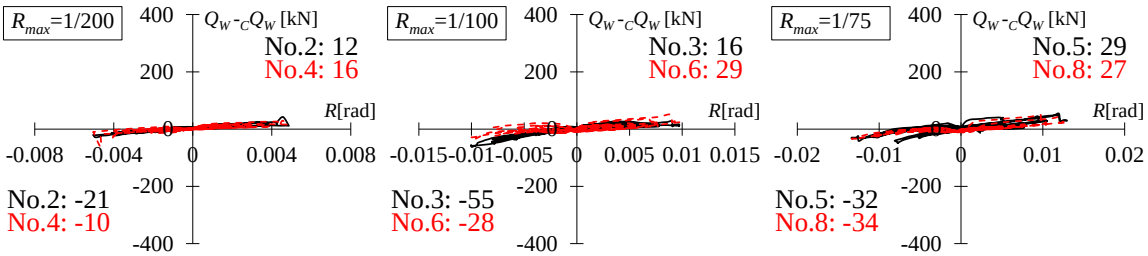

(b) ALC wall of the W-frame (With openings)

Figure 4-14 Comparison of the load-deformation relationships of the nonstructural components for two sets with the same R_{max} values

Figure 4-15 shows the comparison of strength degradation at various levels for both structural and nonstructural components. The strength degradation is calculated by subtracting the total shear force at the R_{max} (shear force at R_{max}(+)−shear force at R_{max}(−)) of the first and second loading sets (no. 2–no. 4 for level 1, no. 3–no. 6 for level 2, no. 5–no. 8 for level 3). The bar chart shows the percentage of strength degradation, while the value above each bar shows the absolute value of strength degradation (in kN) for each case. For the structural component, the trends of strength degradation are the same. In general, the strength decreases by approximately 6−9% at level 1 and by less than 6% at levels 2 and 3. Meanwhile, for the nonstructural components, the trend is different for each type. The most significant reduction is on the LGS wall in the E-frame case. Both the percentage and the absolute value increase as a function of the level. For the other three types, no definite trends are identified that are related to the earthquake level. However, overall, the strength decreases. The absolute strength degradation ranges from 0 to 30 kN which is less than 4% of the strength of the structural components, except for the LGS wall in the W-frame at level 1 (8.8%).

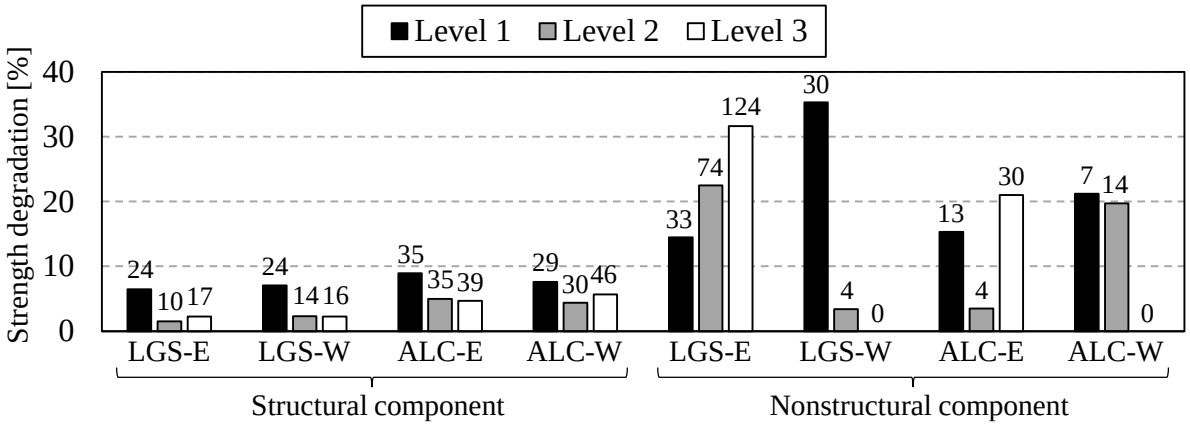

Figure 4-15 Strength degradation of two sets with the same R_{max} values at various levels

4.3.6 Transition of Strength and Stiffness under Multiple Earthquakes

The strength and stiffness transition are represented according to the set number. Both the strength and stiffness of each set are calculated from the load-deformation relationship obtained in the experiment that indicates the strength and stiffness at the story level. Figure 4-16 shows the strength transitions of the structural components subjected to various levels of story drift angles (R_L), i.e., 0.5%, 1%, 1.33%, and 2%. The strength in each set is calculated by averaging the absolute strength at each R_L value. However, only cycles with peaks within the range of

$1.0R_L$–$1.4R_L$ are considered in the calculation because when the difference of the cycle peak is quite higher, the difference of the offset point at ${}_cQ = 0$ is also quite higher. Thus, the strengths at the R_L level will not be comparable. Figure 4-16(a) shows the cycles in each set that are considered in the calculation. As an example, for R_L = 1%, at set no. 7, only the 3rd and 7th cycles (peak = 1.2%) are considered in the calculation because the 1st, 2nd, 8th, and 9th cycles have peaks that are less than R_L (1%). Thus, the absolute strength at R = 1% is unknown. By contrast, the 4th–6th cycles have peak values over 1.4%.

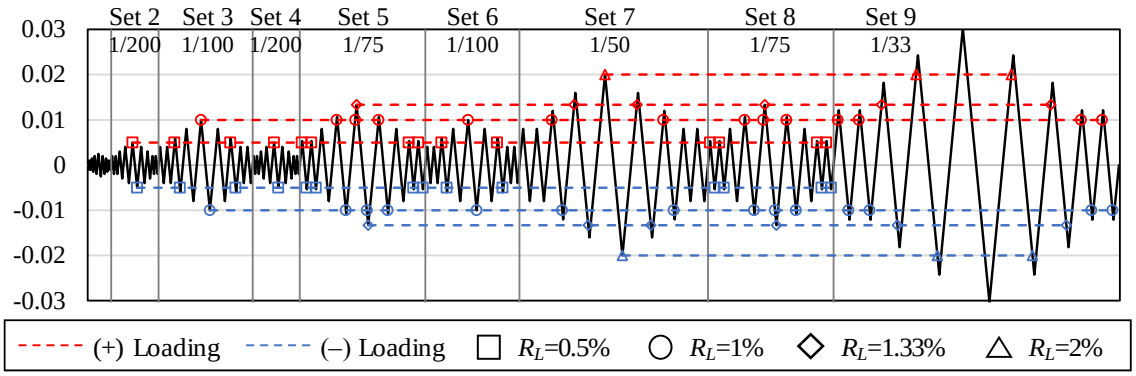

(a) Cycles within the range of 1.0–1.4R_L in each set

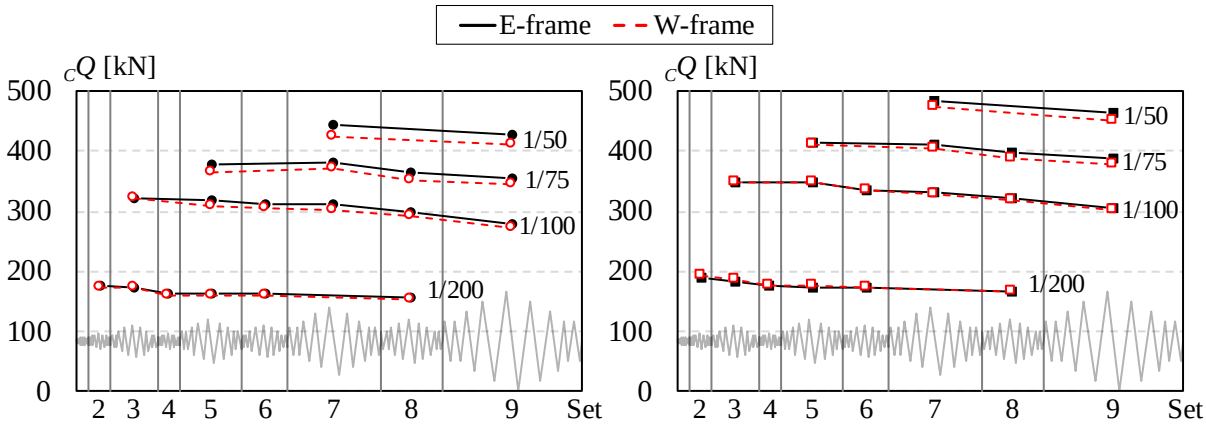

(b) LGS frame (c) ALC frame

Figure 4-16 Strength transitions of steel frames at various levels

The results are shown in Figure 4-16(b) and Figure 4-16(c) for the LGS and ALC frames, respectively. As shown in the figure, at all levels, the strengths of the steel frames, either in the LGS or ALC frames, gradually decreases as the number of sets increases. There is no considerable difference between the E-frame (without weld access hole) and the W-frame (with weld access hole), although the strength of the E-frame is slightly higher than that of the W-

frame. On average, the reductions of the strength from the first until the last set for R_L = 0.5%, 1%, 1.33%, and 2%, are 12.5%, 13.6%, 7.2%, and 3.8%, respectively.

The transition of the unloading stiffness (elastic stiffness) of the steel frames is shown in Figure 4-17. For every cycle, the elastic stiffness is calculated from the point where the unloading started (R_{unload}) until the point R reached the value of R_{unload} + 1/200 (for unloading to the positive direction) or the value of R_{unload} − 1/200 (for unloading to the negative direction). The range ±1/200 is used because the structure is still in the elastic range under set no. 2 (R_{max} = 1/200). The elastic stiffness for each set ($_CK_E$), as plotted in Figure 4-17, is then calculated by averaging the elastic stiffness of all cycles within the set. As shown in the figure, either for the LGS or ALC frames, despite the fluctuated trend, the elastic stiffness is barely changed across the sets. For the LGS frame, the stiffness ranges from 9.1 to 10.2 kN/mm (with an average of 9.7 KN/mm), while for the ALC frame, the stiffness ranges from 9.9 to 10.9 kN/mm (with an average of 10.5 kN/mm). Therefore, it can be implied that the multiple earthquake excitations (from level 1 to 3) barely affect the elastic stiffness of the steel frames.

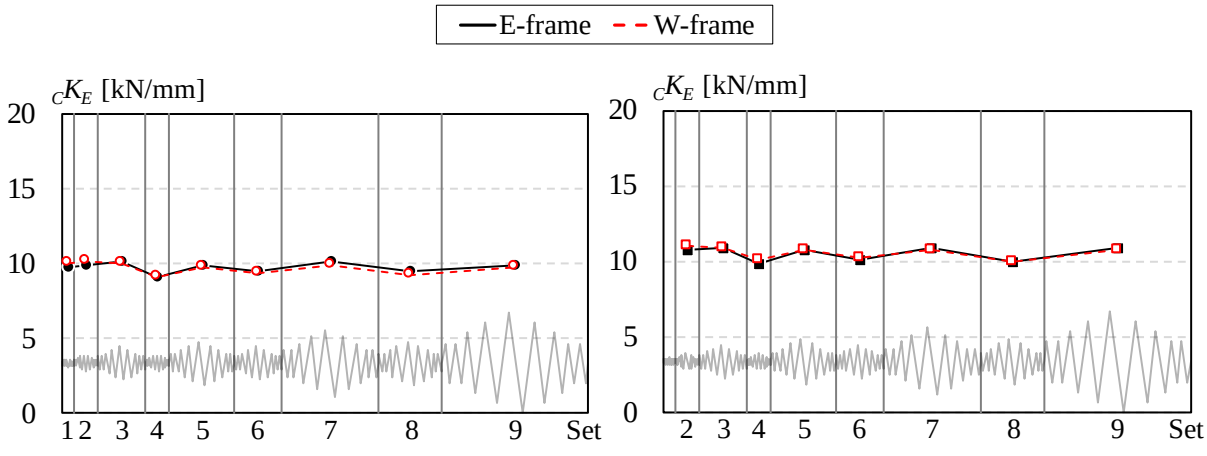

(a) LGS frame (b) ALC frame

Figure 4-17 Unloading stiffness/elastic stiffness transitions of steel frames

For the nonstructural component, the strength and stiffness are presented relative to those of the structural component (contribution of strength and stiffness). Figure 4-18 shows the transition of the strength contribution ($(Q - {}_cQ)/{}_cQ$) of the LGS wall and ALC wall across the sets. The strength contribution for each set is calculated by averaging the $(Q - {}_cQ)/{}_cQ$ ratio within the set. Given that the ratio will be excessively high (close to infinity) when the

denominator ($_cQ$) is close to zero, the calculation of the average only included points for which the $_cQ$ value was over 50% of the peak value of the $_cQ$ within the cycle.

As shown in Figure 4-18(a), for the LGS wall, the trend of the contribution tends to be higher for the lower level of the earthquake, and the contribution monotonically decreases as the number of sets increases. For the LGS wall in the E-frame (without an opening), excluding the level 1 set (set nos. 2 and 4), the contribution ranges from 22.6% to 37.1% (with an average value of 28.1%); while for the LGS wall in the W-frame (with an opening and eccentric part), the contribution ranges from 18.1% to 24.2% (with an average of 21.4%). Meanwhile, for the ALC wall (Figure 4-18(b)), no definite trend is found that is related to the earthquake level or the number of sets. The contribution rather fluctuates but is within the close range. For the ALC wall in the E-frame (without openings) excluding the last set no. 9, the contribution ranges from 18.9% to 26.1% (with an average of 23.2%), while for the ALC wall in the W-frame (with openings), the contribution ranges from 0.8% to 7.7% (with an average of 4.6%).

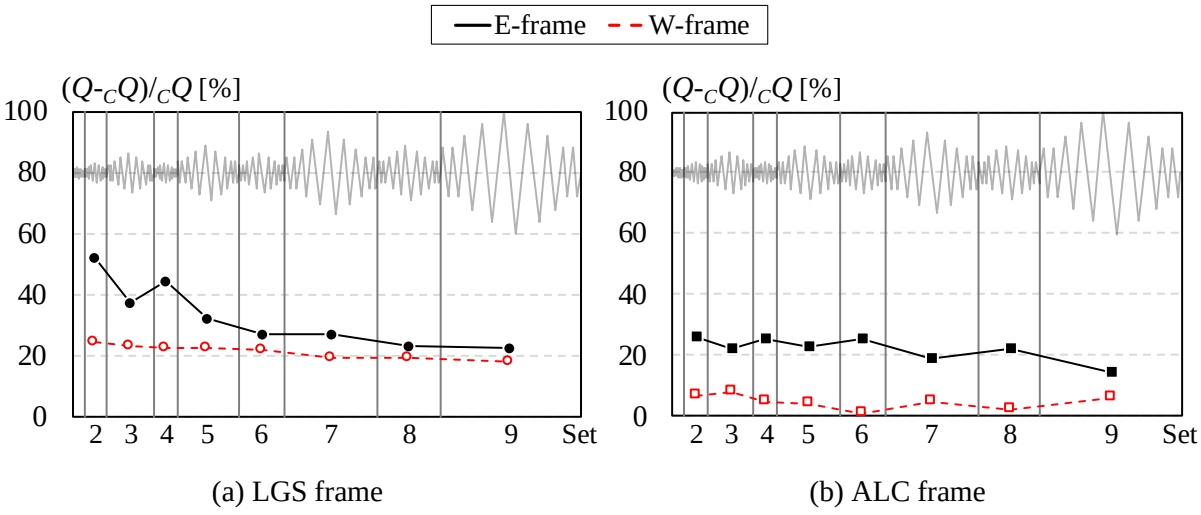

(a) LGS frame (b) ALC frame

Figure 4-18 Transitions of strength contribution of nonstructural components

The stiffness contributions of the nonstructural components are shown in Figure 4-19. $_CK_E$ is the average stiffness of the structural component within a set (the same as that shown in Figure 4-17), while $_{NS}K$ is the average stiffness of the nonstructural component within a set. By assuming that the load-deformation relationship of the nonstructural component is almost linear, for every set, the linear regression is performed to obtain a single linear equation that is

approximately close to the load-deformation relationship. In addition, the $_{NS}K$ value is considered to be equal to the slope/gradient of the line.

As shown in Figure 4-19(a) for the LGS wall, the trend is similar with that of the strength contribution of the nonstructural component. The LGS wall tends to contribute more at the lower level earthquakes. As the number of loading sets increases, the stiffness contribution gradually decreases. Meanwhile, for the ALC wall (Figure 4-19(b)), despite the fluctuated trend at the early set, the contribution tends to be permanently decreased after they pass a certain point across the sets. For the ALC wall in the E-frame (without openings), the point corresponds to set no. 7 (level 3, R_{max} = 1/50), while for the ALC wall in the W-frame (with openings), the point is set no. 5 (level 3, R_{max} = 1/75).

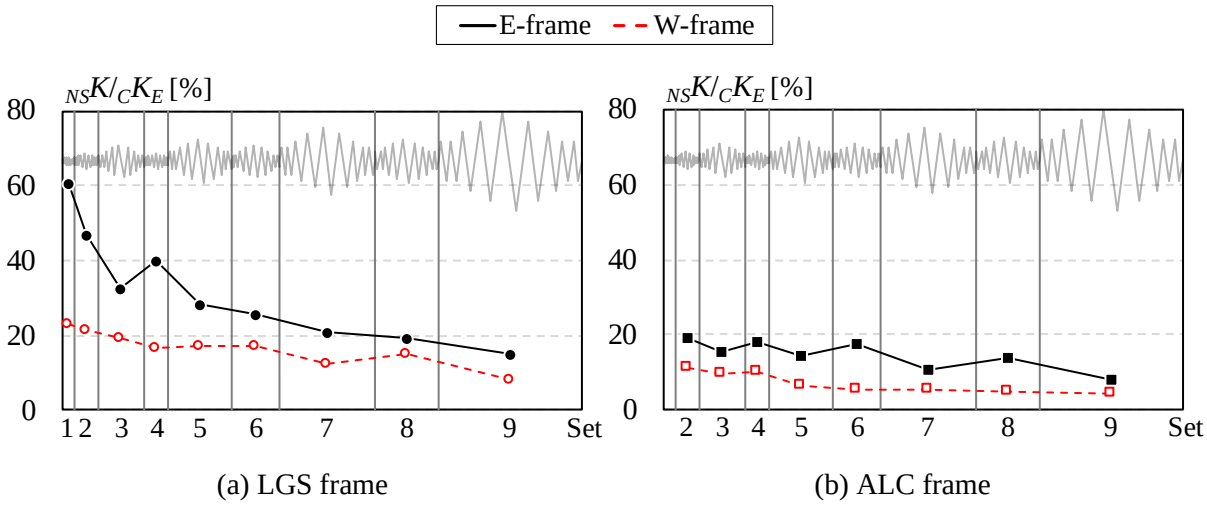

(a) LGS frame (b) ALC frame

Figure 4-19 Transitions of stiffness contribution of nonstructural components

4.4 Examination by Numerical Analysis

The performance of subassembly of SMRFs under multiple earthquakes with various levels of R_{max} has been verified in the previous section through the experimental test. To further analyze and verify the performance of the full structure, an inelastic time-history response analysis using both the non-deteriorated and deteriorated models is conducted. Different from the numerical analysis conducted in Chapters 2 and 3 where the input intensity level (PGV) is set prior to the analysis, in the numerical analysis in this section, the input intensity level is adjusted accordingly to reach the target story drift angle (SDA). The target SDA is the same as the R_{max} used in the test. However, since in the response analysis the input real records are not

symmetrical (maximum and minimum value is equal) like the loading set used in the test, also considering the existence of residual SDA between the excitation in the analysis, to make the models reach the same degree of deformation, story drift angle range (SDAR) is used instead of SDA. SDAR is the range from the minimum SDA to maximum SDA ($SDA_{max} - SDA_{min}$). Thus, in the analysis, the input intensity is adjusted so that the maximum SDAR ($SDAR_{max}$) is equal to $2R_{max}$. Table 4-5 shows the target $SDAR_{max}$ for every excitation. In this case, the excitation no. can be considered similar with the set no. used in the test, and the target SDAR for every excitation corresponds to $2R_{max}$ in the test. It should be noted that in the test, only nine sets are performed, and after nine sets, the loading is continued with a constant amplitude loading of 1/33 for 1st specimen and 1/50 for the 2nd specimen until the flange at the beam end is fully fractured. However, in this analysis, the constant amplitude loading is changed to another excitation (10th excitation) with a target $SDAR_{max}$ of 6% (2/33) by assuming that both have an almost equal degree of deformation.

Table 4-5 Target maximum story drift angle range ($SDAR_{max}$)

Exc. No.	Target $SDAR_{max}$ [rad]
1st	0.5%
2nd	1%
3rd	2%
4th	1%
5th	2.67%
6th	2%
7th	4%
8th	2.67%
9th	6%
10th	6%

A total of four models are used in this analysis, two each from the non-deteriorated and deteriorated models. For the non-deteriorated models, the two models are 3-13 and 6-13 models, while for the deteriorated models, the two models are 3-29-1.5 and 6-29-1.5 models. The four chosen models have the same characteristic, i.e., 3-story and 6-story models (two each), all are designed using strong-type column base, column width-to-thickness ratio (D_c/t) = 29.45, and

column-to-beam moment capacity ratio ($_cM_p/_bM_p$) ≥ 1.5. For the input records, six input records are chosen among the ten records that are previously used, as listed in Table 4-6. Using the four models and six different input records, the inelastic time-history response analysis is conducted by adjusting PGV intensity to achieve the target $SDAR_{max}$. Figure 4-20 and Figure 4-21 show the PGV intensity needed to achieve the target $SDAR_{max}$ in every excitation for the non-deteriorated and deteriorated models, respectively. In general, the PGV intensity for 6-story models is larger than that of the 3-story model because as previously found in Chapters 2 and 3, in the 3-story model, the deformation tends to concentrate at the 1st story; thus, to reach the same degree of $SDAR_{max}$, the PGV intensity needed for the 3-story models is lower than that of 6-story models. Meanwhile, comparing the PGV intensity of non-deteriorated and deteriorated models, the PGV intensity is almost equal until the 8th excitation where the structure is still relatively stable. At the 9th and 10th excitations, because a large amount of strength deterioration starts to occur, the PGV intensity of deteriorated models is lower than that of non-deteriorated models.

Table 4-6 Six input ground motion records used for the analysis

No.	Earthquake	M_w	Seismic Record	Component	PGA (m/s^2)	PGV (m/s)
1	1940 Imperial Valley	6.95	El Centro	North-South	3.42	0.38
2	1952 Kern County	7.36	Taft	East-West	1.76	0.18
3	1968 Tokachi-oki	8.2	Hachinohe	East-West	1.81	0.37
4	1995 Kobe	6.9	JMA Kobe	North-South	8.21	0.89
5	2011 Tohoku	9	JMA Sendai	North-South	4.10	0.54
6	2016 Kumamoto (Apr. 16)	7.3	Kik-net Mashiki	East-West	11.57	1.42

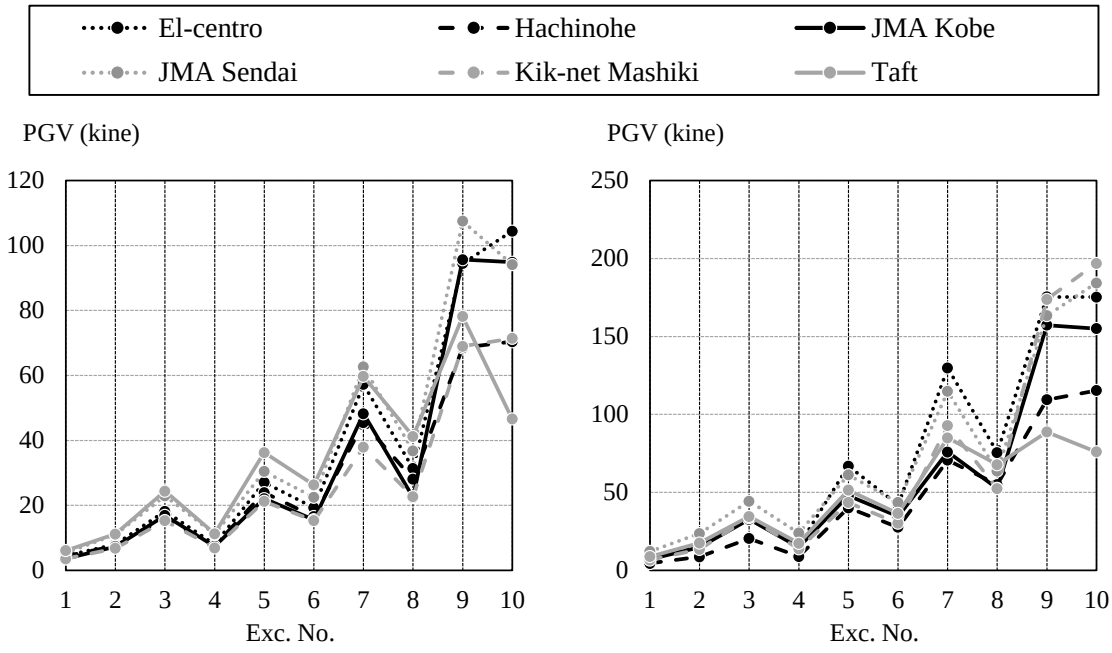

(a) 3-13 model (b) 6-13 model

Figure 4-20 PGV to achieve the target $SDAR_{max}$ for the non-deteriorated models

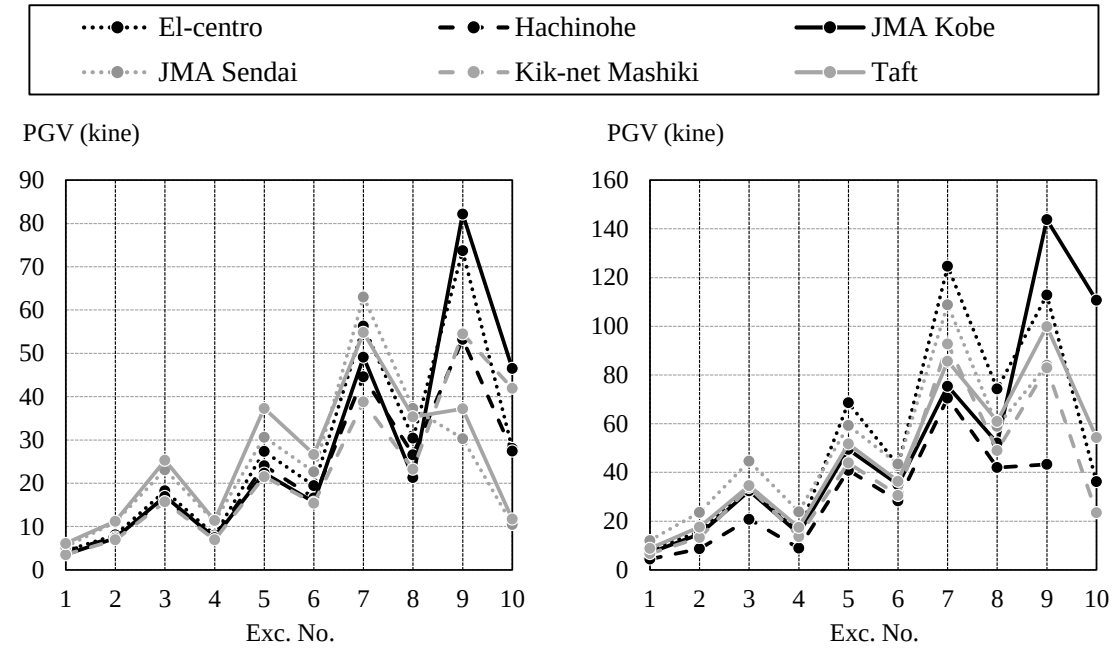

(a) 3-29-1.5 model (b) 6-29-1.5 model

Figure 4-21 PGV to achieve the target $SDAR_{max}$ for the deteriorated models

For the non-deteriorated models, the cumulative damage of the critical beam (D) is computed at every excitation and the result is shown in Figure 4-22. Figure 4-22(a) and Figure 4-22(b) show the cumulative damage of the 3-story and 6-story models, respectively, for various input ground motions. On average, the cumulative damage of the 6-story model is larger than that of the 3-story model. Figure 4-23 shows the comparison of the response of the 3-story and 6-story models excited by El Centro NS records. From Figure 4-23(a), it can be seen that the critical beam is the 1st story beam and the 3rd story beam for the 3-story and 6-story models, respectively. Meanwhile, Figure 4-23(b) shows the response of the critical beam at the 9th excitation in which despite having the same $SDAR_{max}$, the rotation range of the critical beam of the 3-story model is lower than that of the 6-story model. This happens because the rotation range of the beam depends on the SDAR of the upper and lower stories. As shown in Figure 4-23(c), for the 3-story model, the SDAR at the 1st story reached 6% but the SDAR at the 2nd story is much lower than that. On the other hand, for the 6-story, the SDAR at the 3rd and 4th stories are both close to 6%; thus, the rotation range of the 3rd story beam (the critical beam) is also close to 6%. In the experiment, because the steel frame is connected to the jig using a pin joint, the maximum SDA at the lower and upper story is the same (equal to R_{max}). Thus, the case of the 6-story model is more similar with the case in the experiment. Comparing the average cumulative damage at the last excitation of the 6-story model (108.1%) and the fact that in the experiment, the fracture occurred during the constant amplitude loading, it seems that the effect of the local buckling and concrete slab to the cumulative damage under multiple earthquakes might not be too significant. Therefore, evaluating the cumulative damage by mainly considering the ductile fracture failure mode could give a good prediction as well.

Furthermore, Figure 4-22(c) shows the comparison of average margin to fracture and the observed structural (S) and nonstructural (NS) damages found during the experiment. The average margin of fracture is calculated by averaging (100% – D) of all input ground motions at every excitation. In general, the figure provides an image of how much the safety margin to fracture in relation to the observed damages found in the structural and nonstructural components. In terms of the damage of structural components, it could be estimated that when the crack and local buckling initiated at the beam end, the margin to fracture is still over 85%. Moreover, when the crack almost penetrates through the flange thickness, the margin to fracture is about 40% to 65%. Meanwhile, in terms of the damage of nonstructural components, when the LGS board starts to deform out-of-plane or the ALC panel is cracked, the margin to fracture is still over 85%; and the margin is around 40% to 65% when the LGS board fall off.

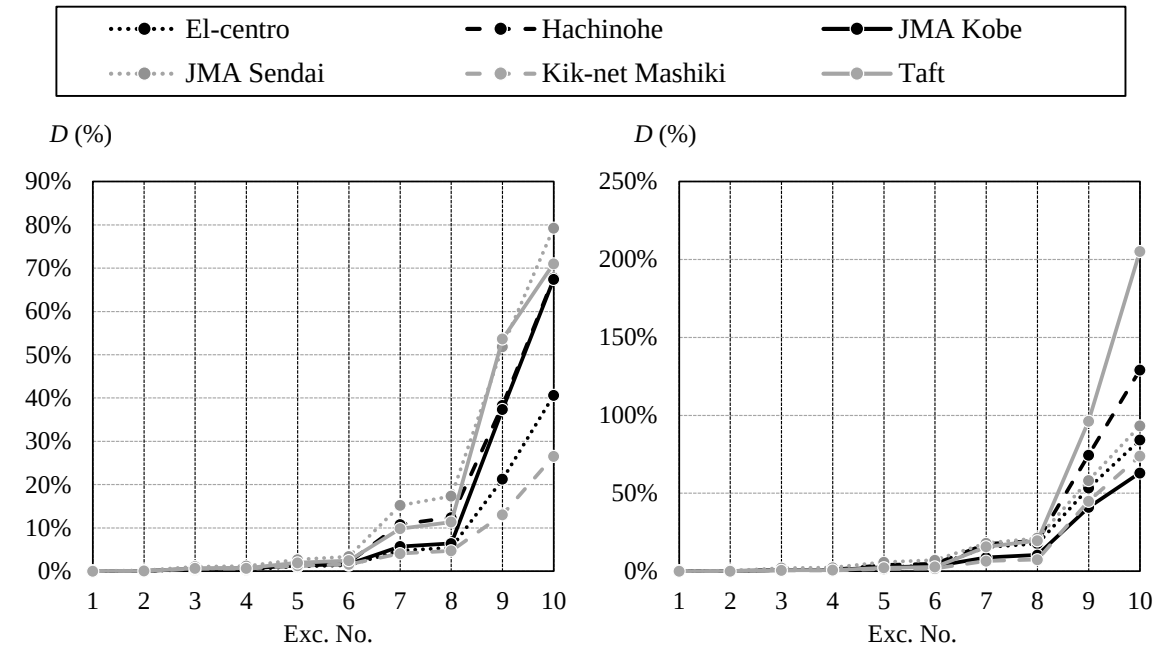

(a) 3-13 model

(b) 6-13 model

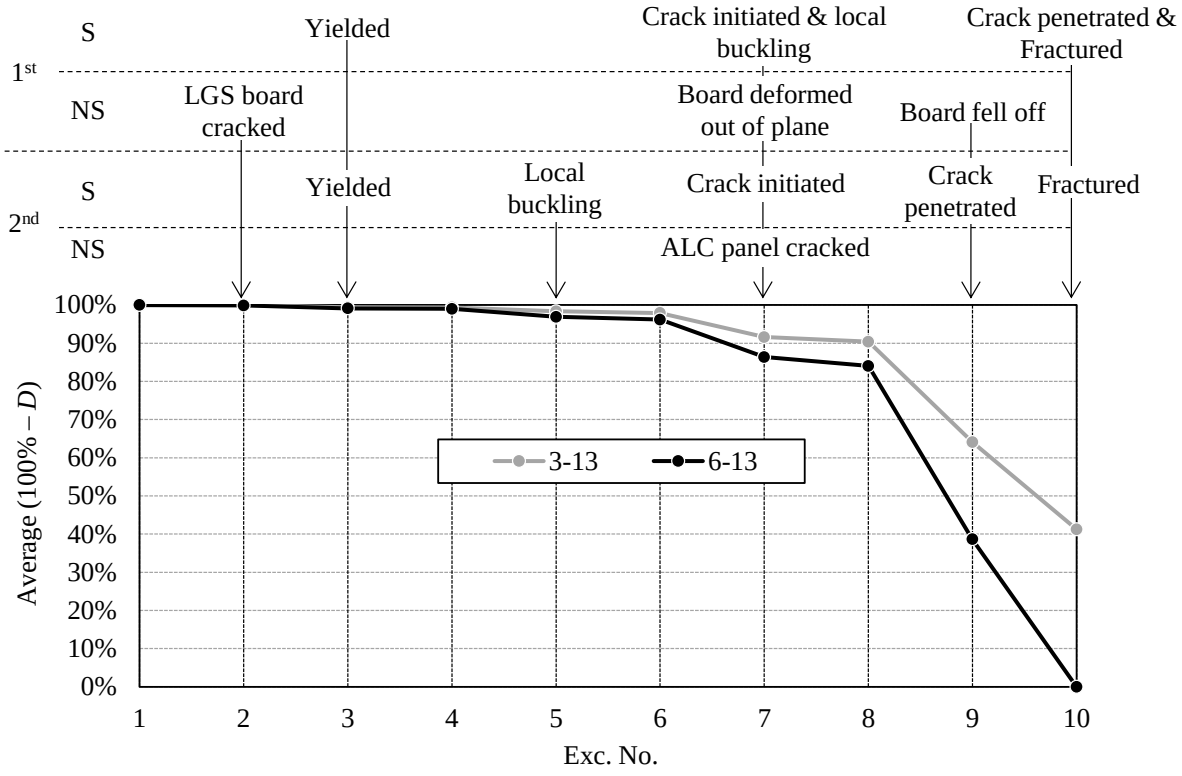

(c) Comparison of average margin to fracture with observed damages

Figure 4-22 Cumulative damage of critical beam (*D*) of the non-deteriorated models

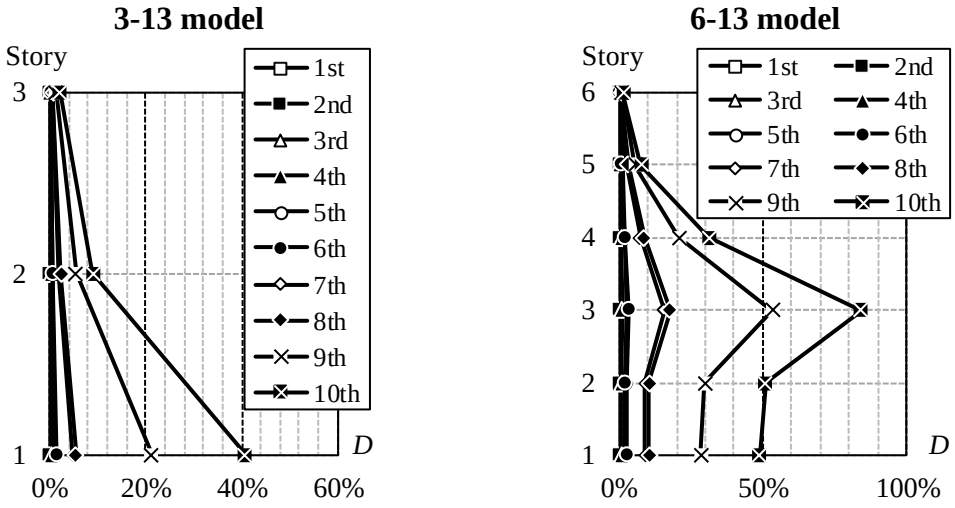

(a) Cumulative damage (*D*) by Exc. No.

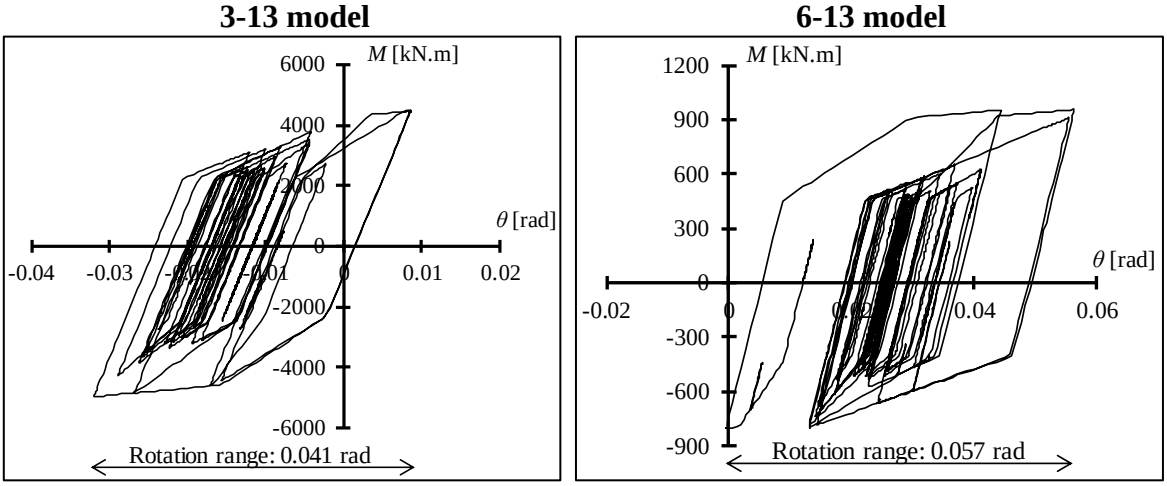

(b) Moment-rotation (*M*-θ) relationship of critical beam at 9th excitation

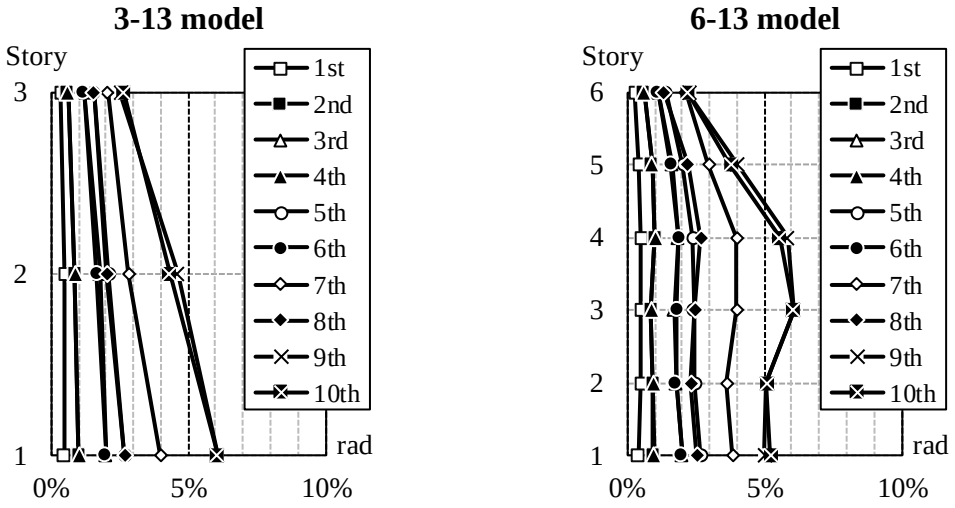

(c) SDAR by Exc. No.

Figure 4-23 Comparison of responses of 3-13 and 6-13 models (Input ground motion: El Centro NS)

From the response analysis using the deteriorated models, Figure 4-24 shows the non-deterioration margin (*NM*) and deterioration index (*DI*) for every excitation. Figure 4-24(a) and Figure 4-24(b) show the *NM* and *DI* of the 3-story and 6-story models, respectively. It can be seen from the figures that the structure is still in the non-deterioration stage until the 6th excitation. The deterioration starts to occur from the 7th excitation. For the 3-story model, at the 7th excitation, all cases have reached stage 2 with the average *DI* around -15% (15% of story strength has deteriorated), while for the 6-story model, most of the cases have reached stage 2 with the average *DI* around -4.5%. In addition, all cases of the 3-story model have reached stage 3 at the 9th excitation with the average *DI* around 51%, while for the 6-story model, most of the cases have reached stage 3 at the 9th excitation with the average *DI* around 54%. Moreover, Figure 4-24(c) shows the comparison of the average *NM* and *DI* with the observed structural (S) and nonstructural (NS) damages observed in the test. This figure could give a general idea of the condition of the 1st story column in relation to the observed damages. In terms of the damage of structural components, it is found that at the excitation where the crack and local buckling initiated at the beam end, the 1st story column also starts to deteriorate, while at the excitation where the crack almost penetrates through the flange thickness, the strength of the 1st story column has been deteriorated until over 50%. Meanwhile, in terms of the damage of nonstructural components, the 1st story column starts to deteriorate at the same excitation where the LGS board starts to deform out-of-plane or the ALC panel cracked. In addition, at the excitation where the LGS board fall off, the strength of the 1st column is estimated to be deteriorated until over 50%.

Furthermore, this result can further give insight that maintaining the stability of the SMRFs under multiple excitations can be achieved by limiting the $SDAR_{max}$ to 4%. By limiting the $SDAR_{max}$ to 4%, the cumulative damage of the non-deteriorated models (until 8th excitation) is still under 25% as shown in Figure 4-22. In terms of structural damages, as found during the experiment, only a small crack initiated at the bottom of the weld access hole and a small degree of local buckling are found until the set no. 7. Meanwhile, in terms of damage on the nonstructural component, it is found during the experiment that the partition wall (gypsum board) fall off at set no. 9 (when the $SDAR_{max}$ is over 4%) which could be dangerous for the occupants during an earthquake event.

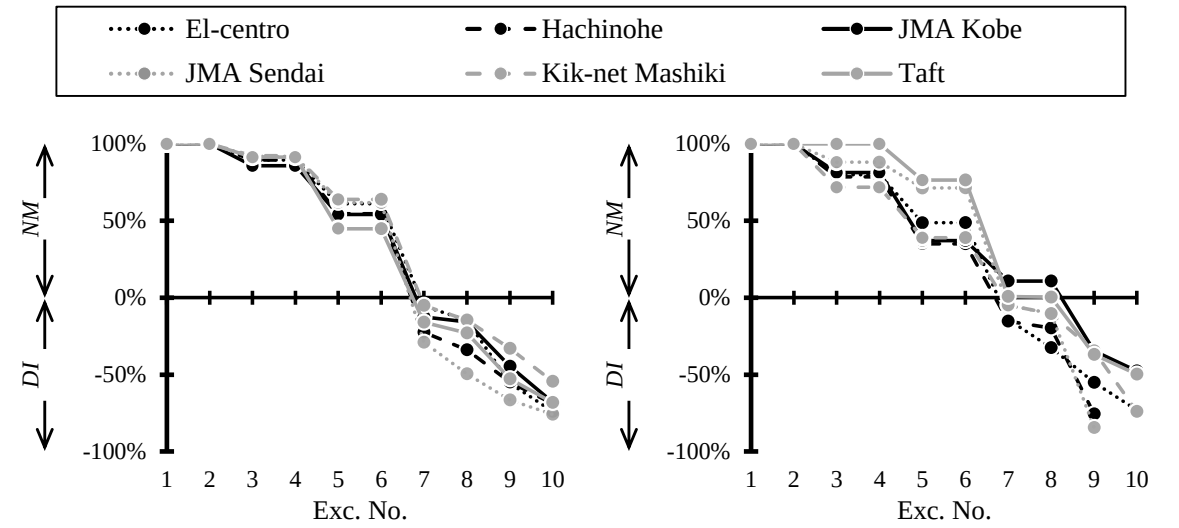

(a) 3-29-1.5 model

(b) 6-29-1.5 model

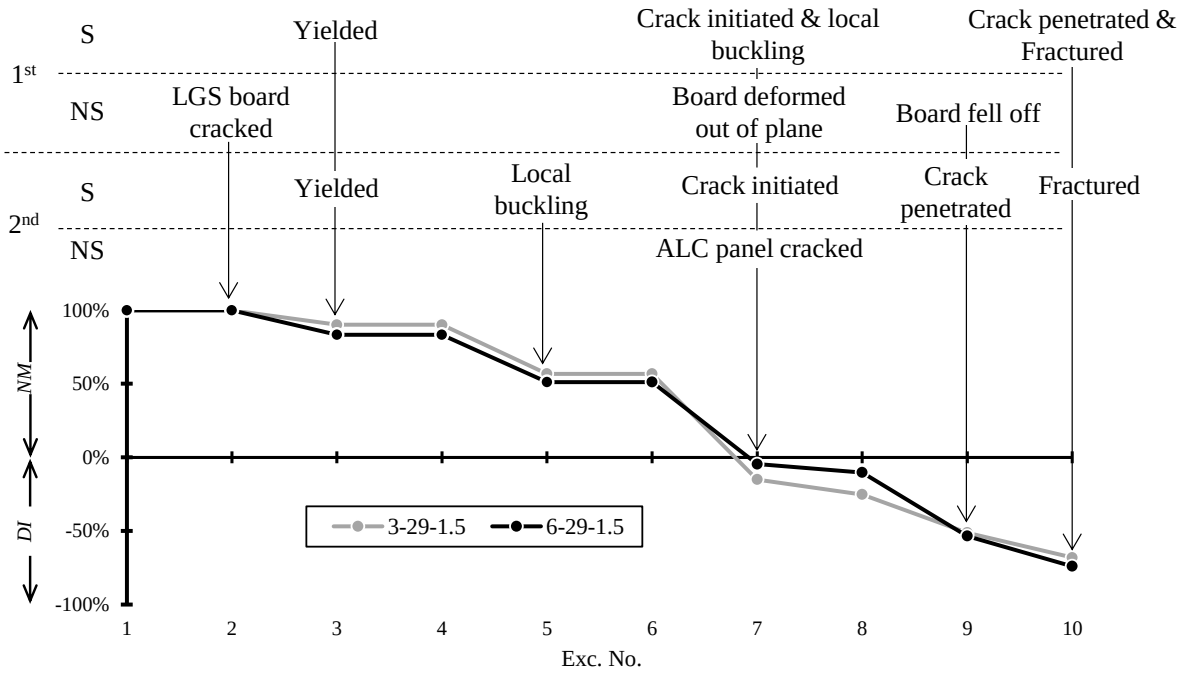

(c) Comparison of average *NM* and *DI* with observed damages

Figure 4-24 Non-deterioration margin (*NM*) and deterioration index (*DI*) of the deteriorated models

4.5 Summary

In this chapter, cyclic loading tests of SMRFs with nonstructural components are presented. Two specimens are tested that considered the variations in the beam-to-column connection detail, i.e., with and without the weld access hole, and the type of the nonstructural component, i.e., the LGS and ALC walls. To simulate the multiple earthquakes, one typical loading set that

corresponded to one earthquake is created using the time history response analysis results. During the test, the maximum story drift angle (R_{max}) of the typical loading set is adjusted to various earthquake levels, and multiple loading sets at various levels are performed to simulate the occurrence of multiple earthquakes. The findings from the experiments are summarized below.

- Based on the observed visible damages, the steel frames perform well when subjected to multiple earthquakes with R_{max} < 1/50 (set nos. 2−6) because there is no heavy damage found on the structure other than the crack on the slab and local buckling. The crack on the beam-to-column connection (with weld access hole) is initiated at set no. 7 (R_{max} = 1/50) and extended at set no. 9 (R_{max} = 1/33).
- Based on the observed visible damages, the ALC wall performs better than the LGS wall when subjected to multiple earthquakes. The existence of opening and eccentric parts also affects the performance. In both specimens, the walls without openings perform better. The damage on the LGS wall without an opening is first found at set no. 1 (R_{max} = 1/400). Furthermore, the damage on the LGS wall without an opening and the ALC wall with openings is first found at set no. 7 (R_{max} = 1/50), and the ALC wall without openings is relatively undamaged until the last set.
- Comparing the load-deformation relationship of the two sets with the same R_{max} values in which the second set occurred after a set with a larger R_{max}, it is found that the strength of the structural component is slightly decreased in the second set, while the stiffness is mostly the same. Moreover, for the nonstructural component, both the strength and stiffness decrease in the second set, and those of the LGS wall decrease by a greater amount than those of the ALC wall.
- Based on the load-deformation relationship obtained from the experiment, the transition of the strength and stiffness of the structural and nonstructural components are investigated. It is found that the strength of the structural component at various story drift angle levels gradually decreases as the number of sets increases. However, the unloading stiffness/elastic stiffness is almost constant across the set. Moreover, the contribution of the strength and stiffness of the LGS wall show two similar trends which contribute more at the lower-level earthquakes and gradually decrease as the number of sets increase. Meanwhile, for the ALC wall, the strength contribution rather fluctuates across the set but within a close range, and the stiffness contribution fluctuates at the early set but tended to

be permanently decreased after the set with R_{max} = 1/75 for the ALC wall with openings, and R_{max} = 1/50 for the ALC wall without openings.

- The response of the full structure is further verified by conducting the inelastic response analysis using both the non-deteriorated and deteriorated models. In the analysis, the target maximum story drift angle range is set to be the same as that used in the experiment. The calculated cumulative damage at the beam end (for non-deteriorated models) and deterioration index of 1st story column (for deteriorated models) obtained from the analysis are compared with the observed damages found in the experiment to examine the relationship between the physical damages and the quantitative damage value. Moreover, it is found that maintaining the performance of the SMRFs under multiple earthquakes can be achieved by limiting the $SDAR_{max}$ to 4%. Under multiple earthquake excitations, when the $SDAR_{max}$ is less than or equal to 4%, the cumulative damage of the critical beam is still under 25% and the story strength deterioration is still less than 30% (stage 2). In addition, as found in the experiment, the structural damage is only a small crack and a small degree of local buckling at the beam end, while the partition wall (nonstructural component) is found to start to fall off when the $SDAR_{max}$ is over 4%.

5. Design Recommendations and Conclusions

5.1 Design Recommendations

In the previous three chapters, the seismic performance of SMRFs subjected to multiple earthquakes has been evaluated in detail through numerical analysis and experimental tests. Through the numerical analysis using non-deteriorated models, it is found that the actual performance of SMRFs is quite satisfying. Using the criterion of ≥ 90% uncollapsed cases, it is found that the structure can withstand until five excitations with PGV intensity of 0.75 m/s and until three excitations with PGV intensity of 1.0 m/s. Even though in a few cases, collapses could occur, most of the collapses are ductile collapses caused by the ductile fracture at the beam end. However, when the possibility of strength deterioration caused by local buckling of column members is taking into account in the analysis (deteriorated models), it is found that the weak story collapse due to excessive story strength deterioration becomes more likely to occur. Compare to the ductile collapse caused by fracture at the beam end, the weak story collapse is less favorable and should be avoided. Through the numerical analysis using the deteriorated models considering various models with a wide variety of column-to-beam moment capacity ratio and column width-to-thickness ratio, it is found that by providing enough non-deterioration margin (*NM*) at the 1st excitation (under single excitation), the strength deterioration and even story collapse could be prevented. Furthermore, through an experimental test of full-scale steel frames, the actual structural and nonstructural damages found under multiple earthquakes with various level is identified. By comparing and verifying the test result with an additional examination through numerical analysis, it is found that a limitation of maximum story drift angle range (SDAR = maximum story drift angle – minimum story drift angle) is necessary to ensure the performance of SMRFs under multiple earthquake excitations.

Considering all those findings, further investigation is conducted to find a necessary limitation to ensure the performance of SMRFs under multiple earthquakes. Two levels of safety are considered in the investigation, namely collapse prevention level and deterioration prevention level. For the collapse prevention level, the main goal is to prevent collapse under multiple earthquake excitations, the structure is allowed to reach stage 2 (refer to section 3.3.2 for the definition of stages to collapse) but not stage 3 because at stage 3 the mechanism is

shifting to weak story mechanism and the structure is very vulnerable to story collapse. To achieve that goal, the deterioration index (*DI*) is limited to -25% (maximum up to 25% strength deteriorated). Although there is no exact number of *DI* as the limit between stages 2 and 3, a limitation up to 25% of *DI* is considered to be enough because most of the cases are still in stage 2 when the *DI* is more than -25%. Meanwhile, for the deterioration prevention level, the main goal to prevent strength deterioration of the column caused by local buckling; thus, the structure can still maintain its stable behavior at stage 1. The deterioration prevention level is recommended to earthquake shelter or evacuation center because these facilities are essential to be able to operate continuously during an earthquake event, while the collapse prevention level is recommended for ordinary residential houses or other buildings where the severe damages during an earthquake event are acceptable as long as the structure does not collapse.

To ensure the performance of SRMFs under multiple excitations under both levels, the reserved strength and deformation limits are introduced. The structure has to be designed to fulfill both the reserved strength and deformation limit criteria to ensure its performance. The reserved strength limit is represented as the available *NM* at the 1st excitation (NM_1) because as found in Chapter 3, the structures generally could maintain its stable behavior if it has a certain amount of NM_1 available. From the analytical results using the deteriorated models, all cases where the $DI = 0\%$ and $DI > -25\%$ under a various number of excitations and input intensities are collected, and the minimum NM_1 value is determined among the collected cases. Figure 5.1 and Figure 5.2 show the minimum NM_1 for deterioration prevention and collapse prevention levels, respectively. In the figures, there are three criteria included, i.e., including all collected cases and excluding 10% and 20% extreme cases among the collected cases. As shown in both figures, if all cases are included, the NM_1 needed for both levels is very low. Thus, to provide a more conservative value, some of the extreme cases should be excluded. Those cases that being excluded is considered to be extremely good because, with such a low NM_1, it could prevent the deterioration or collapse. The more the cases excluded, the safer the performance will be; however, using either criterion of 10% or 20% excluded is considered to be acceptable. For example, if the target is to make the structure being able to withstand three excitations with PGV intensity of 0.75 m/s without any strength deterioration, then it should be ensured that under the single excitation with PGV intensity of 0.75 m/s, the NM_1 is over 40.4% (if the criterion of excluding 10% extreme cases is used).

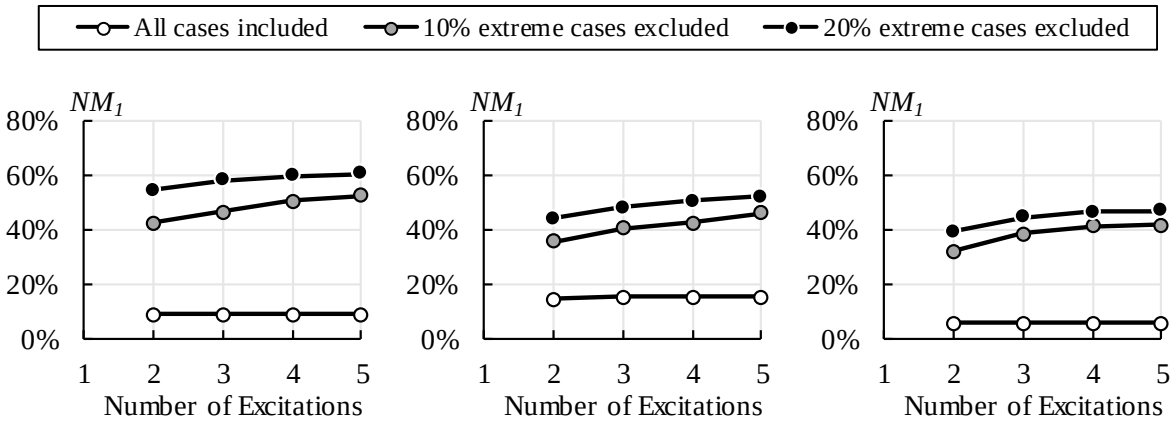

(a) PGV 0.5 m/s (b) PGV 0.75 m/s (c) PGV 1.0 m/s

Figure 5-1 Minimum non-deterioration margin (*NM*) at the 1st excitation for deterioration prevention level

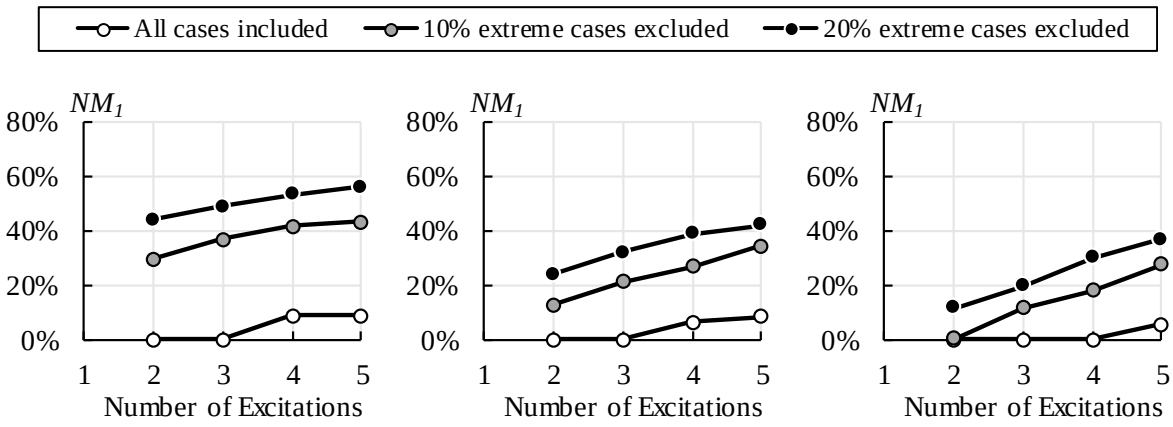

(a) PGV 0.5 m/s (b) PGV 0.75 m/s (c) PGV 1.0 m/s

Figure 5-2 Minimum non-deterioration margin (*NM*) at the 1st excitation for collapse prevention level

For the deformation limit, the limitation of maximum story drift angle range ($SDAR_{max}$) is used because as found in Chapter 4, by limiting the $SDAR_{max}$ to a certain level, the performance of SMRFs under multiple earthquakes could be ensured. The relationship between $SDAR_{max}$ and the cumulative damage of the critical beam (analyzed using the non-deteriorated models) under a various number of excitations and input intensities are included in Appendix H, while the relationship between $SDAR_{max}$ and the *NM* and *DI* (deteriorated models) are included in Appendix I. Figure 5.3 shows the limitation of $SDAR_{max}$ for the collapse prevention and deterioration prevention levels under a various number of excitations and input intensities. The

limitation is chosen considering the criterion of more than 95% of the cases have DI = 0% (for deterioration prevention level) or DI > -25% (for collapse prevention level). For example, under two excitations with PGV intensity of 0.5 m/s, for the deterioration prevention limit, the $SDAR_{max}$ limit is 4.14%, which means that for all cases with $SDAR_{max} \leq 4.14\%$, more than 95% of them have DI = 0%. It should be noted that the upper limit of the $SDAR_{max}$ is set to 6% because as found during the full-scale steel frame test, both the structural and nonstructural components are severely damaged when the $SDAR_{max}$ under multiple earthquakes reached 6%. Thus, a 6% upper limit is adopted to prevent structural collapse and even the falling of nonstructural walls. For each limitation of $SDAR_{max}$ shown in Figure 5.3, the maximum cumulative damage of the critical beam (D) is shown in Figure 5.4. As shown in the figure, for the deterioration prevention level, the maximum D is around 20% for PGV intensity of 0.5 m/s and 0.75 m/s and around 40% for PGV intensity of 1.0 m/s. Meanwhile, for the collapse prevention level, the maximum D is around 45%, 70%, and 90% for PGV intensity of 0.5 m/s, 0.75 m/s, and 1.0 m/s, respectively.

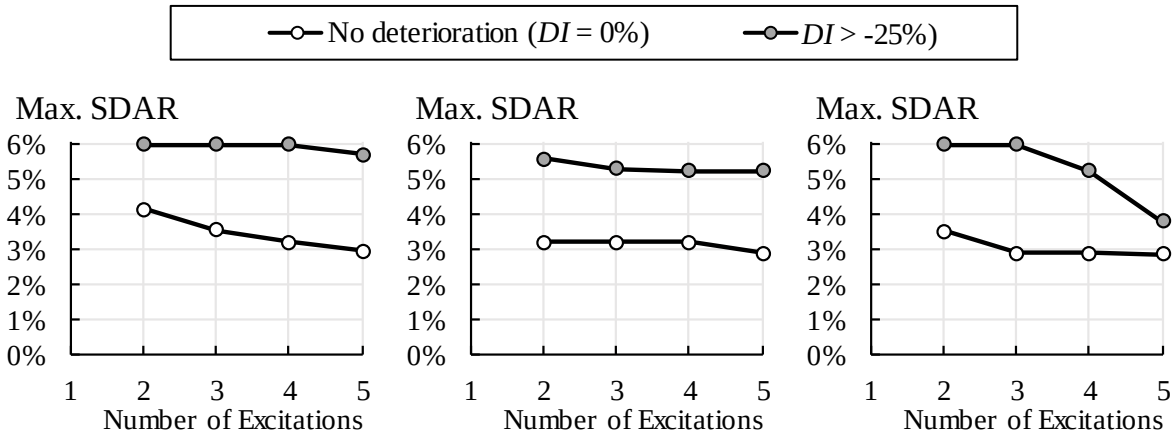

(a) PGV 0.5 m/s (b) PGV 0.75 m/s (c) PGV 1.0 m/s

Figure 5-3 Limitation of maximum story drift angle range ($SDAR_{max}$) under multiple earthquakes

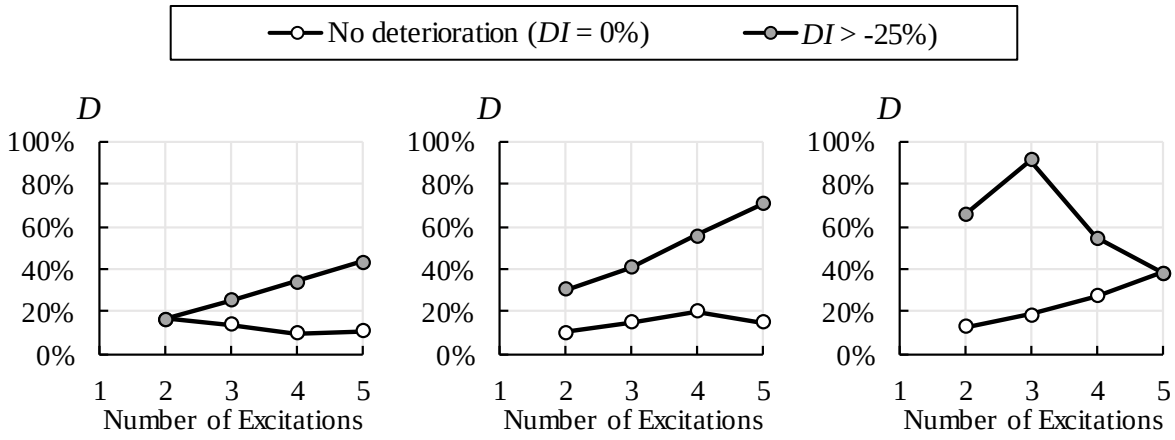

(a) PGV 0.5 m/s (b) PGV 0.75 m/s (c) PGV 1.0 m/s

Figure 5-4 Maximum cumulative damage of critical beam (*D*) for each limitation of $SDAR_{max}$

The $SDAR_{max}$ limitation shown in Figure 5.3 is the limitation under multiple earthquake excitations. To further estimate the limitation under single excitation, the $SDAR_{max}$ limit under multiple excitations needs to be divided by the increment ratio of $SDAR_{max}$ under multiple excitations. The increment ratio is calculated by dividing the $SDAR_{max}$ until the i-th excitation (i = 2–5 excitations) by $SDAR_{max}$ at the 1st excitation. All the cases where the *DI* = 0% or *DI* > -25% are collected, and after excluding 10% extreme cases, the maximum increment ratio of $SDAR_{max}$ under a various number of excitations and input intensities for both deterioration prevention and collapse prevention levels are determined. The results are shown in Figure 5.5. Figure 5.6 shows the limitation of $SDAR_{max}$ at the 1st excitation. Using this estimation, the structure could be ensured to fulfill its deformation limit by simply checking its $SDAR_{max}$ under single excitation. For example, if the target is to make the structure being able to withstand four excitations with PGV intensity of 0.5 m/s without any strength deterioration, then it should be ensured that under the single excitation with PGV intensity of 0.5 m/s, the $SDAR_{max}$ is not over 3%. As an additional consideration, the limitation of $SDAR_{max}$ for different D_c/t values is also investigated because decreasing the D_c/t significantly affect the ductility of the columns; thus, the limitation of $SDAR_{max}$ is expected to change quite significantly as well. The results can be seen in Appendix J.

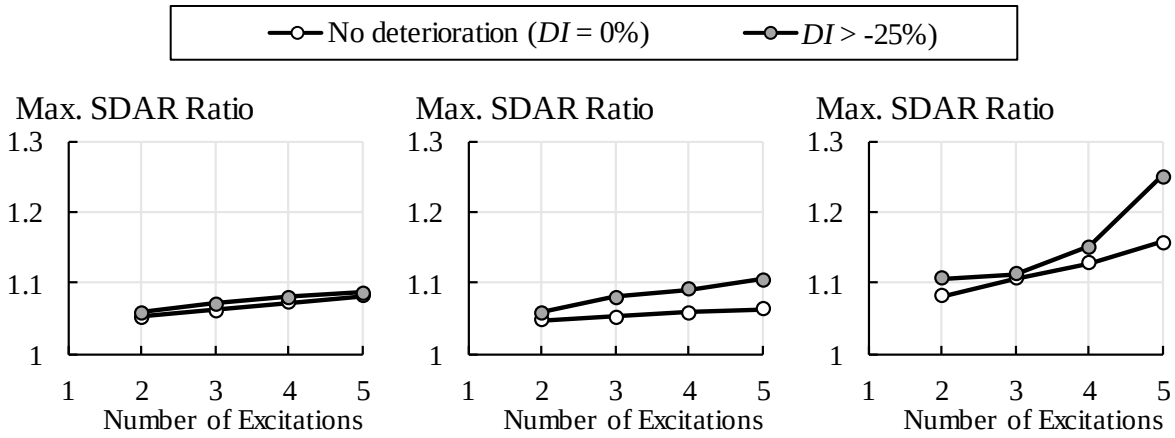

(a) PGV 0.5 m/s (b) PGV 0.75 m/s (c) PGV 1.0 m/s

Figure 5-5 Maximum increment ratio of $SDAR_{max}$ under multiple earthquakes

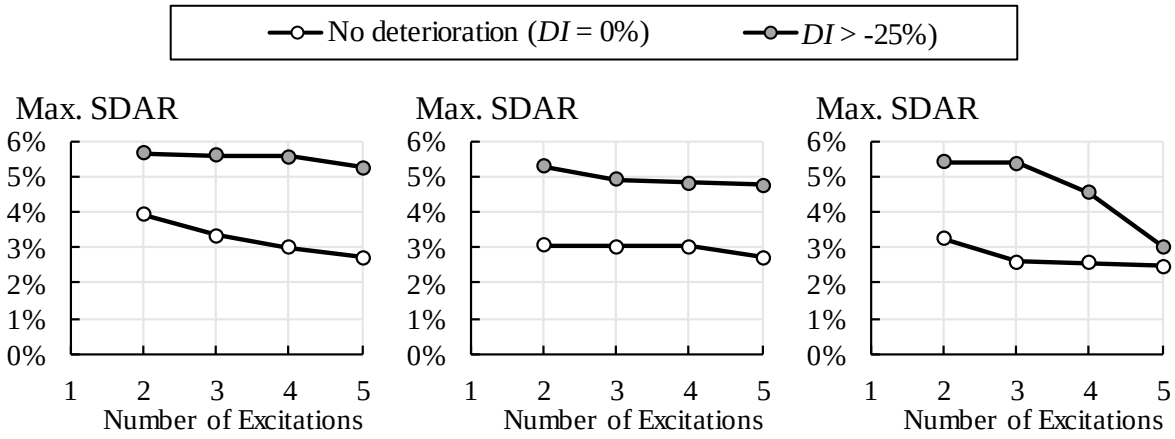

(a) PGV 0.5 m/s (b) PGV 0.75 m/s (c) PGV 1.0 m/s

Figure 5-6 Limitation of maximum story drift angle range ($SDAR_{max}$) at the 1st excitation

5.2 Conclusions

The seismic performance of steel moment-resisting frames subjected to multiple earthquakes has been comprehensively evaluated in this study through the numerical analysis and experimental test. In **Chapter 2**, the numerical analysis is conducted using a non-deteriorated model. In this model, any deterioration effect is not considered. Instead, the main focus is the ductile fracture of beams because the application of the strong column weak beam concept is resulting in the beam members weaker than the column members. Various non-deteriorated SMRF models are analyzed by conducting a series of inelastic time-history

response analyses that simulate the occurrence of multiple earthquakes. The damage of the structure under multiple excitations is evaluated by the cumulative damage at the beam end. Overall, it is found that the structure could maintain stable behavior under multiple excitations. Although in a few cases, it is found that the ductile fracture might occur or the ultimate state might be reached when the input intensity is larger than the design level, the performance of the structure is satisfying. By adopting the criterion of over 90% uncollapsed cases, the structure can resist up to five excitations with an intensity of peak ground velocity (PGV) 0.75 m/s or three excitations with PGV 1.0 m/s. Moreover, the beam-to-column connection test is conducted to further verify the reliability of the cumulative damage evaluation method under random cyclic loading. The loading history used in the test is created from the response analysis of the non-deteriorated model and simulating the occurrence of multiple earthquakes. By calculating the cumulative damage value of the test specimens, it can be verified that the reliability of the cumulative damage evaluation method is acceptable.

In **Chapter 3**, the numerical analysis is conducted using a deteriorated model that considers the effect of strength deterioration due to local buckling of columns. Various deteriorated SMRF models are created for the analysis. These models are designed considering the combination of two main design parameters, i.e., the width-to-thickness ratio of the column member (D_c/t) and the column-to-beam moment capacity ratio ($_cM_p/_bM_p$). Then, an inelastic response analysis that simulates the occurrence of multiple shocks is carried out. Overall, it is found that the performance of SMRFs under multiple excitations is lower than that of the non-deteriorated model because the weak story collapse is more likely to occur. The behavior of the structure can be divided based on whether the structure reaches the deteriorated stage or not. If the structure stays in the non-deterioration stage, then stable behavior can be achieved. In general, it is found that in the cases where the structure is having a non-deterioration margin of over 50% at the 1st excitation, the stable behavior can be achieved under five excitations. Moreover, to achieve the same criterion of 90% uncollapsed cases, a lower D_c/t value or a higher $_cM_p/_bM_p$ value is necessary. The combination of D_c/t and $_cM_p/_bM_p$ that can achieve the criterion are provided.

In **Chapter 4**, to further verify the analytical result, a full-scale steel frame test is conducted. To simulate the occurrence of multiple earthquakes, one typical set of loading history that corresponds to one earthquake is created. During the test, multiple loading sets with various levels of intensities are loaded to simulate the occurrence of multiple earthquakes. Two specimens are tested in the experiment. The specimens are single-floor, one-span

substructures of an intermediate story of typical current Japanese middle- or low-rise steel buildings. In addition to the test, an inelastic response analysis is conducted by matching the maximum story drift angle range ($SDAR_{max}$) with those of the loading sets used in the test. It is found that by limiting the $SDAR_{max}$ under multiple earthquakes to 4%, an acceptable performance could be achieved. From the test result, until loading set with $SDAR_{max}$ of 4%, the strength and stiffness of the steel frames barely deteriorate and only a small crack and local buckling are found at the beam end. A similar result is obtained from the response analysis, until the $SDAR_{max}$ of 4%, the cumulative damage at the beam ends are all less than 25% and the column is still in an early stage of deterioration.

In **Chapter 5**, all the findings found in the numerical analysis and experimental test are comprehensively summarized. To ensure the performance of SMRFs under multiple earthquakes, the reserved strength and deformation limits are introduced for two levels of performance, namely, collapse prevention level and deterioration prevention level. The reserved strength limit is represented by the minimum non-deterioration margin at the 1st excitation (NM_1), while the deformation limit is represented by the $SDAR_{max}$ under multiple excitations. Both the reserved strength and deformation limits are provided for a various number of excitations and various input intensities. The performance of SMRFs under multiple earthquake excitation is ensured by designing the structure to fulfill both the reserved strength and deformation limits.

The effect of multiple earthquake excitations has not been widely considered in seismic design, mainly because the of multiple strong shocks with almost equal intensity during an earthquake event is not very common compared to the occurrence of the single strong main shock only. However, it should be noted that this phenomenon is possible to occur and has been found in several earthquake events all around the world. To what extent the effect of multiple strong earthquakes needs to be considered in the seismic design might be varied from one structural engineer to the others or from country to country. It will depend on the structural judgment of the experts and engineers, the earthquake disaster risk assessments, or even the economic conditions and political judgment of the decision-makers. Hopefully, what has been found through this research and presented in this dissertation could provide the basic insights on the actual seismic performance of SMRFs subjected to multiple earthquakes or even the basic guidelines on how to design SMRFs considering the effect of multiple earthquakes, which both might be useful to cope with the devastating damage caused by the occurrence of multiple strong earthquakes in the future.

References

Abdollahzadeh, G., Mohammadgholipour, A., and Omranian, E., 2019. Seismic Evaluation of Steel Moment Frames under Mainshock–Aftershock Sequence Designed by Elastic Design and PBPD Methods, *Journal of Earthquake Engineering* **23**(10), 1605−1628.

Akiyama, H. and Takahashi, M., 1990. Influence of Bauschinger Effect on Seismic Resistance of Steel Structures (in Japanese), *Journal of Structural and Construction Engineering Transactions of AIJ* **418**, 49–57.

American Institute of Steel Construction, 2005. Seismic Provisions for Structural Steel Buildings (Including Supplement No.1).

Architectural Institute of Japan (AIJ), 2010. *Design Recommendations for Composite Constructions* (in Japanese), Tokyo, Japan.

Architectural Institute of Japan (AIJ), 2018. *Japan Architectural Standard Specification JASS 6 Steel Work* (in Japanese), Tokyo, Japan.

Asano, K. and Iwata, T., 2016. Source Rupture Processes of the Foreshock and Mainshock in the 2016 Kumamoto Earthquake Sequence Estimated from the Kinematic Waveform Inversion of Strong Motion Data, *Earth, Planets and Space* **68**(147).

Brandenberg, S. J. et al., 2019. Preliminary Report on Engineering and Geological Effects of the July 2019 Ridgecrest Earthquake Sequence, *Geotechnical Extreme Event Reconnaissance Association* Report No. GEER-064.

Building Center of Japan, 2013a. Stipulation of Horizontal Load-carrying Capacity Calculation and Allowable stress and Supplemental Analysis Calculation, *The Building Standard Law of Japan: Notifications of Ministry of Land, Infrastructure, Transport, and Tourism (MLIT) No. 594*, Tokyo, Japan.

Building Center of Japan, 2013b. Stipulation of the value of *Z*, methods of calculating and *Rt* and *Ai* and standards for the designation by the Designated Administrative Organization of districts where the ground is extremely soft, *The Building Standard Law of Japan:*

Notifications of Ministry of Land, Infrastructure, Transport, and Tourism (MLIT) No. 597, Tokyo, Japan.

Building Center of Japan, 2013c. Stipulation of Methods of Calculating *Ds* and *Fes*, *The Building Standard Law of Japan: Notifications of Ministry of Land, Infrastructure, Transport, and Tourism (MLIT) No. 596*, Tokyo, Japan.

Building Research Institute and Japan Iron and Steel Federation, 2002. Testing Methods of the Evaluation of Structural Performance for the Steel Structures.

Earthquake Engineering Research Institute, 2012. Learning from Earthquakes: April 11, 2012, M 8+ Sumatra Earthquakes, *EERI Newsletter May 2012* **46**(5), available at https://www.eeri.org/wp-content/uploads/SumatraMay12.pdf (last accessed 23 December 2019).

Endo, T., Matsuishi, M., Mitsunaga, K., Kobayashi, K., and Takahashi, K., 1974. Rainflow Method, the Proposal and the Applications (in Japanese), *Bulletin of Kyushu Institute of Technology* **28**, 33–62.

Fragiacomo, M., Amadio, C., and Macorini, L., 2004. Seismic Response of Steel Frames under Repeated Earthquake Ground Motions, *Engineering Structures* **26**(13), 2021−2035.

Goel, S. C., Liao, W. C., Reza Bayat, M., and Chao, S. H., 2010. Performance-Based Plastic Design (PBPD) Method for Earthquake-Resistant Structures: An Overview, *The structural design of tall and special buildings* **19**(1–2), 115-137.

Hatzigeorgiou, G. D. and Beskos, D. E., 2009. Inelastic Displacement Ratios for SDOF Structures Subjected to Repeated Earthquakes, *Engineering Structures* **31**(11), 2744−2755.

Hatzigeorgiou, G. D., 2010. Behavior Factors for Nonlinear Structures Subjected to Multiple Near-Fault Earthquakes, *Computers and Structures* **88**(5-6), 309-321.

Iancovici, M. and Ionică, G., 2007. Evaluation of the Inelastic Demand of Structures subjected to Multiple Ground Motions, *INTERSECTII/INTERSECTIONS "Structural Engineering"* **4**(2), 143−154.

Ibarra, L. F., Medina, R. A., and Krawinkler, H., 2005. Hysteretic Models that Incorporate Strength and Stiffness Deterioration, *Earthquake Engineering and Structural Dynamics* **34**(12), 1489−1511.

Japanese Industrial Standard Committee, 2011. *Japanese Industrial Standard (JIS) Z 2241, Metallic materials —Tensile testing —Method of test at room temperature*, Tokyo, Japan.

Kato, A., Nakamura, K., and Hiyama, Y., 2016. The 2016 Kumamoto Earthquake Sequence, *Proceedings of Japan Academy Series B* **92**(8), 358–371.

Kato, B., Akiyama, H., and Yamanouchi, H., 1973. Predictable Properties of Structural Steels Subjected to Incremental Cyclic Loading, *Preliminary Publication of IABSE Symposium on Resistance and Ultimate Deformability of Structures Acted on by well Defined Loads*.

Kishiki, S., Lee, D., Yamada, S., Ishida, T., and Jiao, Y., 2019. Low-Cycle Fatigue Performance Assessment of Current Japanese Steel Beam-to-Column Connections Determined by Ductile Fracture, *Engineering Structures* **182**, 241−250.

Kojima, K. and Takewaki, I., 2016. A Simple Evaluation Method of Seismic Resistance of Residential House under Two Consecutive Severe Ground Motions with Intensity 7, *Journal of Frontiers in Built Environment* **2**, Article 15.

Krawinkler, H. and Zohrei, M., 1983. Cumulative Damage in Steel Structures Subjected to Earthquake Ground Motions, *Computers and Structures* **16**(14), 531−541.

Krawinkler, H., Gupta, A., Medina, R., and Luco, N., 2000. Loading Histories for Seismic Performance Testing of SMRF Components and Assemblies, *SAC Joint Venture* Report No. SAC/BD-00/10.

Lee, K. and Foutch, D. A., 2004. Performance Evaluation of Damaged Steel Frame Buildings Subjected to Seismic Loads, *Journal of Structural Engineering ASCE* **130**(4), 588−599.

Li, Q. and Ellingwood, B. R., 2007. Performance Evaluation and Damage Assessment of Steel Frame Buildings under Main Shock−Aftershock Earthquake Sequences, *Earthquake Engineering and Structural Dynamics* **36**(3), 405−427.

Li, Y., Song, R., and Van De Lindt, J. W., 2014. Collapse Fragility of Steel Structures Subjected to Earthquake Mainshock−Aftershock Sequences, *Journal of Structural Engineering ASCE* **140**(12), 04014095-1−10.

Lignos, D. G. and Krawinkler, H., 2011. Deterioration Modeling of Steel Components in Support of Collapse Prediction of Steel Moment Frames under Earthquake Loading, *Journal of Structural Engineering ASCE* **137**(11), 1291−1302.

Loulelis, D., Hatzigeorgiou, G. D., and Beskos, D. E., 2012. Moment Resisting Steel Frames under Repeated Earthquakes, *Journal of Earthquakes and Structures* **3**(3-4), 231−248.

Mazzolani, F. and Piluso, V., 1996. Theory and Design of Seismic Resistant Steel Frames, London: CRC Press.

Nakashima, M., Matsumiya, T., Suita, K., and Liu, D., 2006. Test on Full-Scale Three-Storey Steel Moment Frame and Assessment of Ability of Numerical Simulation to Trace Cyclic Inelastic Behaviour, *Earthquake Engineering and Structural Dynamics* **35**(1), 3−19.

Nakashima, M., Matsumiya, T., Suita, K., and Zhou, F., 2007. Full-Scale Test of Composite Frame under Large Cyclic Loading, *Journal of Structural Engineering ASCE* **133**(2), 297−304.

Park, Y. and Ang, A. H., 1985. Mechanistic Seismic Damage Model for Reinforced Concrete, *Journal of Structural Engineering* **111**(4), 722−739.

Ruiz-García, J. and Negrete-Manriquez, J. C., 2011. Evaluation of Drift Demands in Existing Steel Frames under As-recorded Far-Field and Near-Fault Mainshock−Aftershock Seismic Sequences, *Engineering Structures* **33**(2), 621−634.

Ruiz-García, J. and Aguilar, J. D., 2015. Aftershock Seismic Assessment Taking into Account Postmainshock Residual Drifts, *Earthquake Engineering and Structural Dynamics* **44**(9), 1391−1407.

Sato, R., Kishiki, S., and Yamada, S., 2017. Cyclic Rotation Capacity of Beam-to-Column Connections using Various Steel Grades, Paper No. 3644, in *Proceedings, of the 16th World Conference on Earthquake Engineering*, 9-13 January 2017, Santiago, Chile.

Stewart, J. P. et al., 2018. Reconnaissance of 2016 Central Italy Earthquake Sequence, *Earthquake Spectra* **34**(4), 1547–1555.

Suita, K., Yamada, S., Tada, M., Kasai, K., Matsuoka, Y., and Shimada, Y., 2008. Collapse Experiment on 4-story Steel Moment Frame: Part 2 Detail of Collapse Behavior, in *Proceeding, of the 14th World Conference on Earthquake Engineering*, October 2008, Beijing, China.

Yamada, S. and Akiyama, H., 1994. Inelastic Response Analysis of Multi-Story Steel Frames based on the Realistic Behaviors of Members Governed by Local Buckling (in Japanese), *Journal of Structural and Construction Engineering Transactions of AIJ* **463**, 125–133.

Yamada, S., Akiyama, H., and Mizutani, H., 1996. Ultimate Earthquake Resistance of Multi-Story Steel Frames Accompanied by the Plastic Deformation of Panel Zone (in Japanese), *Journal of Structural and Construction Engineering Transactions of AIJ* **481**, 137–144.

Yamada, S., Akiyama, H., and Sadamoto, M., 1997. Influence of the Elasto-Plastic Behavior of Column Bases with Slip-type Hysteresis Characteristics on The Ultimate Earthquake Resistance of Multi-Story Steel Moment Frames (in Japanese), *Journal of Structural and Construction Engineering Transactions of AIJ* **502**, 141–147.

Yamada, S., Suita, K., Tada, M., Kasai, K., Matsuoka, Y., and Shimada, Y., 2008. Collapse Experiment on 4-story Steel Moment Frame: Part 1 Outline of Test Results, in *Proceeding, of the 14th World Conference on Earthquake Engineering*, October 2008, Beijing, China.

Yamada, S., Ishida, T., and Jiao, Y., 2018. Hysteretic Behavior of RHS Columns under Random Cyclic Loading Considering Local Buckling, *International Journal of Steel Structures* **18**(5), 1761-1771.

Zhai, C. H., Wen, W. P., Chen, Z. Q., Li, S., and Xie, L. L., 2013. Damage Spectra for the Mainshock−Aftershock Sequence-type Ground Motions, *Soil Dynamics and Earthquake Engineering* **45**, 1−12.

Zhai, C. H., Wen, W. P., Li, S., Chen, Z. Q., Chang, Z., and Xie, L. L., 2014. The Damage Investigation of Inelastic SDOF Structure under the Mainshock−Aftershock Sequence-type Ground Motions, *Soil Dynamics and Earthquake Engineering* **59**, 30-41.

Zhai, C., Ji, D., Wen, W., Lei, W., Xie, L., and Gong, M., 2016. The Inelastic Input Energy Spectra for Main Shock−Aftershock Sequences, *Earthquake Spectra* **32**(4), 2149-2166.

Appendix A Infinite Uniform Plane Frame Model

Infinite uniform plane frame model is used for the numerical modeling. In this model, infinite number of plane frames with uniform size is assumed to exist throughout the plane. Since the frame in every span is uniform (in terms of size and weight), the lateral seismic load can be assumed to be distributed equally to every span. Because every span has the same size and resists the same amount of lateral seismic load, the response is expected to be the same as well. Therefore, in the modeling, a single span is modeled to represent the response of the whole frame. The single span consists of a single column and half of the beam length on the left and right side each at every story as shown in Figure A-1. In the time-history analysis using this model, the gravity load (self-weight) is firstly applied to the beam as a uniformly distributed vertical load; then, the lateral seismic load (from the input ground motion) is applied afterwards.

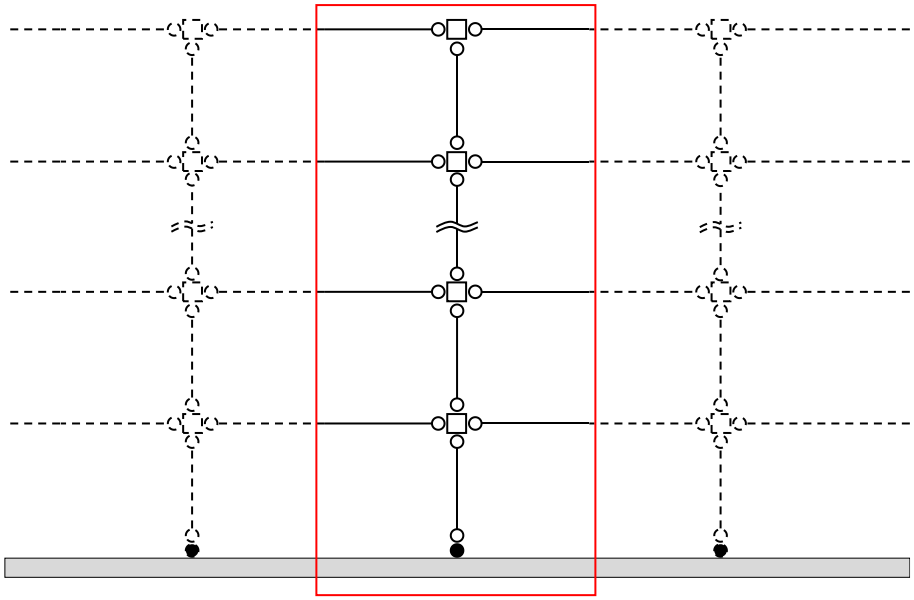

Figure A-1 Single span of infinite uniform plane frame

Appendix B Details of Non-deteriorated SMRF Models

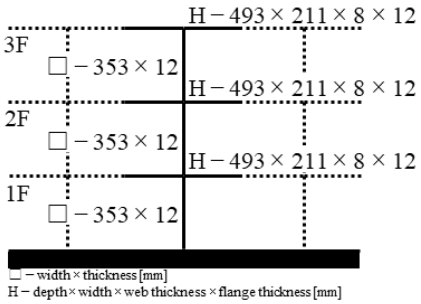

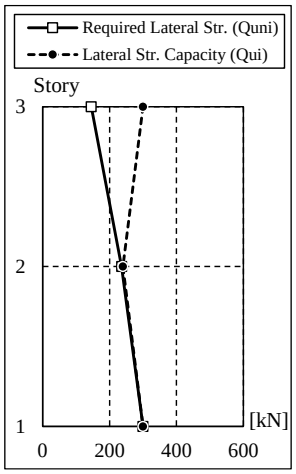

Column-to-Beam Moment Capacity Ratio			
Story	${}_cM_p$ [kN.m]	${}_bM_p$ [kN.m]	${}_cM_p/{}_bM_p$
3	671.5	420.3	-
2	656.0	420.3	1.58
1	630.3	420.3	1.53

Anchor Bolt	
Diameter [mm]	Ultimate Strength [kN.m]
39.2	819.0

Natural Period	
1st Mode [sec.]	2nd Mode [sec.]
0.925	0.277

(a) Model details

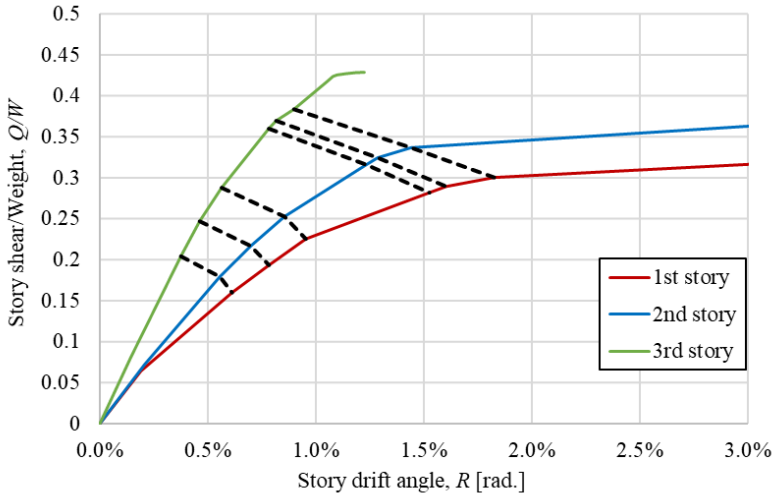

※ The dashed lines (-----) indicate the steps where the plastic hinges are formed

(b) Pushover analysis result

Figure B-1 Model 3-13

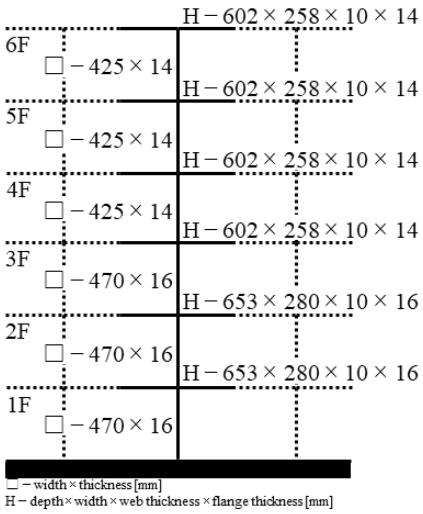

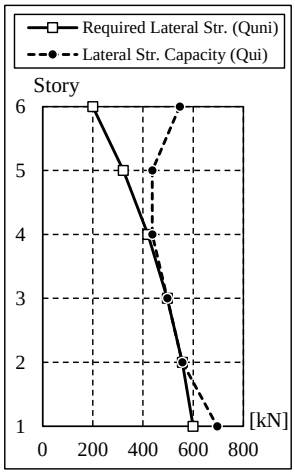

Column-to-Beam Moment Capacity Ratio			
Story	${}_cM_p$ [kN.m]	${}_bM_p$ [kN.m]	${}_cM_p / {}_bM_p$
6	1182.5	765.6	-
5	1169.7	765.6	1.54
4	1148.4	765.6	1.51
3	1539.5	765.6	1.76
2	1504.7	974.9	1.56
1	1462.2	974.9	1.52

Anchor Bolt	
Diameter [mm]	Ultimate Strength [kN.m]
50.5	1901.2

Natural Period	
1st Mode [sec.]	2nd Mode [sec.]
1.135	0.369

(a) Model details

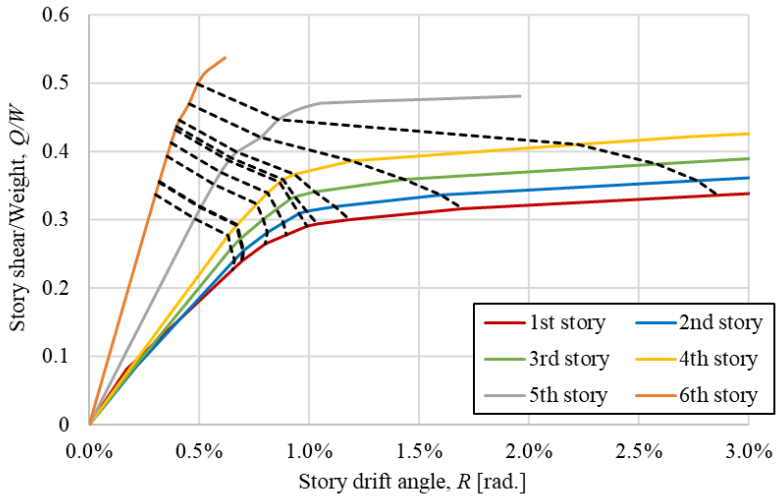

※ The dashed lines (-----) indicate the steps where the plastic hinges are formed

(b) Pushover analysis result

Figure B-2 Model 6-13

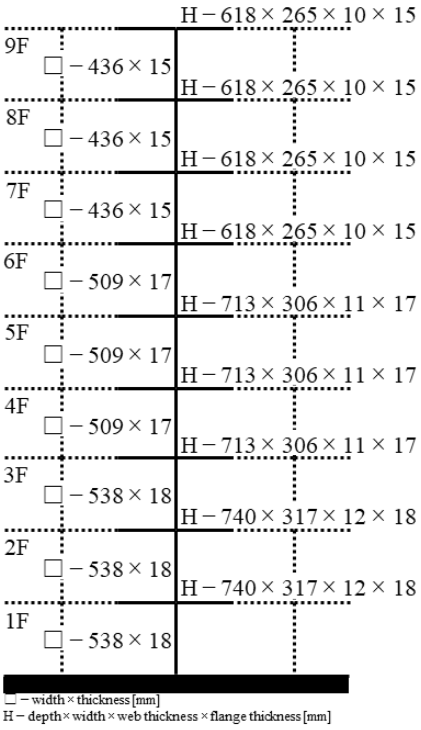

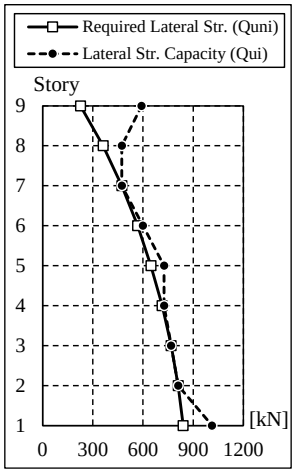

Column-to-Beam Moment Capacity Ratio			
Story	${}_cM_p$ [kN.m]	${}_bM_p$ [kN.m]	${}_cM_p / {}_bM_p$
9	1275.6	828.2	-
8	1263.1	828.2	1.53
7	1242.3	828.2	1.51
6	1978.4	828.2	1.94
5	1946.3	1271.3	1.54
4	1907.0	1271.3	1.52
3	2235.1	1271.3	1.63
2	2184.4	1418.0	1.56
1	2127.0	1418.0	1.52

Anchor Bolt	
Diameter [mm]	Ultimate Strength [kN.m]
55.1	2764.9

Natural Period	
1st Mode [sec.]	2nd Mode [sec.]
1.367	0.491

(a) Model details

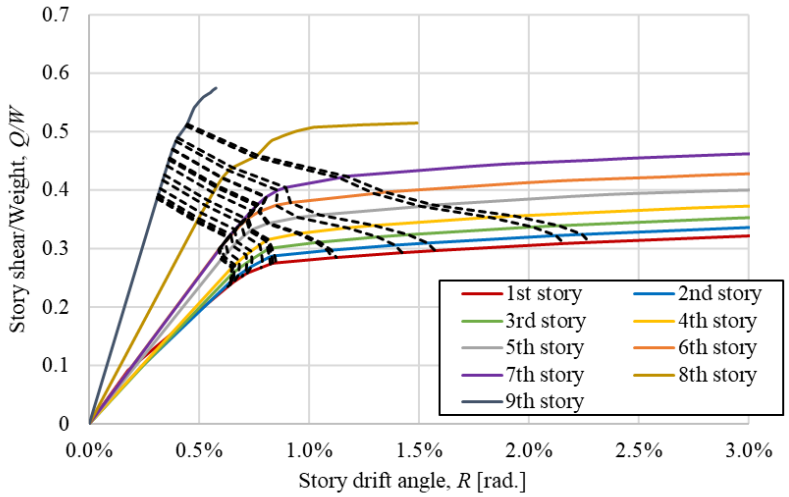

※ The dashed lines (-----) indicate the steps where the plastic hinges are formed

(b) Pushover analysis result

Figure B-3 Model 9-13

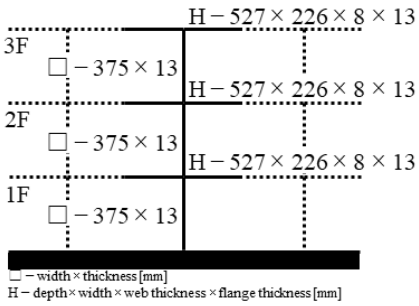

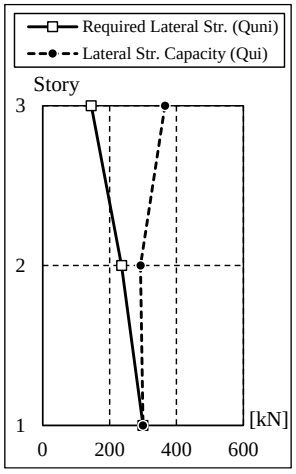

Column-to-Beam Moment Capacity Ratio			
Story	${}_cM_p$ [kN.m]	${}_bM_p$ [kN.m]	${}_cM_p / {}_bM_p$
3	807.3	512.3	-
2	792.7	512.3	1.56
1	768.5	512.3	1.52

Anchor Bolt	
Diameter [mm]	Ultimate Strength [kN.m]
28.4	537.9

Natural Period	
1st Mode [sec.]	2nd Mode [sec.]
0.816	0.244

(a) Model details

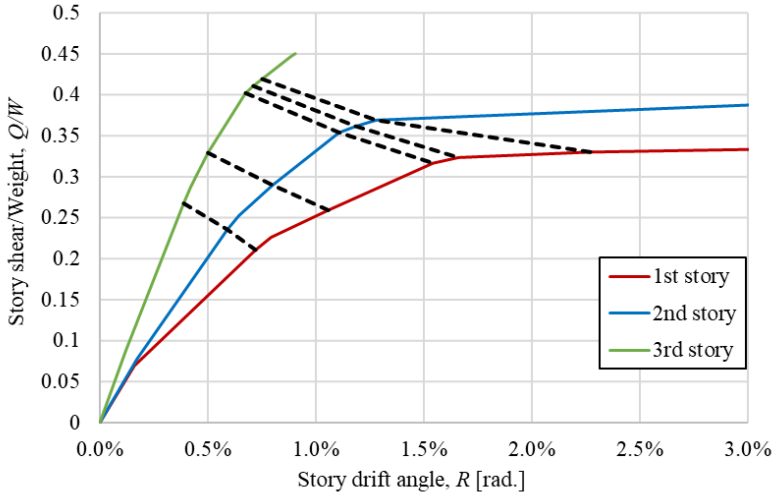

※ The dashed lines (-----) indicate the steps where the plastic hinges are formed

(b) Pushover analysis result

Figure B-4 Model 3-07

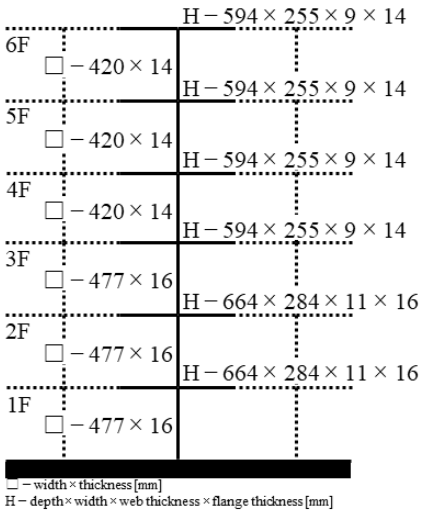

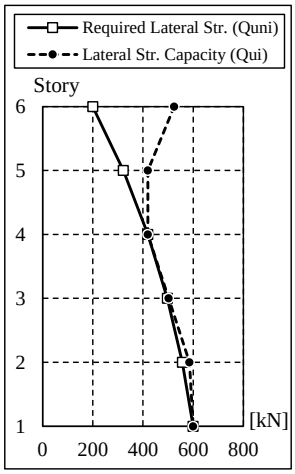

Column-to-Beam Moment Capacity Ratio			
Story	${}_cM_p$ [kN.m]	${}_bM_p$ [kN.m]	${}_cM_p/{}_bM_p$
6	1135.6	734.0	-
5	1122.6	734.0	1.54
4	1101.0	734.0	1.51
3	1612.3	734.0	1.85
2	1578.0	1024.2	1.56
1	1536.1	1024.2	1.52

Anchor Bolt	
Diameter [mm]	Ultimate Strength [kN.m]
32.3	1076.4

Natural Period	
1st Mode [sec.]	2nd Mode [sec.]
1.128	0.371

(a) Model details

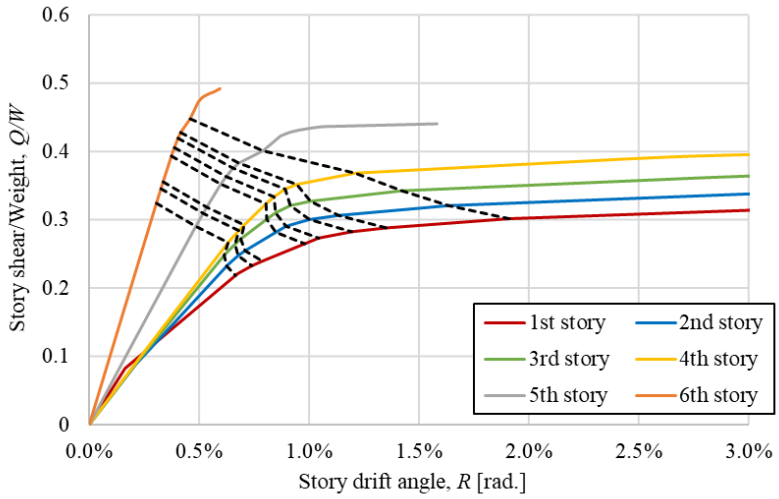

※ The dashed lines (-----) indicate the steps where the plastic hinges are formed

(b) Pushover analysis result

Figure B-5 Model 6-07

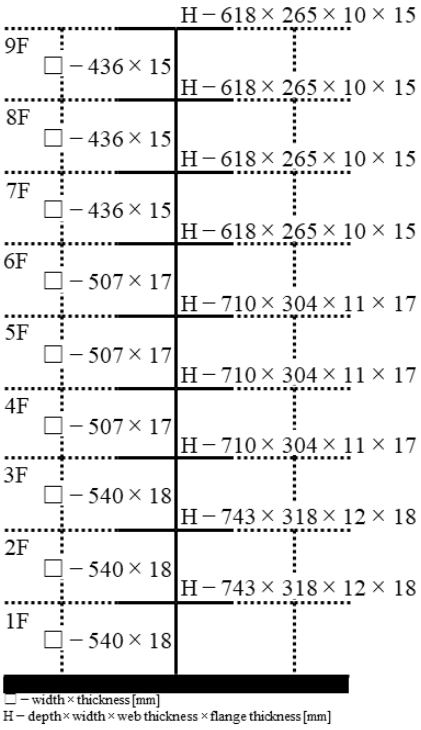

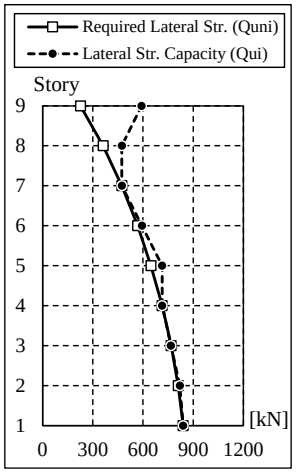

Column-to-Beam Strength Ratio			
Story	M_{pc} [kN.m]	M_{pg} [kN.m]	M_{pc}/M_{pg}
9	1275.6	828.2	-
8	1263.1	828.2	1.53
7	1242.3	828.2	1.51
6	1947.0	828.2	1.93
5	1914.7	1250.2	1.54
4	1875.3	1250.2	1.52
3	2259.9	1250.2	1.65
2	2209.4	1434.9	1.56
1	2152.2	1434.9	1.52

Anchor Bolt	
Diameter [mm]	Ultimate Strength [kN.m]
31.6	1506.7

Natural Period	
1st Mode [sec.]	2nd Mode [sec.]
1.368	0.49

(a) Model details

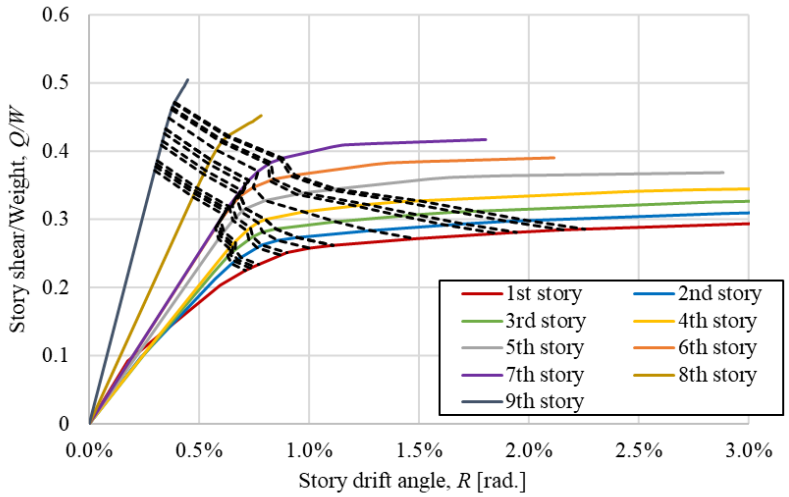

※ The dashed lines (-----) indicate the steps where the plastic hinges are formed

(b) Pushover analysis result

Figure B-6 Model 9-07

Appendix C Cumulative Damage of Critical Beam of Non-deteriorated SMRF Models

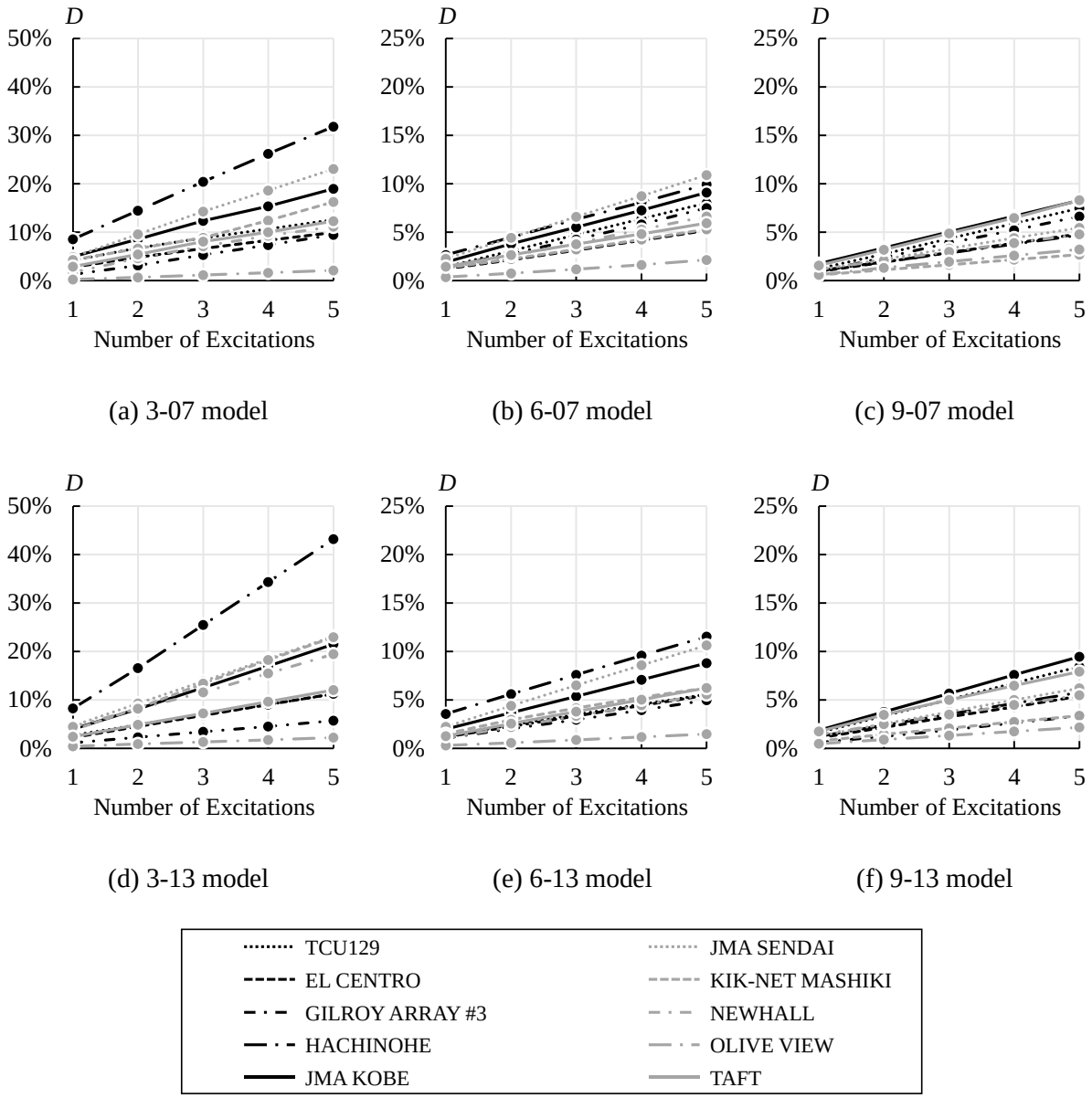

Figure C-1 Cumulative damage of critical beam under input ground motion intensity of PGV 0.5 m/s

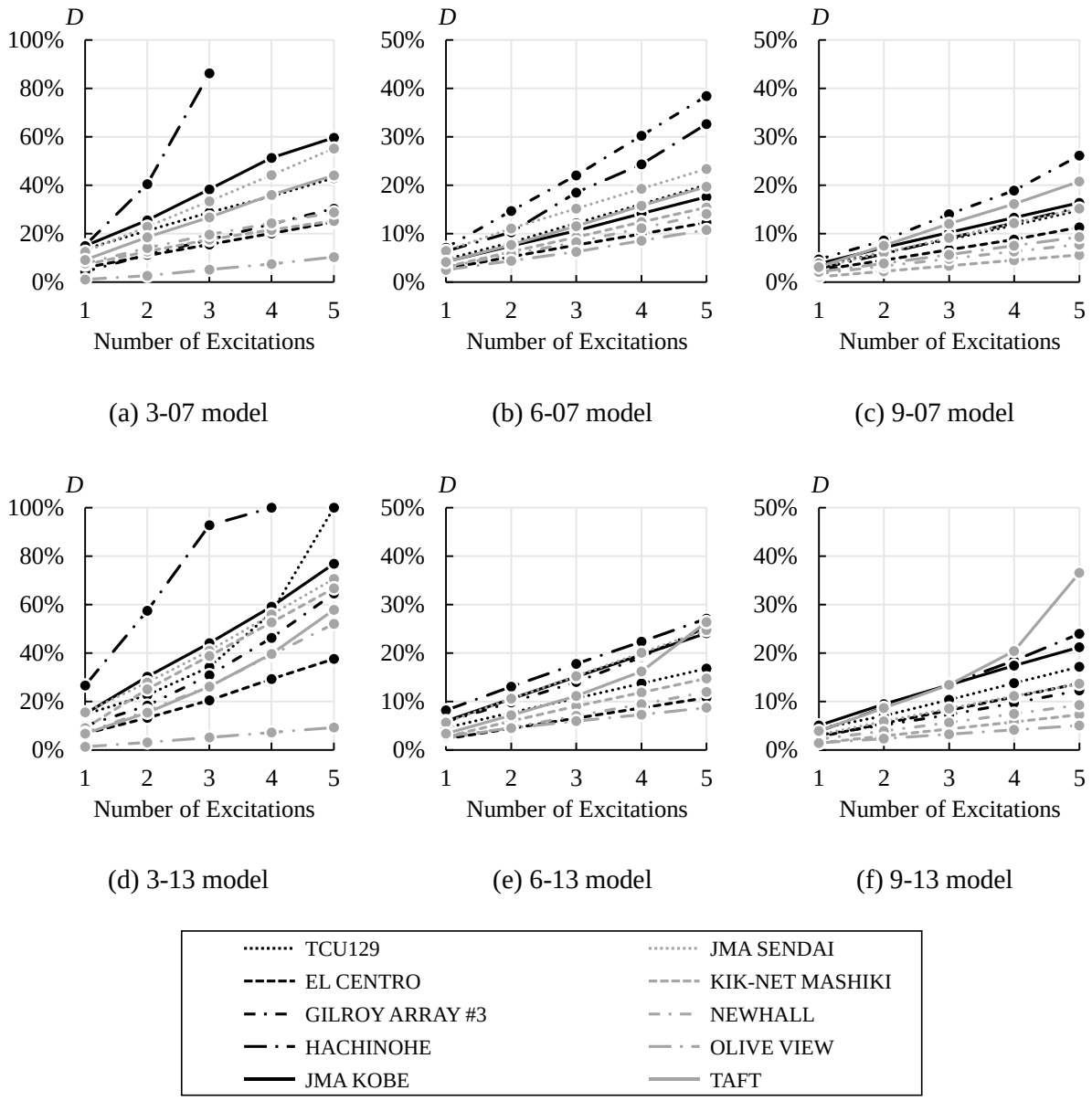

Figure C-2 Cumulative damage of critical beam under input ground motion intensity of PGV 0.75 m/s

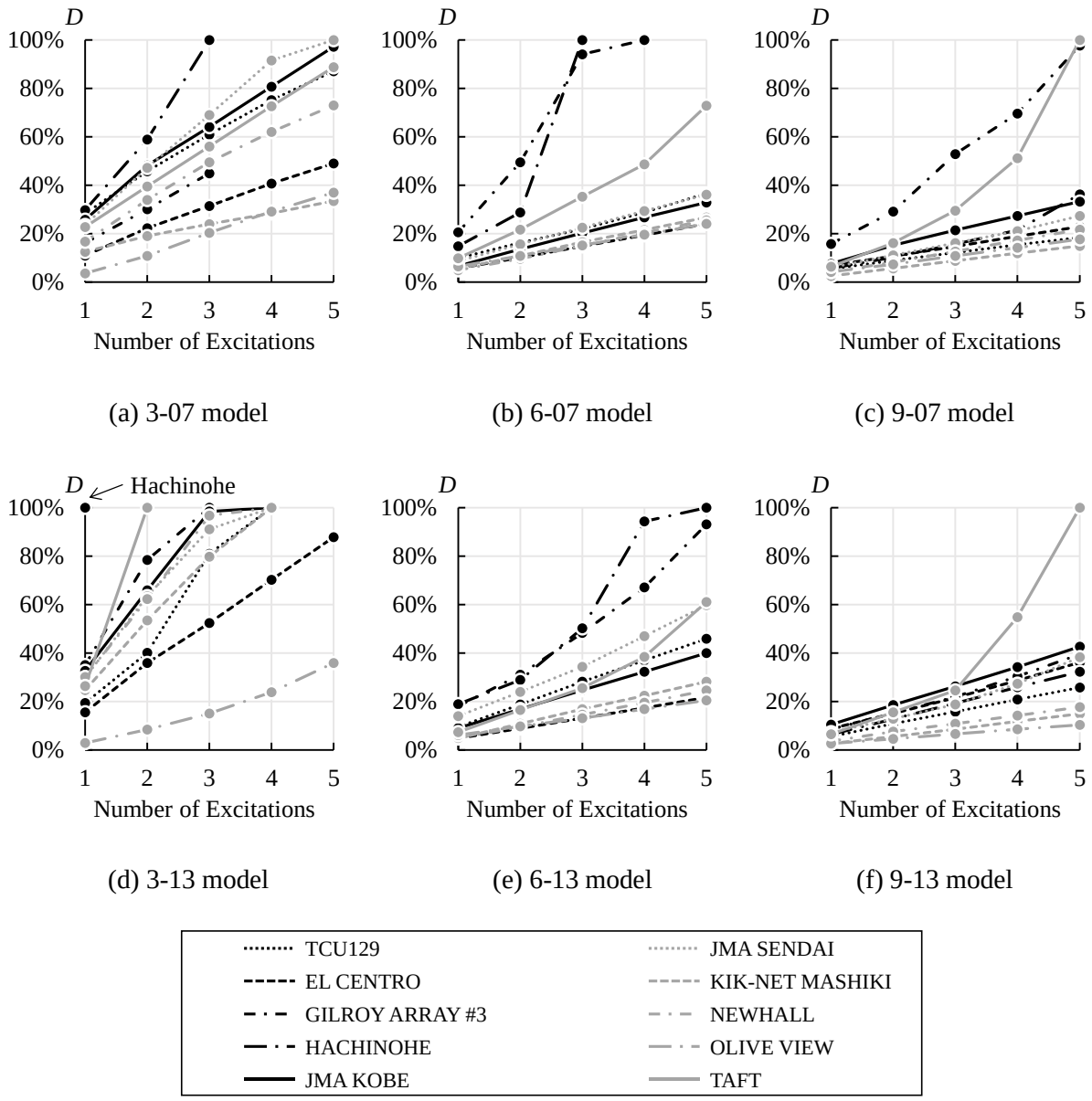

Figure C-3 Cumulative damage of critical beam under input ground motion intensity of PGV 1.0 m/s

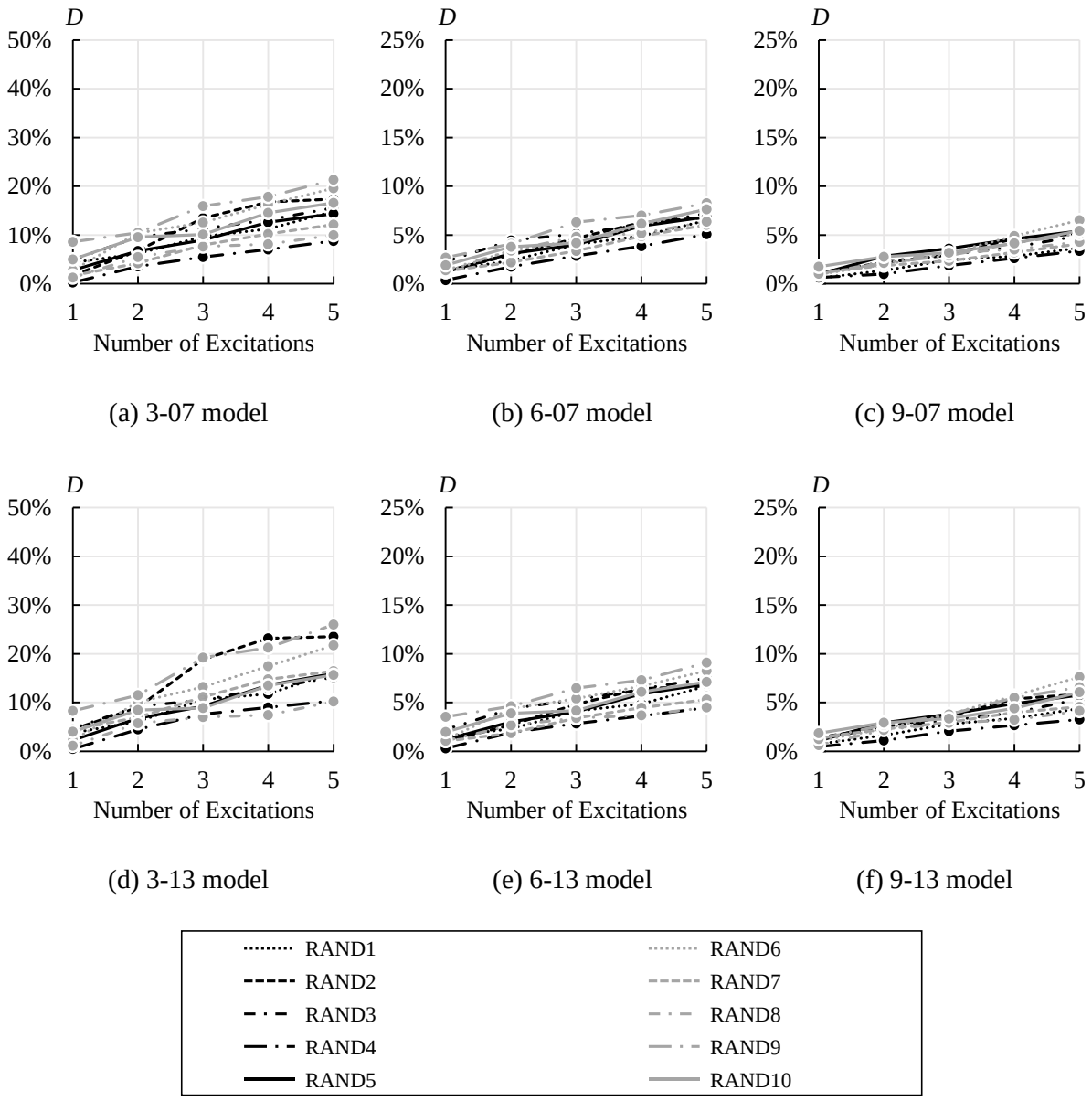

Figure C-4 Cumulative damage of critical beam under random sequence input ground motion group 1 with an intensity of PGV 0.5 m/s

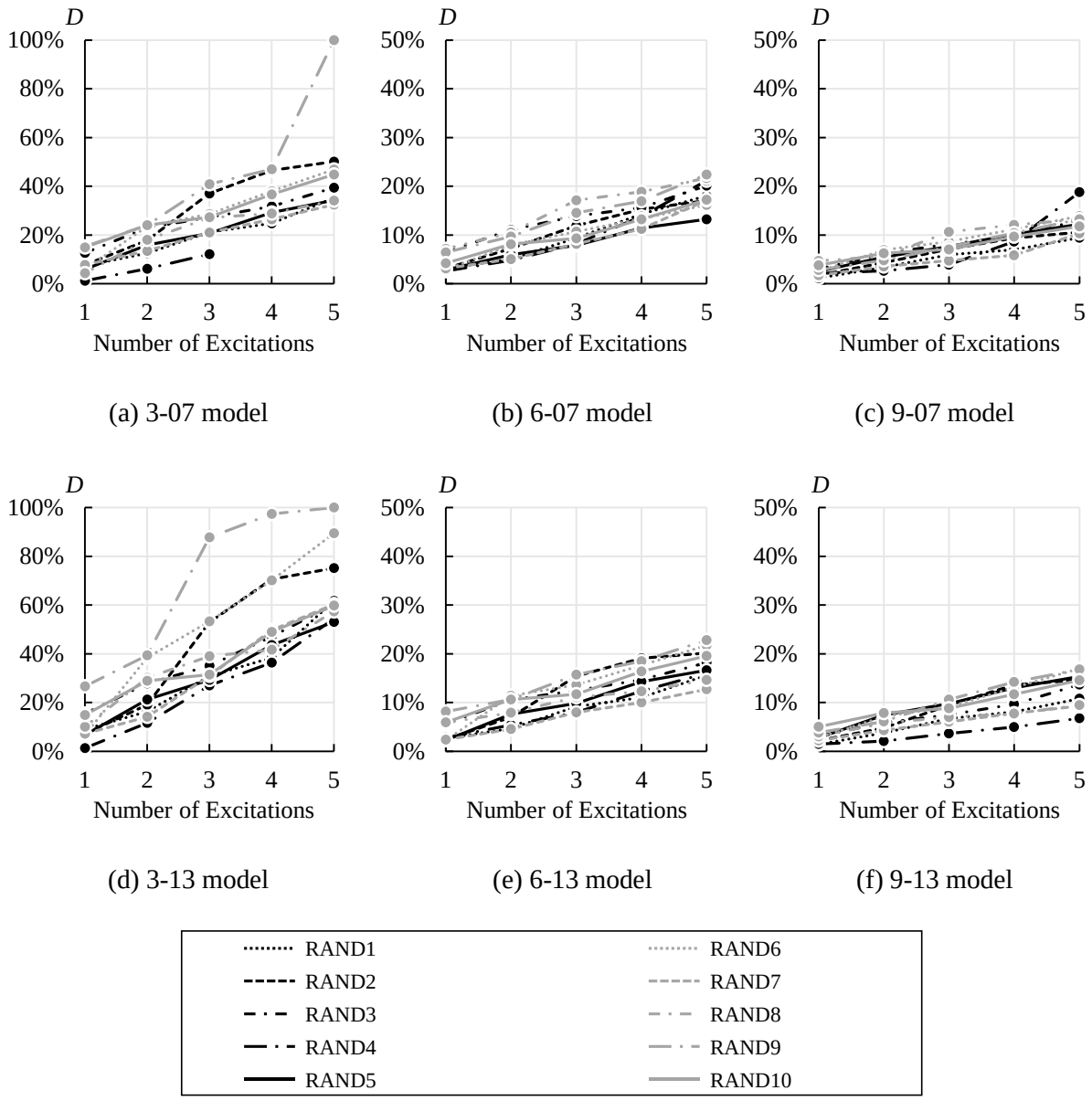

Figure C-5 Cumulative damage of critical beam under random sequence input ground motion group 1 with an intensity of PGV 0.75 m/s

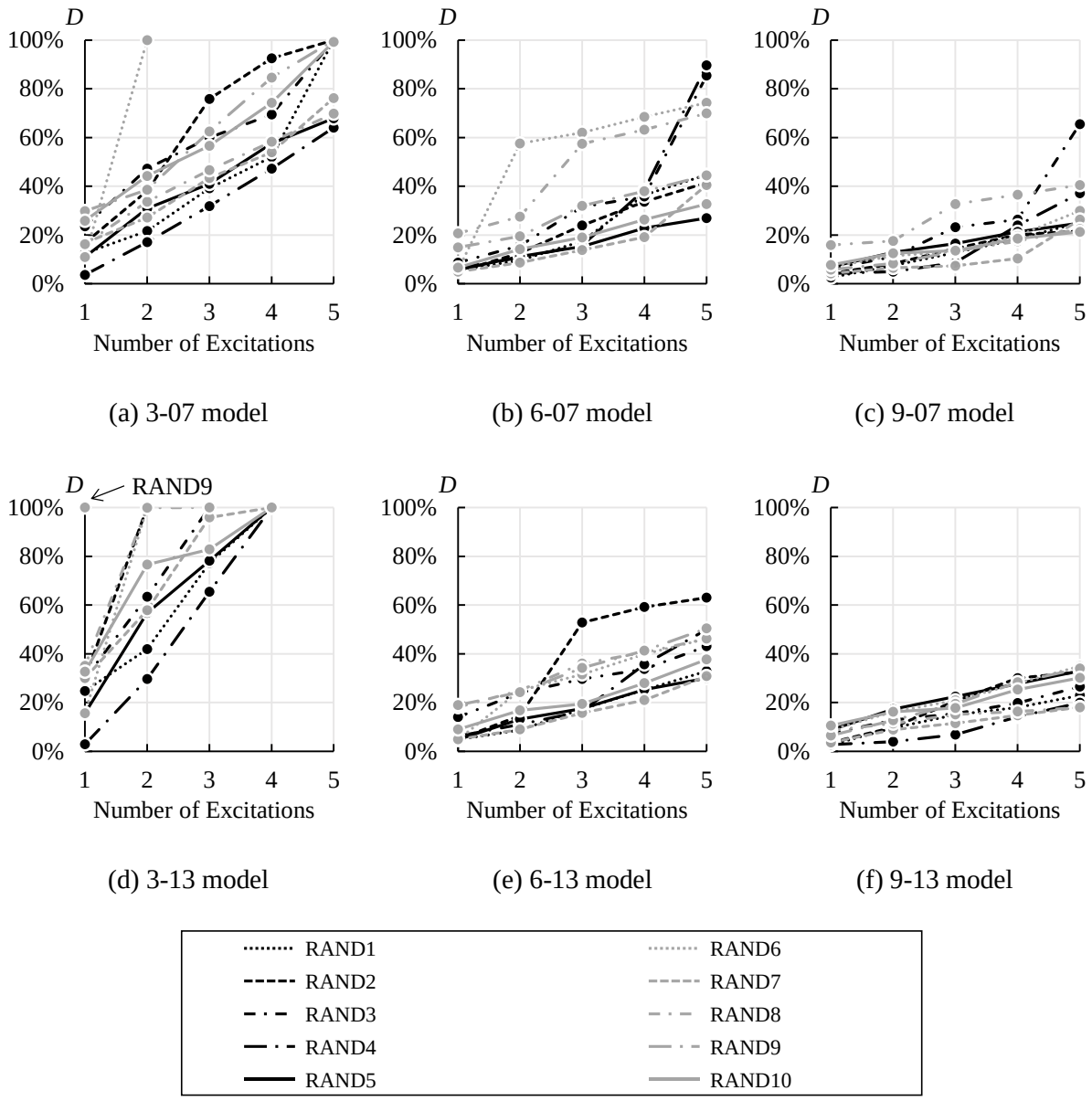

Figure C-6 Cumulative damage of critical beam under random sequence input ground motion group 1 with an intensity of PGV 1.0 m/s

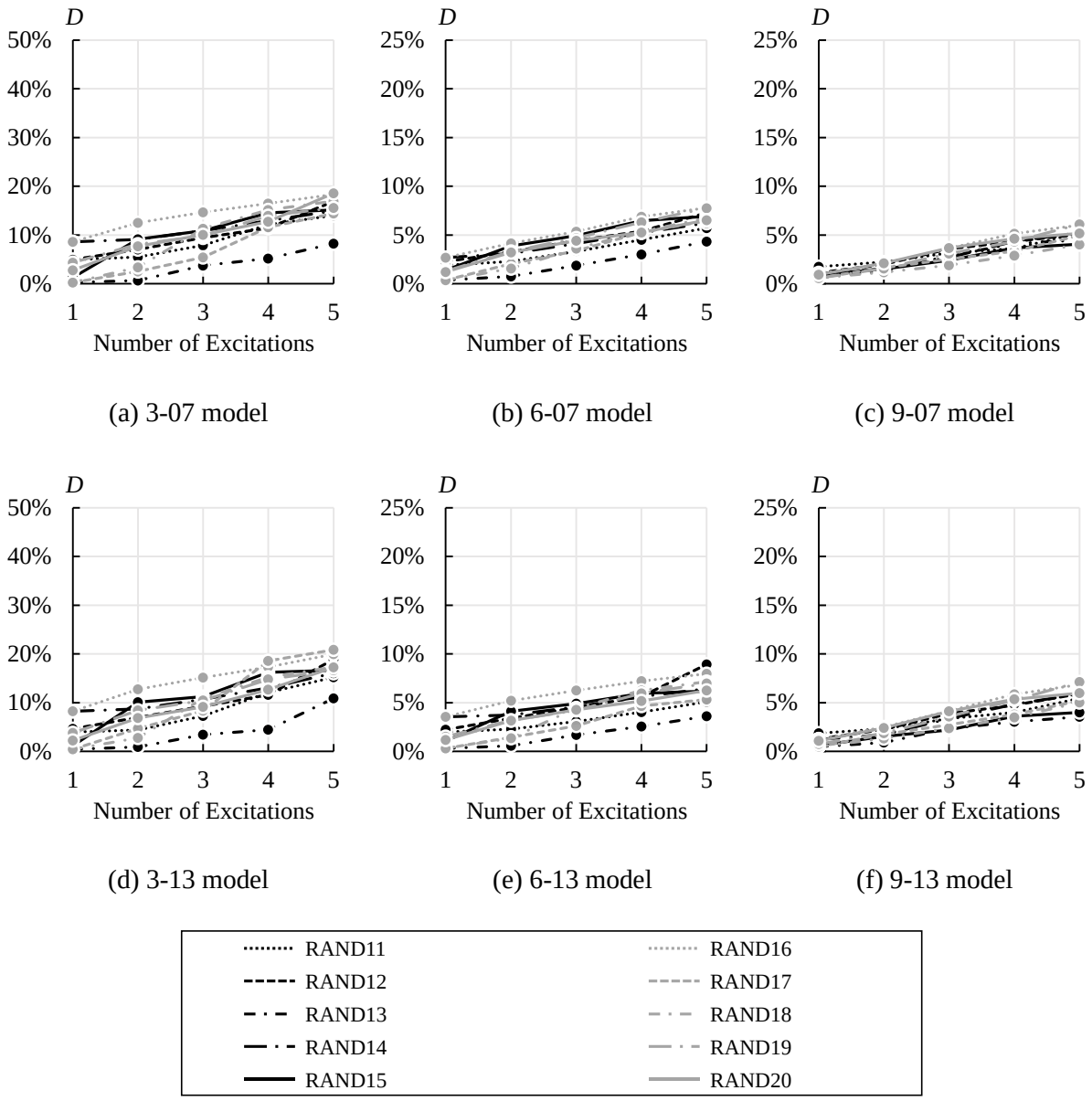

Figure C-7 Cumulative damage of critical beam under random sequence input ground motion group 2 with an intensity of PGV 0.5 m/s

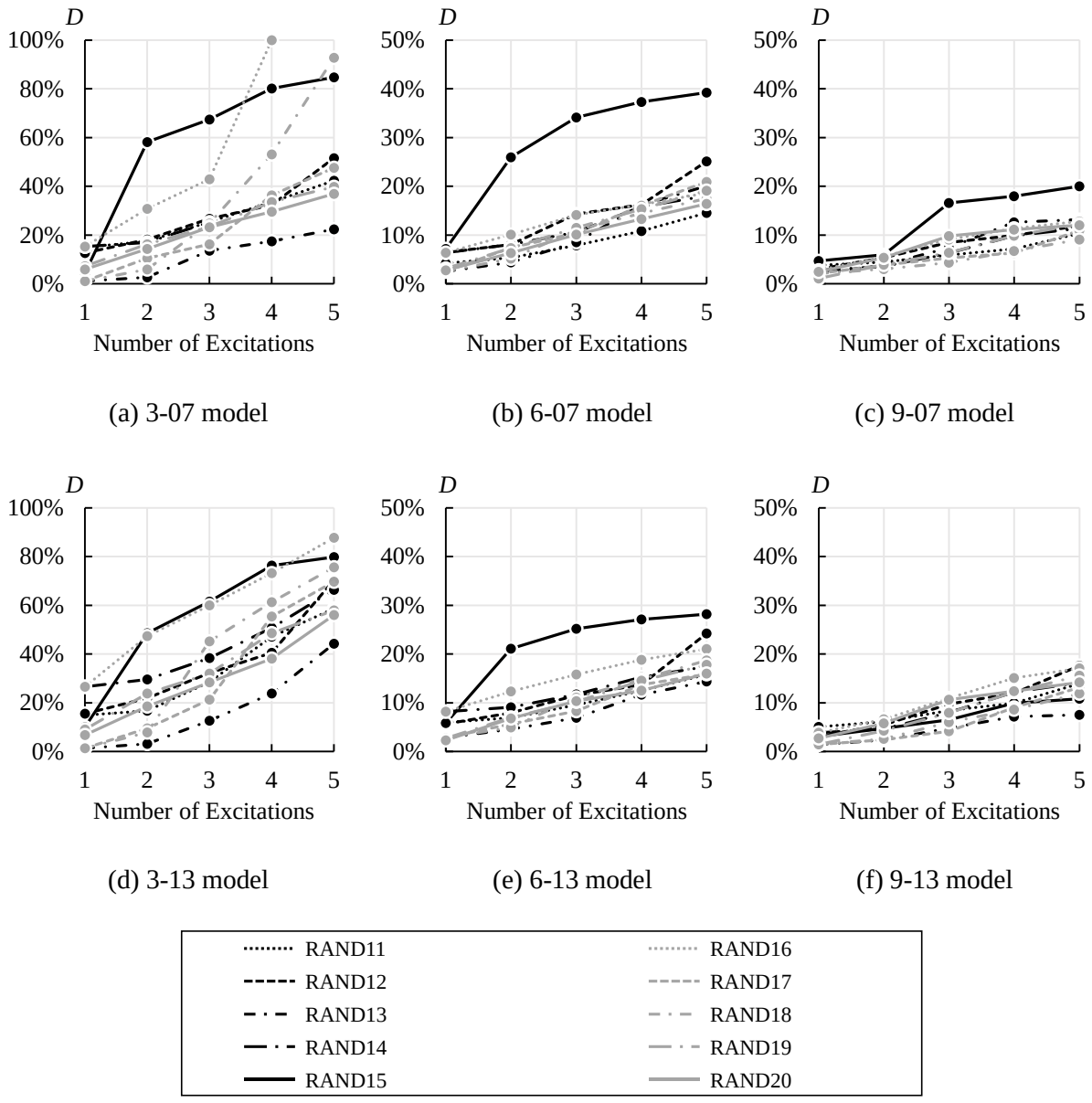

Figure C-8 Cumulative damage of critical beam under random sequence input ground motion group 2 with an intensity of PGV 0.75 m/s

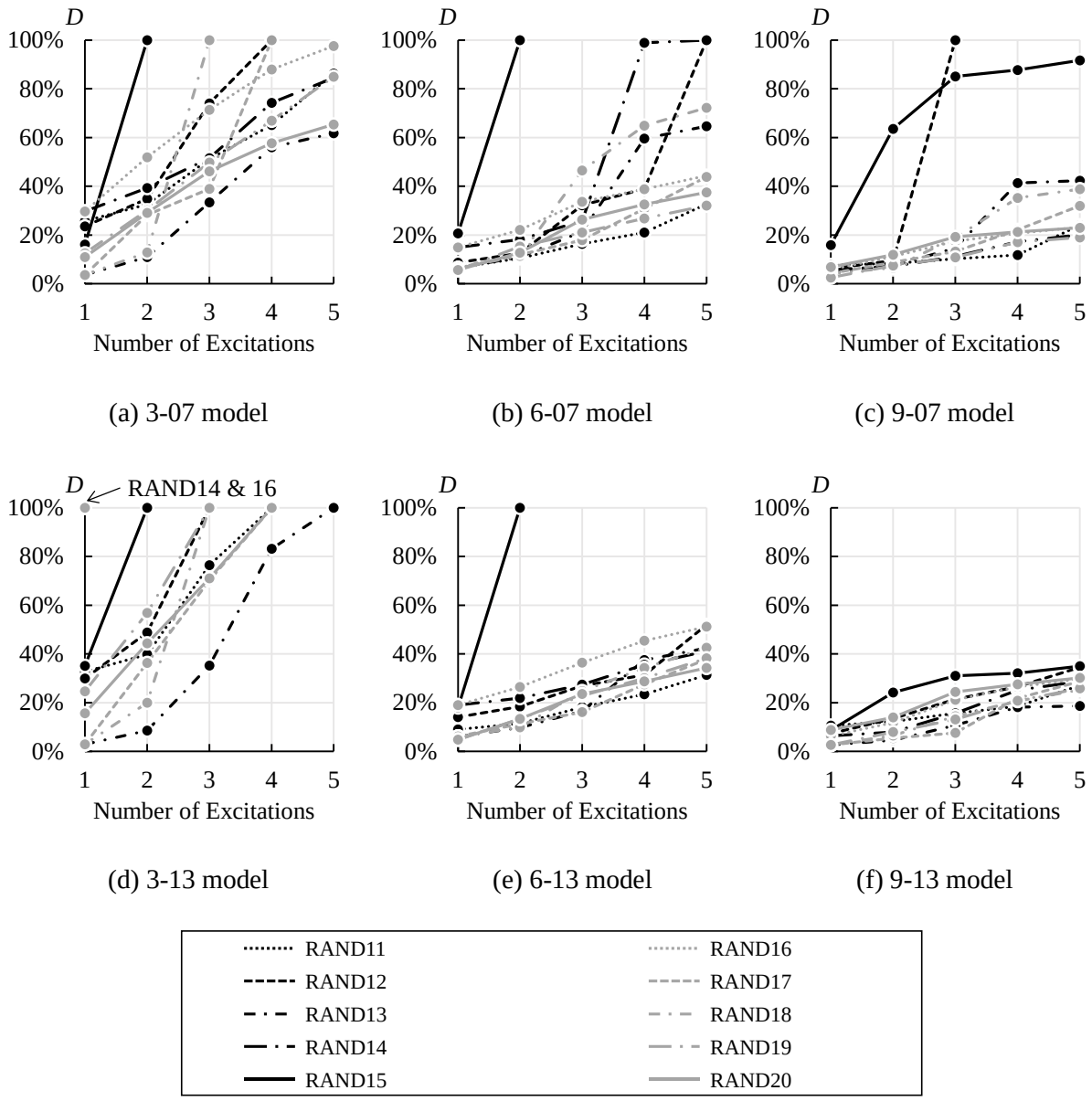

Figure C-9 Cumulative damage of critical beam under random sequence input ground motion group 2 with an intensity of PGV 1.0 m/s

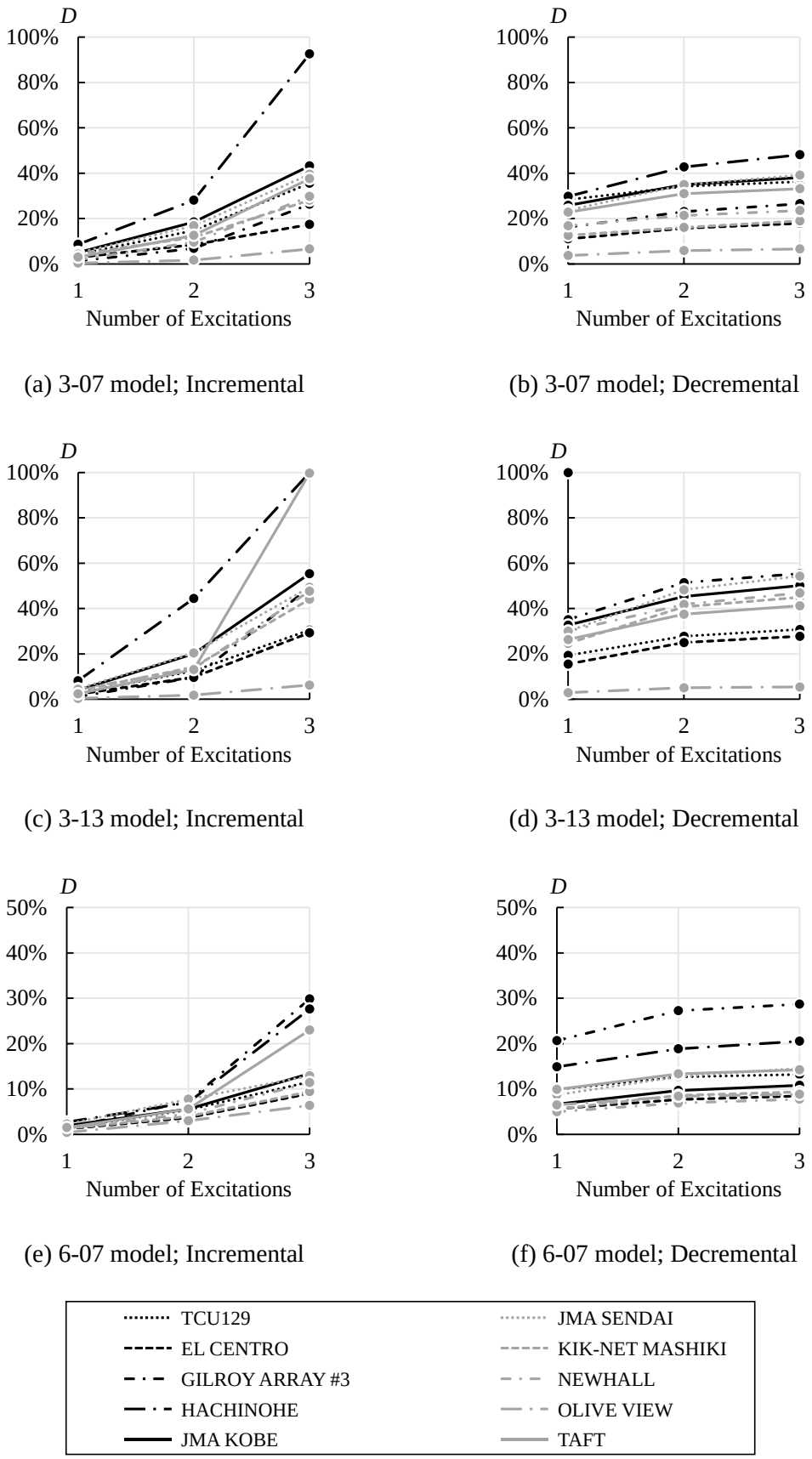

(a) 3-07 model; Incremental

(b) 3-07 model; Decremental

(c) 3-13 model; Incremental

(d) 3-13 model; Decremental

(e) 6-07 model; Incremental

(f) 6-07 model; Decremental

Figure C-10 Cumulative damage of critical beam under incremental-decremental sequence input ground motion

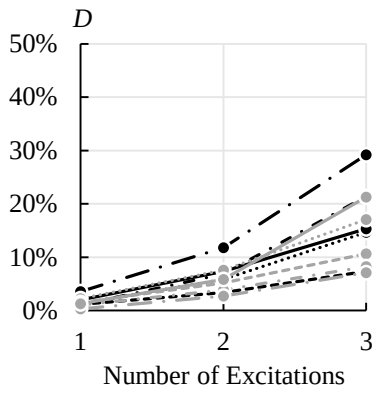

(g) 6-13 model; Incremental

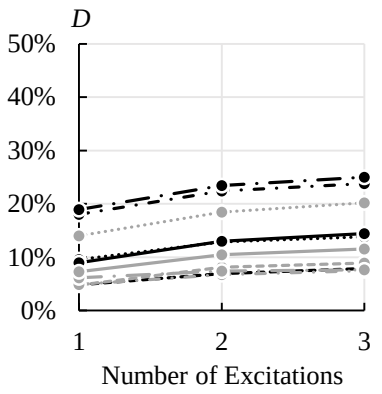

(h) 6-13 model; Decremental

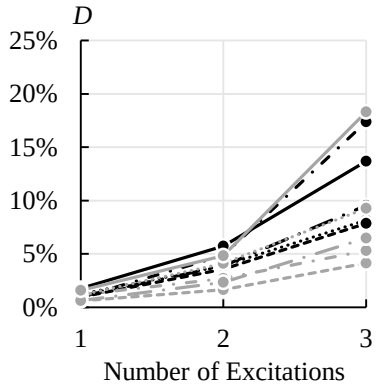

(i) 9-07 model; Incremental

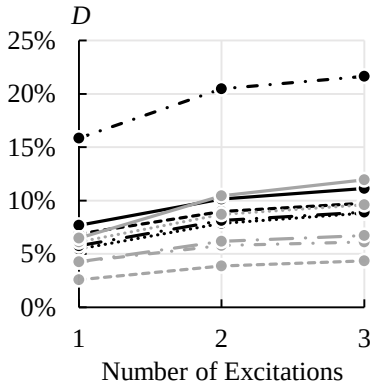

(j) 9-07 model; Decremental

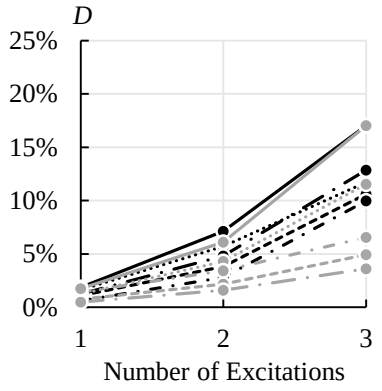

(k) 9-13 model; Incremental

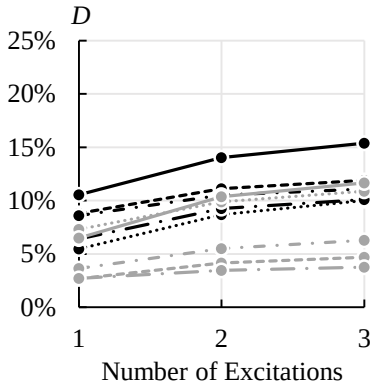

(l) 9-13 model; Decremental

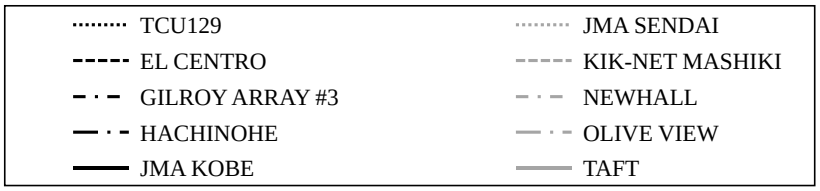

Figure C-10 Cumulative damage of critical beam under incremental-decremental sequence input ground motion (*continued*)

Appendix D Details of Deteriorated SMRF Models

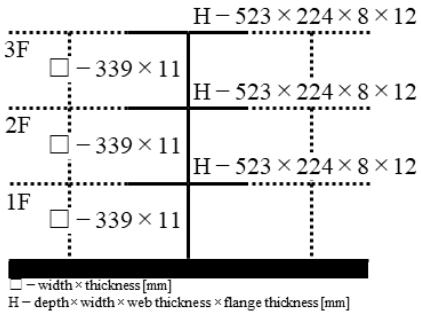

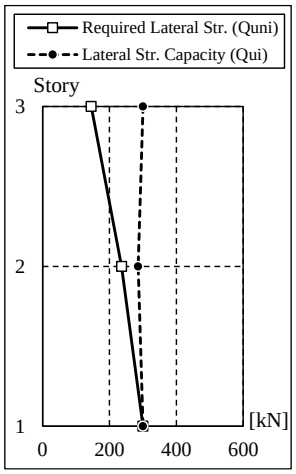

Column-to-Beam Moment Capacity Ratio			
Story	${}_cM_p$ [kN.m]	${}_bM_p$ [kN.m]	${}_cM_p/{}_bM_p$
3	593.2	500.5	-
2	577.1	500.5	1.17
1	550.2	500.5	1.13

Natural Period	
1st Mode [sec.]	2nd Mode [sec.]
0.927	0.285

(a) Model details

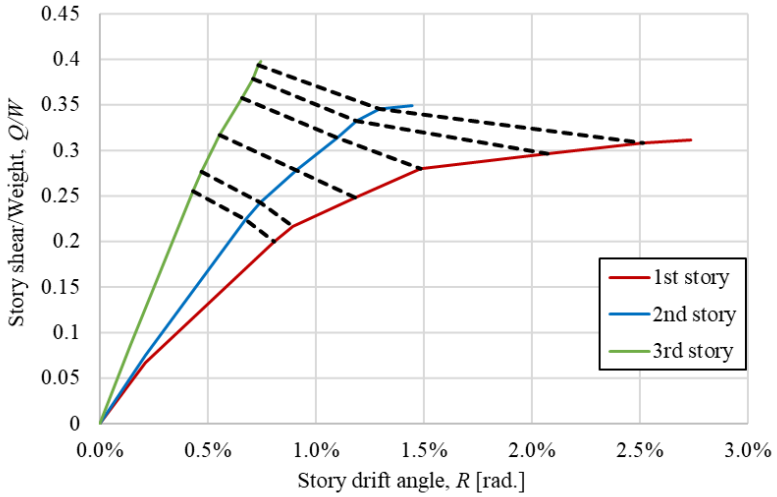

※ The dashed lines (-----) indicate the steps where the plastic hinges are formed

(b) Pushover analysis result

Figure D-1 Model 3-29-1.1

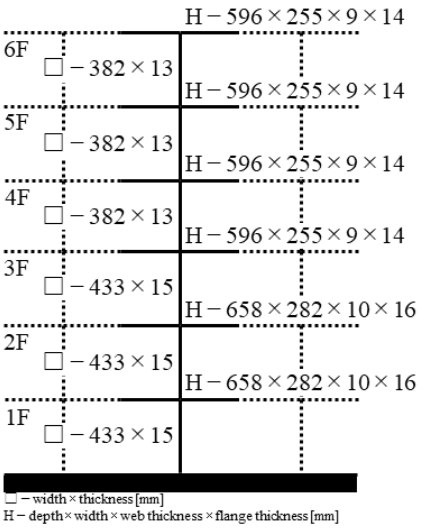

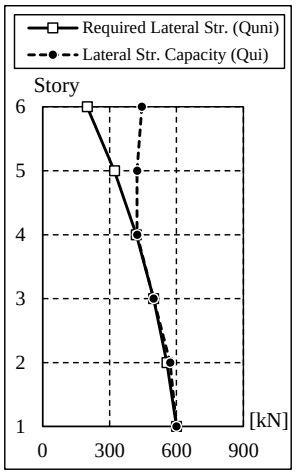

Column-to-Beam Moment Capacity Ratio			
Story	${}_cM_p$ [kN.m]	${}_bM_p$ [kN.m]	${}_cM_p/{}_bM_p$
6	852.4	740.3	-
5	838.1	740.3	1.14
4	814.3	740.3	1.12
3	1183.4	740.3	1.35
2	1145.6	999.5	1.17
1	1099.5	999.5	1.12

Natural Period	
1st Mode [sec.]	2nd Mode [sec.]
1.237	0.415

(a) Model details

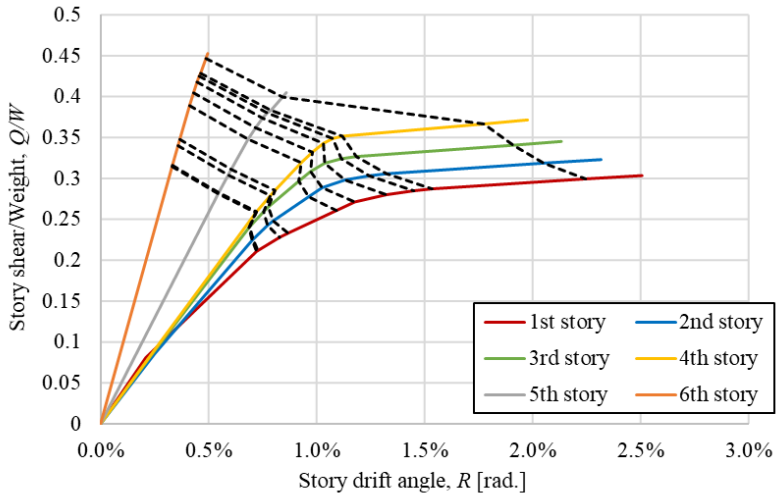

※ The dashed lines (-----) indicate the steps where the plastic hinges are formed

(b) Pushover analysis result

Figure D-2 Model 6-29-1.1

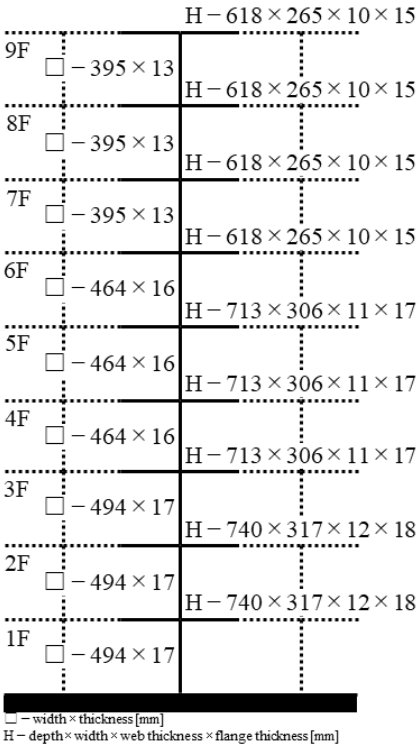

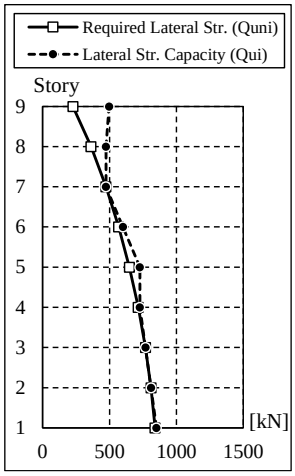

Column-to-Beam Moment Capacity Ratio			
Story	${}_cM_p$ [kN.m]	${}_bM_p$ [kN.m]	${}_cM_p/{}_bM_p$
9	947.9	828.2	-
8	934.1	828.2	1.14
7	911.1	828.2	1.11
6	1476.9	828.2	1.44
5	1441.7	1271.3	1.15
4	1398.6	1271.3	1.12
3	1677.6	1271.3	1.21
2	1622.4	1418.0	1.16
1	1559.9	1418.0	1.12

Natural Period	
1st Mode [sec.]	2nd Mode [sec.]
1.475	0.538

(a) Model details

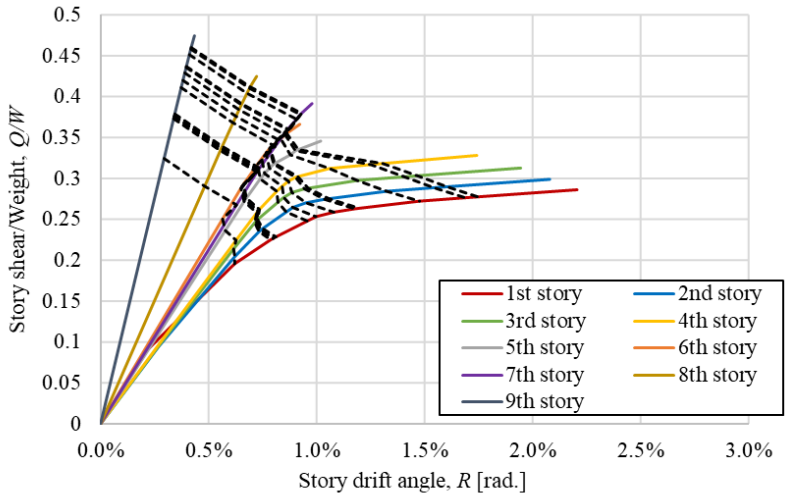

※ The dashed lines (-----) indicate the steps where the plastic hinges are formed

(b) Pushover analysis result

Figure D-3 Model 9-29-1.1

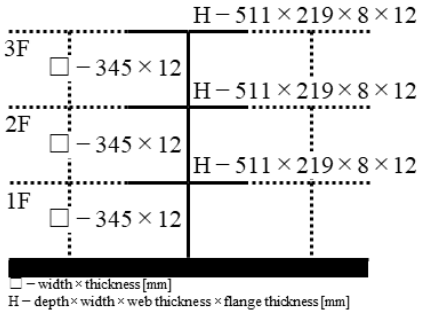

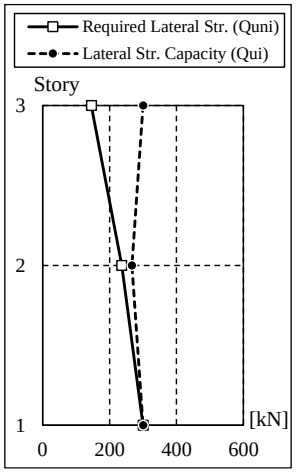

Column-to-Beam Moment Capacity Ratio			
Story	${}_cM_p$ [kN.m]	${}_bM_p$ [kN.m]	${}_cM_p/{}_bM_p$
3	626.1	466.6	-
2	610.3	466.6	1.32
1	583.9	466.6	1.28

Natural Period	
1st Mode [sec.]	2nd Mode [sec.]
0.924	0.281

(a) Model details

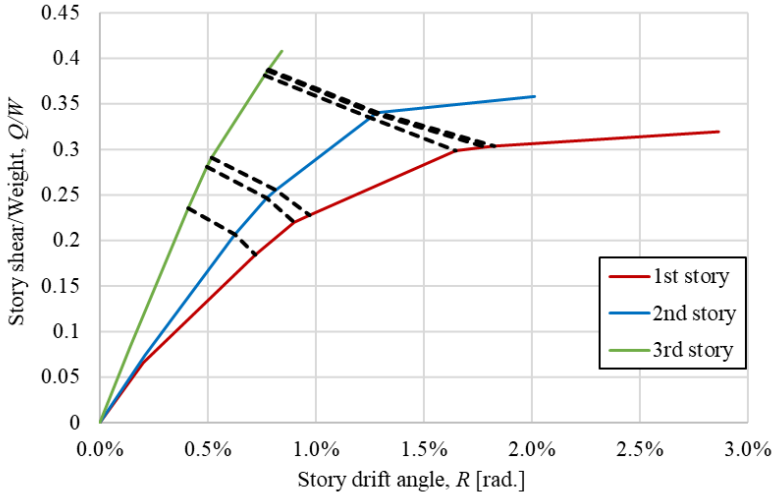

※ The dashed lines (-----) indicate the steps where the plastic hinges are formed

(b) Pushover analysis result

Figure D-4 Model 3-29-1.25

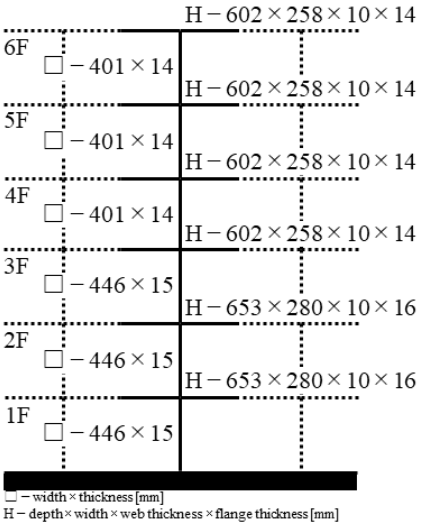

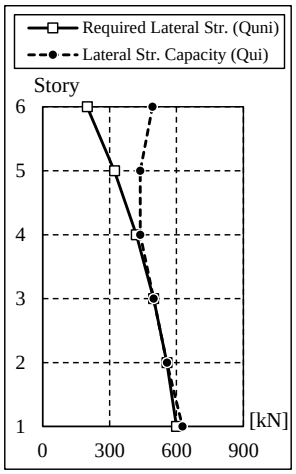

Column-to-Beam Moment Capacity Ratio			
Story	${}_cM_p$ [kN.m]	${}_bM_p$ [kN.m]	${}_cM_p/{}_bM_p$
6	992.5	765.3	-
5	979.0	765.3	1.29
4	956.3	765.3	1.26
3	1299.6	765.3	1.47
2	1262.9	974.5	1.31
1	1218.1	974.5	1.27

Natural Period	
1st Mode [sec.]	2nd Mode [sec.]
1.194	0.394

(a) Model details

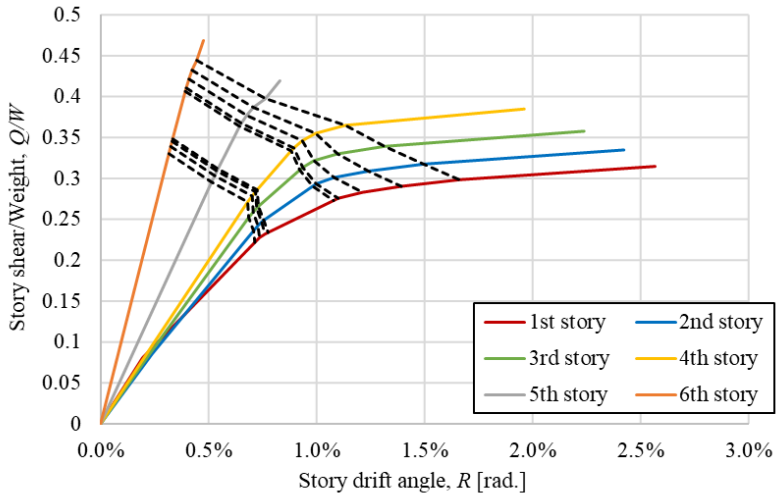

※ The dashed lines (-----) indicate the steps where the plastic hinges are formed

(b) Pushover analysis result

Figure D-5 Model 6-29-1.25

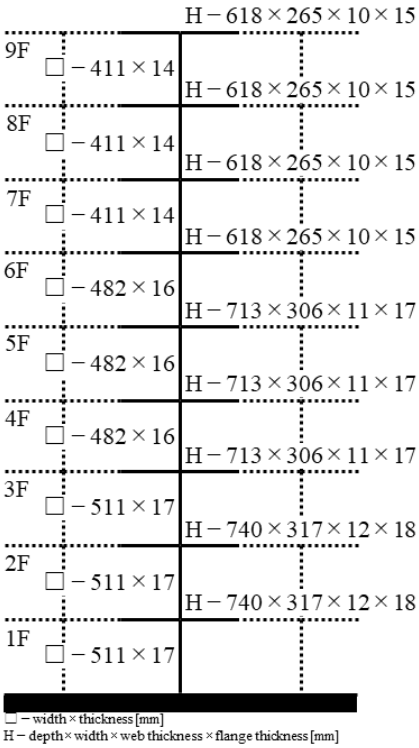

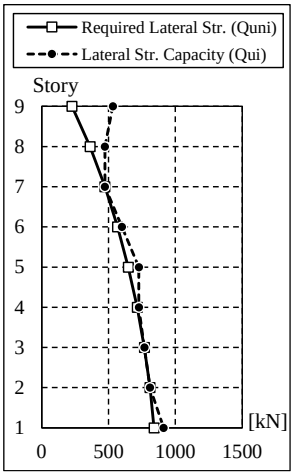

Column-to-Beam Moment Capacity Ratio			
Story	${}_cM_p$ [kN.m]	${}_bM_p$ [kN.m]	${}_cM_p/{}_bM_p$
9	1070.5	828.2	-
8	1057.3	828.2	1.28
7	1035.2	828.2	1.26
6	1664.6	828.2	1.63
5	1630.6	1271.3	1.30
4	1589.2	1271.3	1.27
3	1886.2	1271.3	1.37
2	1832.9	1418.0	1.31
1	1772.5	1418.0	1.27

Natural Period	
1st Mode [sec.]	2nd Mode [sec.]
1.429	0.518

(a) Model details

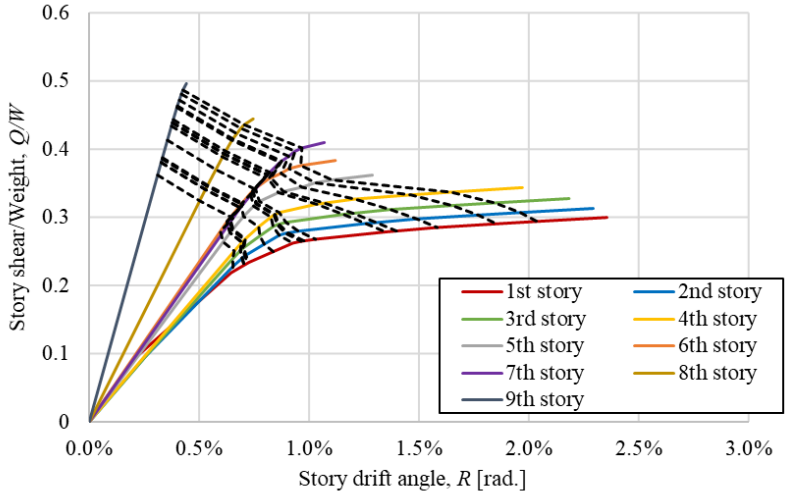

※ The dashed lines (-----) indicate the steps where the plastic hinges are formed

(b) Pushover analysis result

Figure D-6 Model 9-29-1.25

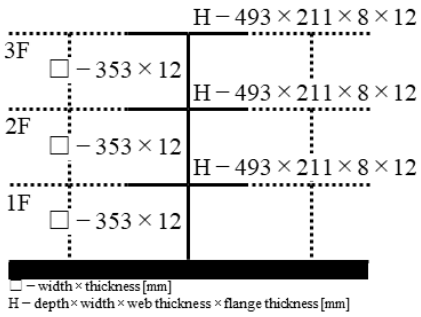

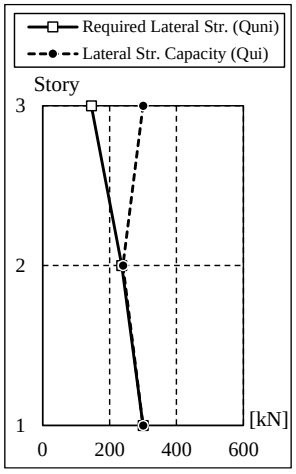

Column-to-Beam Moment Capacity Ratio			
Story	${}_cM_p$ [kN.m]	${}_bM_p$ [kN.m]	${}_cM_p/{}_bM_p$
3	671.5	420.3	-
2	656.0	420.3	1.58
1	630.3	420.3	1.53

Natural Period	
1st Mode [sec.]	2nd Mode [sec.]
0.925	0.277

(a) Model details

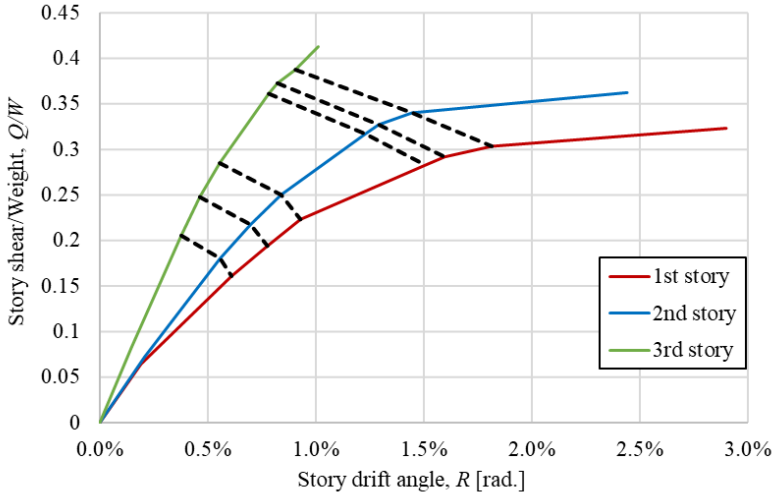

※ The dashed lines (-----) indicate the steps where the plastic hinges are formed

(b) Pushover analysis result

Figure D-7 Model 3-29-1.5

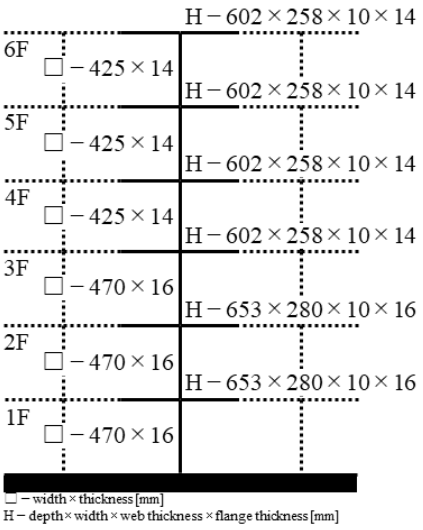

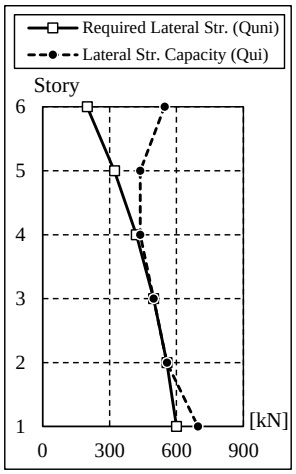

Column-to-Beam Moment Capacity Ratio			
Story	${}_cM_p$ [kN.m]	${}_bM_p$ [kN.m]	${}_cM_p/{}_bM_p$
6	1182.5	765.6	-
5	1169.7	765.6	1.54
4	1148.4	765.6	1.51
3	1539.5	765.6	1.76
2	1504.7	974.9	1.56
1	1462.2	974.9	1.52

Natural Period	
1st Mode [sec.]	2nd Mode [sec.]
1.135	0.369

(a) Model details

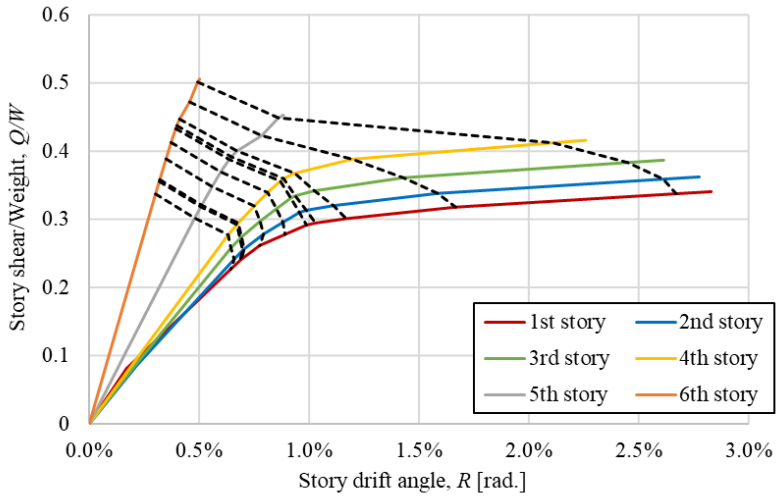

※ The dashed lines (-----) indicate the steps where the plastic hinges are formed

(b) Pushover analysis result

Figure D-8 Model 6-29-1.5

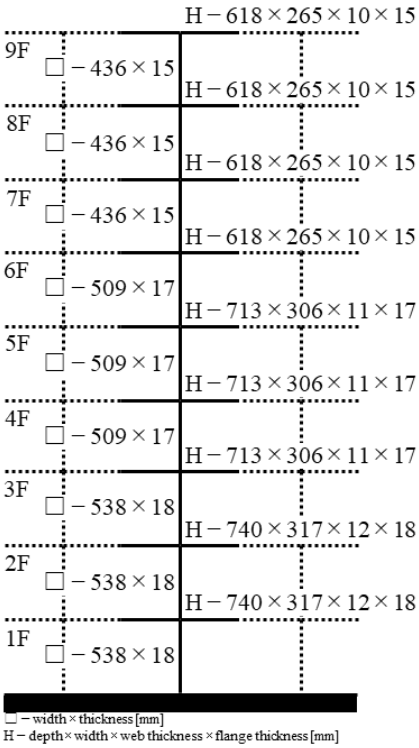

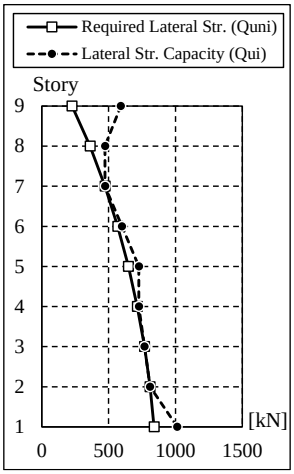

Column-to-Beam Moment Capacity Ratio			
Story	${}_cM_p$ [kN.m]	${}_bM_p$ [kN.m]	${}_cM_p/{}_bM_p$
9	1275.6	828.2	-
8	1263.1	828.2	1.53
7	1242.3	828.2	1.51
6	1978.4	828.2	1.94
5	1946.3	1271.3	1.54
4	1907.0	1271.3	1.52
3	2235.1	1271.3	1.63
2	2184.4	1418.0	1.56
1	2127.0	1418.0	1.52

Natural Period	
1st Mode [sec.]	2nd Mode [sec.]
1.367	0.491

(a) Model details

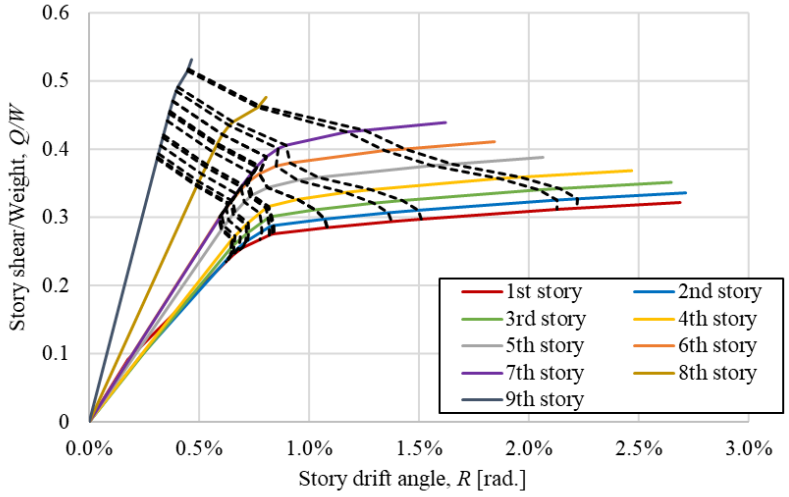

※ The dashed lines (-----) indicate the steps where the plastic hinges are formed

(b) Pushover analysis result

Figure D-9 Model 9-29-1.5

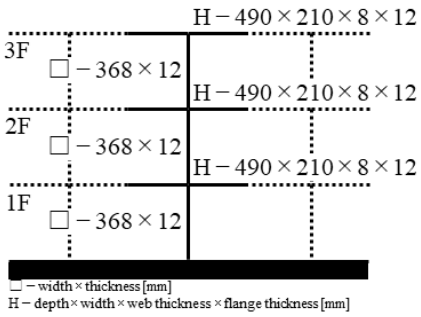

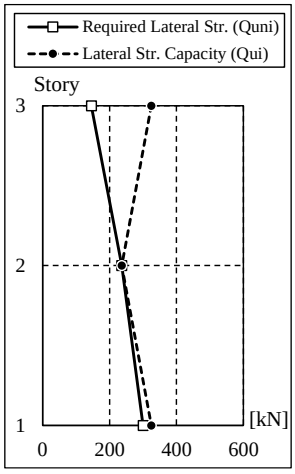

Column-to-Beam Moment Capacity Ratio			
Story	${}_cM_p$ [kN.m]	${}_bM_p$ [kN.m]	${}_cM_p/{}_bM_p$
3	762.3	413.3	-
2	747.5	413.3	1.83
1	722.8	413.3	1.78
Natural Period			
1st Mode [sec.]		2nd Mode [sec.]	
0.886		0.261	

(a) Model details

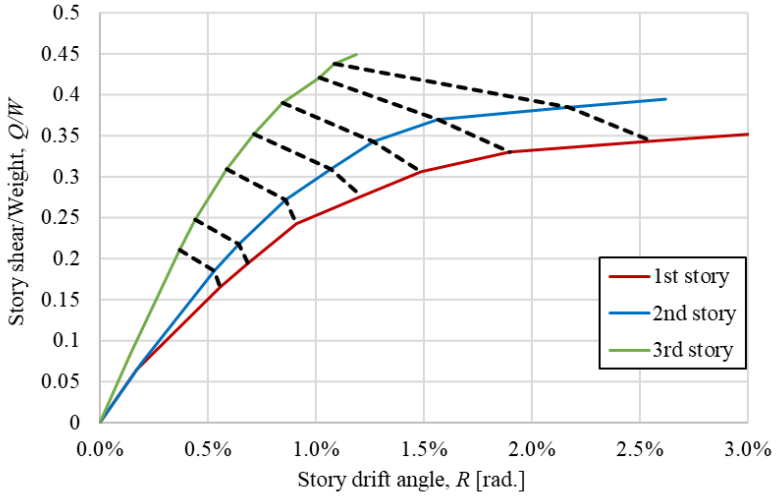

※ The dashed lines (-----) indicate the steps where the plastic hinges are formed

(b) Pushover analysis result

Figure D-10 Model 3-29-1.75

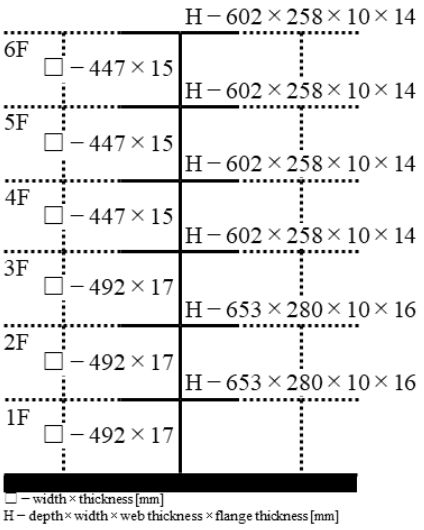

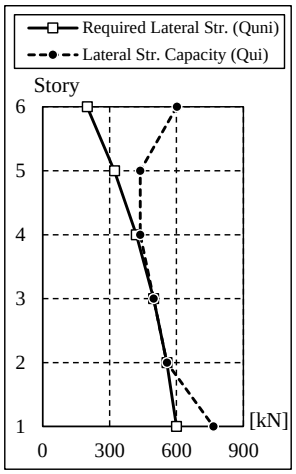

Column-to-Beam Moment Capacity Ratio			
Story	${}_cM_p$ [kN.m]	${}_bM_p$ [kN.m]	${}_cM_p/{}_bM_p$
6	1372.9	765.3	-
5	1360.7	765.3	1.79
4	1340.4	765.3	1.76
3	1779.2	765.3	2.04
2	1746.0	974.5	1.81
1	1705.4	974.5	1.77

Natural Period	
1st Mode [sec.]	2nd Mode [sec.]
1.088	0.350

(a) Model details

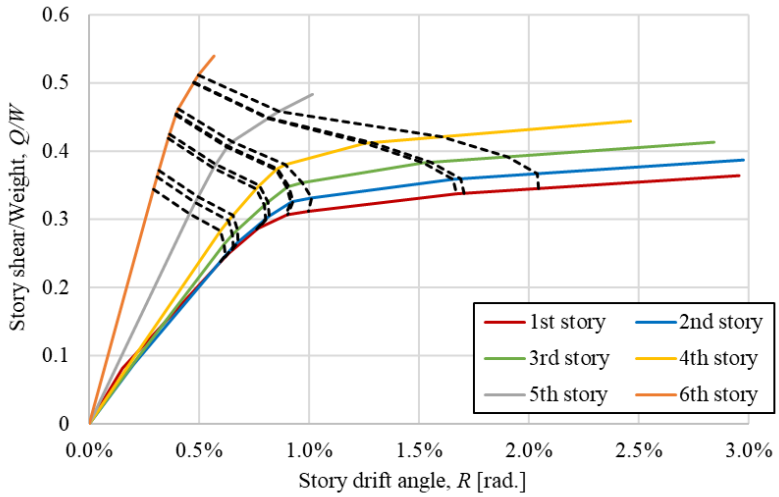

※ The dashed lines (-----) indicate the steps where the plastic hinges are formed

(b) Pushover analysis result

Figure D-11 Model 6-29-1.75

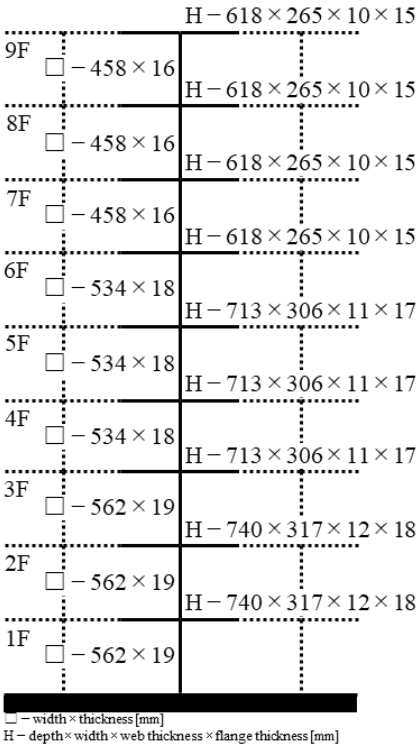

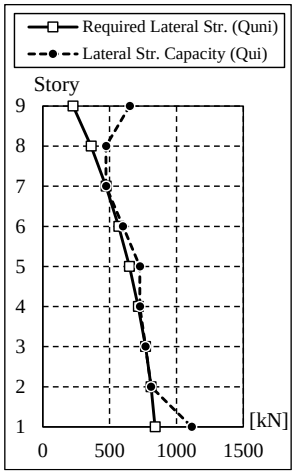

Column-to-Beam Moment Capacity Ratio			
Story	${}_cM_p$ [kN.m]	${}_bM_p$ [kN.m]	${}_cM_p/{}_bM_p$
9	1481.1	828.2	-
8	1469.2	828.2	1.78
7	1449.4	828.2	1.76
6	2292.0	828.2	2.26
5	2261.4	1271.3	1.79
4	2224.0	1271.3	1.76
3	2585.0	1271.3	1.89
2	2536.5	1418.0	1.81
1	2481.6	1418.0	1.77

Natural Period	
1st Mode [sec.]	2nd Mode [sec.]
1.318	0.469

(a) Model details

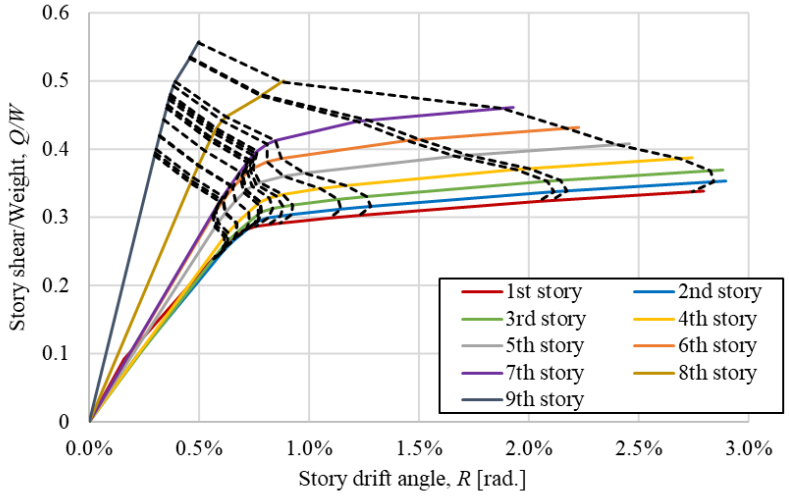

※ The dashed lines (-----) indicate the steps where the plastic hinges are formed

(b) Pushover analysis result

Figure D-12 Model 9-29-1.75

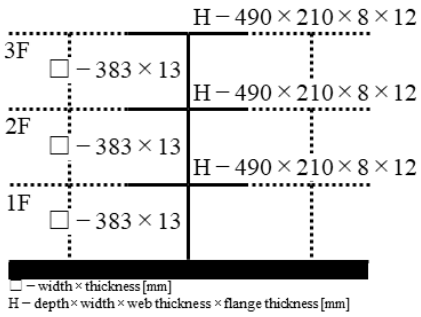

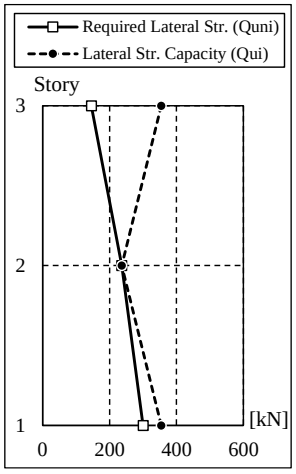

Column-to-Beam Moment Capacity Ratio			
Story	${}_cM_p$ [kN.m]	${}_bM_p$ [kN.m]	${}_cM_p/{}_bM_p$
3	864.3	413.3	-
2	850.1	413.3	2.07
1	826.4	413.3	2.03

Natural Period	
1st Mode [sec.]	2nd Mode [sec.]
0.846	0.246

(a) Model details

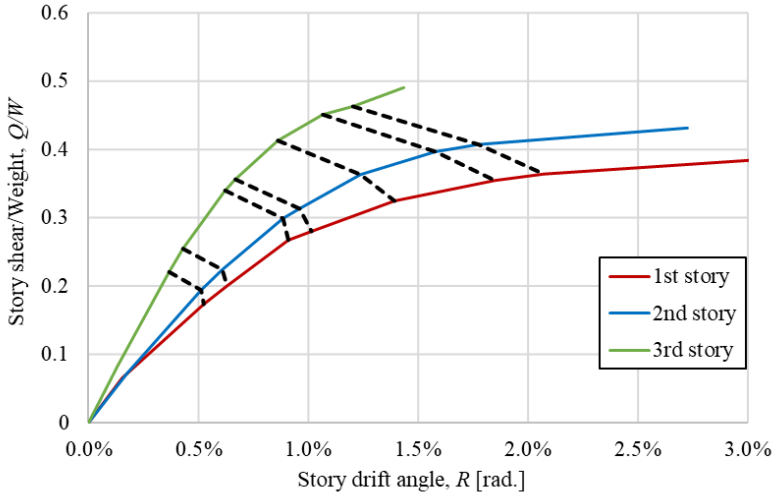

※ The dashed lines (-----) indicate the steps where the plastic hinges are formed

(b) Pushover analysis result

Figure D-13 Model 3-29-2.0

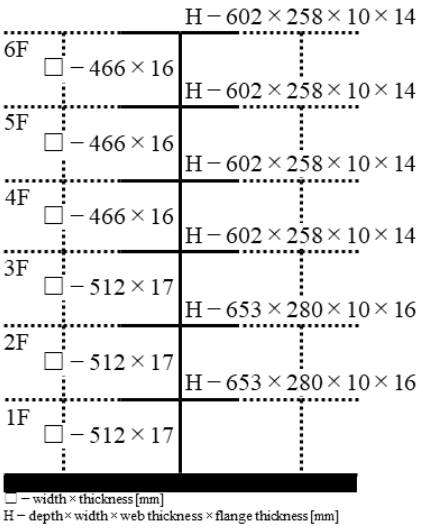

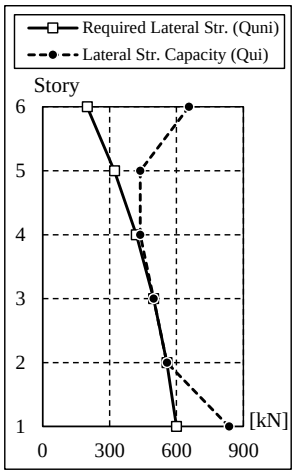

Column-to-Beam Moment Capacity Ratio			
Story	${}_cM_p$ [kN.m]	${}_bM_p$ [kN.m]	${}_cM_p/{}_bM_p$
6	1561.5	765.3	-
5	1549.8	765.3	2.03
4	1530.3	765.3	2.01
3	2019.7	765.3	2.32
2	1987.8	974.5	2.06
1	1948.8	974.5	2.02

Natural Period	
1st Mode [sec.]	2nd Mode [sec.]
1.051	0.335

(a) Model details

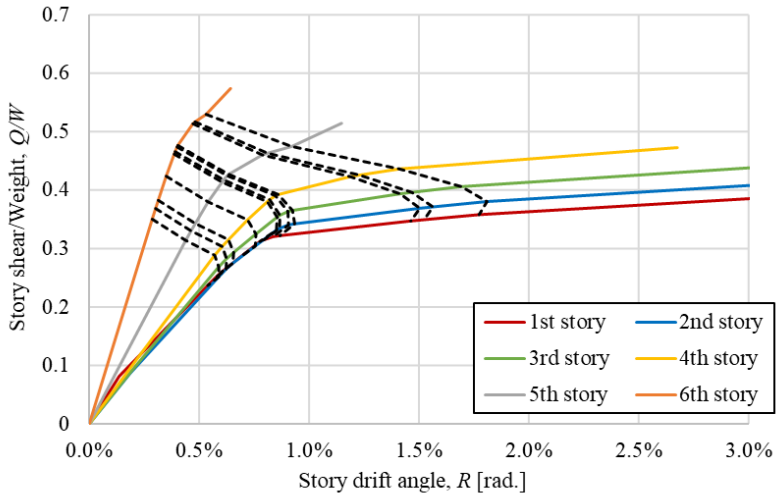

※ The dashed lines (-----) indicate the steps where the plastic hinges are formed

(b) Pushover analysis result

Figure D-14 Model 6-29-2.0

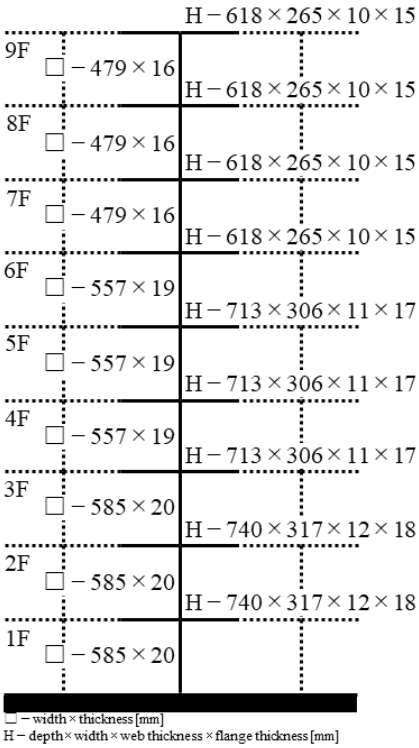

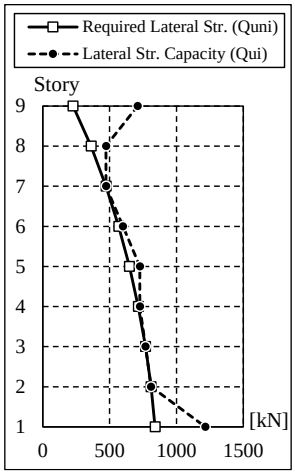

Column-to-Beam Moment Capacity Ratio			
Story	${}_cM_p$ [kN.m]	${}_bM_p$ [kN.m]	${}_cM_p/{}_bM_p$
9	1686.6	828.2	-
8	1675.2	828.2	2.03
7	1656.3	828.2	2.01
6	2607.8	828.2	2.57
5	2578.4	1271.3	2.04
4	2542.6	1271.3	2.01
3	2935.3	1271.3	2.15
2	2888.7	1418.0	2.05
1	2835.9	1418.0	2.02

Natural Period	
1st Mode [sec.]	2nd Mode [sec.]
1.279	0.452

(a) Model details

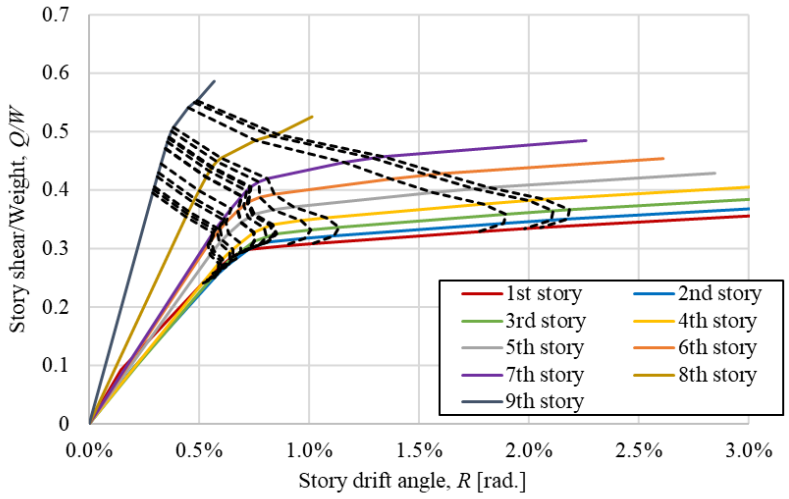

※ The dashed lines (-----) indicate the steps where the plastic hinges are formed

(b) Pushover analysis result

Figure D-15 Model 9-29-2.0

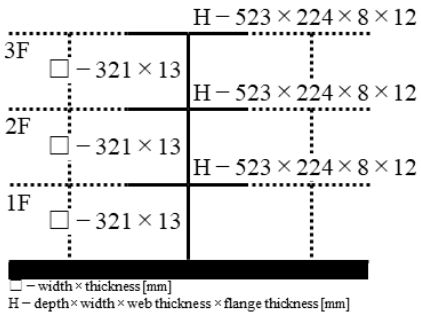

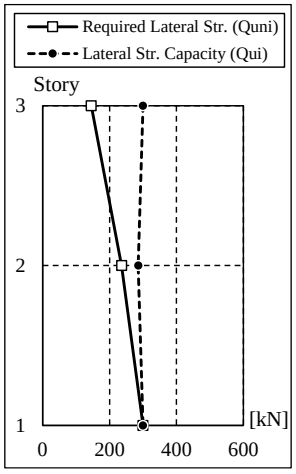

Column-to-Beam Moment Capacity Ratio			
Story	${}_cM_p$ [kN.m]	${}_bM_p$ [kN.m]	${}_cM_p/{}_bM_p$
3	588.7	500.5	-
2	574.3	500.5	1.16
1	550.3	500.5	1.12

Natural Period	
1st Mode [sec.]	2nd Mode [sec.]
0.941	0.291

(a) Model details

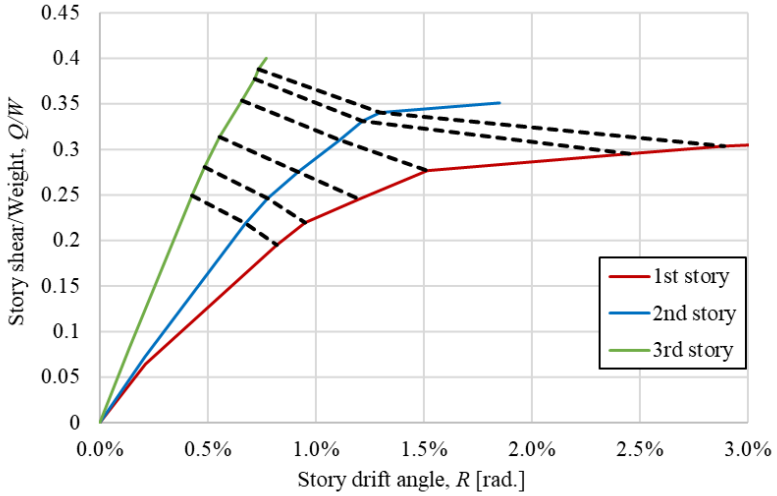

※ The dashed lines (-----) indicate the steps where the plastic hinges are formed

(b) Pushover analysis result

Figure D-16 Model 3-25-1.1

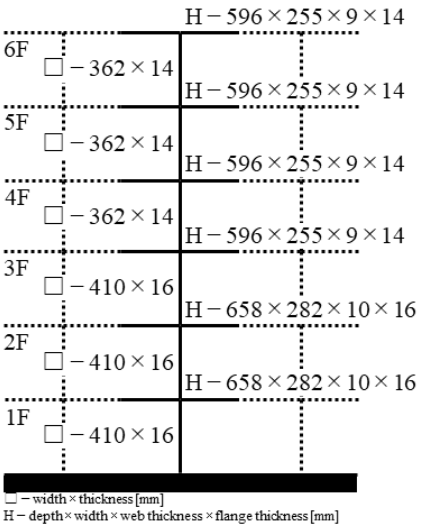

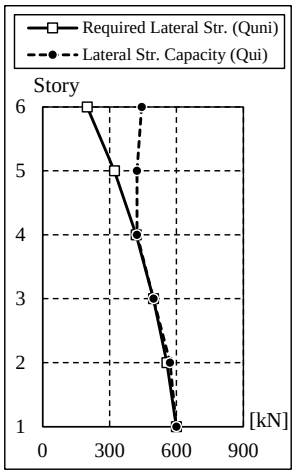

Column-to-Beam Moment Capacity Ratio			
Story	${}_cM_p$ [kN.m]	${}_bM_p$ [kN.m]	${}_cM_p/{}_bM_p$
6	848.8	740.3	-
5	836.0	740.3	1.14
4	814.8	740.3	1.11
3	1175.2	740.3	1.34
2	1141.4	999.5	1.16
1	1100.0	999.5	1.12

Natural Period	
1st Mode [sec.]	2nd Mode [sec.]
1.249	0.420

(a) Model details

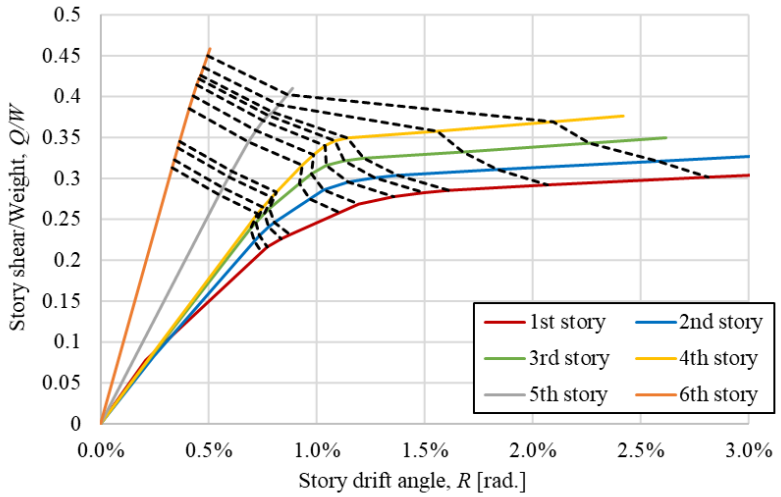

※ The dashed lines (-----) indicate the steps where the plastic hinges are formed

(b) Pushover analysis result

Figure D-17 Model 6-25-1.1

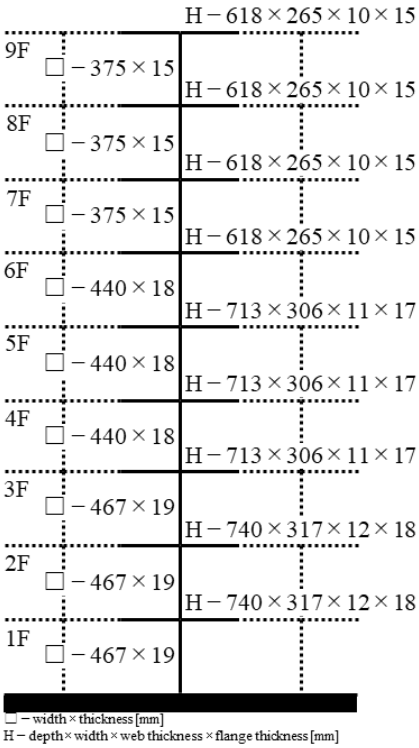

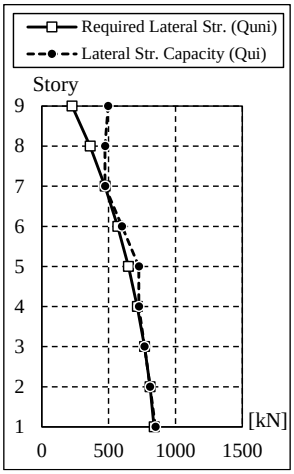

Column-to-Beam Moment Capacity Ratio			
Story	${}_cM_p$ [kN.m]	${}_bM_p$ [kN.m]	${}_cM_p/{}_bM_p$
9	944.5	828.2	-
8	932.1	828.2	1.13
7	911.6	828.2	1.11
6	1469.4	828.2	1.44
5	1437.9	1271.3	1.14
4	1399.3	1271.3	1.12
3	1666.2	1271.3	1.21
2	1616.7	1418.0	1.16
1	1560.6	1418.0	1.12

Natural Period	
1st Mode [sec.]	2nd Mode [sec.]
1.487	0.544

(a) Model details

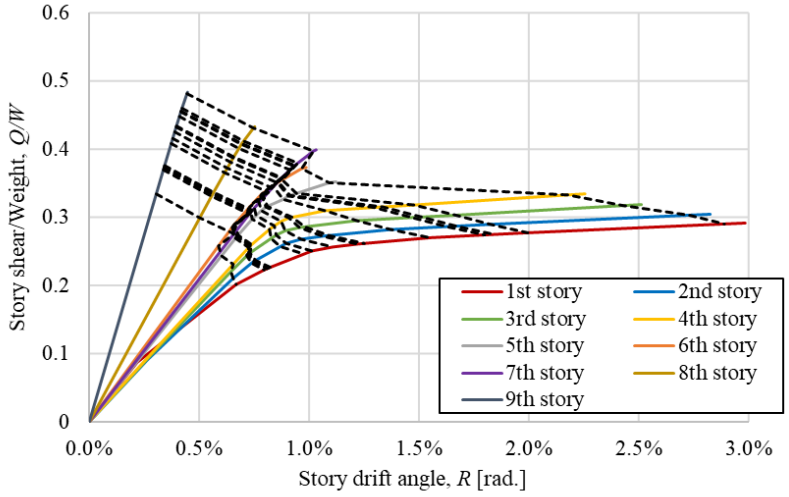

※ The dashed lines (-----) indicate the steps where the plastic hinges are formed

(b) Pushover analysis result

Figure D-18 Model 9-25-1.1

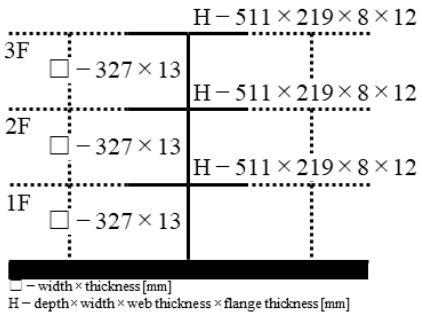

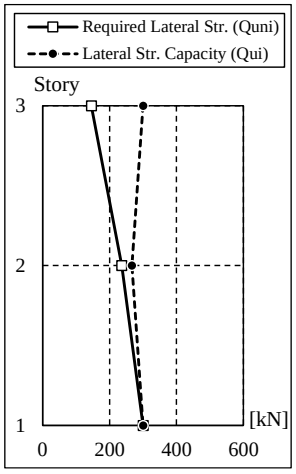

Column-to-Beam Moment Capacity Ratio			
Story	${}_cM_p$ [kN.m]	${}_bM_p$ [kN.m]	${}_cM_p/{}_bM_p$
3	621.4	466.6	-
2	607.2	466.6	1.32
1	583.6	466.6	1.28

Natural Period	
1st Mode [sec.]	2nd Mode [sec.]
0.938	0.287

(a) Model details

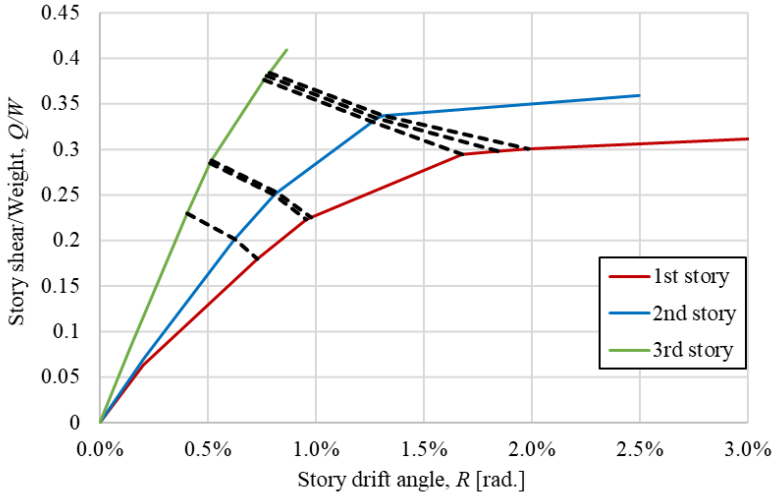

※ The dashed lines (-----) indicate the steps where the plastic hinges are formed

(b) Pushover analysis result

Figure D-19 Model 3-25-1.25

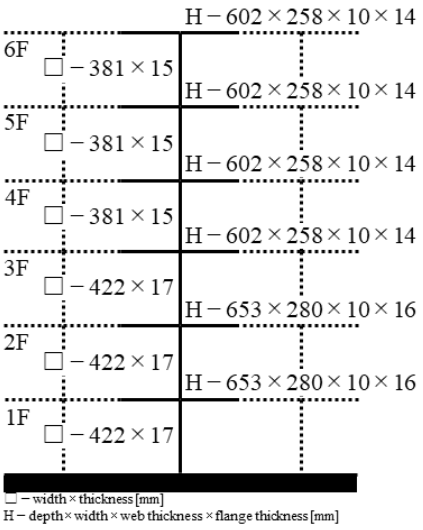

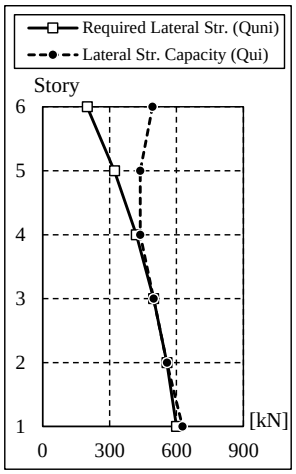

Column-to-Beam Moment Capacity Ratio			
Story	${}_cM_p$ [kN.m]	${}_bM_p$ [kN.m]	${}_cM_p/{}_bM_p$
6	989.5	765.3	-
5	977.4	765.3	1.29
4	957.1	765.3	1.26
3	1291.8	765.3	1.47
2	1258.9	974.5	1.31
1	1218.7	974.5	1.27

Natural Period	
1st Mode [sec.]	2nd Mode [sec.]
1.205	0.398

(a) Model details

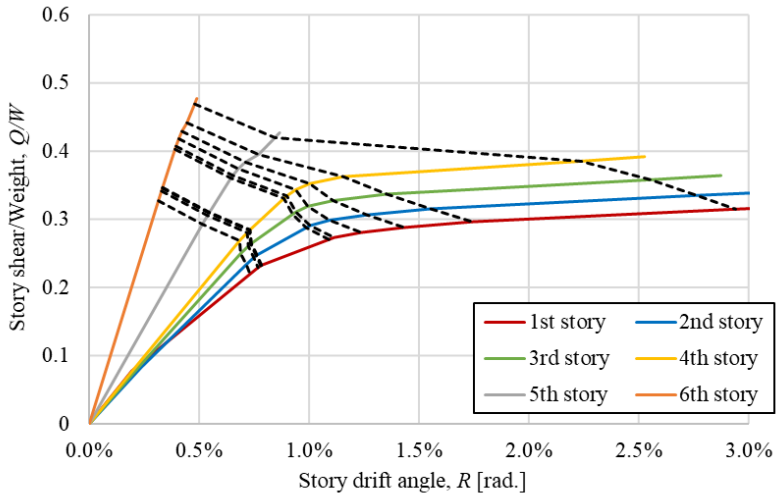

※ The dashed lines (-----) indicate the steps where the plastic hinges are formed

(b) Pushover analysis result

Figure D-20 Model 6-25-1.25

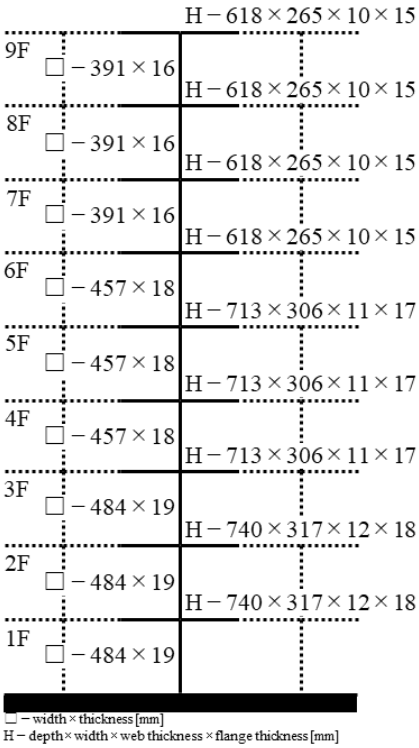

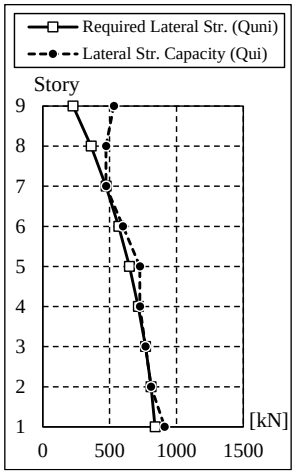

Column-to-Beam Moment Capacity Ratio			
Story	${}_cM_p$ [kN.m]	${}_bM_p$ [kN.m]	${}_cM_p/{}_bM_p$
9	1067.5	828.2	-
8	1055.6	828.2	1.28
7	1035.9	828.2	1.26
6	1657.6	828.2	1.63
5	1627.3	1271.3	1.29
4	1590.2	1271.3	1.27
3	1875.4	1271.3	1.36
2	1827.6	1418.0	1.31
1	1773.4	1418.0	1.27

Natural Period	
1st Mode [sec.]	2nd Mode [sec.]
1.439	0.523

(a) Model details

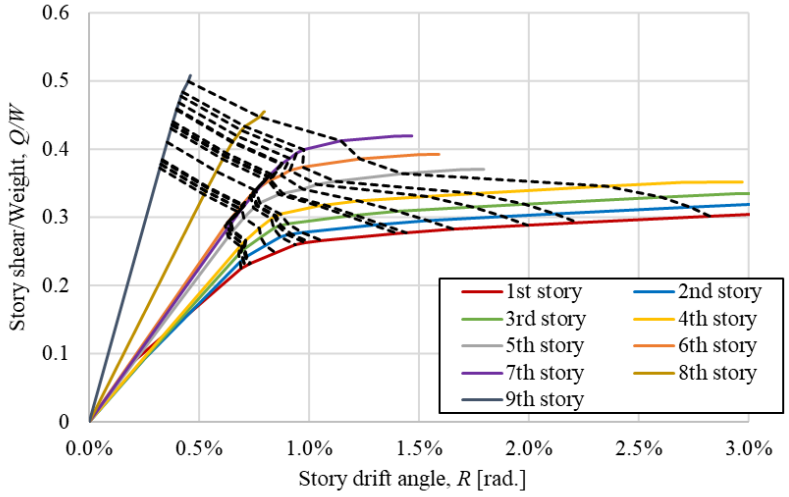

※ The dashed lines (-----) indicate the steps where the plastic hinges are formed

(b) Pushover analysis result

Figure D-21 Model 9-25-1.25

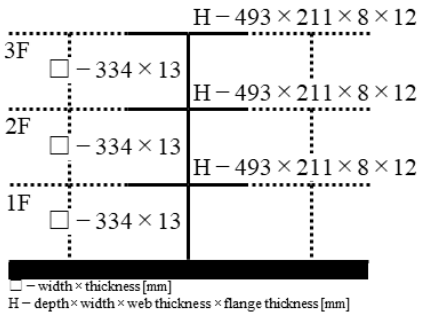

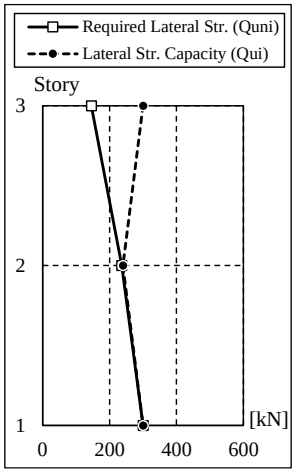

Column-to-Beam Moment Capacity Ratio			
Story	${}_cM_p$ [kN.m]	${}_bM_p$ [kN.m]	${}_cM_p/{}_bM_p$
3	667.2	420.3	-
2	653.4	420.3	1.57
1	630.3	420.3	1.53

Natural Period	
1st Mode [sec.]	2nd Mode [sec.]
0.938	0.282

(a) Model details

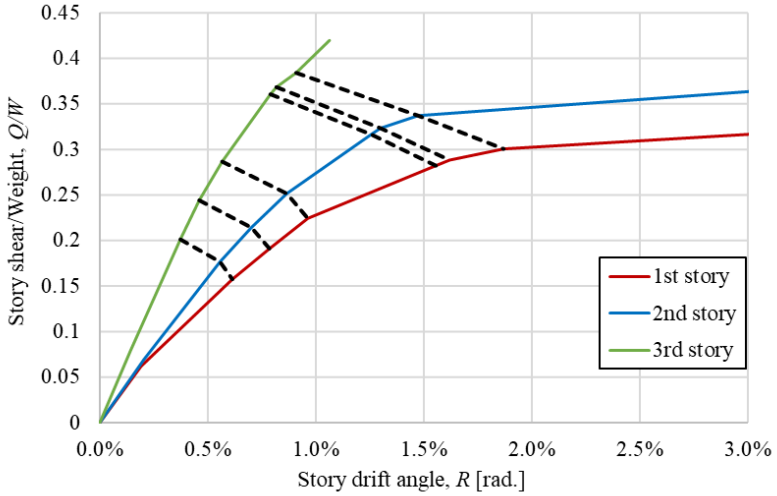

※ The dashed lines (-----) indicate the steps where the plastic hinges are formed

(b) Pushover analysis result

Figure D-22 Model 3-25-1.5

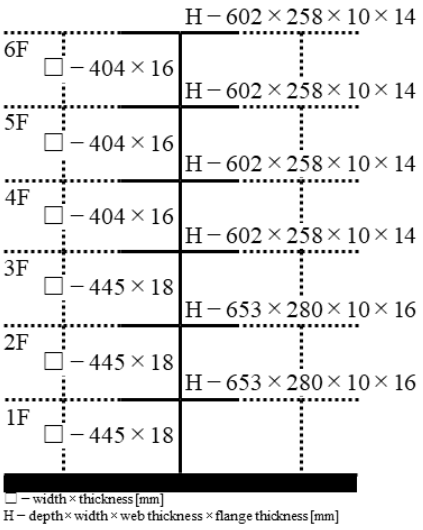

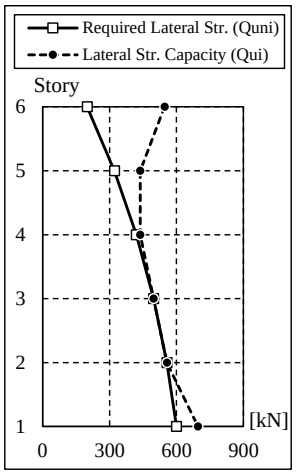

Column-to-Beam Moment Capacity Ratio			
Story	${}_cM_p$ [kN.m]	${}_bM_p$ [kN.m]	${}_cM_p/{}_bM_p$
6	1179.1	765.6	-
5	1167.7	765.6	1.53
4	1148.6	765.6	1.51
3	1531.7	765.6	1.75
2	1500.6	974.9	1.56
1	1462.5	974.9	1.52

Natural Period	
1st Mode [sec.]	2nd Mode [sec.]
1.144	0.373

(a) Model details

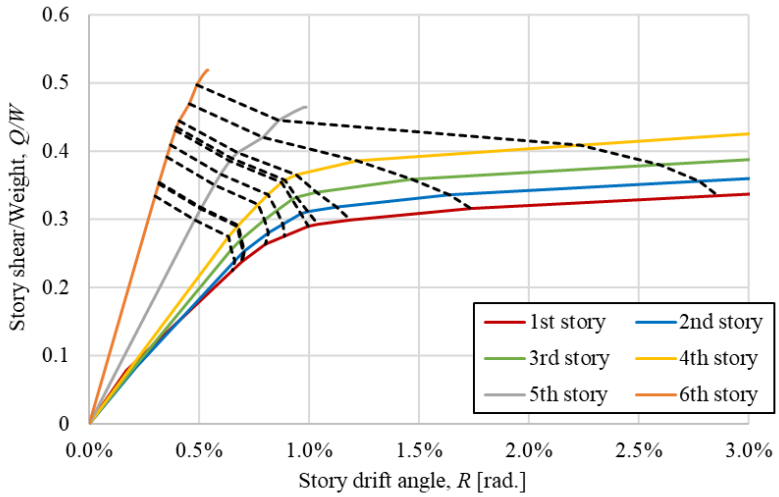

※ The dashed lines (-----) indicate the steps where the plastic hinges are formed

(b) Pushover analysis result

Figure D-23 Model 6-25-1.5

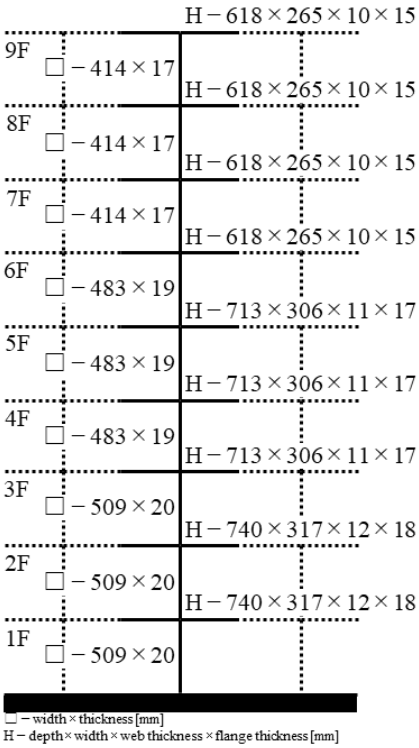

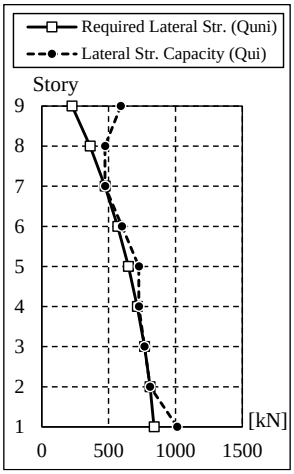

Column-to-Beam Moment Capacity Ratio			
Story	${}_cM_p$ [kN.m]	${}_bM_p$ [kN.m]	${}_cM_p/{}_bM_p$
9	1272.9	828.2	-
8	1261.7	828.2	1.53
7	1243.1	828.2	1.51
6	1972.1	828.2	1.94
5	1943.3	1271.3	1.54
4	1908.2	1271.3	1.51
3	2225.0	1271.3	1.63
2	2179.6	1418.0	1.55
1	2128.2	1418.0	1.52

Natural Period	
1st Mode [sec.]	2nd Mode [sec.]
1.376	0.495

(a) Model details

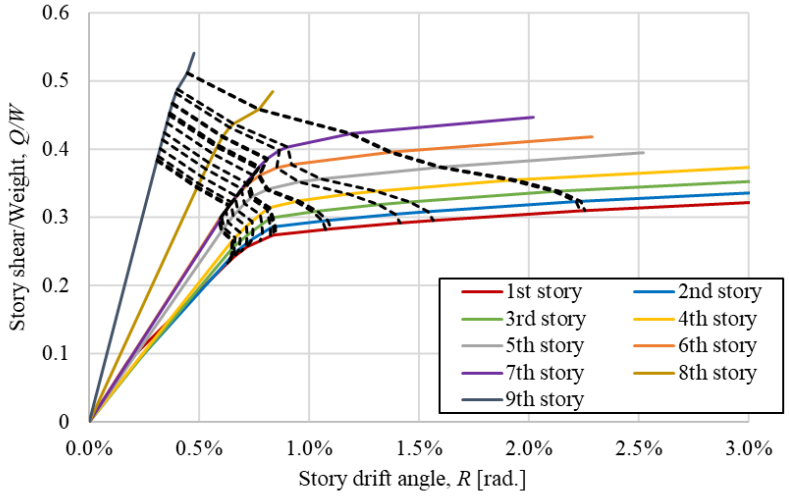

※ The dashed lines (-----) indicate the steps where the plastic hinges are formed

(b) Pushover analysis result

Figure D-24 Model 9-25-1.5

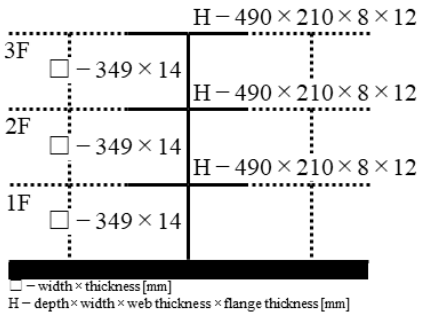

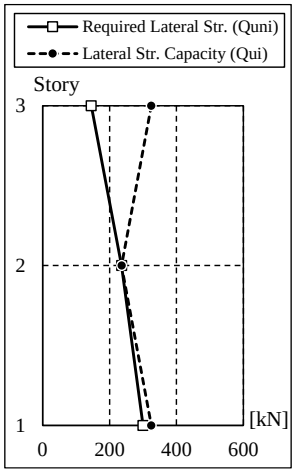

Column-to-Beam Moment Capacity Ratio			
Story	${}_cM_p$ [kN.m]	${}_bM_p$ [kN.m]	${}_cM_p/{}_bM_p$
3	759.0	413.3	-
2	745.7	413.3	1.82
1	723.6	413.3	1.78

Natural Period	
1st Mode [sec.]	2nd Mode [sec.]
0.897	0.266

(a) Model details

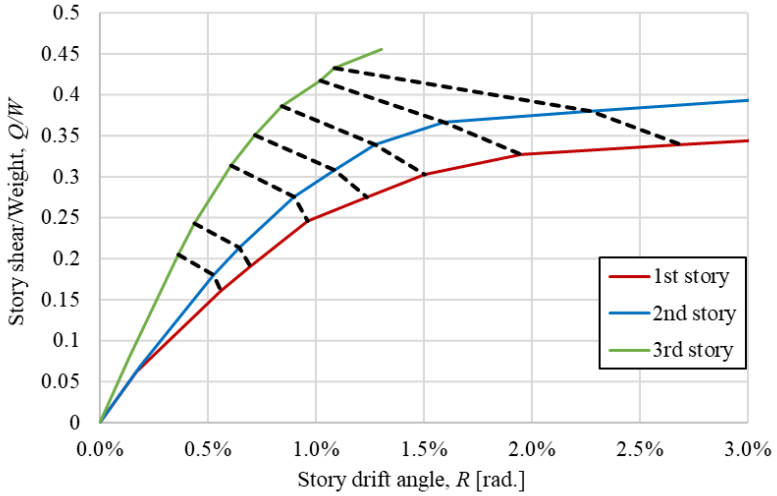

※ The dashed lines (-----) indicate the steps where the plastic hinges are formed

(b) Pushover analysis result

Figure D-25 Model 3-25-1.75

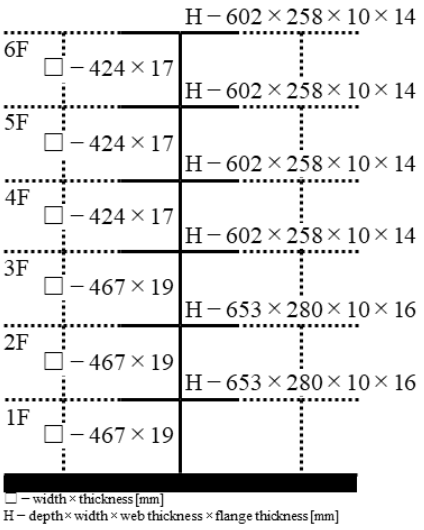

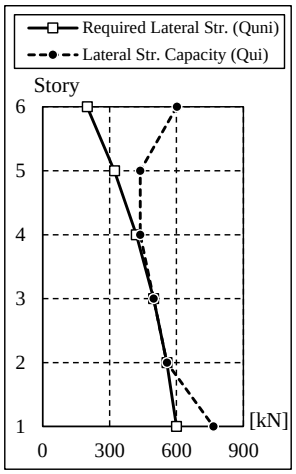

Column-to-Beam Moment Capacity Ratio			
Story	${}_cM_p$ [kN.m]	${}_bM_p$ [kN.m]	${}_cM_p/{}_bM_p$
6	1369.1	765.3	-
5	1358.2	765.3	1.78
4	1340.0	765.3	1.76
3	1772.4	765.3	2.03
2	1742.6	974.5	1.80
1	1706.3	974.5	1.77

Natural Period	
1st Mode [sec.]	2nd Mode [sec.]
1.097	0.354

(a) Model details

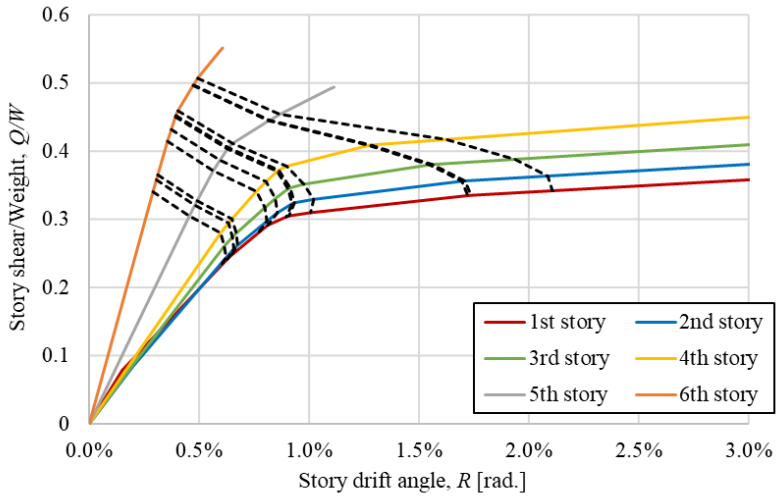

※ The dashed lines (-----) indicate the steps where the plastic hinges are formed

(b) Pushover analysis result

Figure D-26 Model 6-25-1.75

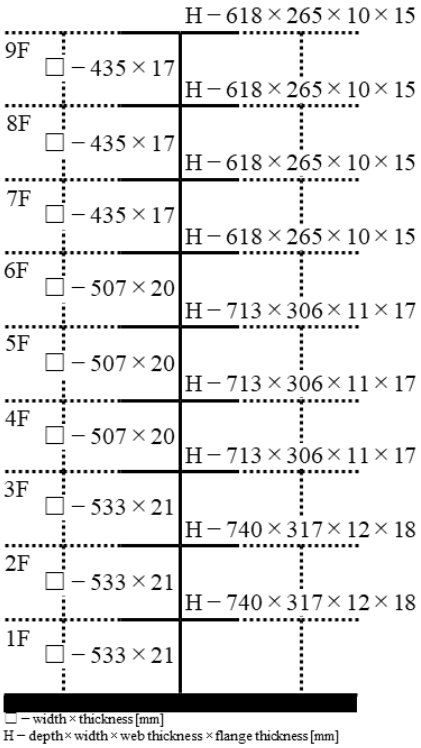

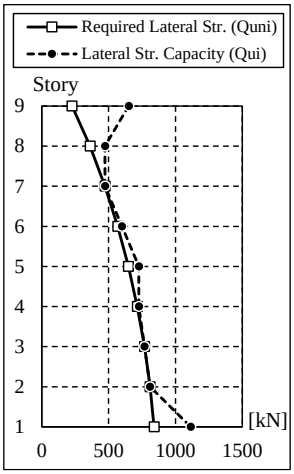

Column-to-Beam Moment Capacity Ratio			
Story	${}_cM_p$ [kN.m]	${}_bM_p$ [kN.m]	${}_cM_p/{}_bM_p$
9	1478.6	828.2	-
8	1468.0	828.2	1.78
7	1450.3	828.2	1.76
6	2287.1	828.2	2.26
5	2259.8	1271.3	1.79
4	2226.3	1271.3	1.76
3	2575.5	1271.3	1.89
2	2532.1	1418.0	1.80
1	2483.0	1418.0	1.77

Natural Period	
1st Mode [sec.]	2nd Mode [sec.]
1.326	0.473

(a) Model details

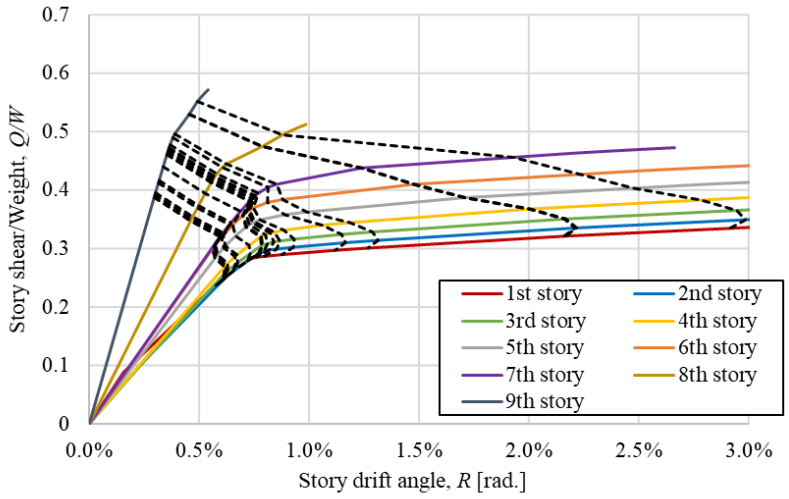

※ The dashed lines (-----) indicate the steps where the plastic hinges are formed

(b) Pushover analysis result

Figure D-27 Model 9-25-1.75

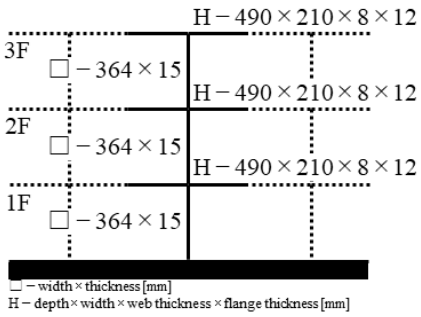

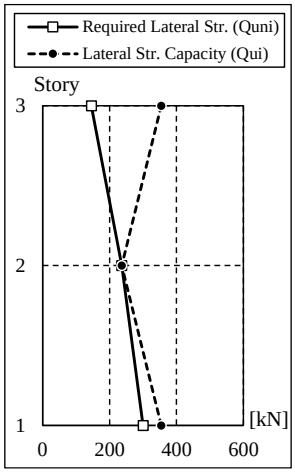

Column-to-Beam Moment Capacity Ratio			
Story	${}_cM_p$ [kN.m]	${}_bM_p$ [kN.m]	${}_cM_p/{}_bM_p$
3	860.9	413.3	-
2	848.2	413.3	2.07
1	827.0	413.3	2.03

Natural Period	
1st Mode [sec.]	2nd Mode [sec.]
0.856	0.250

(a) Model details

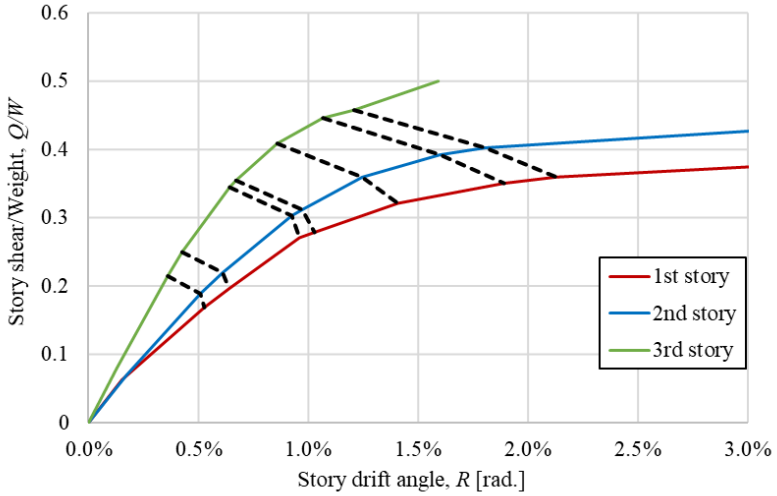

※ The dashed lines (-----) indicate the steps where the plastic hinges are formed

(b) Pushover analysis result

Figure D-28 Model 3-25-2.0

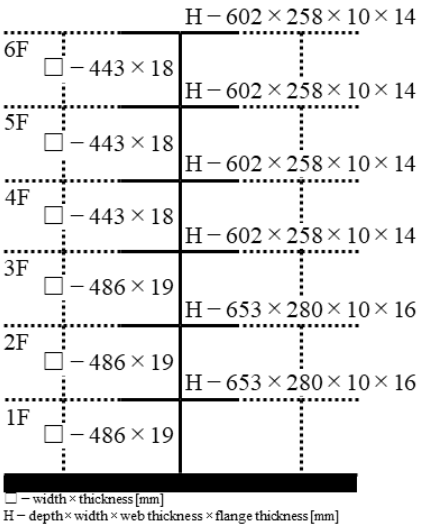

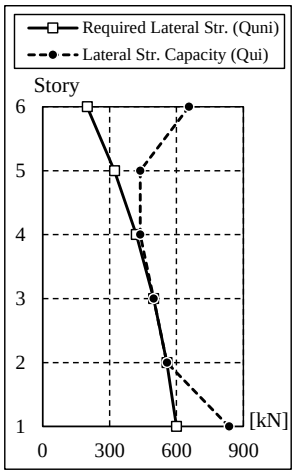

Column-to-Beam Moment Capacity Ratio			
Story	${}_cM_p$ [kN.m]	${}_bM_p$ [kN.m]	${}_cM_p/{}_bM_p$
6	1559.3	765.3	-
5	1548.9	765.3	2.03
4	1531.5	765.3	2.01
3	2013.5	765.3	2.32
2	1985.0	974.5	2.05
1	1950.1	974.5	2.02

Natural Period	
1st Mode [sec.]	2nd Mode [sec.]
1.059	0.338

(a) Model details

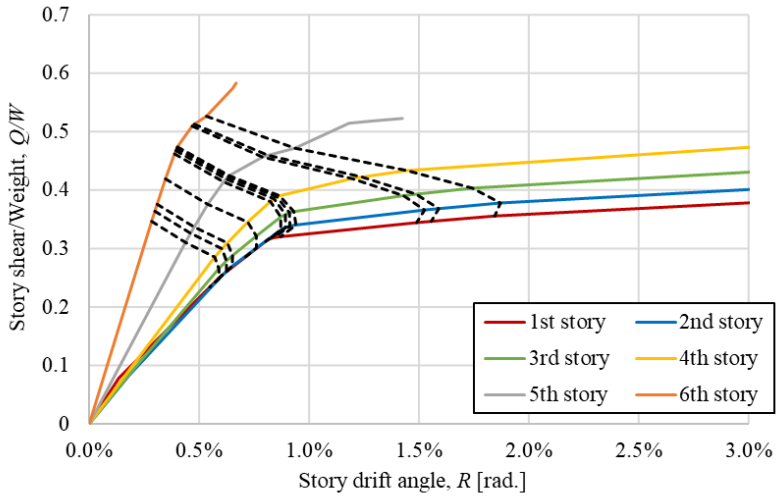

※ The dashed lines (-----) indicate the steps where the plastic hinges are formed

(b) Pushover analysis result

Figure D-29 Model 6-25-2.0

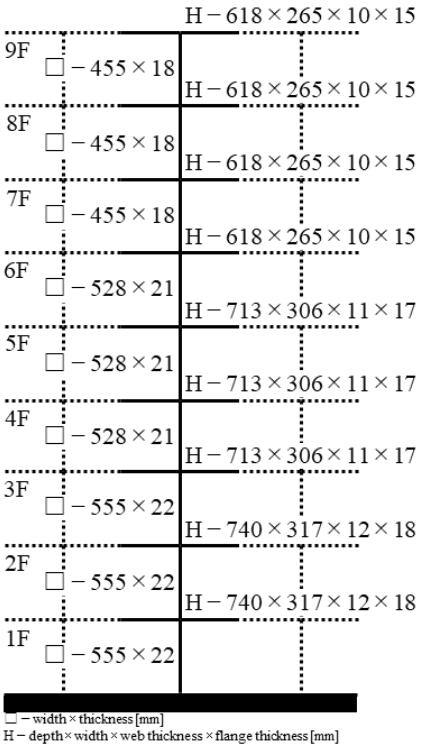

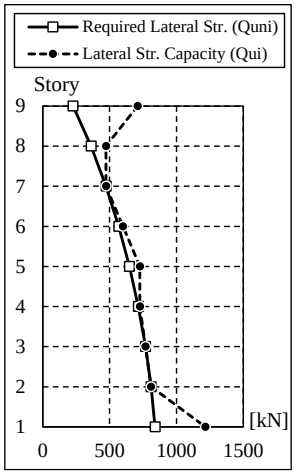

Column-to-Beam Moment Capacity Ratio

Story	${}_cM_p$ [kN.m]	${}_bM_p$ [kN.m]	${}_cM_p/{}_bM_p$
9	1684.6	828.2	-
8	1674.5	828.2	2.03
7	1657.5	828.2	2.01
6	2602.7	828.2	2.57
5	2576.4	1271.3	2.04
4	2544.4	1271.3	2.01
3	2926.7	1271.3	2.15
2	2885.0	1418.0	2.05
1	2837.7	1418.0	2.02

Natural Period

1st Mode [sec.]	2nd Mode [sec.]
1.286	0.455

(a) Model details

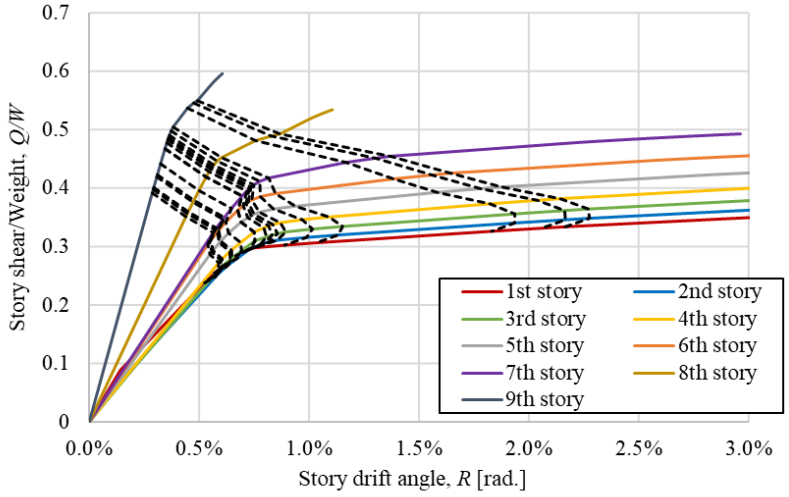

※ The dashed lines (-----) indicate the steps where the plastic hinges are formed

(b) Pushover analysis result

Figure D-30 Model 9-25-2.0

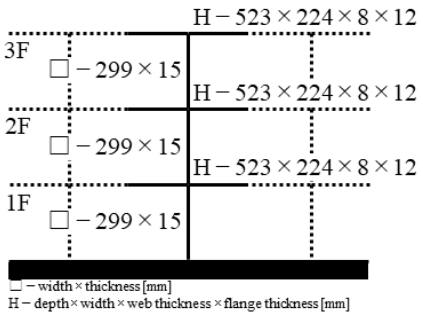

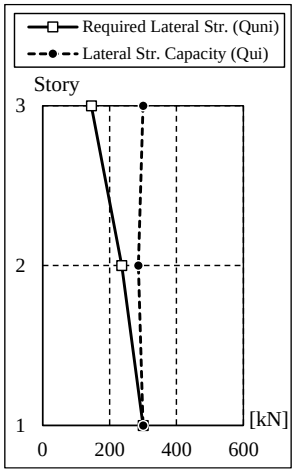

Column-to-Beam Moment Capacity Ratio			
Story	${}_cM_p$ [kN.m]	${}_bM_p$ [kN.m]	${}_cM_p/{}_bM_p$
3	583.0	500.5	-
2	570.6	500.5	1.15
1	550.0	500.5	1.12

Natural Period	
1st Mode [sec.]	2nd Mode [sec.]
0.962	0.299

(a) Model details

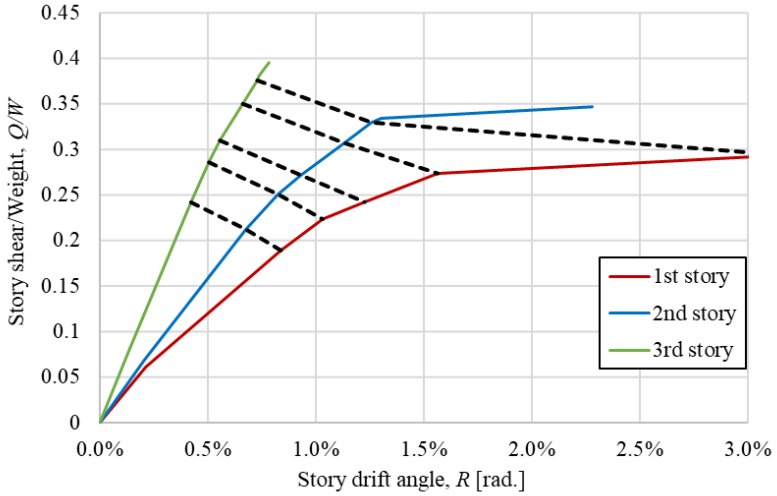

※ The dashed lines (-----) indicate the steps where the plastic hinges are formed

(b) Pushover analysis result

Figure D-31 Model 3-20-1.1

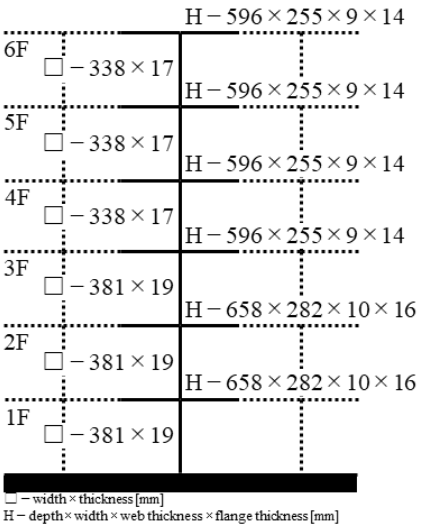

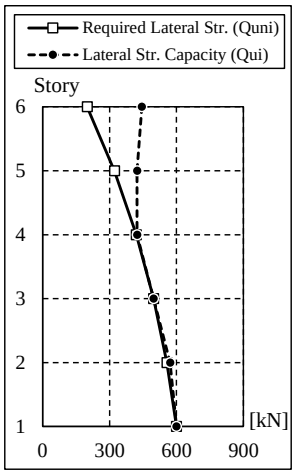

Column-to-Beam Moment Capacity Ratio			
Story	${}_cM_p$ [kN.m]	${}_bM_p$ [kN.m]	${}_cM_p/{}_bM_p$
6	843.5	740.3	-
5	832.6	740.3	1.13
4	814.3	740.3	1.11
3	1164.2	740.3	1.34
2	1135.0	999.5	1.15
1	1099.4	999.5	1.12

Natural Period	
1st Mode [sec.]	2nd Mode [sec.]
1.268	0.428

(a) Model details

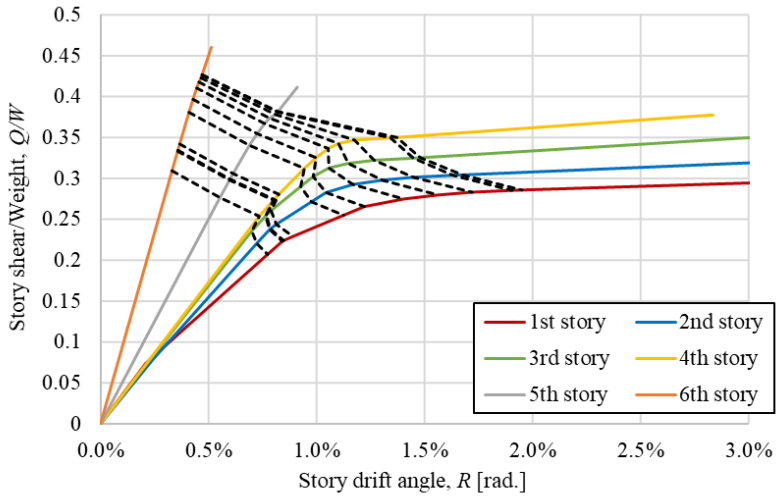

※ The dashed lines (-----) indicate the steps where the plastic hinges are formed

(b) Pushover analysis result

Figure D-32 Model 6-20-1.1

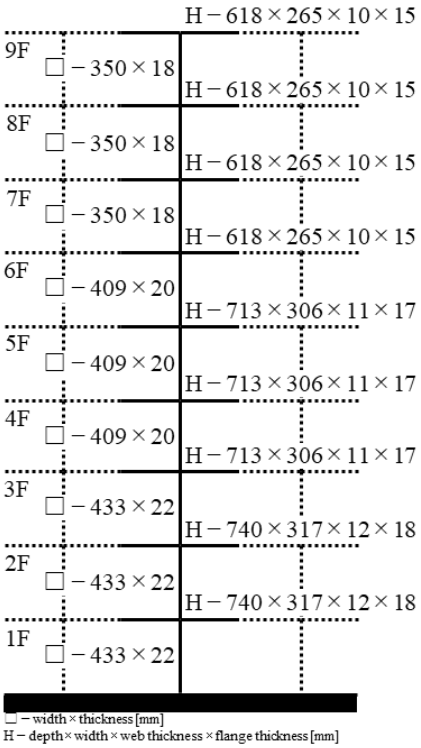

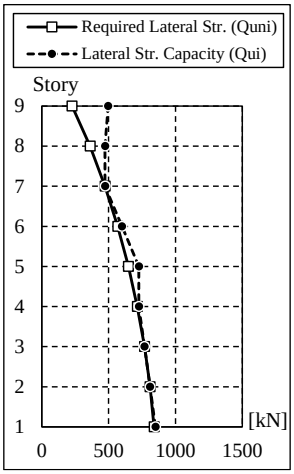

Column-to-Beam Moment Capacity Ratio			
Story	${}_cM_p$ [kN.m]	${}_bM_p$ [kN.m]	${}_cM_p/{}_bM_p$
9	939.3	828.2	-
8	928.7	828.2	1.13
7	911.1	828.2	1.11
6	1458.8	828.2	1.43
5	1431.7	1271.3	1.14
4	1398.5	1271.3	1.11
3	1650.9	1271.3	1.20
2	1608.2	1418.0	1.15
1	1559.8	1418.0	1.12

Natural Period	
1st Mode [sec.]	2nd Mode [sec.]
1.505	0.552

(a) Model details

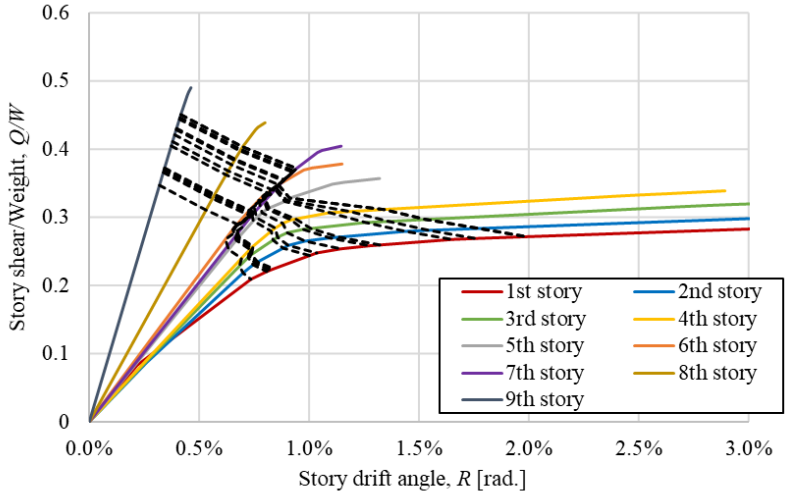

※ The dashed lines (-----) indicate the steps where the plastic hinges are formed

(b) Pushover analysis result

Figure D-33 Model 9-20-1.1

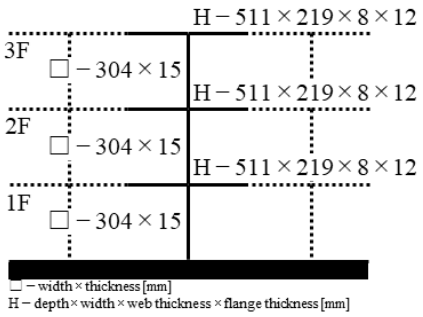

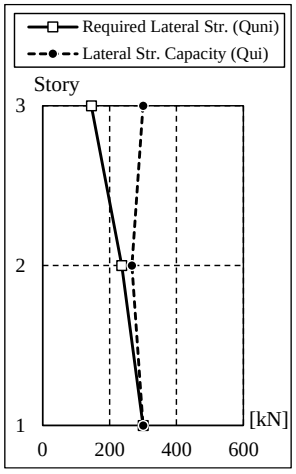

Column-to-Beam Moment Capacity Ratio			
Story	${}_cM_p$ [kN.m]	${}_bM_p$ [kN.m]	${}_cM_p/{}_bM_p$
3	615.8	466.6	-
2	603.6	466.6	1.31
1	583.3	466.6	1.27

Natural Period	
1st Mode [sec.]	2nd Mode [sec.]
0.957	0.295

(a) Model details

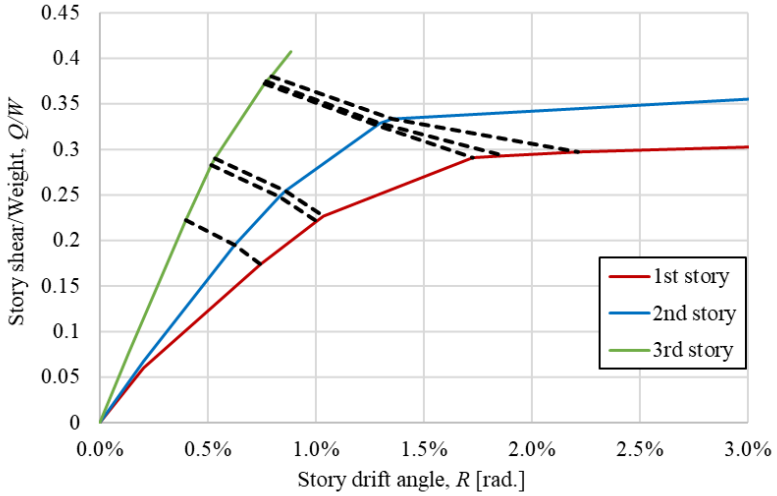

※ The dashed lines (-----) indicate the steps where the plastic hinges are formed

(b) Pushover analysis result

Figure D-34 Model 3-20-1.25

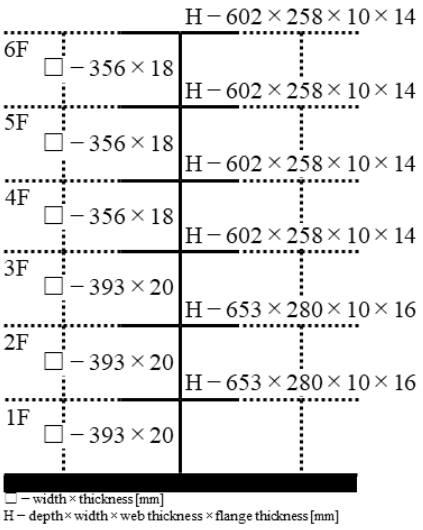

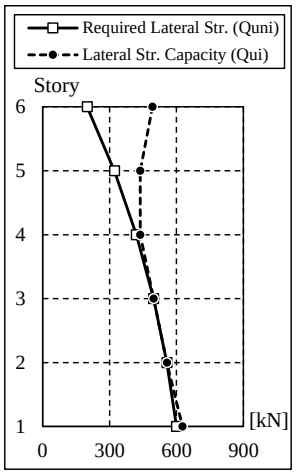

Column-to-Beam Moment Capacity Ratio			
Story	${}_cM_p$ [kN.m]	${}_bM_p$ [kN.m]	${}_cM_p/{}_bM_p$
6	984.3	765.3	-
5	973.9	765.3	1.28
4	956.6	765.3	1.26
3	1280.9	765.3	1.46
2	1252.6	974.5	1.30
1	1218.1	974.5	1.27

Natural Period	
1st Mode [sec.]	2nd Mode [sec.]
1.221	0.406

(a) Model details

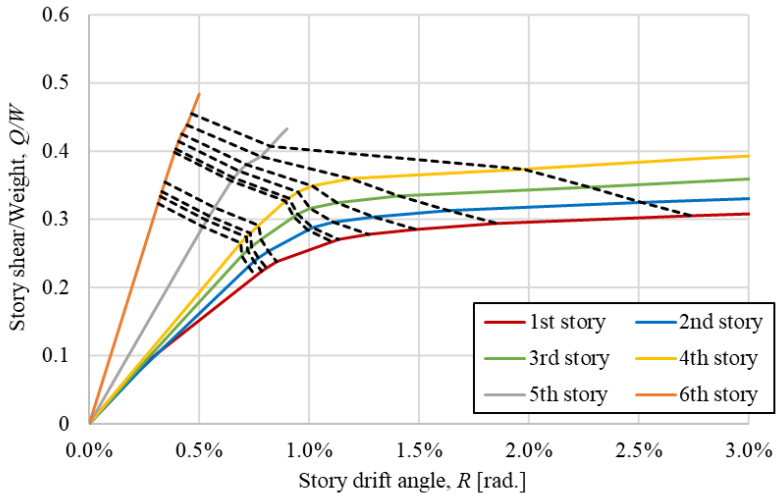

※ The dashed lines (-----) indicate the steps where the plastic hinges are formed

(b) Pushover analysis result

Figure D-35 Model 6-20-1.25

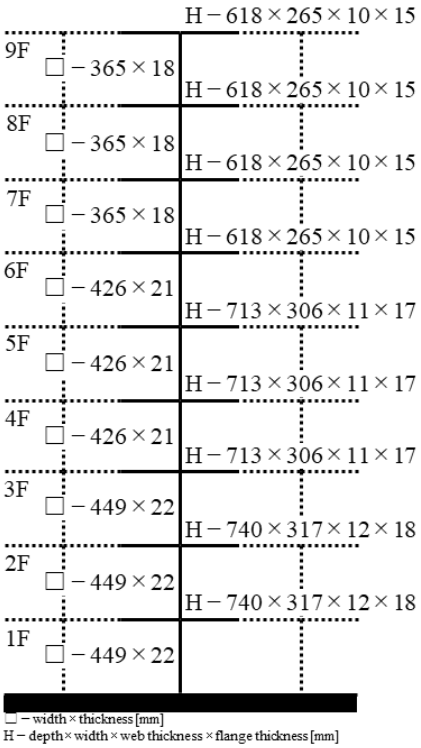

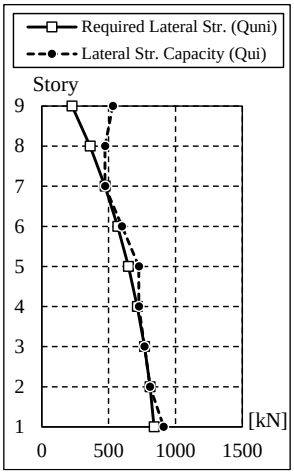

Column-to-Beam Moment Capacity Ratio			
Story	${}_cM_p$ [kN.m]	${}_bM_p$ [kN.m]	${}_cM_p/{}_bM_p$
9	1062.4	828.2	-
8	1052.2	828.2	1.28
7	1035.3	828.2	1.26
6	1647.3	828.2	1.62
5	1621.2	1271.3	1.29
4	1589.3	1271.3	1.26
3	1860.4	1271.3	1.36
2	1819.2	1418.0	1.30
1	1772.5	1418.0	1.27

Natural Period	
1st Mode [sec.]	2nd Mode [sec.]
1.455	0.530

(a) Model details

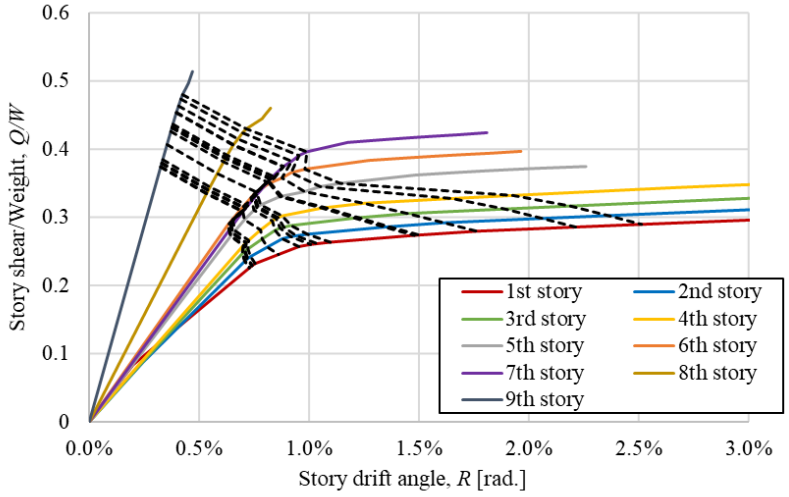

※ The dashed lines (-----) indicate the steps where the plastic hinges are formed

(b) Pushover analysis result

Figure D-36 Model 9-20-1.25

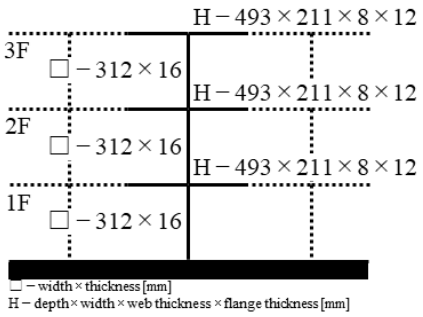

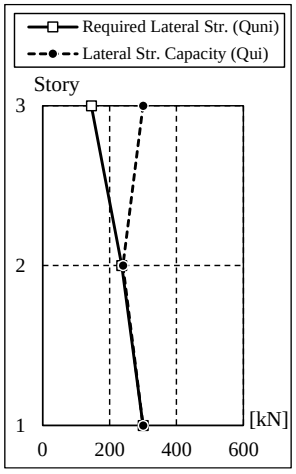

Column-to-Beam Moment Capacity Ratio			
Story	${}_cM_p$ [kN.m]	${}_bM_p$ [kN.m]	${}_cM_p/{}_bM_p$
3	661.7	420.3	-
2	649.8	420.3	1.56
1	630.0	420.3	1.52

Natural Period	
1st Mode [sec.]	2nd Mode [sec.]
0.957	0.290

(a) Model details

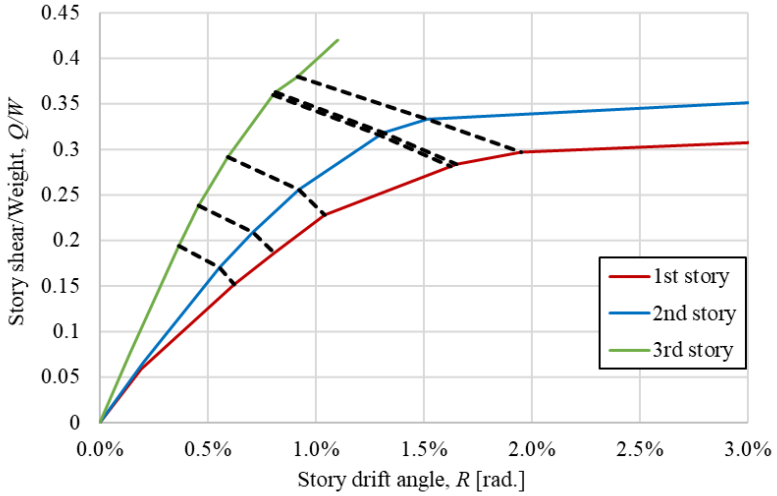

※ The dashed lines (-----) indicate the steps where the plastic hinges are formed

(b) Pushover analysis result

Figure D-37 Model 3-20-1.5

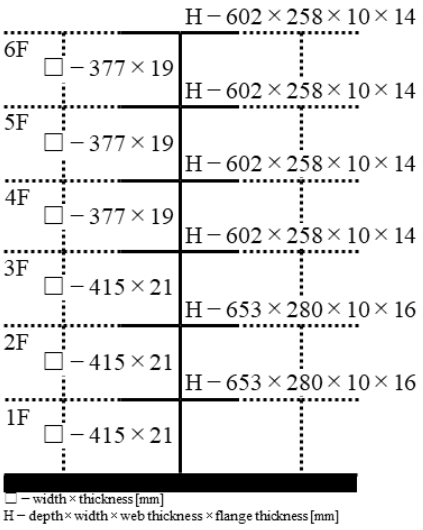

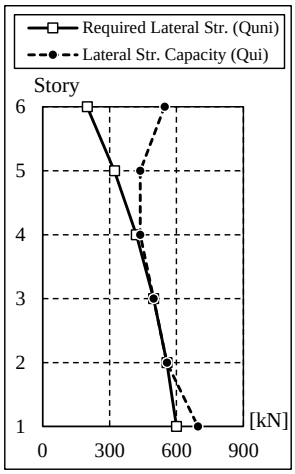

Column-to-Beam Moment Capacity Ratio			
Story	${}_cM_p$ [kN.m]	${}_bM_p$ [kN.m]	${}_cM_p/{}_bM_p$
6	1174.1	765.6	-
5	1164.3	765.6	1.53
4	1147.9	765.6	1.51
3	1521.2	765.6	1.74
2	1494.4	974.9	1.55
1	1461.7	974.9	1.52

Natural Period	
1st Mode [sec.]	2nd Mode [sec.]
1.158	0.380

(a) Model details

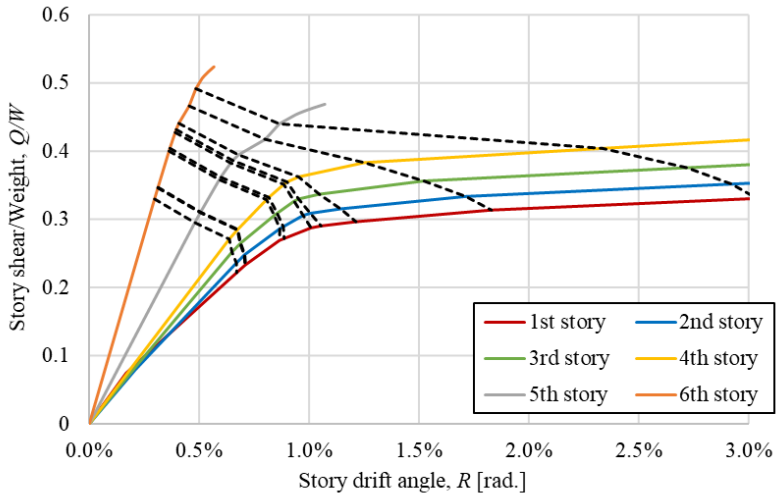

※ The dashed lines (-----) indicate the steps where the plastic hinges are formed

(b) Pushover analysis result

Figure D-38 Model 6-20-1.5

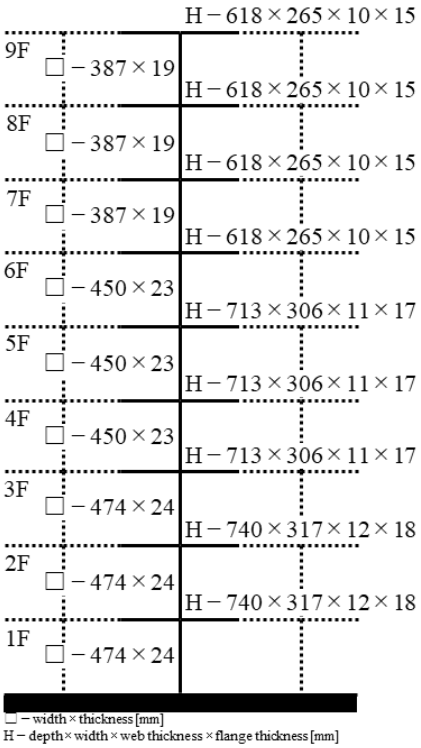

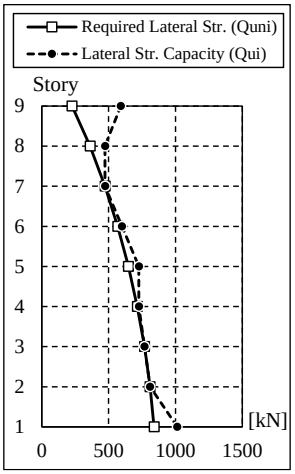

Column-to-Beam Moment Capacity Ratio			
Story	${}_cM_p$ [kN.m]	${}_bM_p$ [kN.m]	${}_cM_p/{}_bM_p$
9	1267.9	828.2	-
8	1258.3	828.2	1.53
7	1242.4	828.2	1.51
6	1961.9	828.2	1.93
5	1937.3	1271.3	1.53
4	1907.1	1271.3	1.51
3	2210.4	1271.3	1.62
2	2171.3	1418.0	1.55
1	2127.1	1418.0	1.52

Natural Period	
1st Mode [sec.]	2nd Mode [sec.]
1.389	0.501

(a) Model details

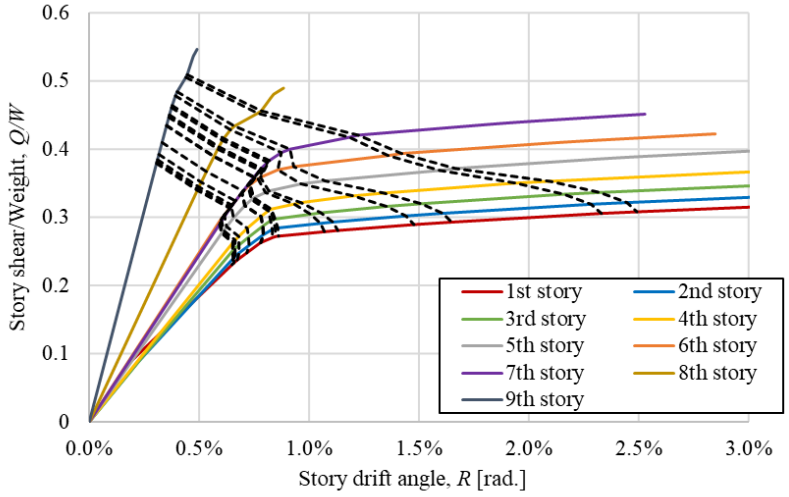

※ The dashed lines (-----) indicate the steps where the plastic hinges are formed

(b) Pushover analysis result

Figure D-39 Model 9-20-1.5

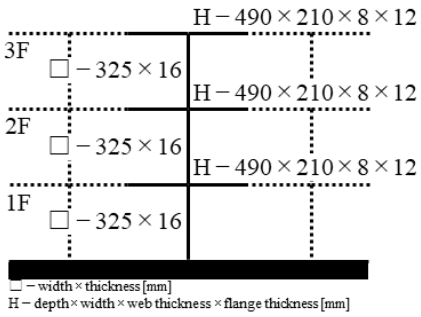

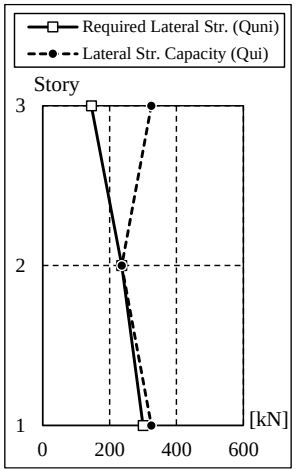

Column-to-Beam Moment Capacity Ratio			
Story	${}_cM_p$ [kN.m]	${}_bM_p$ [kN.m]	${}_cM_p/{}_bM_p$
3	753.5	413.3	-
2	742.2	413.3	1.81
1	723.2	413.3	1.77

Natural Period	
1st Mode [sec.]	2nd Mode [sec.]
0.914	0.273

(a) Model details

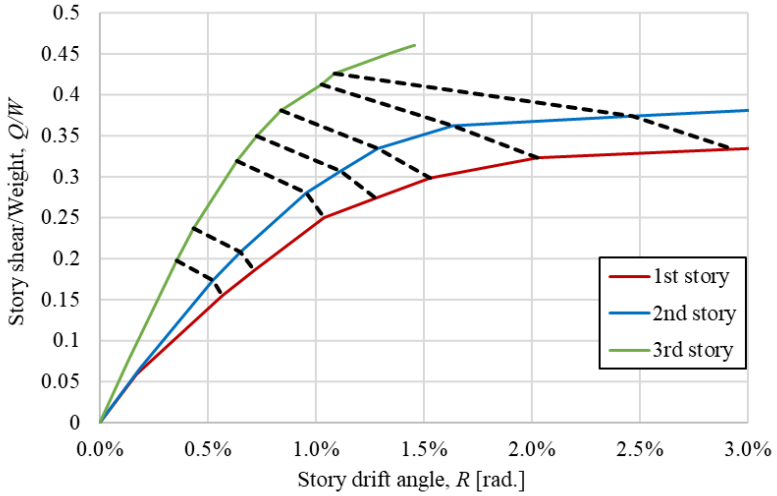

※ The dashed lines (-----) indicate the steps where the plastic hinges are formed

(b) Pushover analysis result

Figure D-40 Model 3-20-1.75

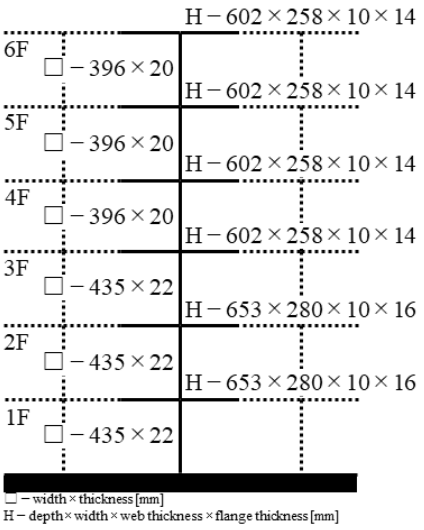

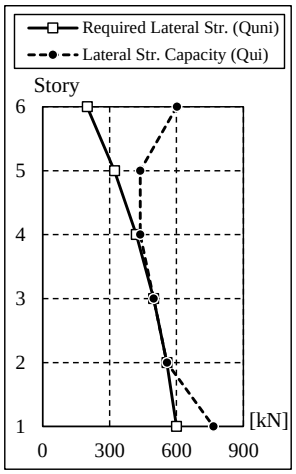

Column-to-Beam Moment Capacity Ratio			
Story	${}_cM_p$ [kN.m]	${}_bM_p$ [kN.m]	${}_cM_p/{}_bM_p$
6	1364.1	765.3	-
5	1354.8	765.3	1.78
4	1339.2	765.3	1.76
3	1762.1	765.3	2.03
2	1736.6	974.5	1.80
1	1705.3	974.5	1.77

Natural Period	
1st Mode [sec.]	2nd Mode [sec.]
1.110	0.360

(a) Model details

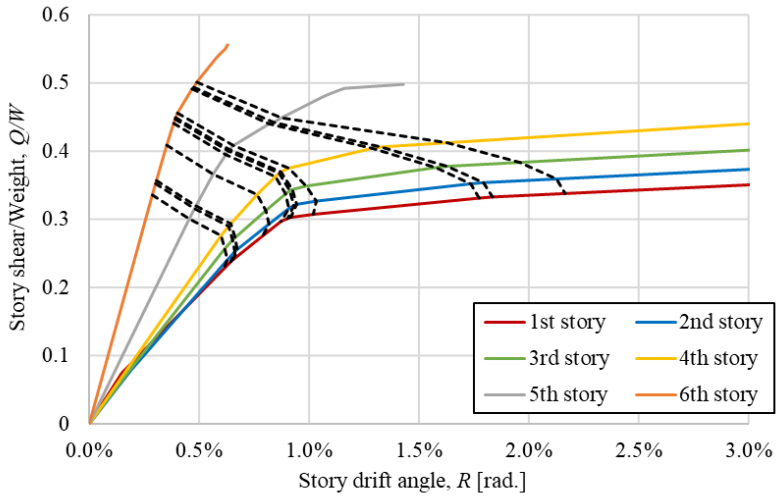

※ The dashed lines (-----) indicate the steps where the plastic hinges are formed

(b) Pushover analysis result

Figure D-41 Model 6-20-1.75

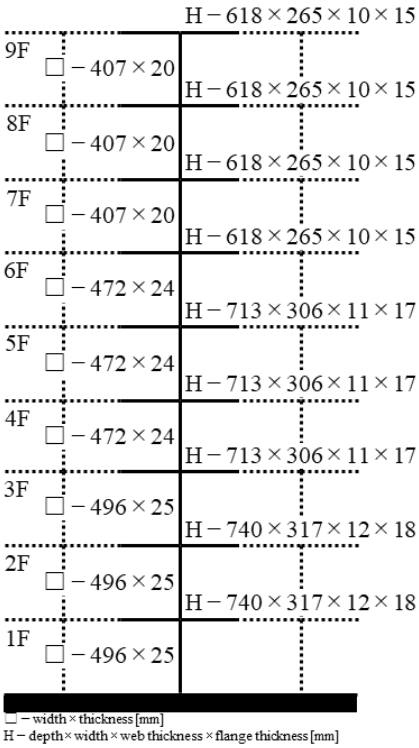

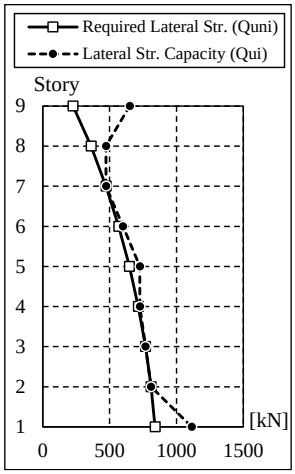

Column-to-Beam Moment Capacity Ratio			
Story	${}_cM_p$ [kN.m]	${}_bM_p$ [kN.m]	${}_cM_p/{}_bM_p$
9	1473.7	828.2	-
8	1464.6	828.2	1.77
7	1449.4	828.2	1.76
6	2277.2	828.2	2.25
5	2253.7	1271.3	1.78
4	2225.0	1271.3	1.76
3	2561.2	1271.3	1.88
2	2523.9	1418.0	1.79
1	2481.6	1418.0	1.76

Natural Period	
1st Mode [sec.]	2nd Mode [sec.]
1.338	0.479

(a) Model details

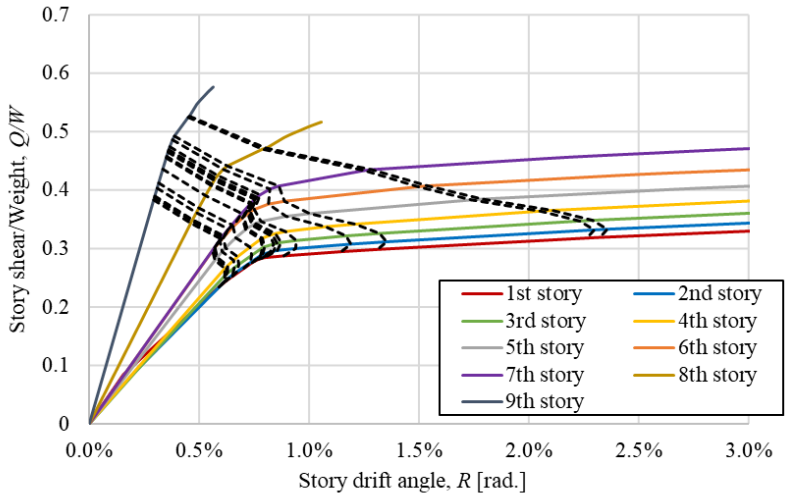

※ The dashed lines (-----) indicate the steps where the plastic hinges are formed

(b) Pushover analysis result

Figure D-42 Model 9-20-1.75

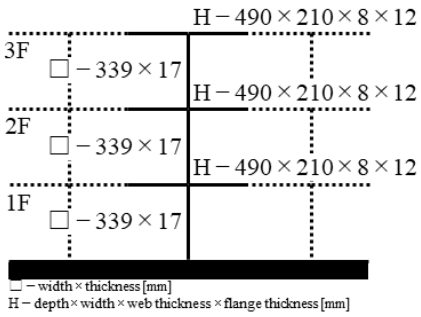

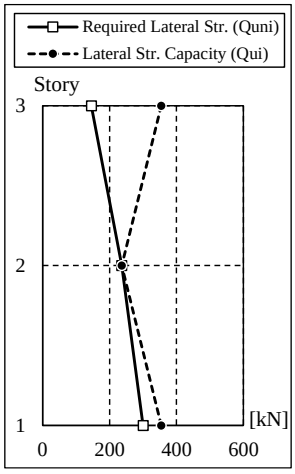

Column-to-Beam Moment Capacity Ratio			
Story	${}_cM_p$ [kN.m]	${}_bM_p$ [kN.m]	${}_cM_p/{}_bM_p$
3	855.6	413.3	-
2	844.7	413.3	2.06
1	826.5	413.3	2.02
Natural Period			
1st Mode [sec.]		2nd Mode [sec.]	
0.872		0.257	

(a) Model details

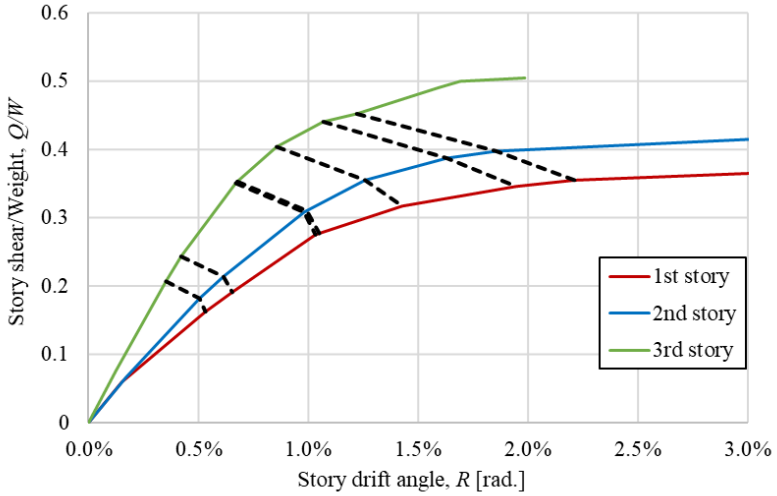

※ The dashed lines (-----) indicate the steps where the plastic hinges are formed

(b) Pushover analysis result

Figure D-43 Model 3-20-2.0

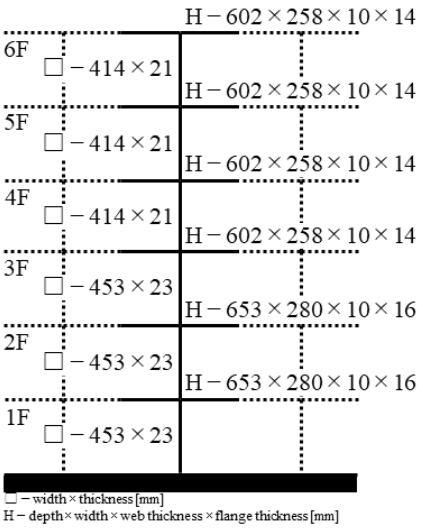

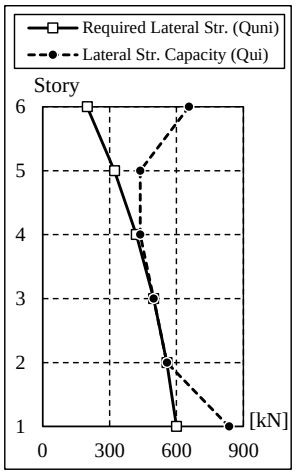

Column-to-Beam Moment Capacity Ratio			
Story	${}_cM_p$ [kN.m]	${}_bM_p$ [kN.m]	${}_cM_p/{}_bM_p$
6	1554.4	765.3	-
5	1545.4	765.3	2.03
4	1530.5	765.3	2.01
3	2003.4	765.3	2.31
2	1978.9	974.5	2.04
1	1949.0	974.5	2.02

Natural Period	
1st Mode [sec.]	2nd Mode [sec.]
1.070	0.343

(a) Model details

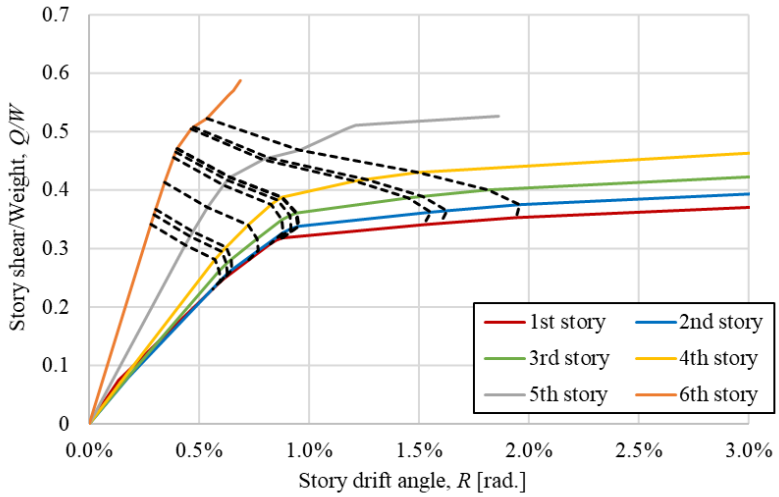

※ The dashed lines (-----) indicate the steps where the plastic hinges are formed

(b) Pushover analysis result

Figure D-44 Model 6-20-2.0

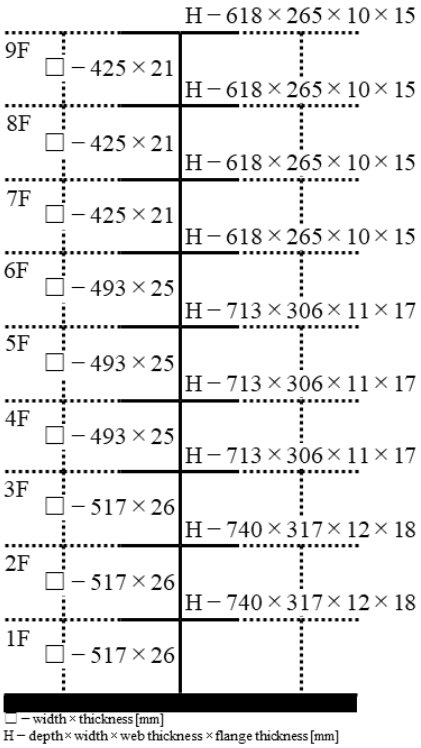

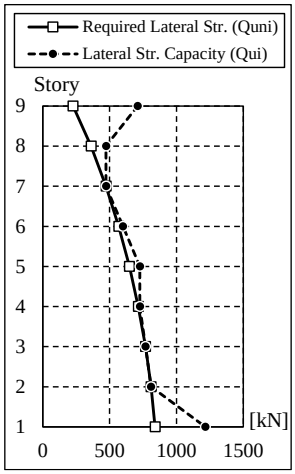

Column-to-Beam Moment Capacity Ratio			
Story	${}_cM_p$ [kN.m]	${}_bM_p$ [kN.m]	${}_cM_p/{}_bM_p$
9	1679.7	828.2	-
8	1671.0	828.2	2.02
7	1656.5	828.2	2.01
6	2592.9	828.2	2.57
5	2570.4	1271.3	2.03
4	2542.9	1271.3	2.01
3	2912.6	1271.3	2.15
2	2876.7	1418.0	2.04
1	2836.1	1418.0	2.01

Natural Period	
1st Mode [sec.]	2nd Mode [sec.]
1.297	0.460

(a) Model details

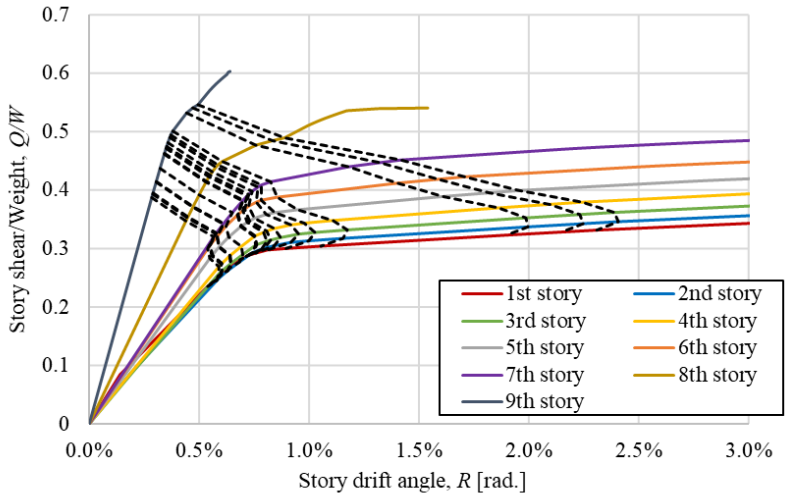

※ The dashed lines (-----) indicate the steps where the plastic hinges are formed

(b) Pushover analysis result

Figure D-45 Model 9-20-2.0

Appendix E Non-deterioration Margin and Deterioration Index of Deteriorated SMRF Models

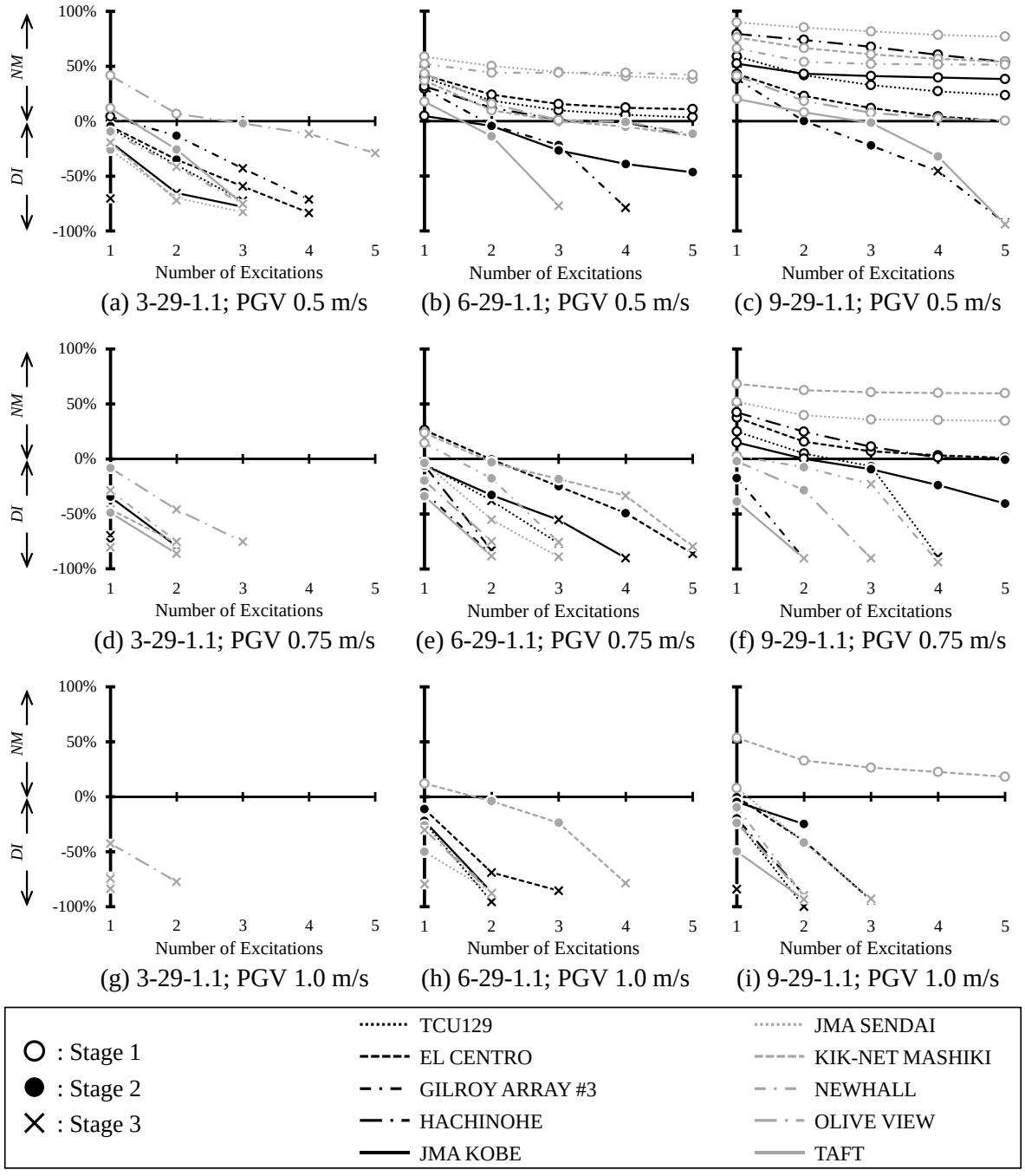

Figure E-1 Non-deterioration margin and deterioration index of A-29-1.1 series models

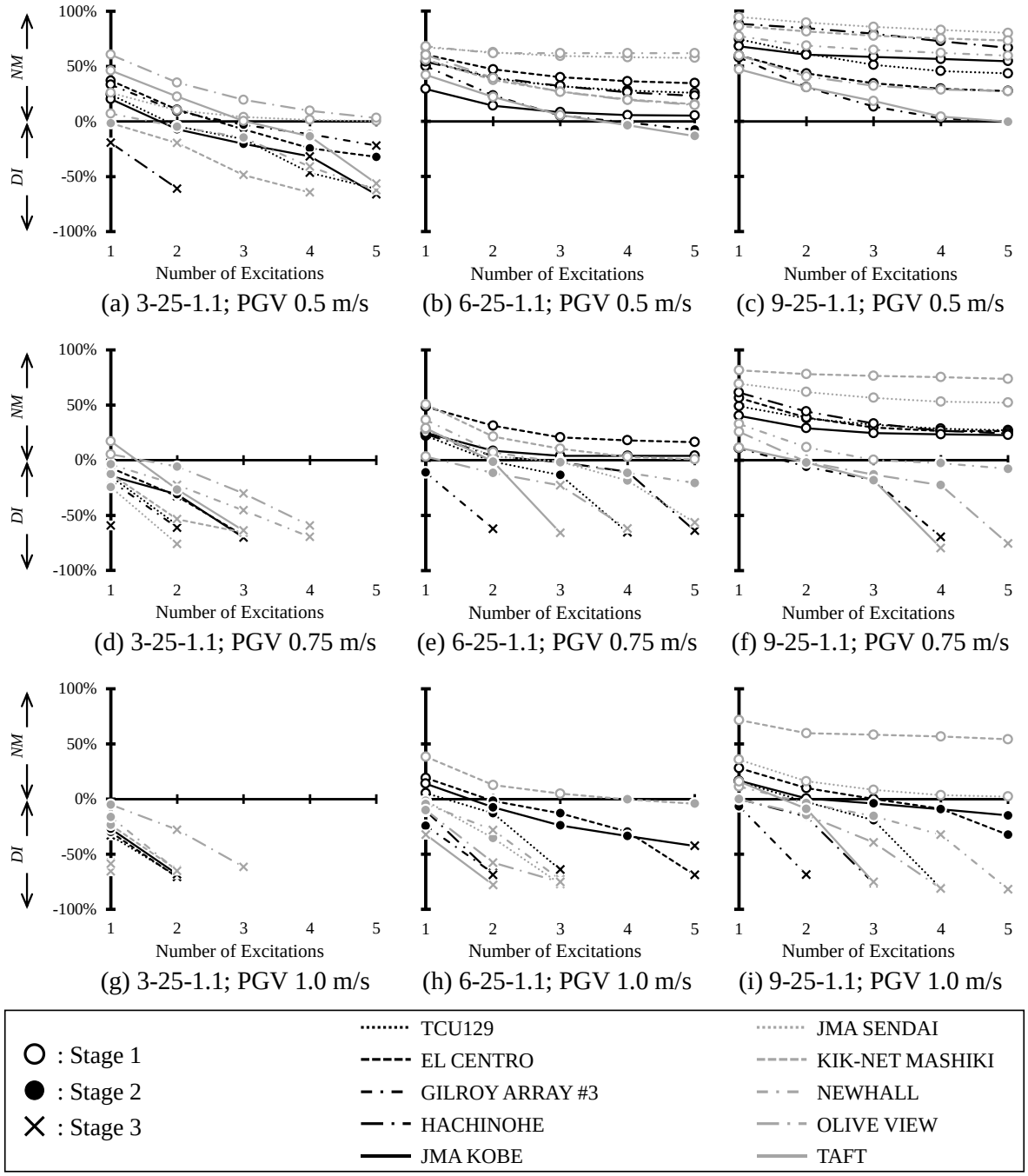

Figure E-2 Non-deterioration margin and deterioration index of A-25-1.1 series models

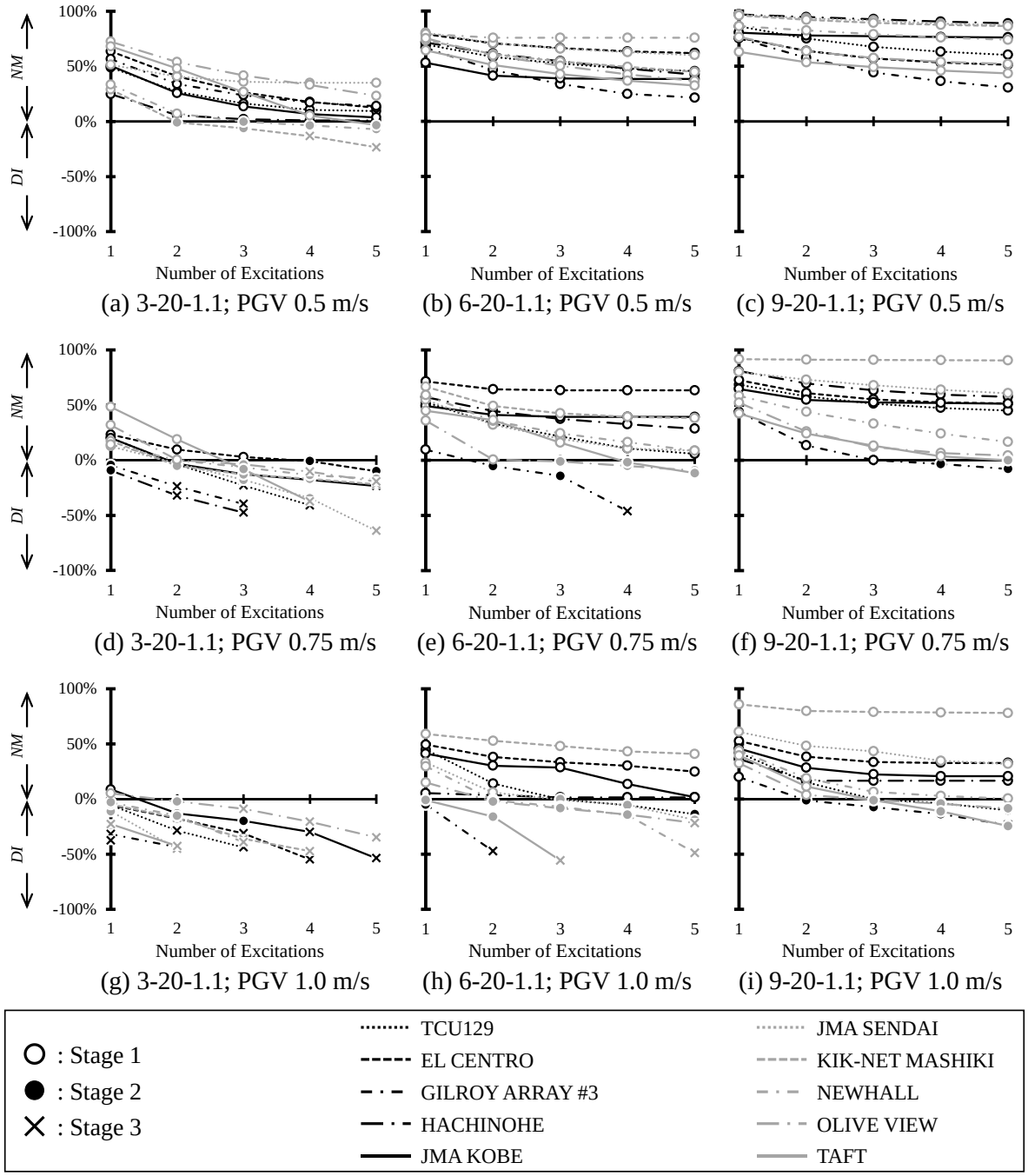

Figure E-3 Non-deterioration margin and deterioration index of A-20-1.1 series models

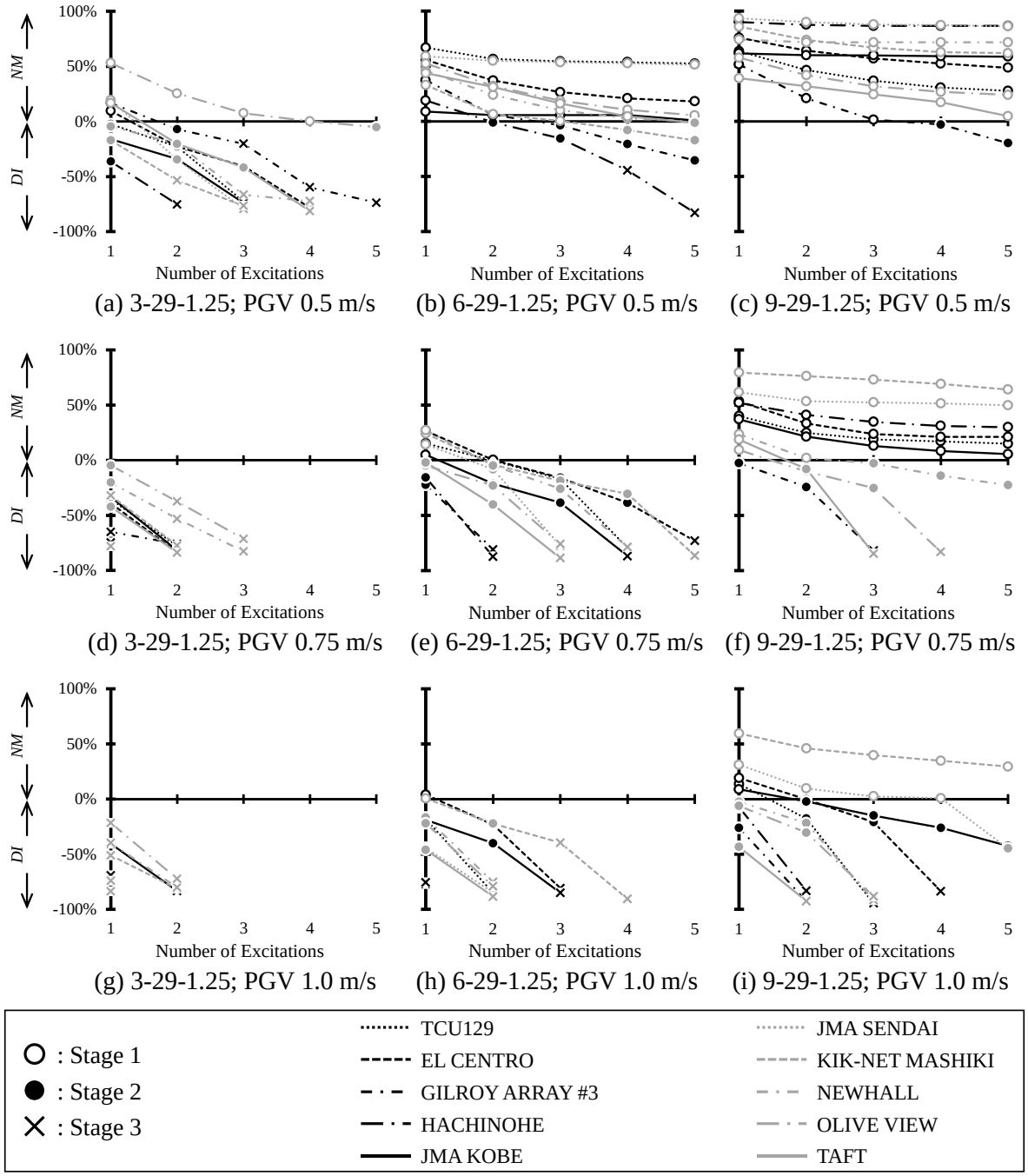

Figure E-4 Non-deterioration margin and deterioration index of A-29-1.25 series models

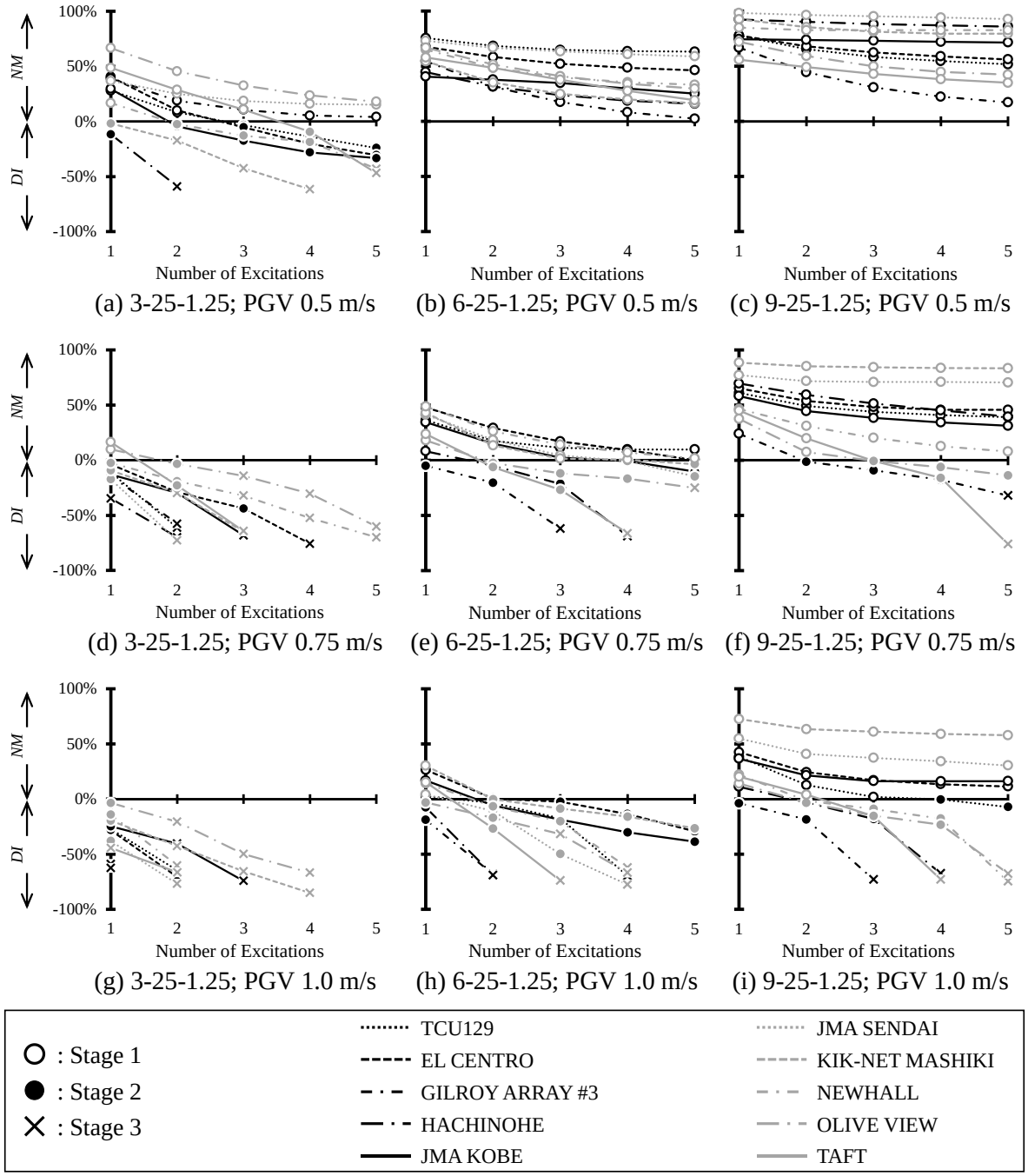

Figure E-5 Non-deterioration margin and deterioration index of A-25-1.25 series models

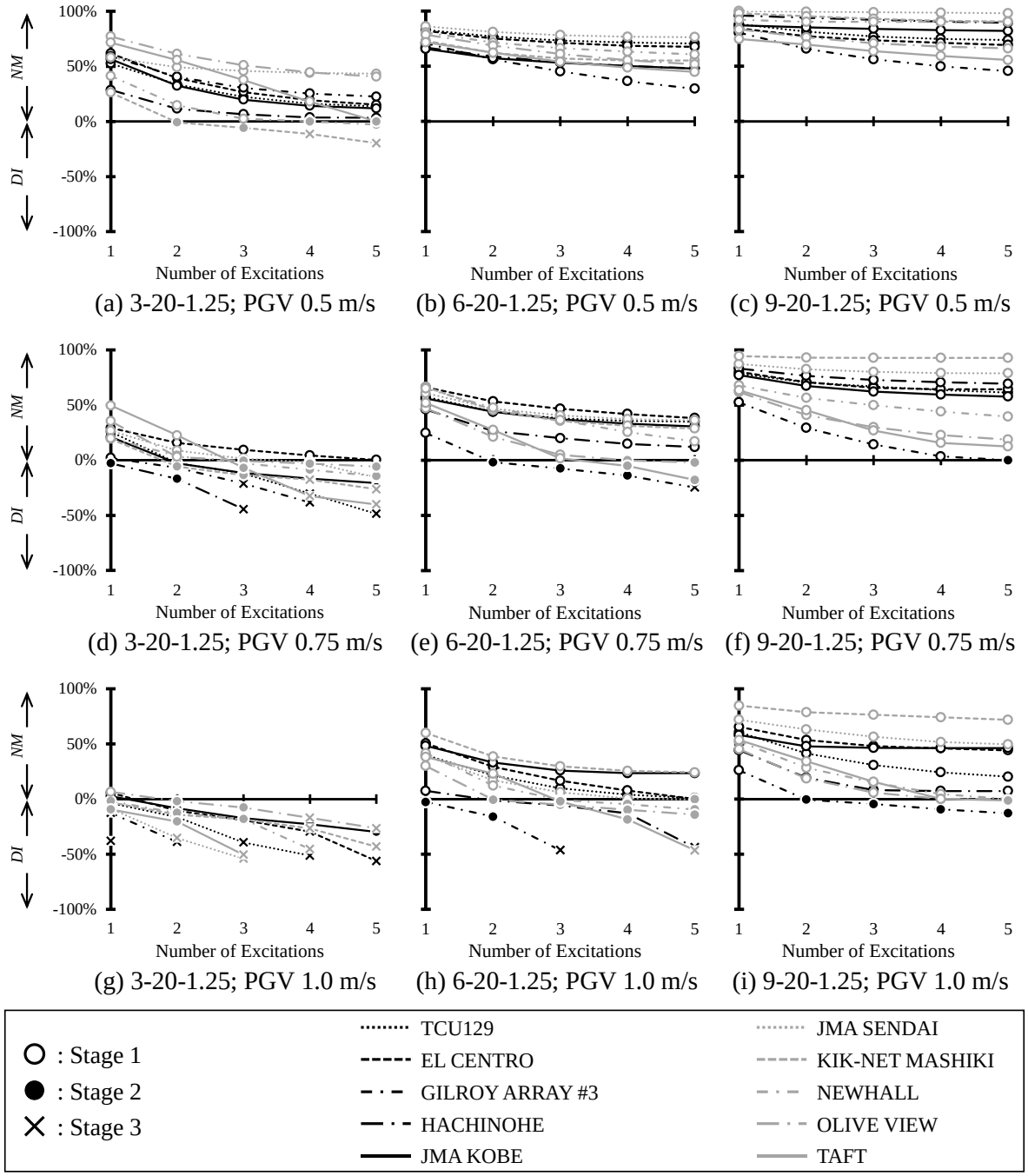

Figure E-6 Non-deterioration margin and deterioration index of A-20-1.25 series models

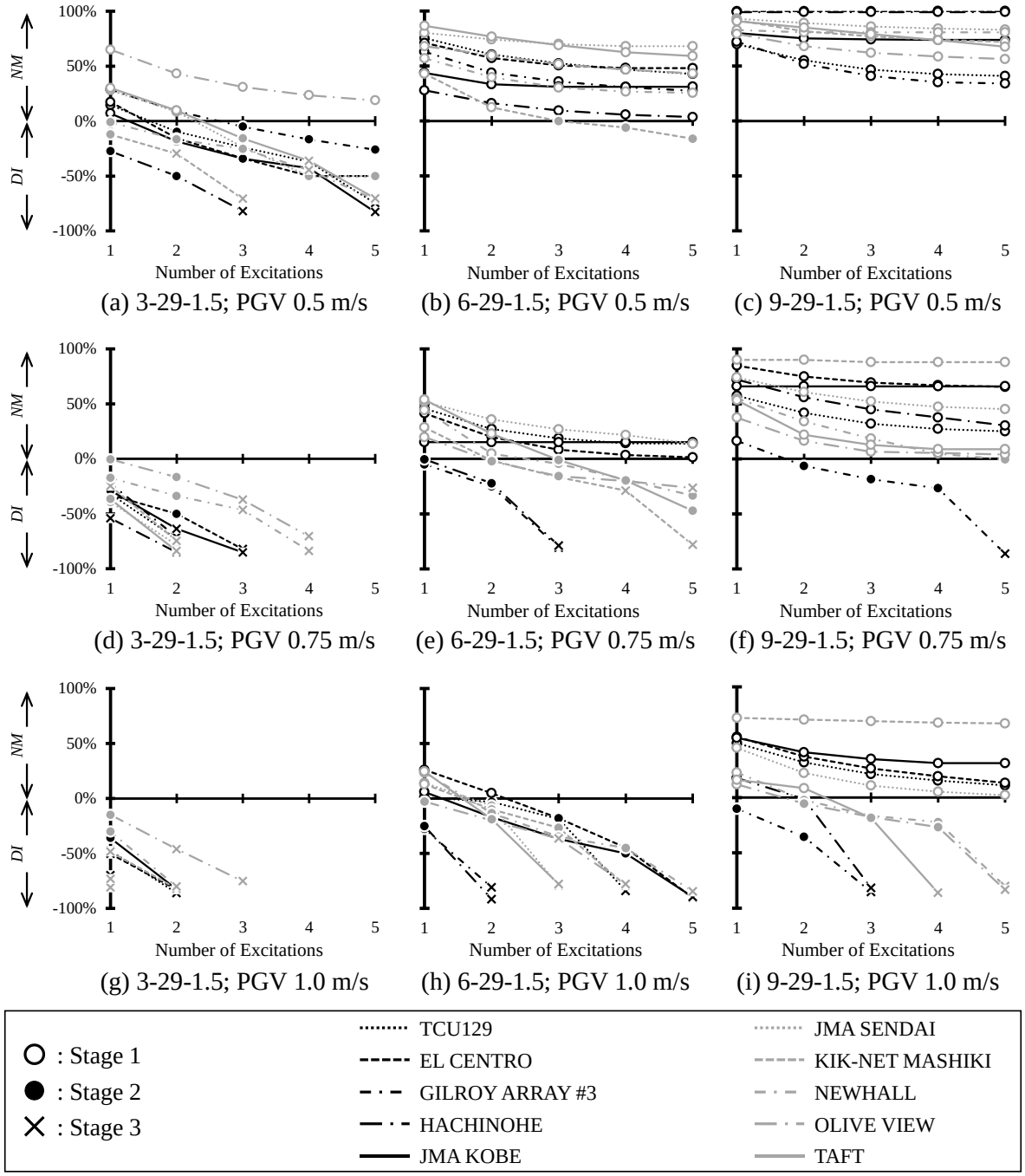

Figure E-7 Non-deterioration margin and deterioration index of A-29-1.5 series models

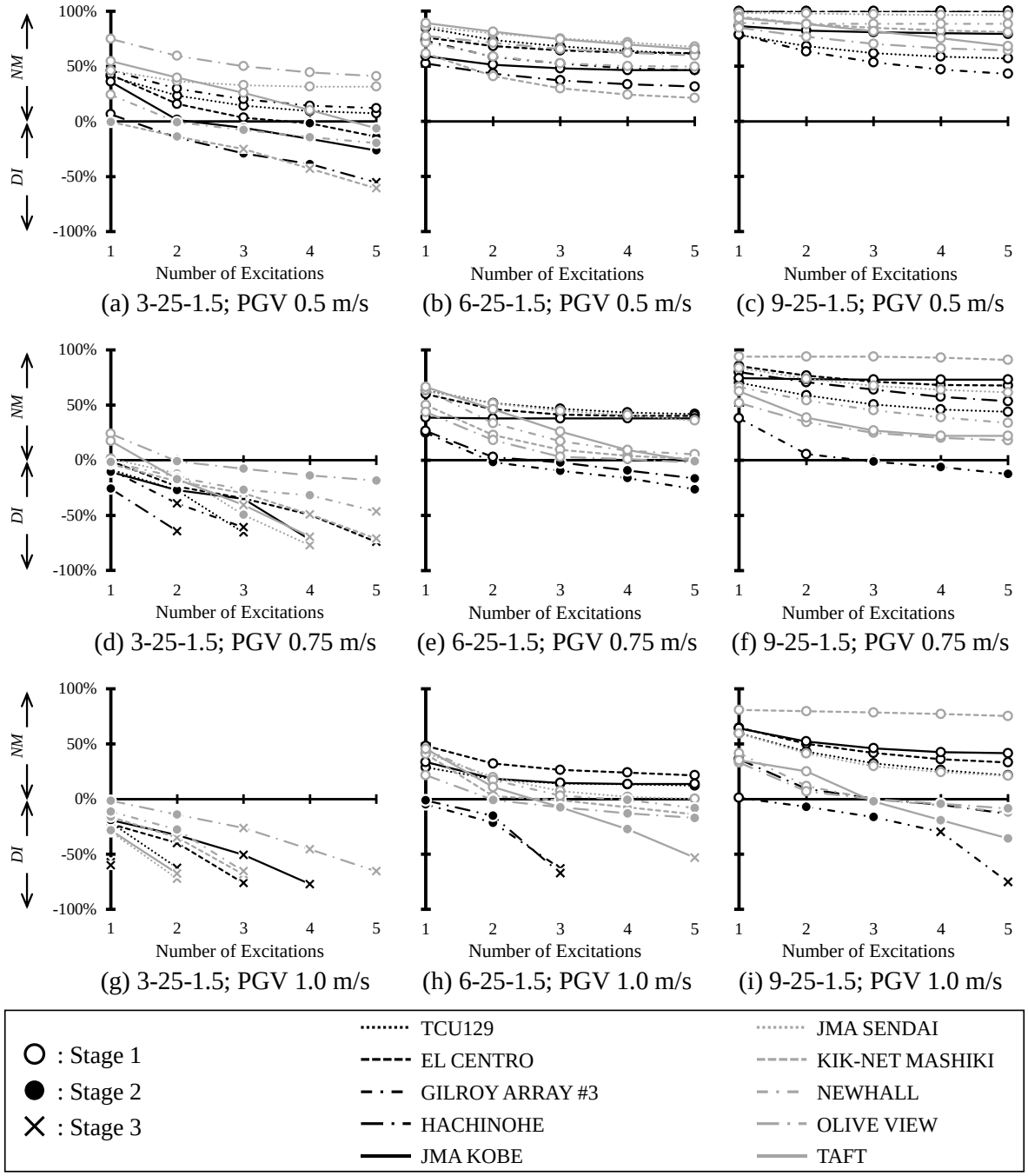

Figure E-8 Non-deterioration margin and deterioration index of A-25-1.5 series models

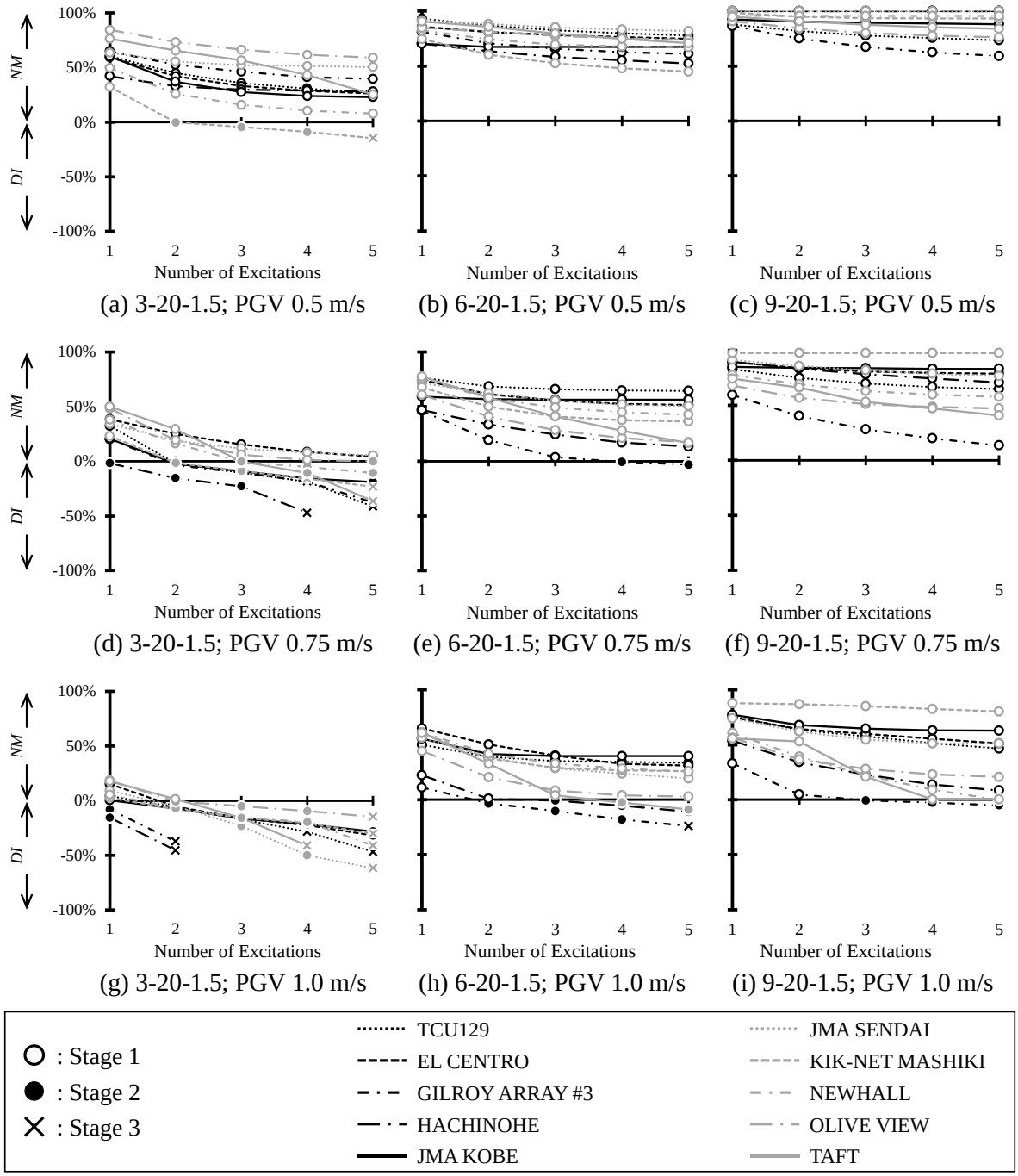

Figure E-9 Non-deterioration margin and deterioration index of A-20-1.5 series models

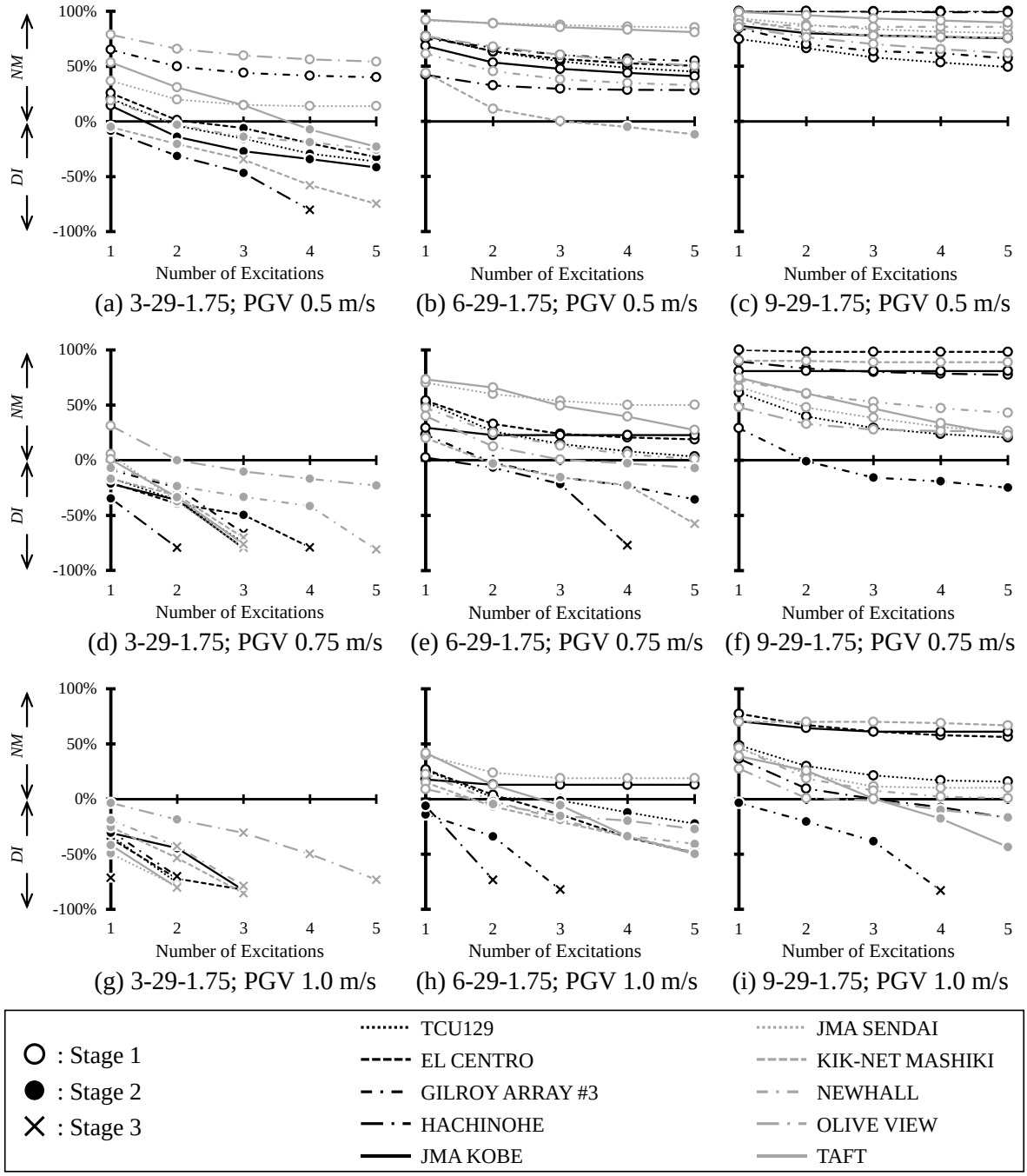

Figure E-10 Non-deterioration margin and deterioration index of A-29-1.75 series models

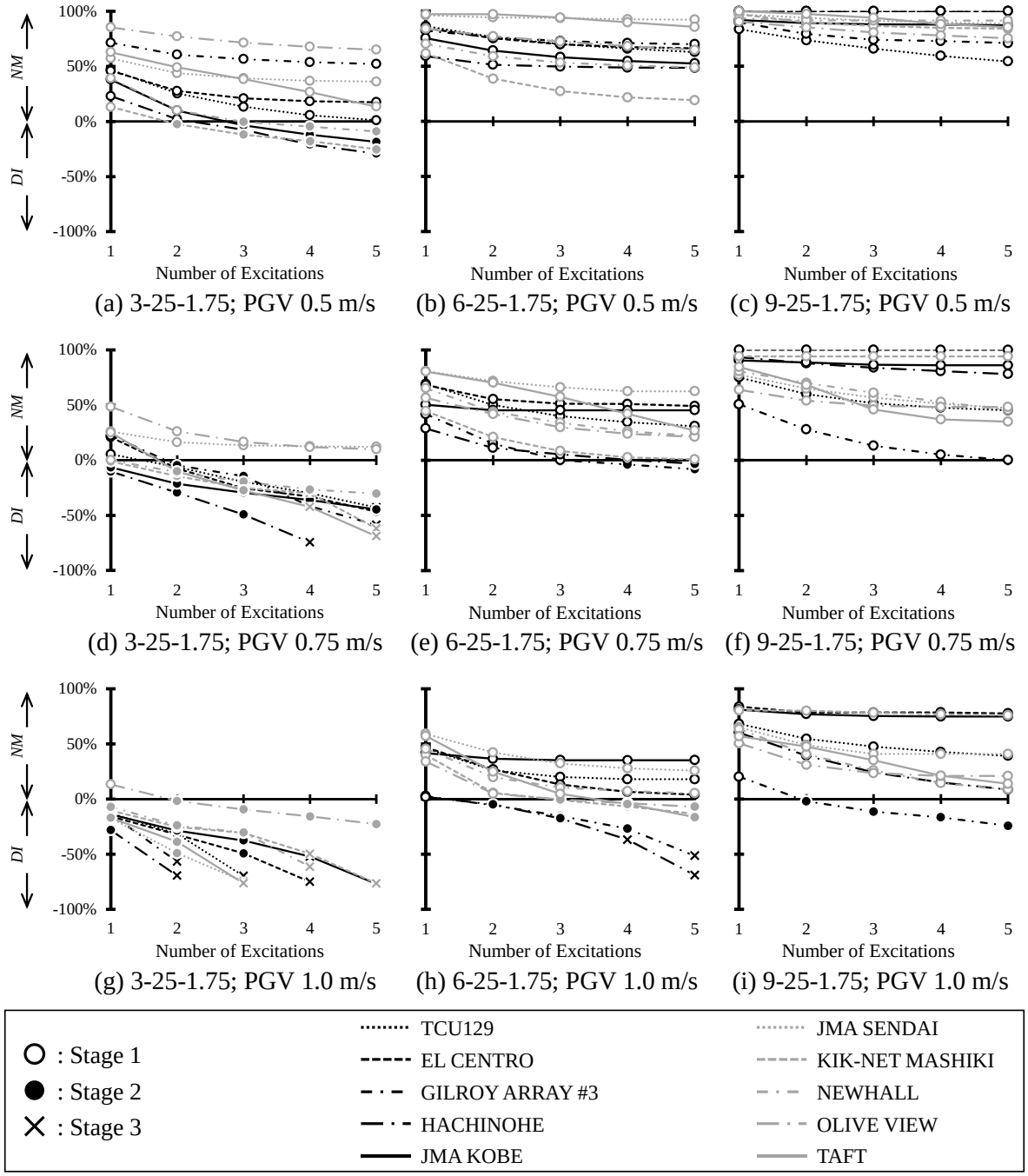

Figure E-11 Non-deterioration margin and deterioration index of A-25-1.75 series models

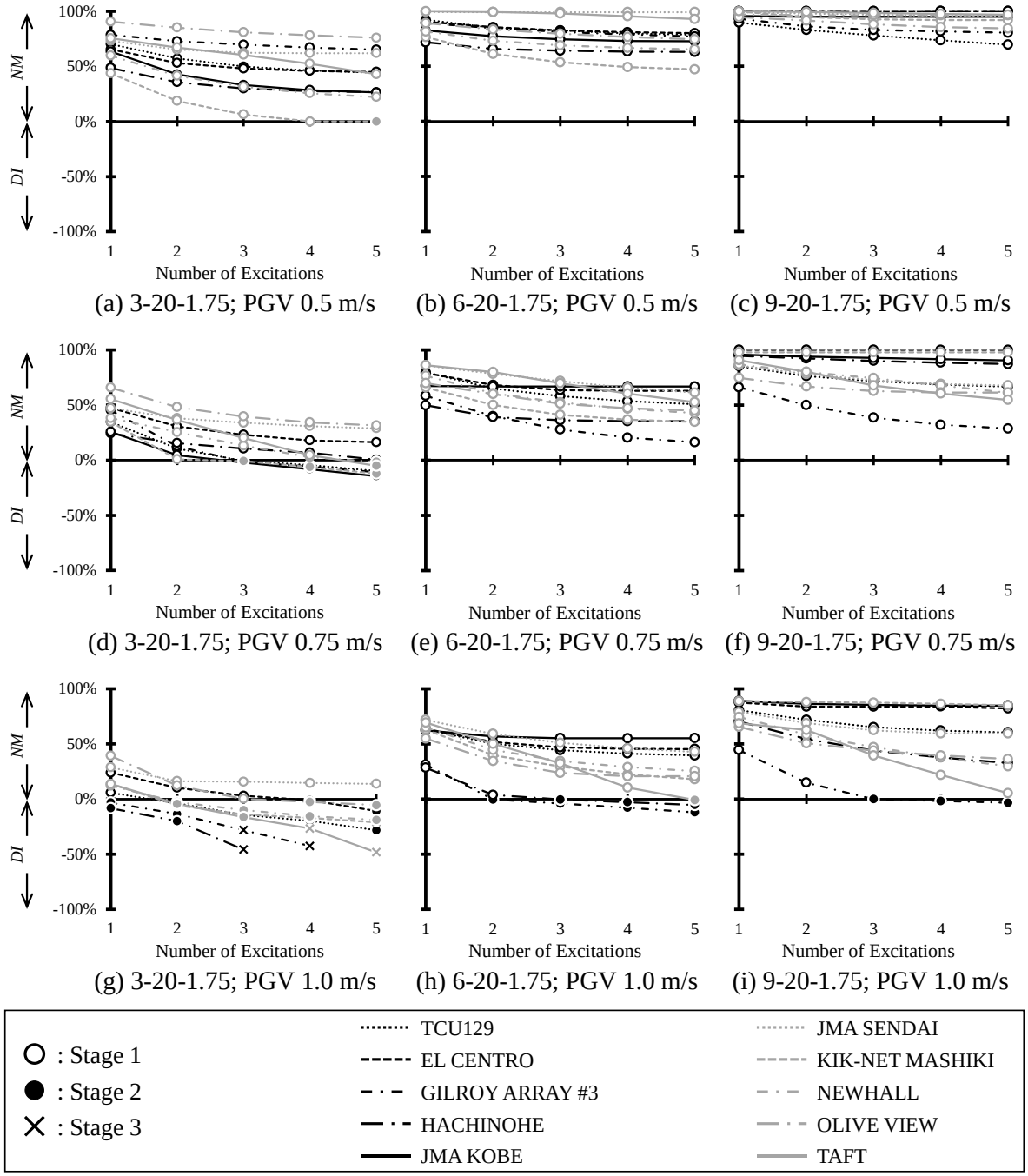

Figure E-12 Non-deterioration margin and deterioration index of A-20-1.75 series models

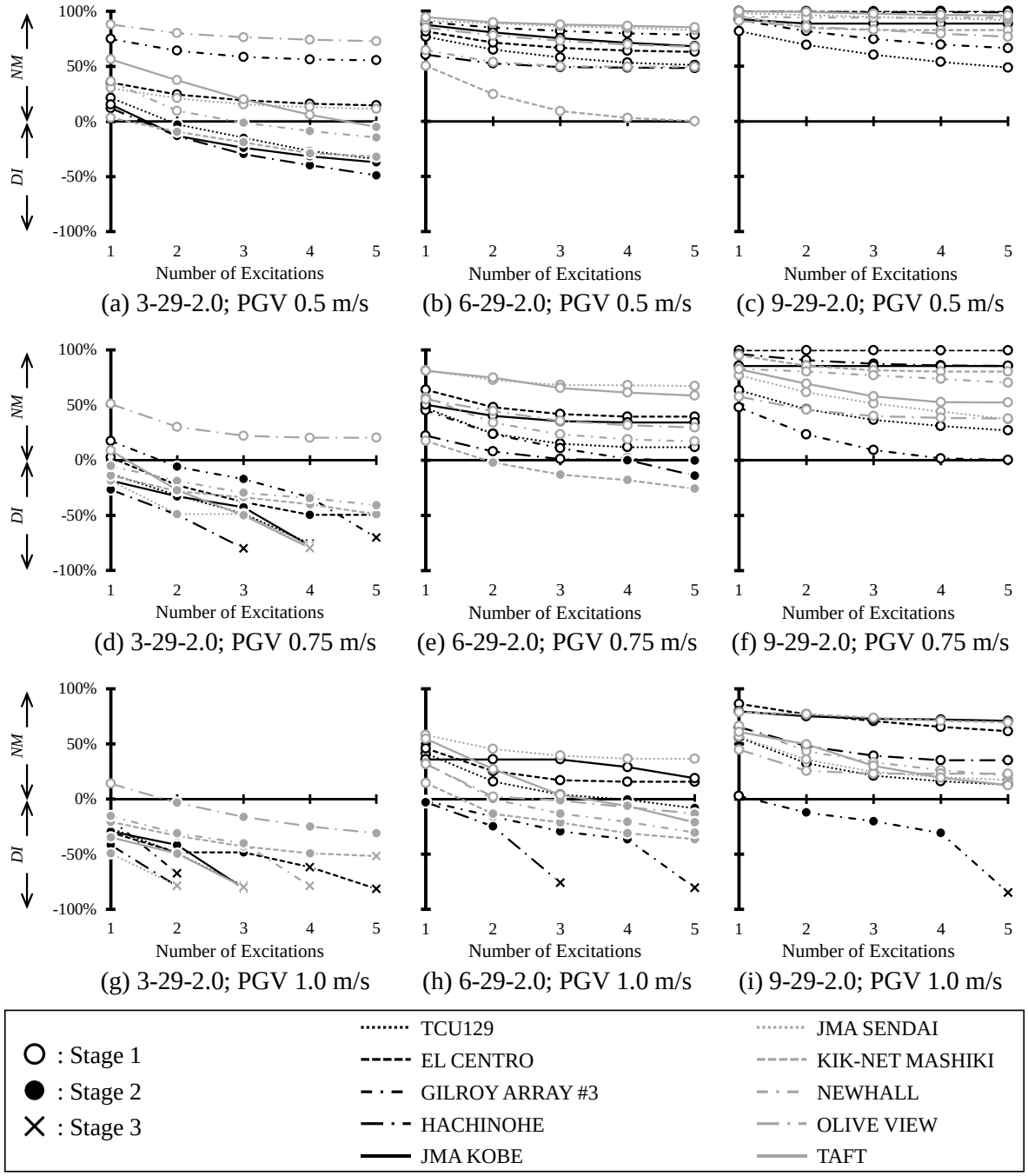

Figure E-13 Non-deterioration margin and deterioration index of A-29-2.0 series models

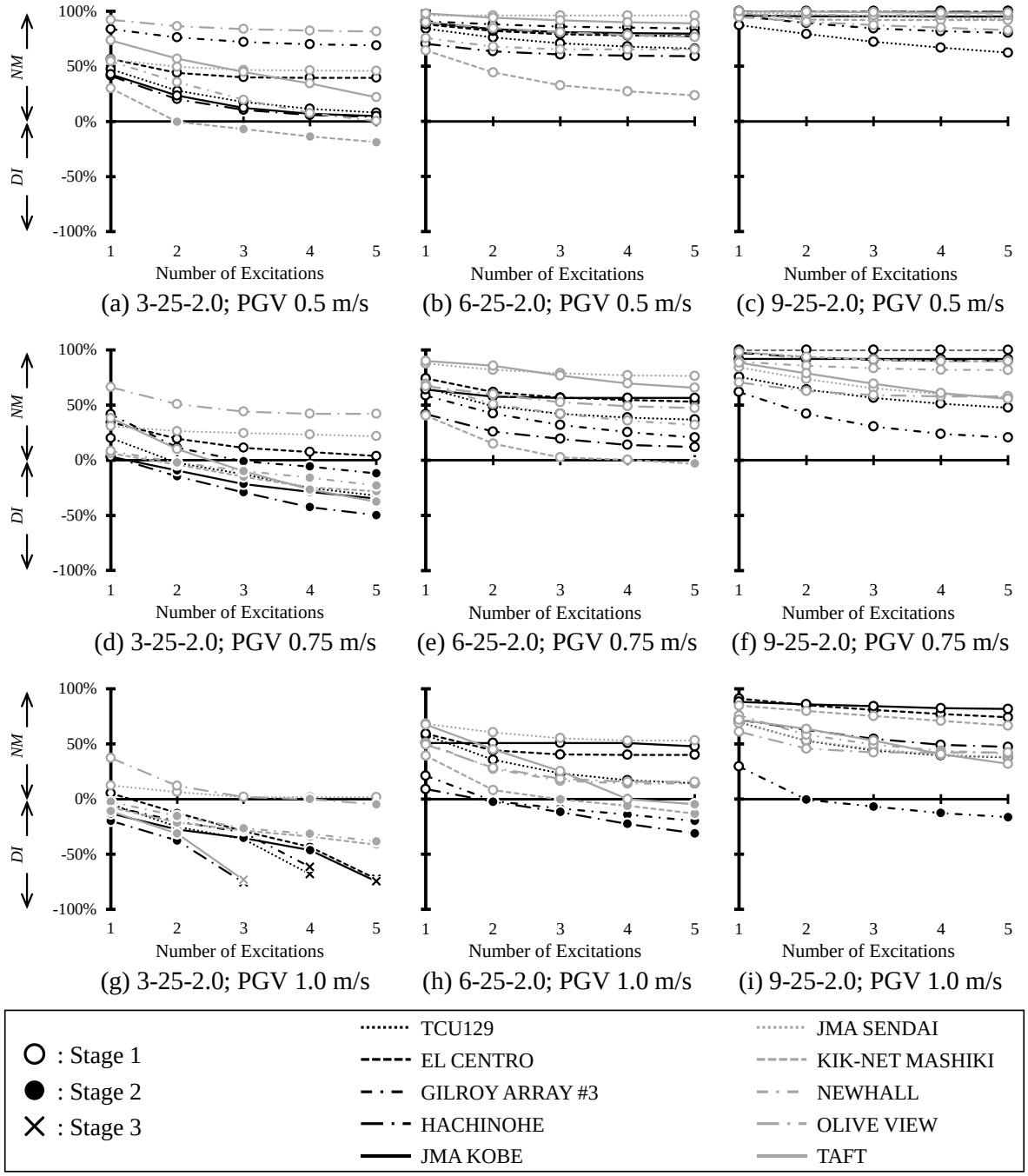

Figure E-14 Non-deterioration margin and deterioration index of A-25-2.0 series models

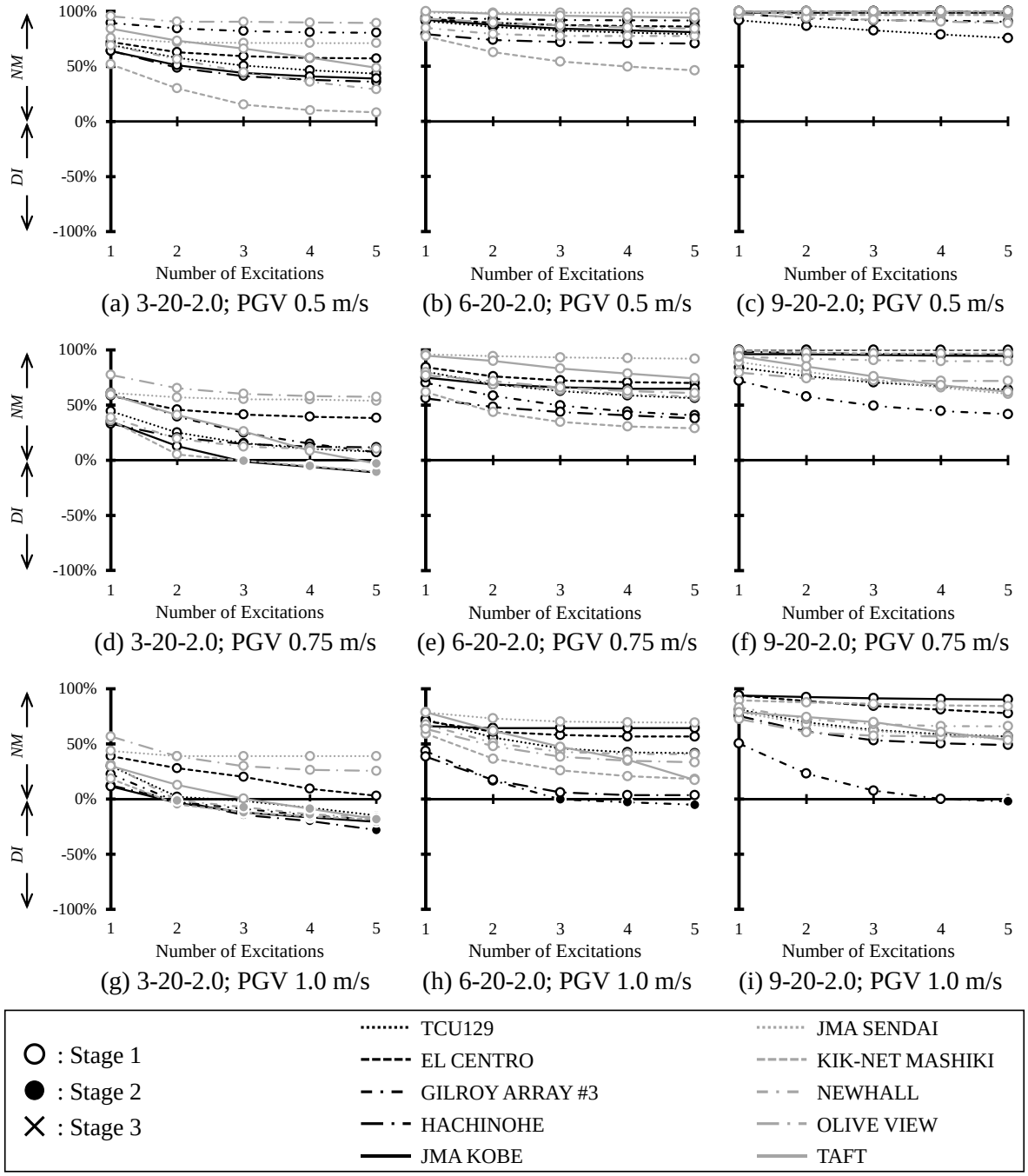

Figure E-15 Non-deterioration margin and deterioration index of A-20-2.0 series models

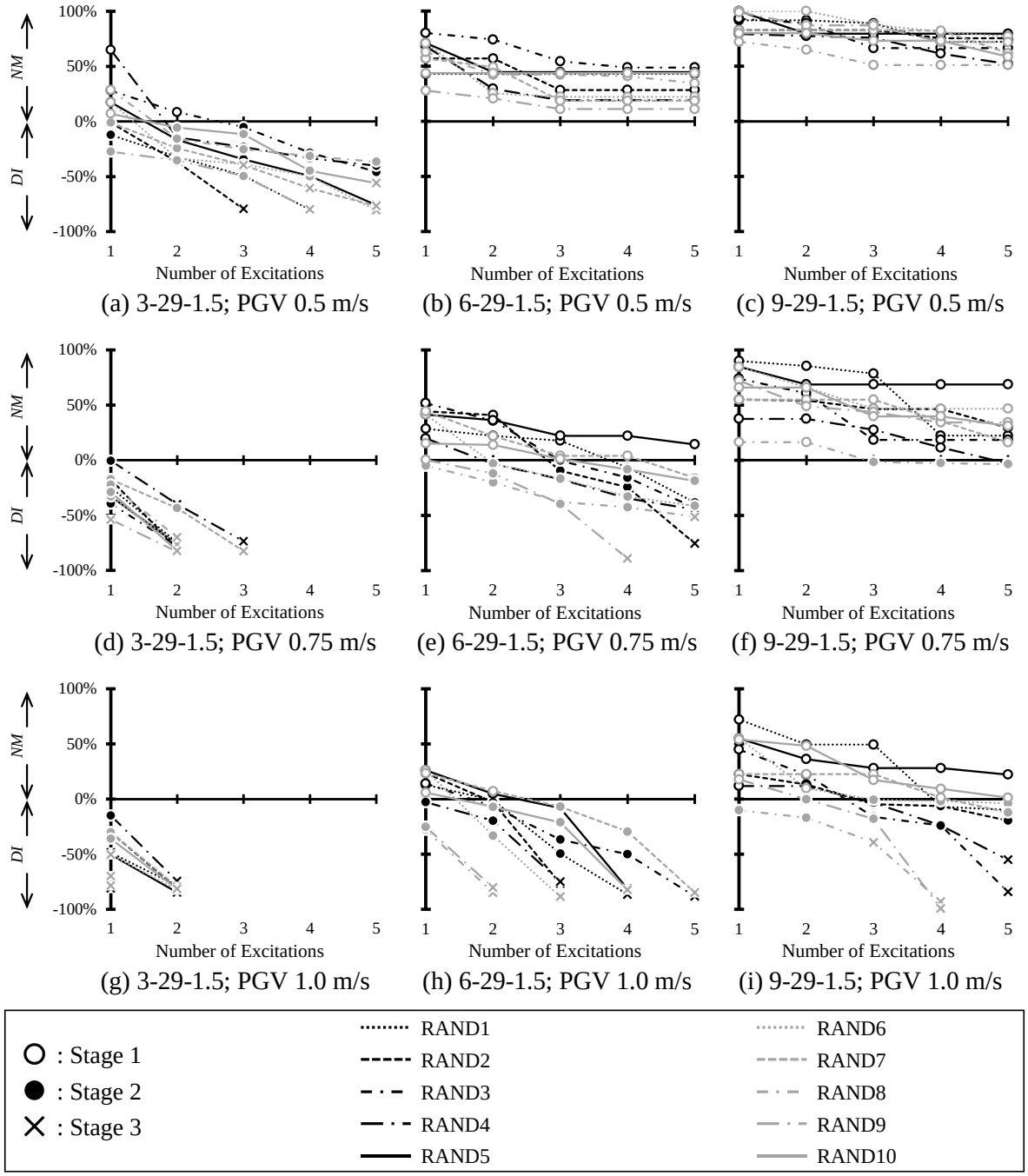

Figure E-16 Non-deterioration margin and deterioration index of A-29-1.5 series models under random sequence input ground motion group 1

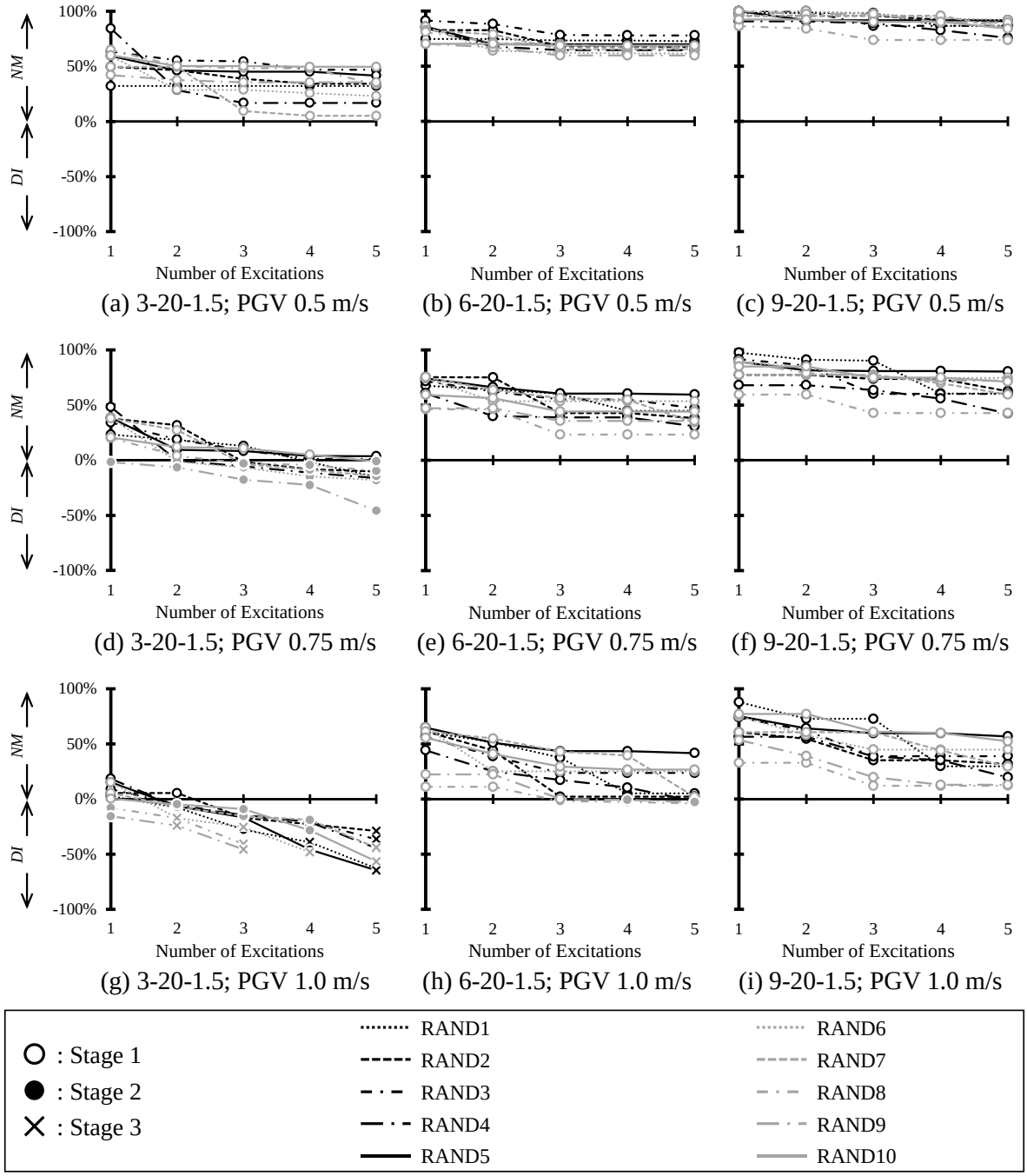

Figure E-17 Non-deterioration margin and deterioration index of A-20-1.5 series models under random sequence input ground motion group 1

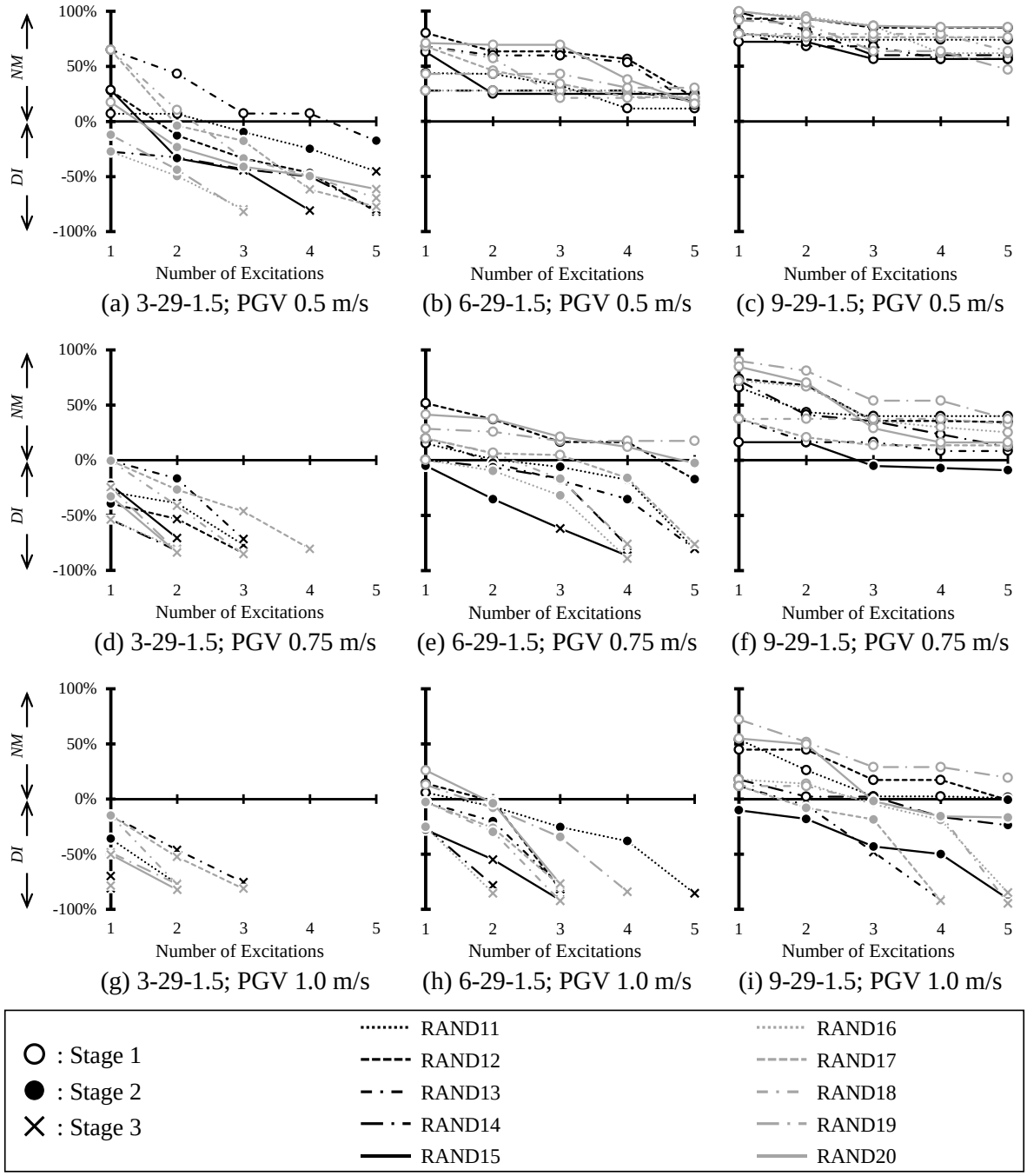

Figure E-18 Non-deterioration margin and deterioration index of A-29-1.5 series models under random sequence input ground motion group 2

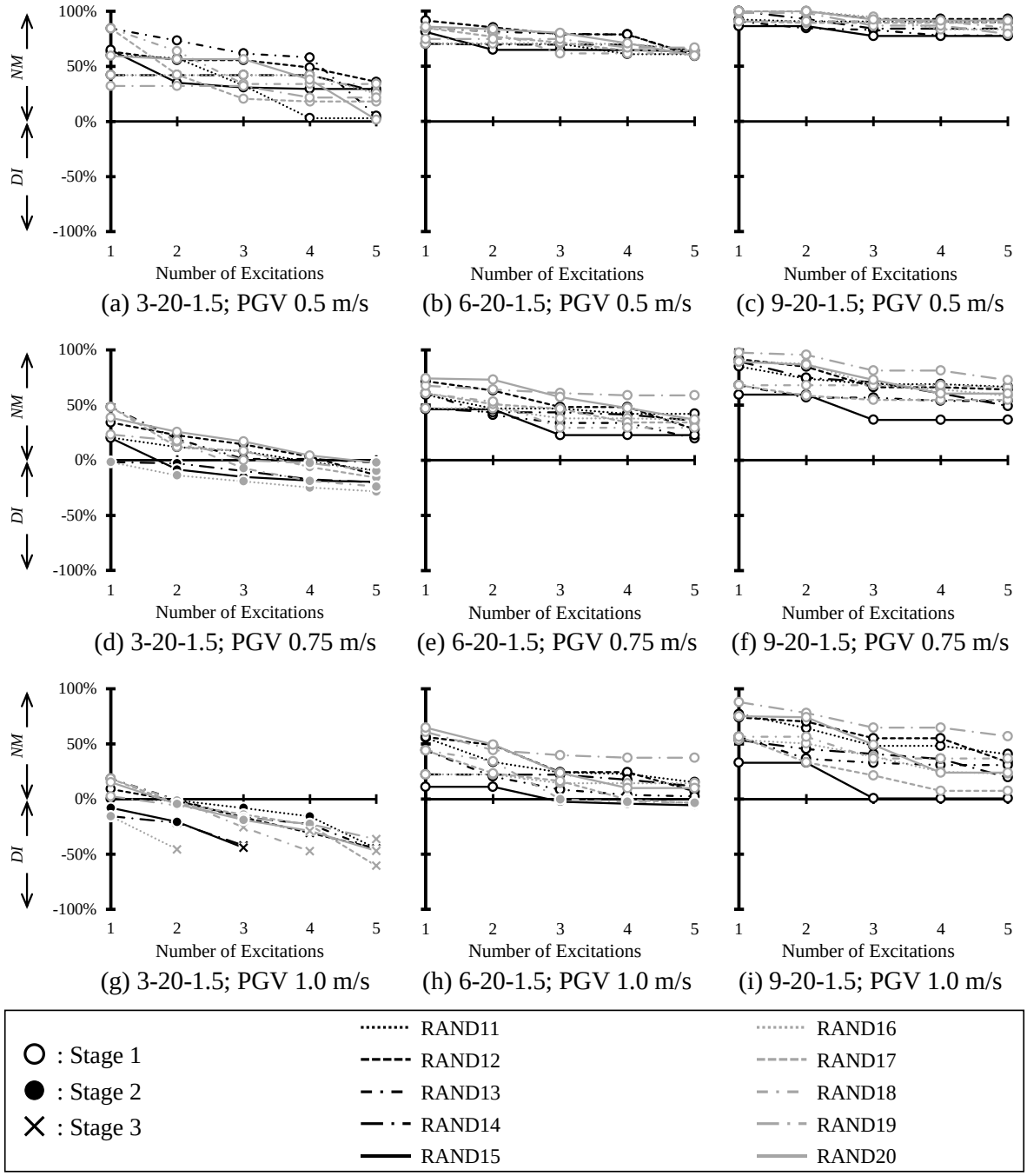

Figure E-19 Non-deterioration margin and deterioration index of A-20-1.5 series models under random sequence input ground motion group 2

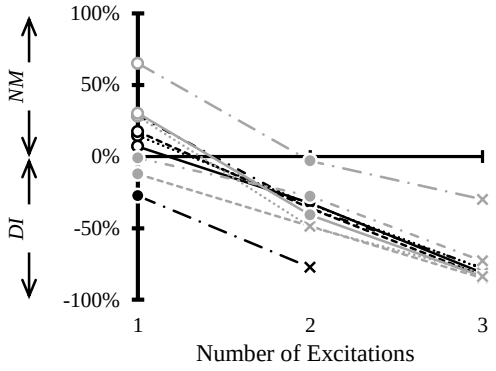

(a) 3-29-1.5 model; Incremental

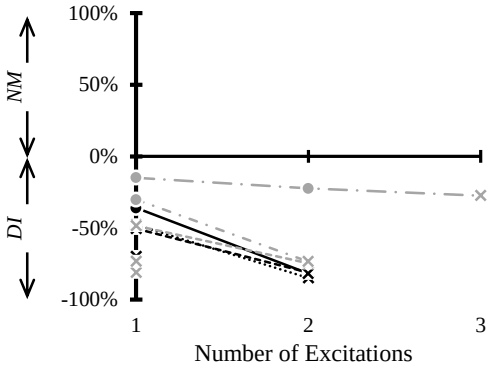

(b) 3-29-1.5 model; Decremental

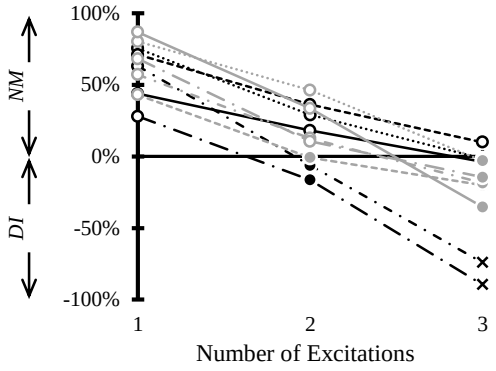

(c) 6-29-1.5 model; Incremental

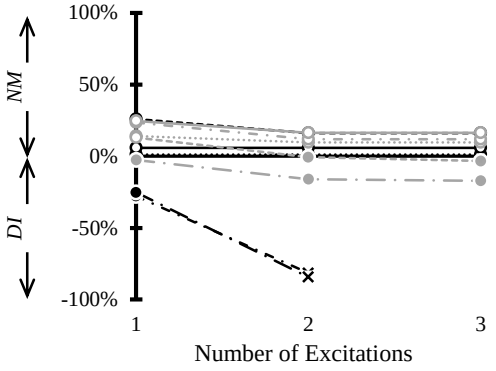

(d) 6-29-1.5 model; Decremental

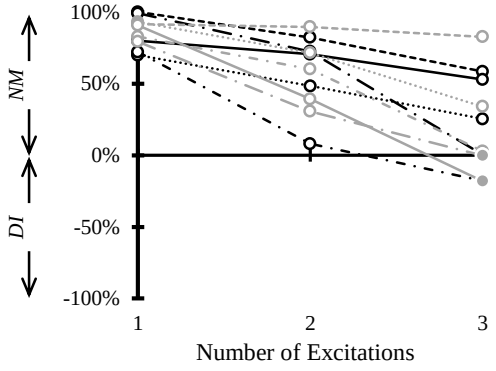

(e) 9-29-1.5 model; Incremental

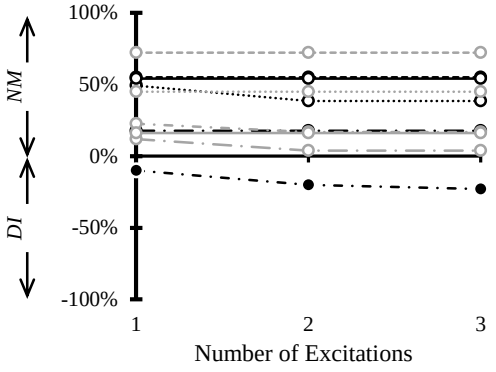

(f) 9-29-1.5 model; Decremental

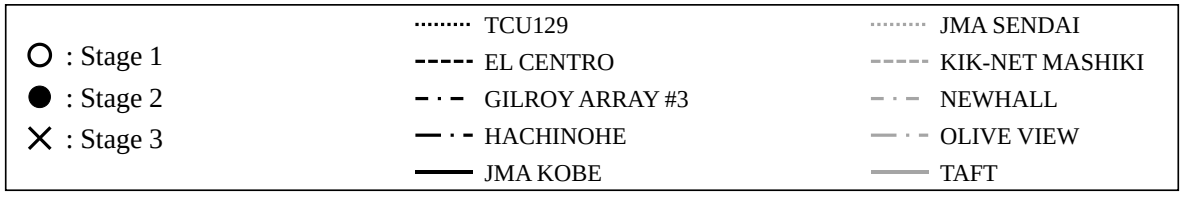

Figure E-20 Non-deterioration margin and deterioration index of A-29-1.5 series models under incremental-decremental sequence input ground motion

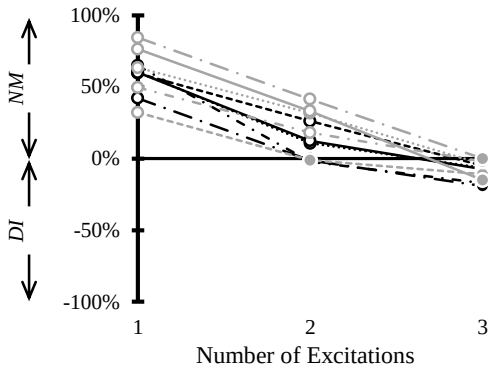

(a) 3-20-1.5 model; Incremental

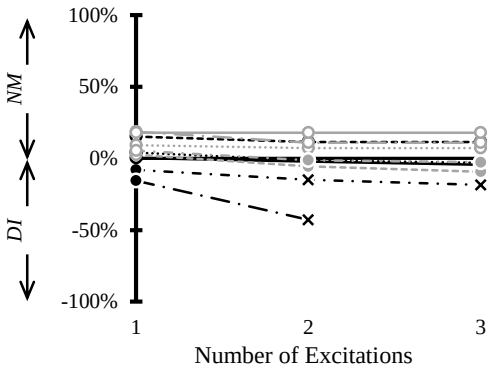

(b) 3-20-1.5 model; Decremental

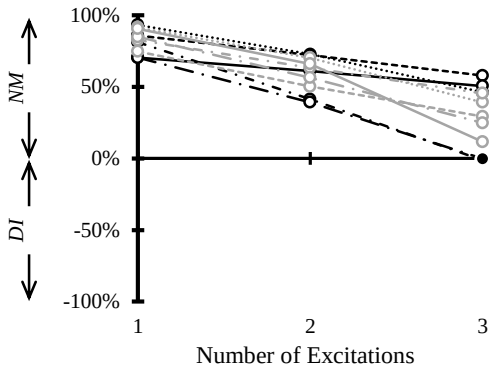

(c) 6-20-1.5 model; Incremental

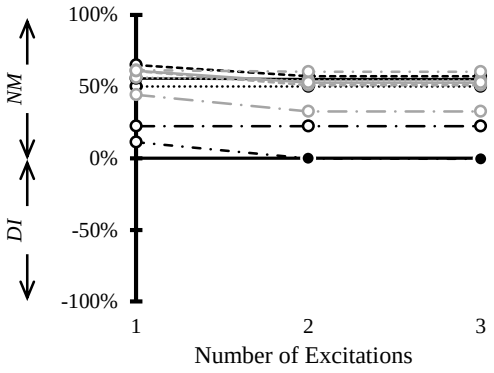

(d) 6-20-1.5 model; Decremental

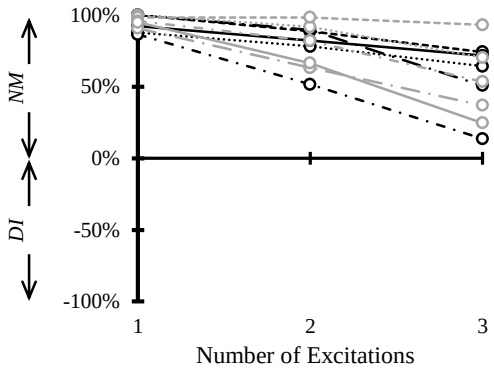

(e) 9-20-1.5 model; Incremental

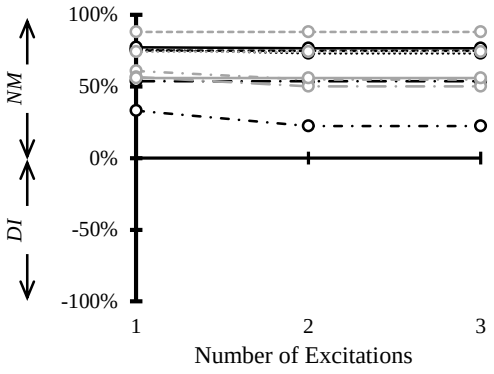

(f) 9-20-1.5 model; Decremental

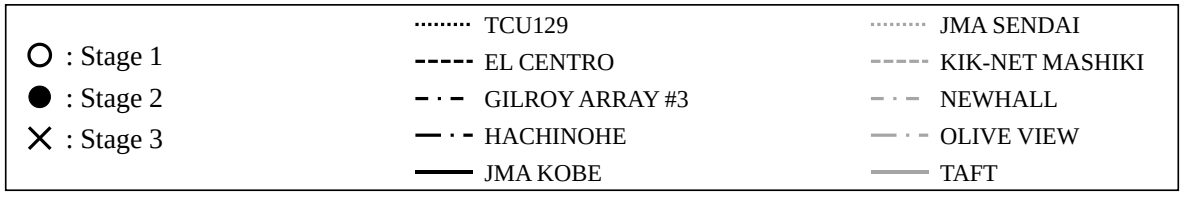

Figure E-21 Non-deterioration margin and deterioration index of A-20-1.5 series models under incremental-decremental sequence input ground motion

Appendix F Calculation Method of Bending Moment Acting on Columns

To calculate the bending moment and shear force that acted on the steel frame, the measured strain on the columns was used. The stress-strain relationship on the column was obtained from the material test of the column member (material type: BCR295). The black line in Figure D-1 shows the stress-strain curve obtained from the material test. From this curve, the elastic limit of the strain was assumed to be approximately 1000 [$\varepsilon\mu$]; however, the maximum measured strain on the columns was approximately 2200 [$\varepsilon\mu$] which means that the column reached the inelastic region. To simplify the calculation, the stress-strain curve obtained from the material test was idealized as a bilinear curve in which the secondary stiffness was assumed to be half of the elastic stiffness. The idealized bilinear curve is shown as the red dashed line in Figure D-1. As an example, Figure D-2 shows the stress-strain relationship of a section with the maximum measured strain obtained based on the use of the idealized bilinear curve.

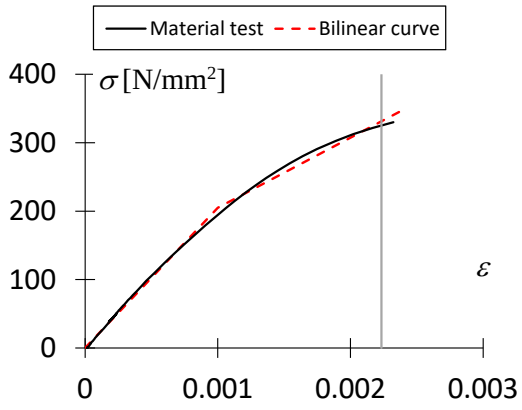

Figure F-1. Stress-strain curve of column members

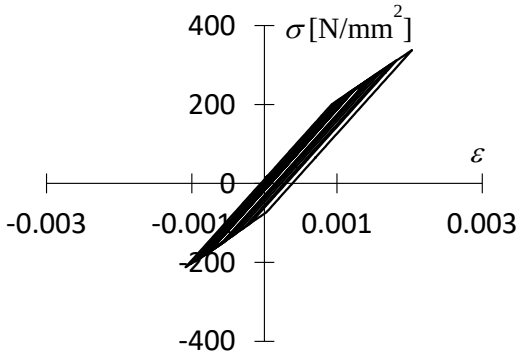

Figure F-2. Stress-strain curve at the section with the maximum measured strain

Appendix G Load-Deformation Relationship Obtained from the Full-Scale Steel Frame Test

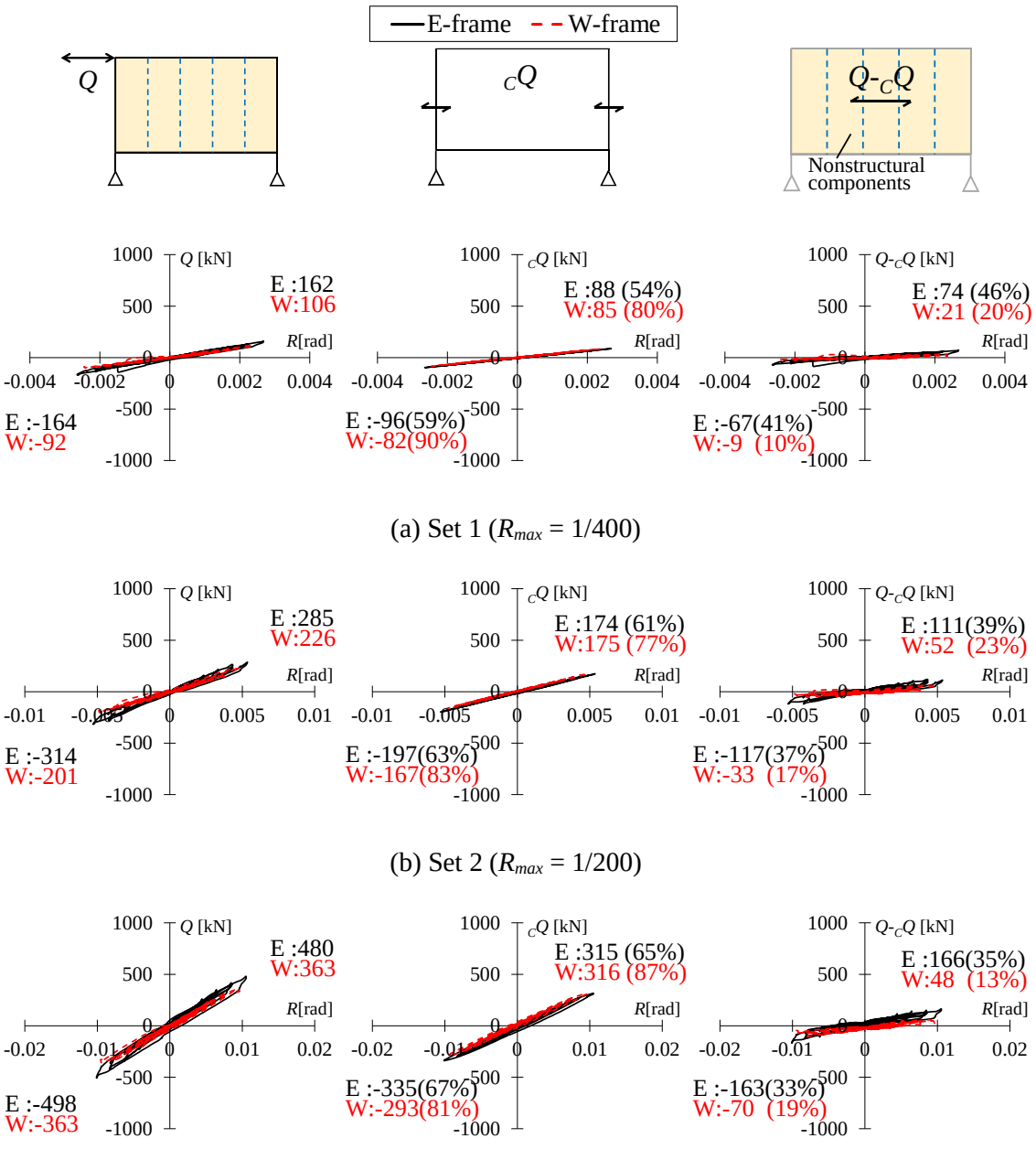

(a) Set 1 (R_{max} = 1/400)

(b) Set 2 (R_{max} = 1/200)

(c) Set 3 (R_{max} = 1/100)

Figure G-1 Load–deformation relationship of the LGS frame

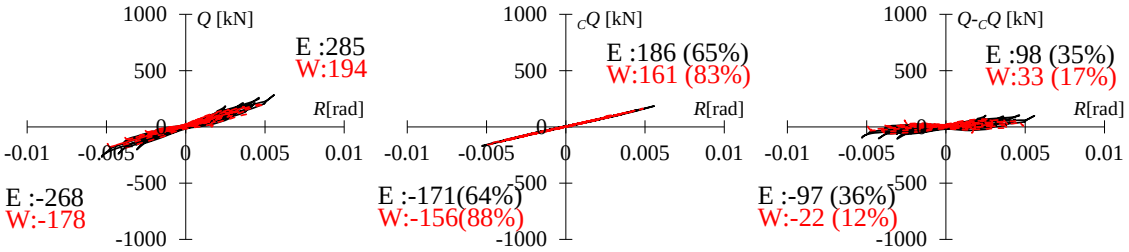

(d) Set 4 (R_{max} = 1/200)

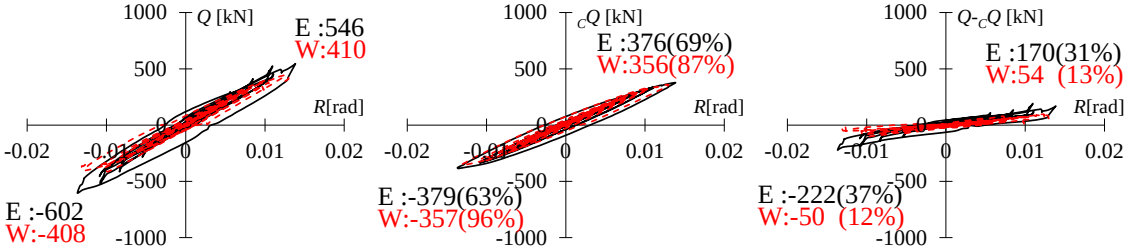

(e) Set 5 (R_{max} = 1/75)

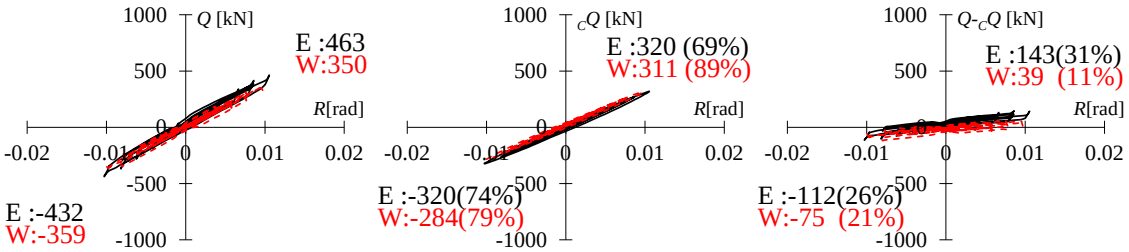

(f) Set 6 (R_{max} = 1/100)

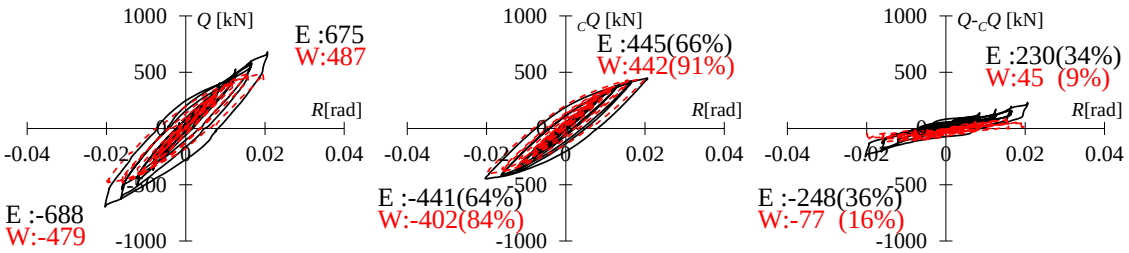

(g) Set 7 (R_{max} = 1/50)

Figure G-1 Load–deformation relationship of the LGS frame (*continued*)

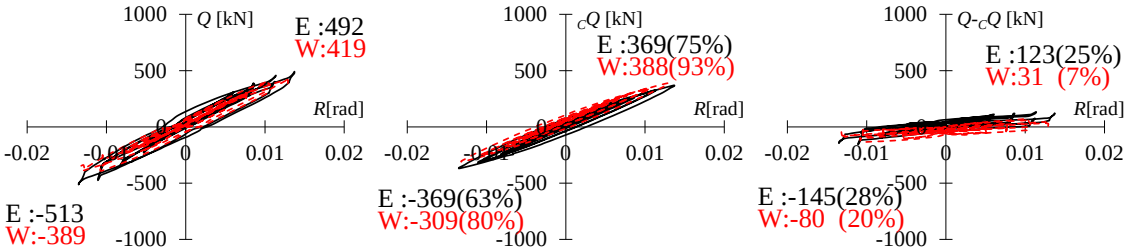

(h) Set 8 (R_{max} = 1/75)

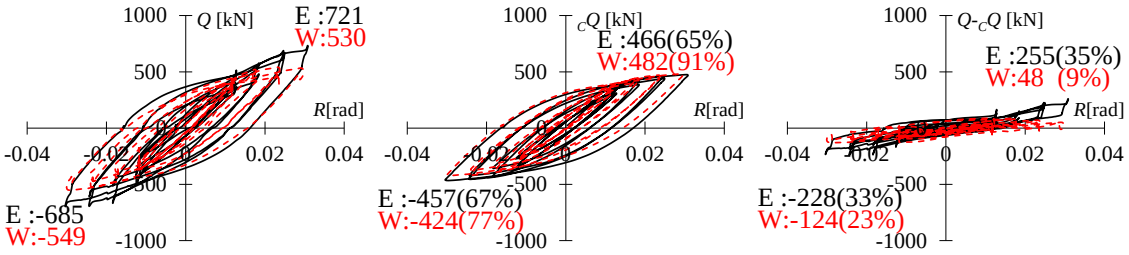

(i) Set 9 (R_{max} = 1/33)

Figure G-1 Load–deformation relationship of the LGS frame (*continued*)

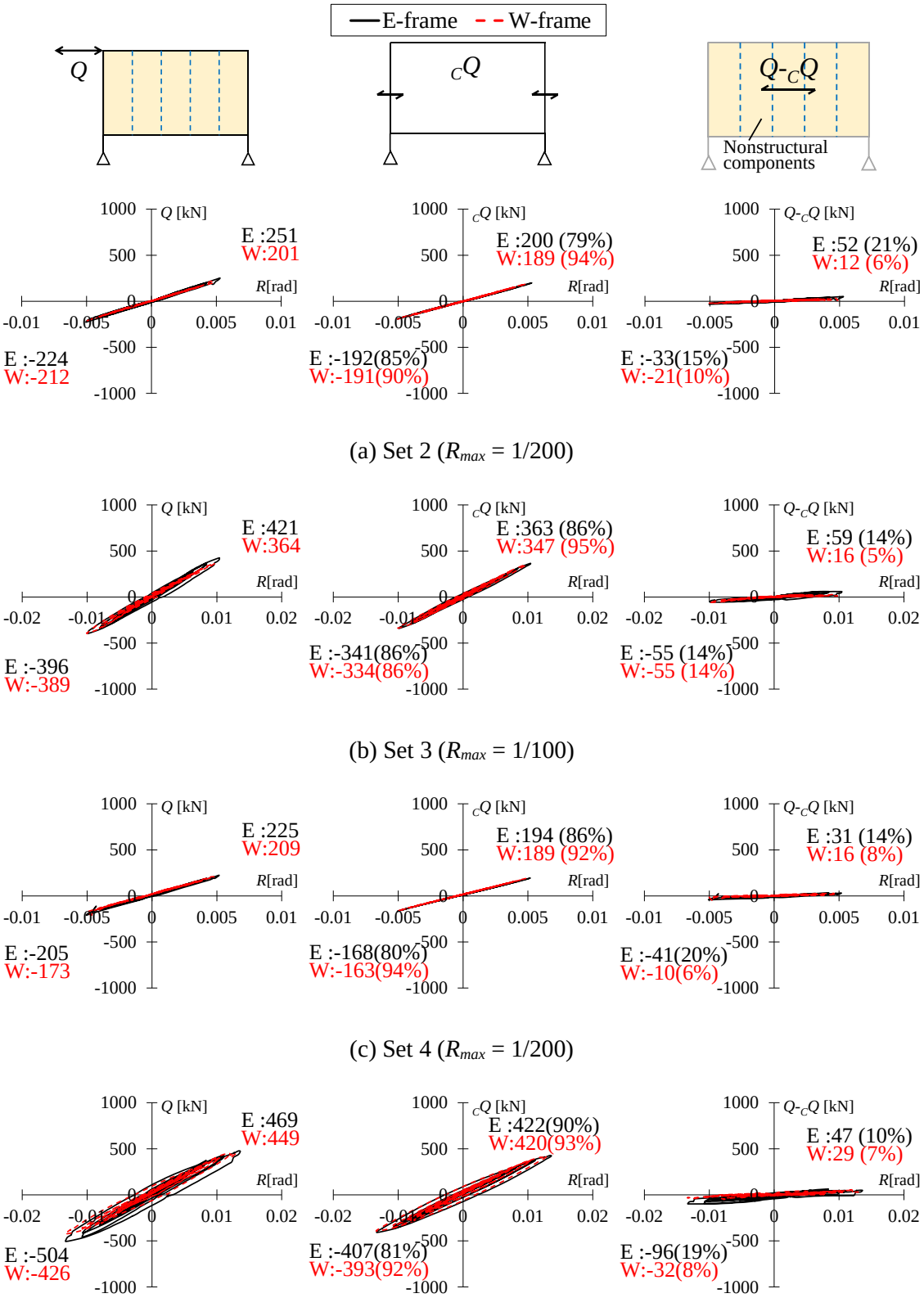

(a) Set 2 (R_{max} = 1/200)

(b) Set 3 (R_{max} = 1/100)

(c) Set 4 (R_{max} = 1/200)

(d) Set 5 (R_{max} = 1/75)

Figure G-2 Load–deformation relationship of the ALC frame

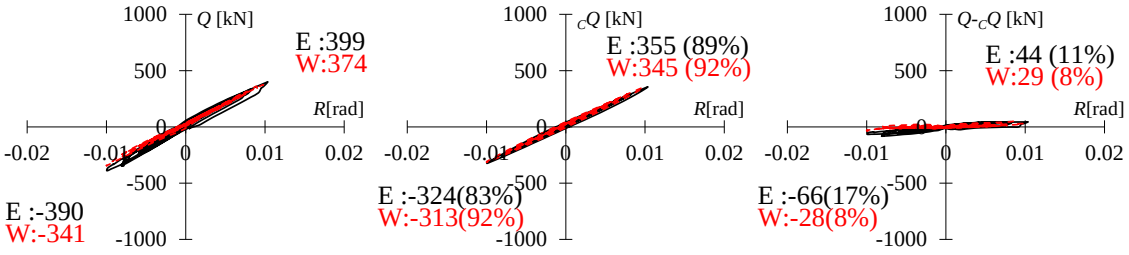

(e) Set 6 (R_{max} = 1/100)

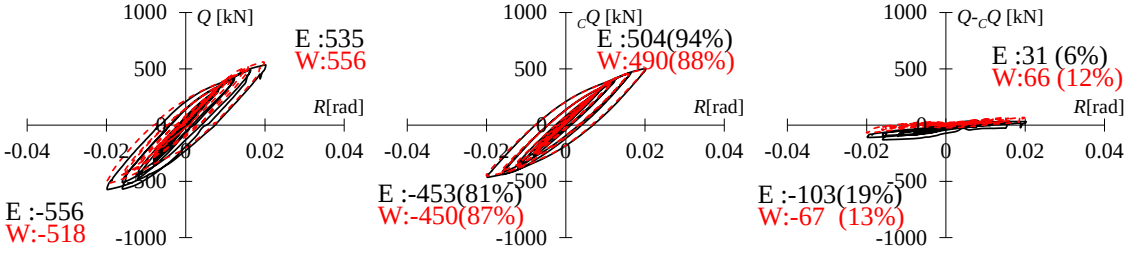

(f) Set 7 (R_{max} = 1/50)

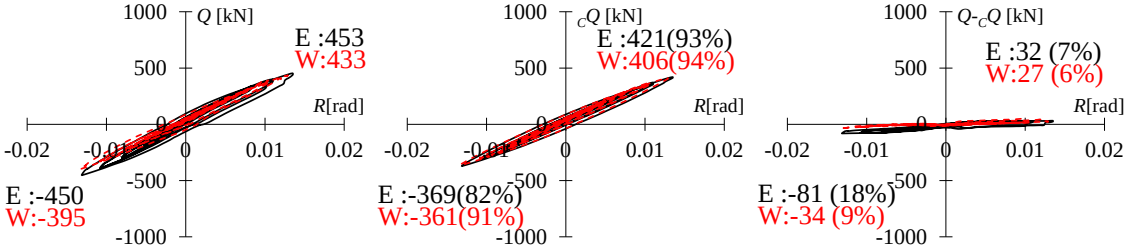

(g) Set 8 (R_{max} = 1/75)

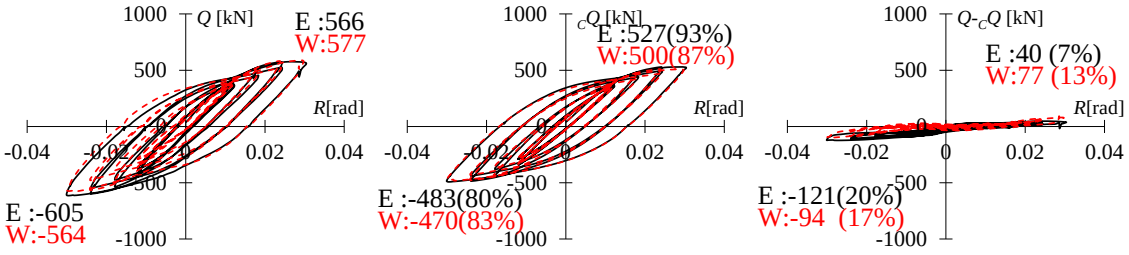

(h) Set 9 (R_{max} = 1/33)

Figure G-2 Load–deformation relationship of the ALC frame (*continued*)

Appendix H Relationship between Maximum Story Drift Angle Range ($SDAR_{max}$) and Cumulative Damage of Critical Beam (D)

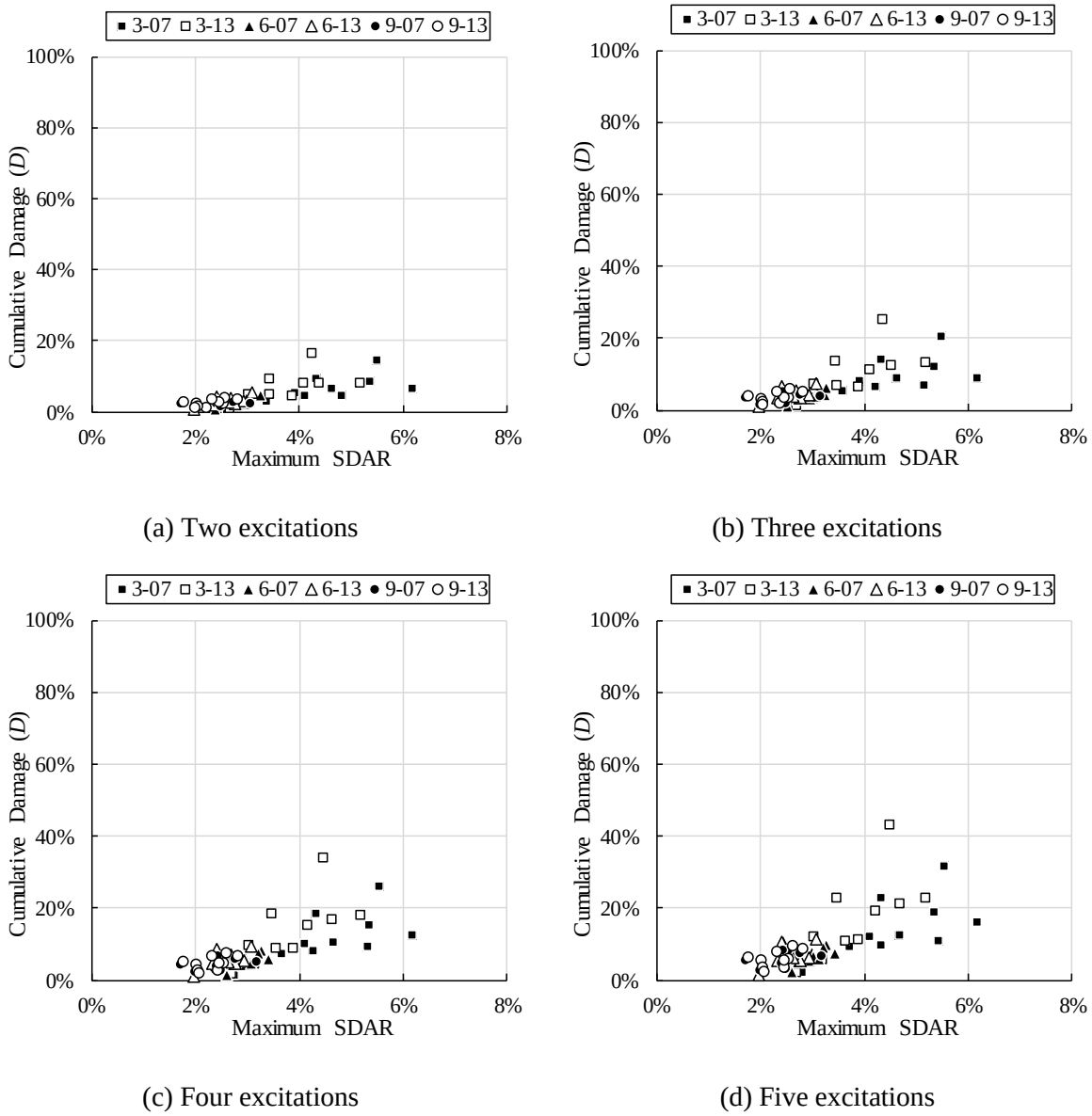

(a) Two excitations

(b) Three excitations

(c) Four excitations

(d) Five excitations

Figure H-1 Relationship between $SDAR_{max}$ and cumulative damage (D) under input ground motion intensity of PGV 0.5 m/s

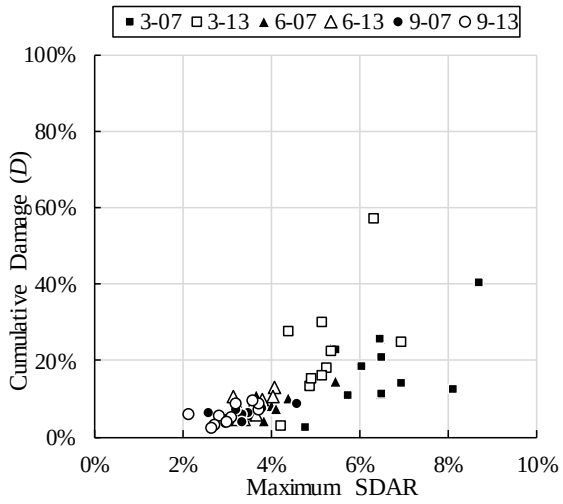

(a) Two excitations

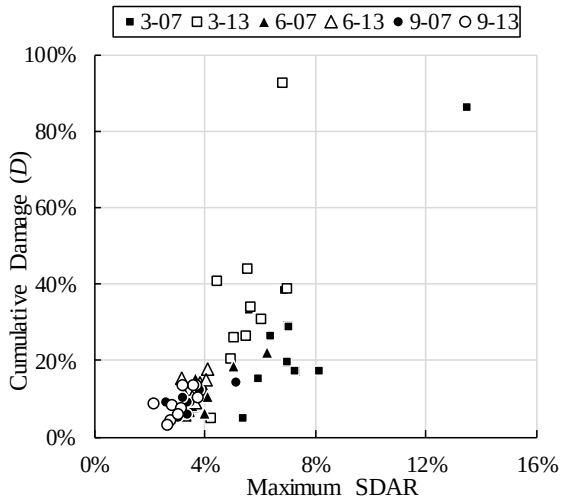

(b) Three excitations

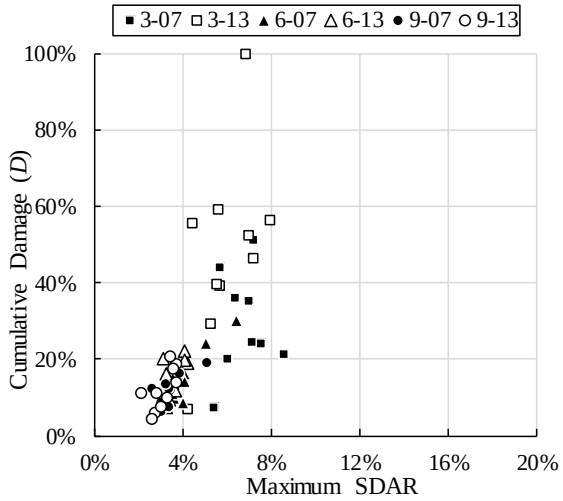

(c) Four excitations

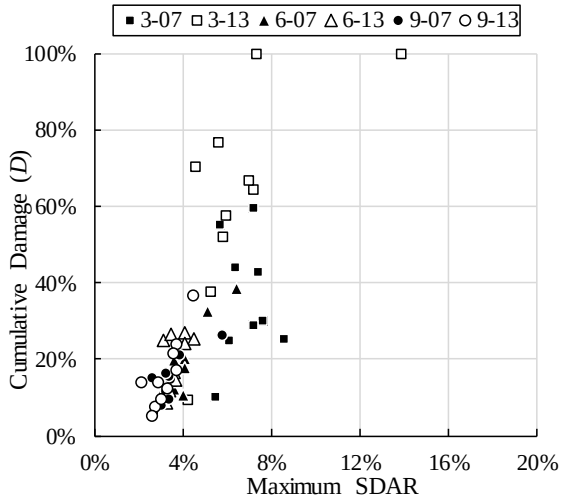

(d) Five excitations

Figure H-2 Relationship between $SDAR_{max}$ and cumulative damage (D) under input ground motion intensity of PGV 0.75 m/s

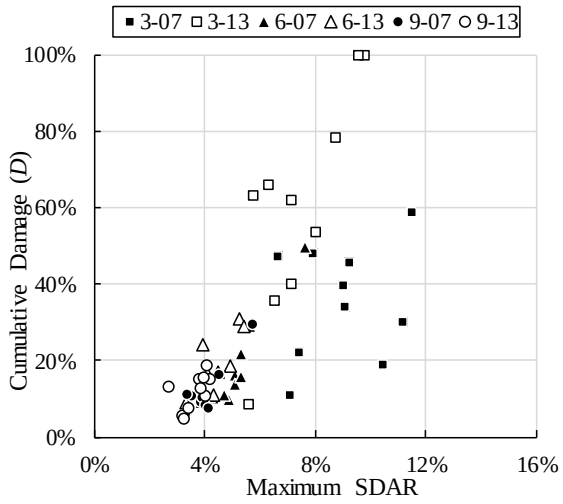

(a) Two excitations

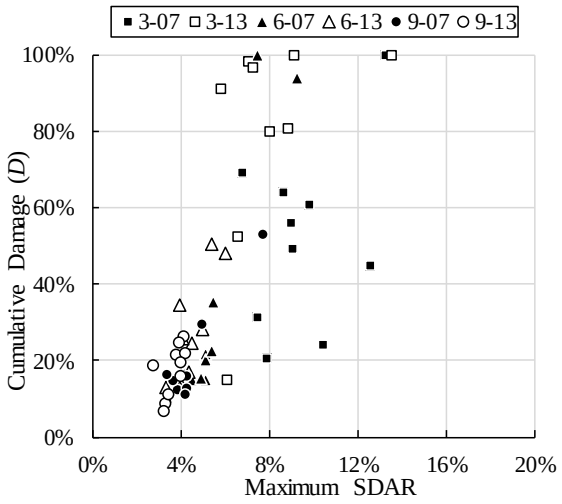

(b) Three excitations

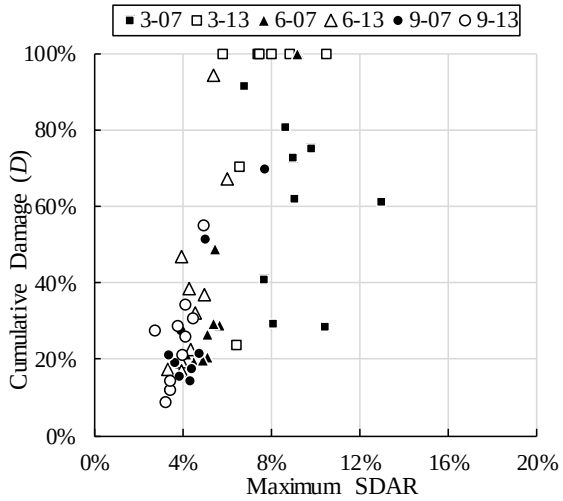

(c) Four excitations

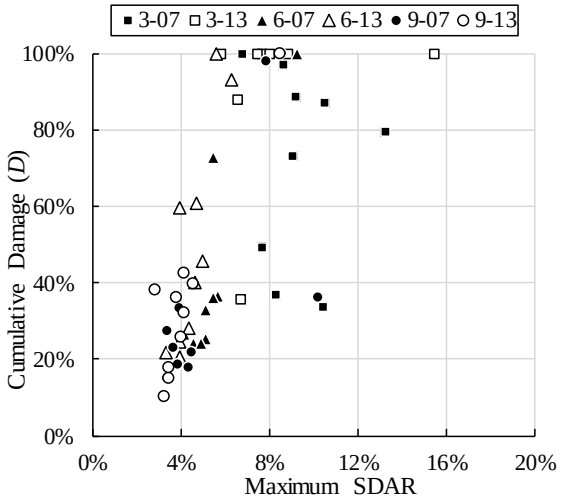

(d) Five excitations

Figure H-3 Relationship between $SDAR_{max}$ and cumulative damage (D) under input ground motion intensity of PGV 1.0 m/s

Appendix I Relationship between Maximum Story Drift Angle Range ($SDAR_{max}$) and Non-deterioration Margin (NM) and Deterioration Index (DI)

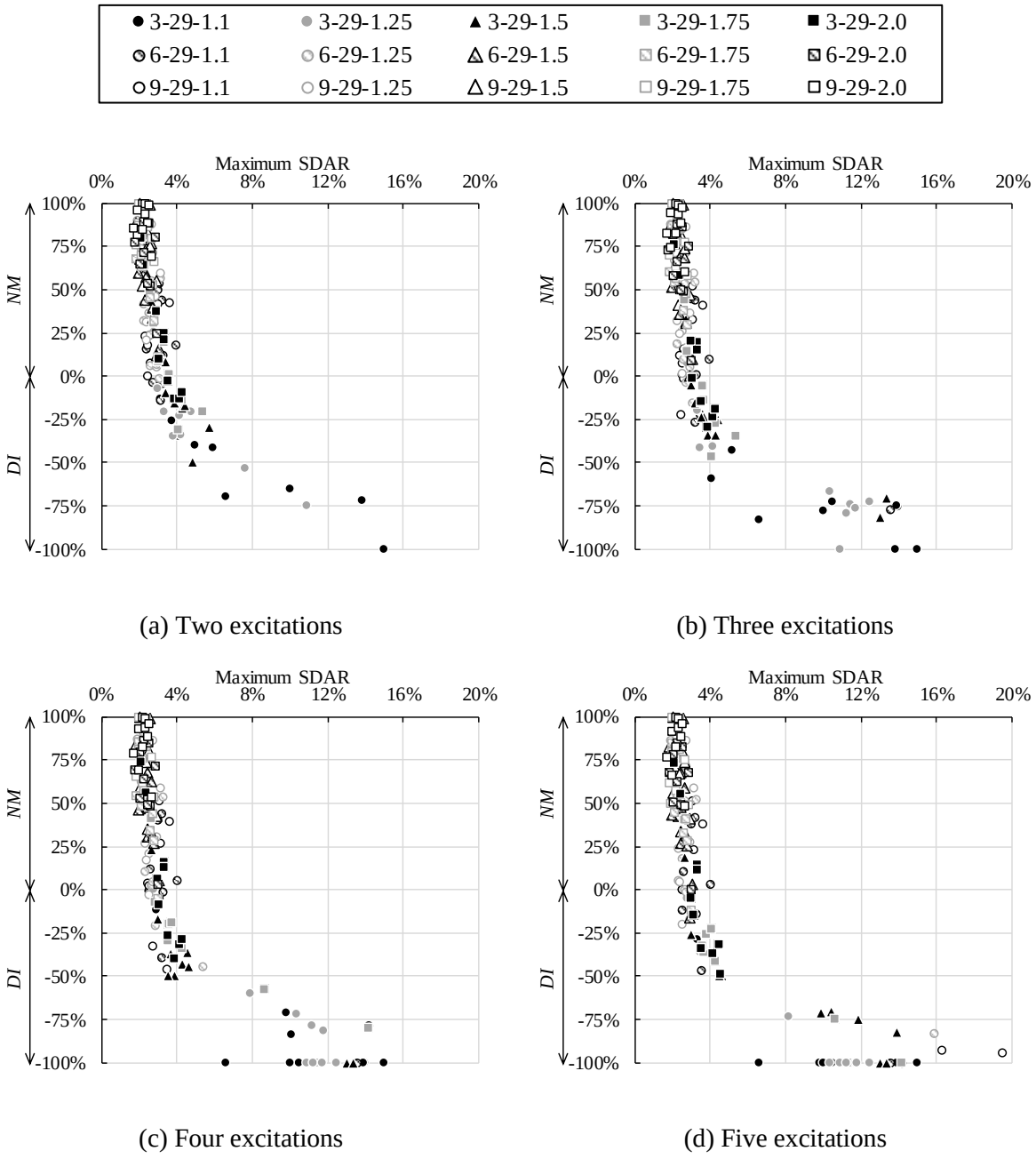

(a) Two excitations

(b) Three excitations

(c) Four excitations

(d) Five excitations

Figure I-1 Relationship between $SDAR_{max}$ and NM and DI under input ground motion intensity of PGV 0.5 m/s for models with D_c/t = 29.45

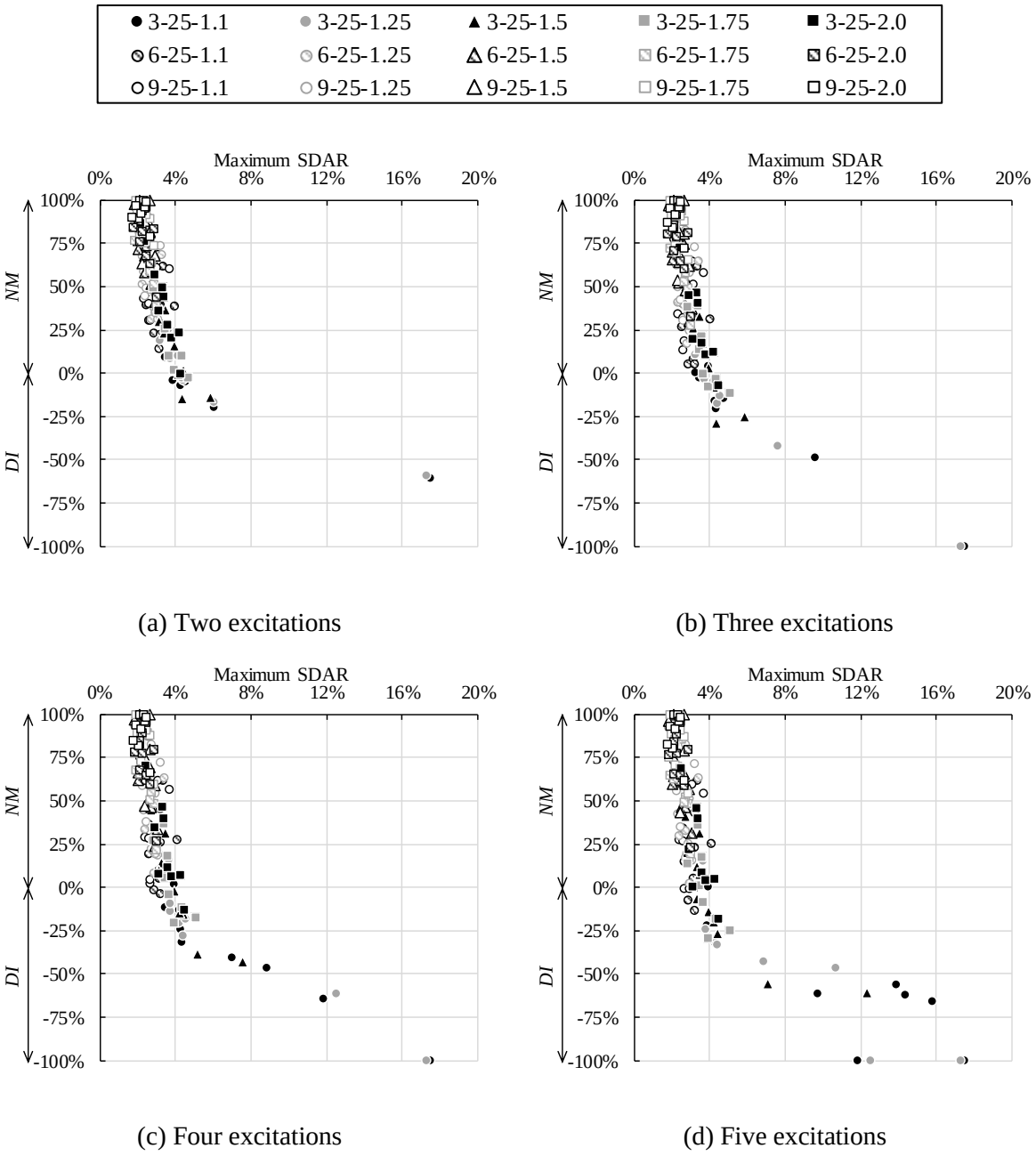

(a) Two excitations

(b) Three excitations

(c) Four excitations

(d) Five excitations

Figure I-2 Relationship between $SDAR_{max}$ and *NM* and *DI* under input ground motion intensity of PGV 0.5 m/s for models with D_c/t = 25

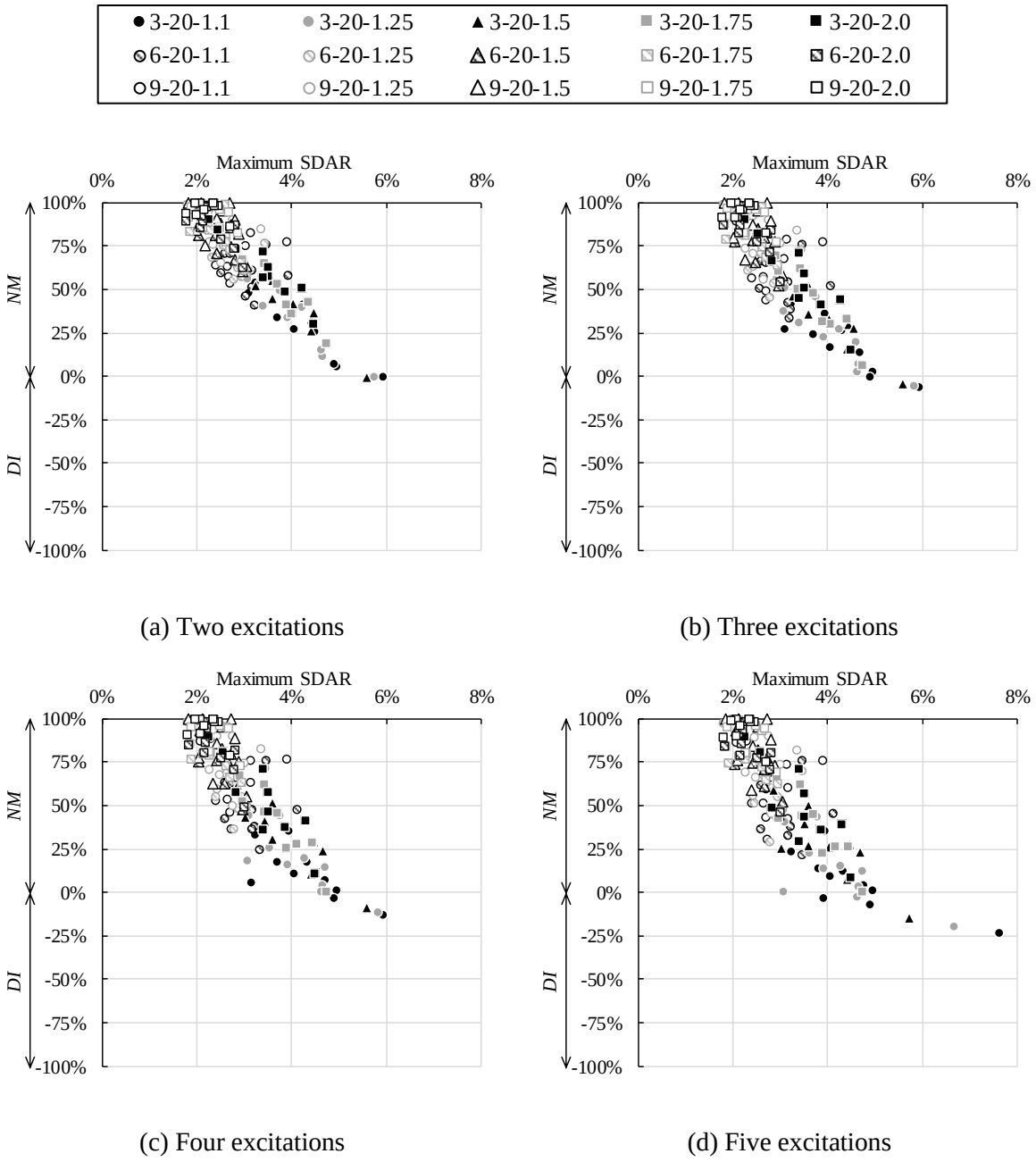

(a) Two excitations

(b) Three excitations

(c) Four excitations

(d) Five excitations

Figure I-3 Relationship between $SDAR_{max}$ and *NM* and *DI* under input ground motion intensity of PGV 0.5 m/s for models with D_c/t = 20

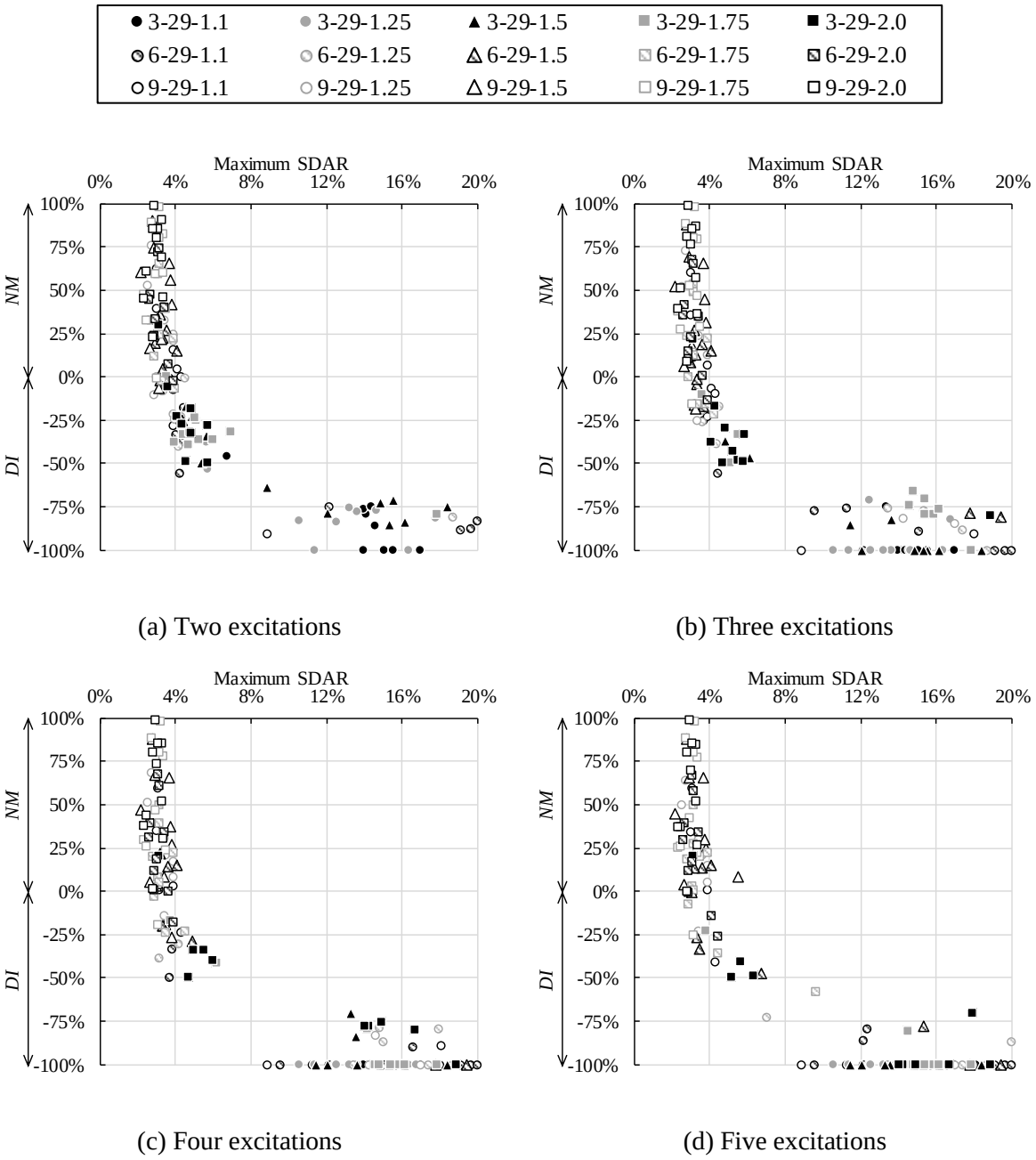

(a) Two excitations

(b) Three excitations

(c) Four excitations

(d) Five excitations

Figure I-4 Relationship between $SDAR_{max}$ and *NM* and *DI* under input ground motion intensity of PGV 0.75 m/s for models with D_c/t = 29.45

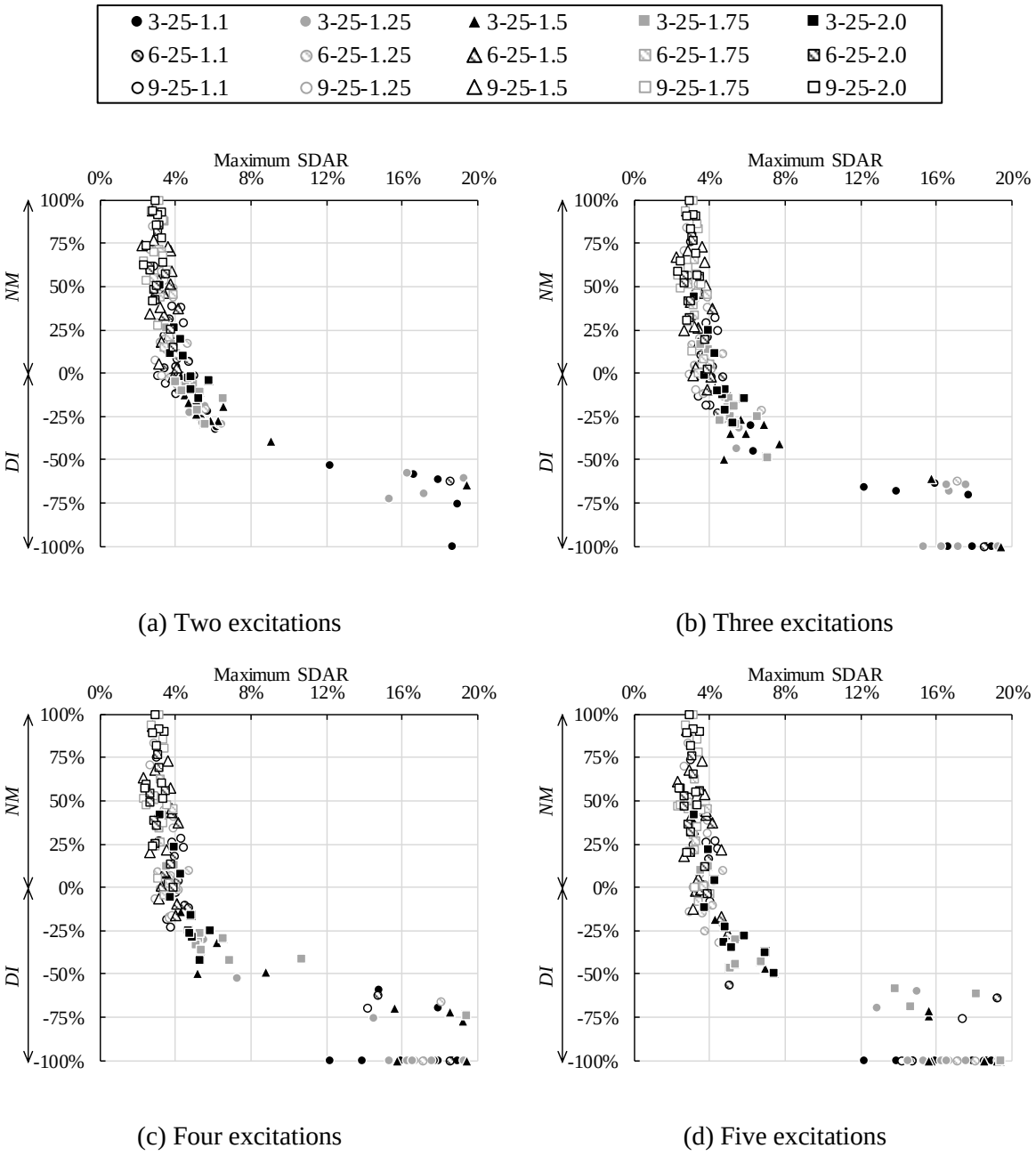

(a) Two excitations

(b) Three excitations

(c) Four excitations

(d) Five excitations

Figure I-5 Relationship between $SDAR_{max}$ and *NM* and *DI* under input ground motion intensity of PGV 0.75 m/s for models with D_c/t = 25

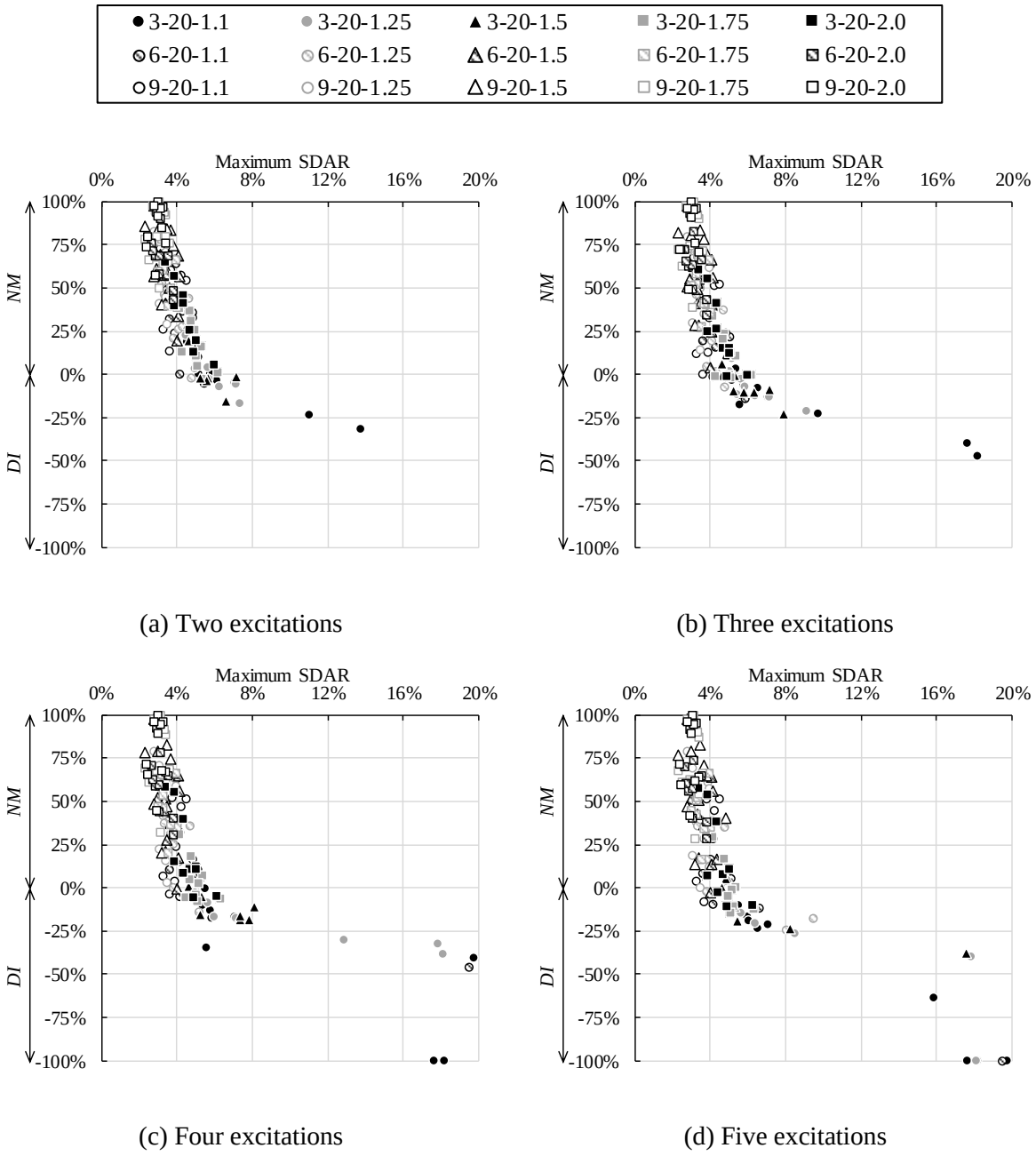

(a) Two excitations

(b) Three excitations

(c) Four excitations

(d) Five excitations

Figure I-6 Relationship between $SDAR_{max}$ and *NM* and *DI* under input ground motion intensity of PGV 0.75 m/s for models with D_c/t = 20

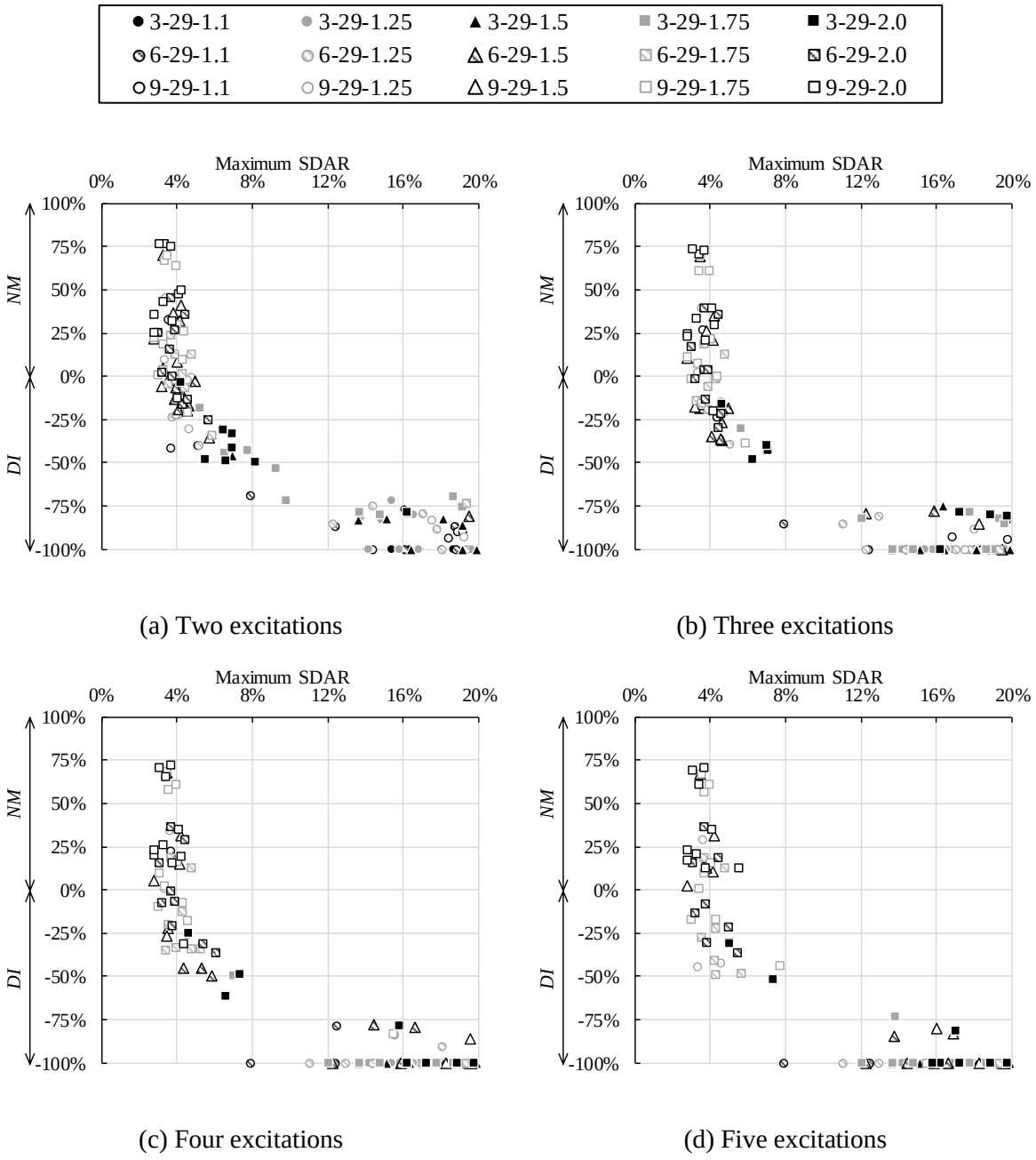

(a) Two excitations

(b) Three excitations

(c) Four excitations

(d) Five excitations

Figure I-7 Relationship between $SDAR_{max}$ and *NM* and *DI* under input ground motion intensity of PGV 1.0 m/s for models with D_c/t = 29.45

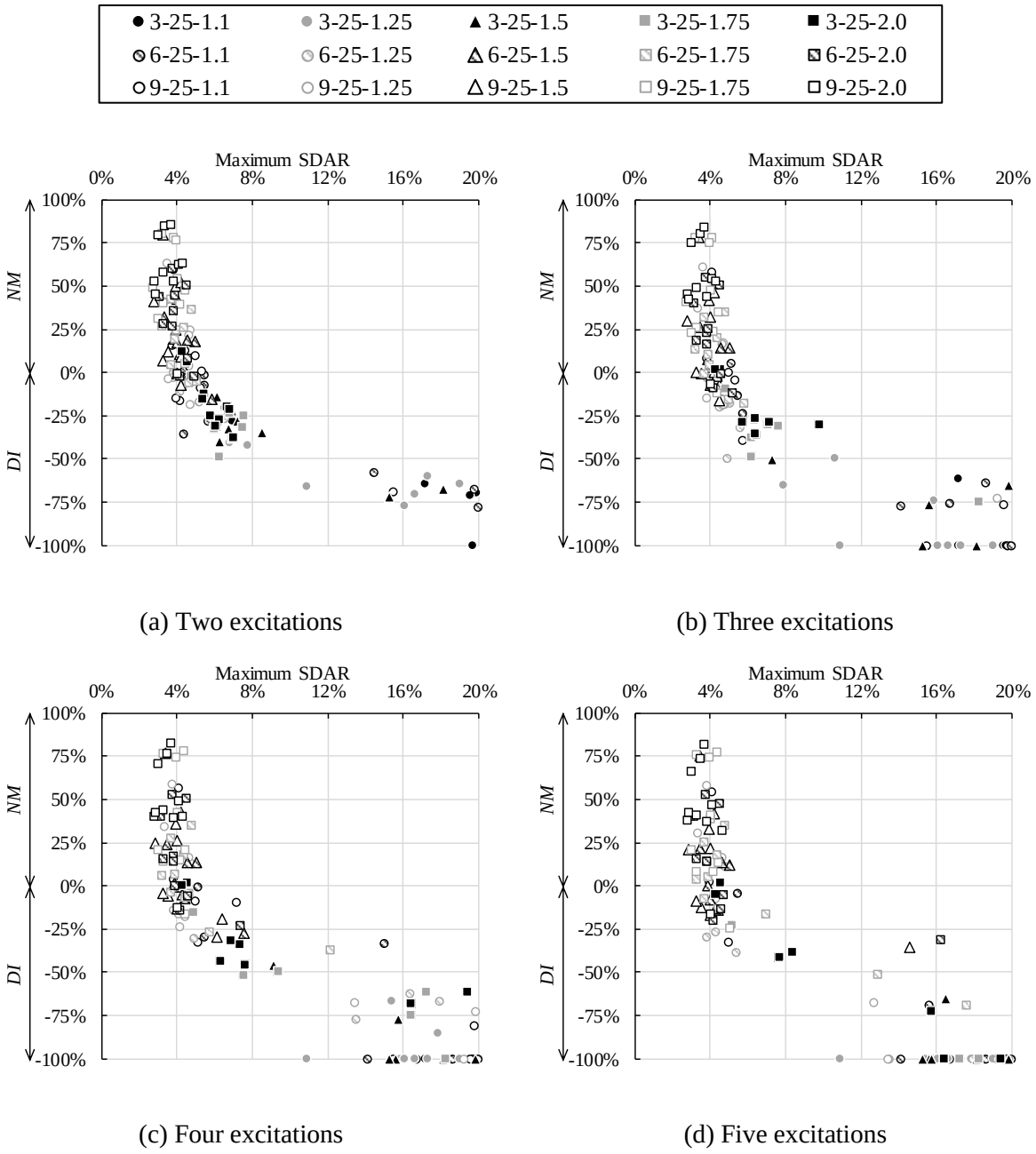

(a) Two excitations

(b) Three excitations

(c) Four excitations

(d) Five excitations

Figure I-8 Relationship between $SDAR_{max}$ and *NM* and *DI* under input ground motion intensity of PGV 1.0 m/s for models with D_c/t = 25

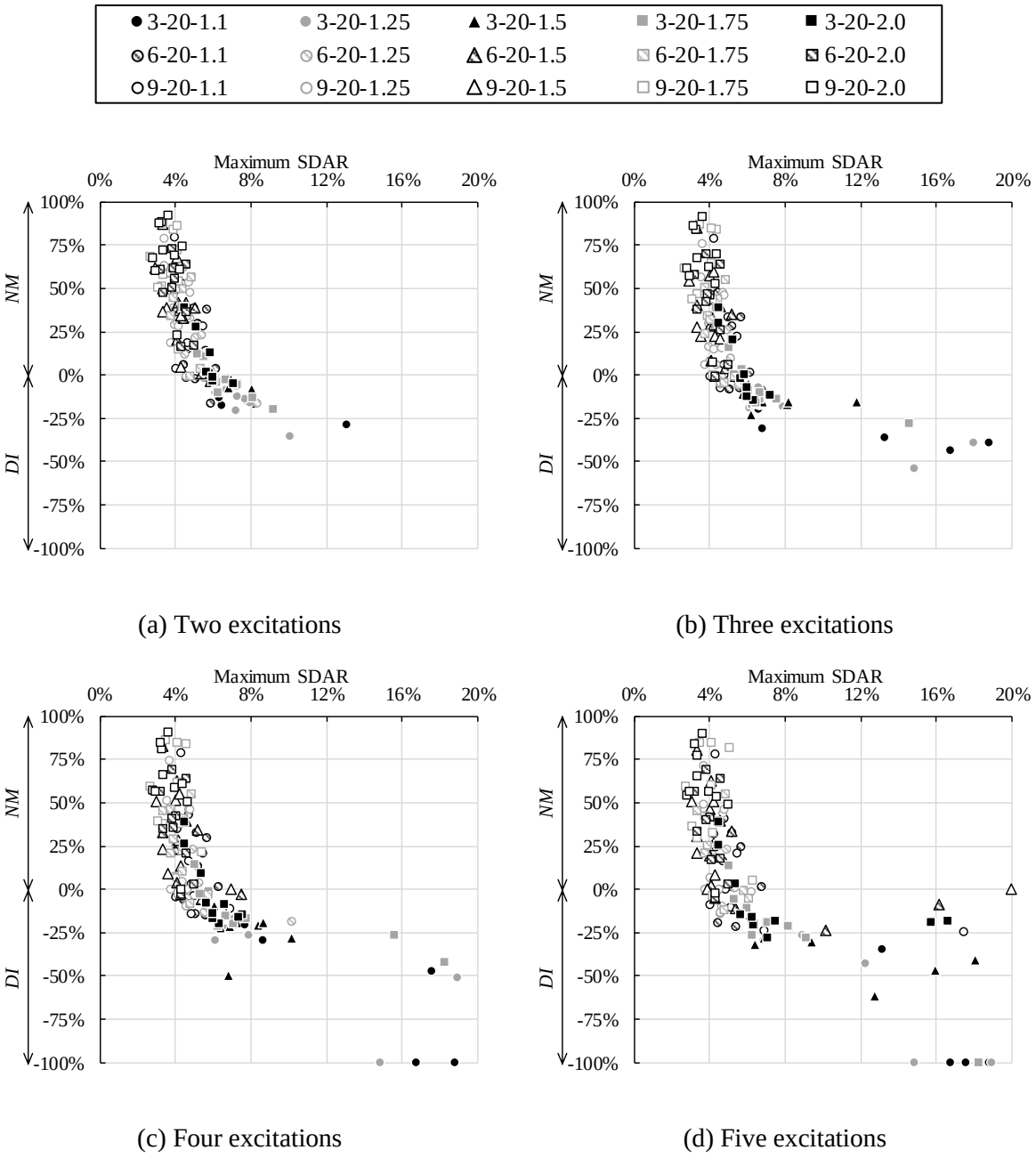

(a) Two excitations

(b) Three excitations

(c) Four excitations

(d) Five excitations

Figure I-9 Relationship between $SDAR_{max}$ and *NM* and *DI* under input ground motion intensity of PGV 1.0 m/s for models with D_c/t = 20

Appendix J Limitation of Maximum Story Drift Angle Range ($SDAR_{max}$) under Multiple Earthquake Excitations by Column Width-to-Thickness Ratio (D_c/t)

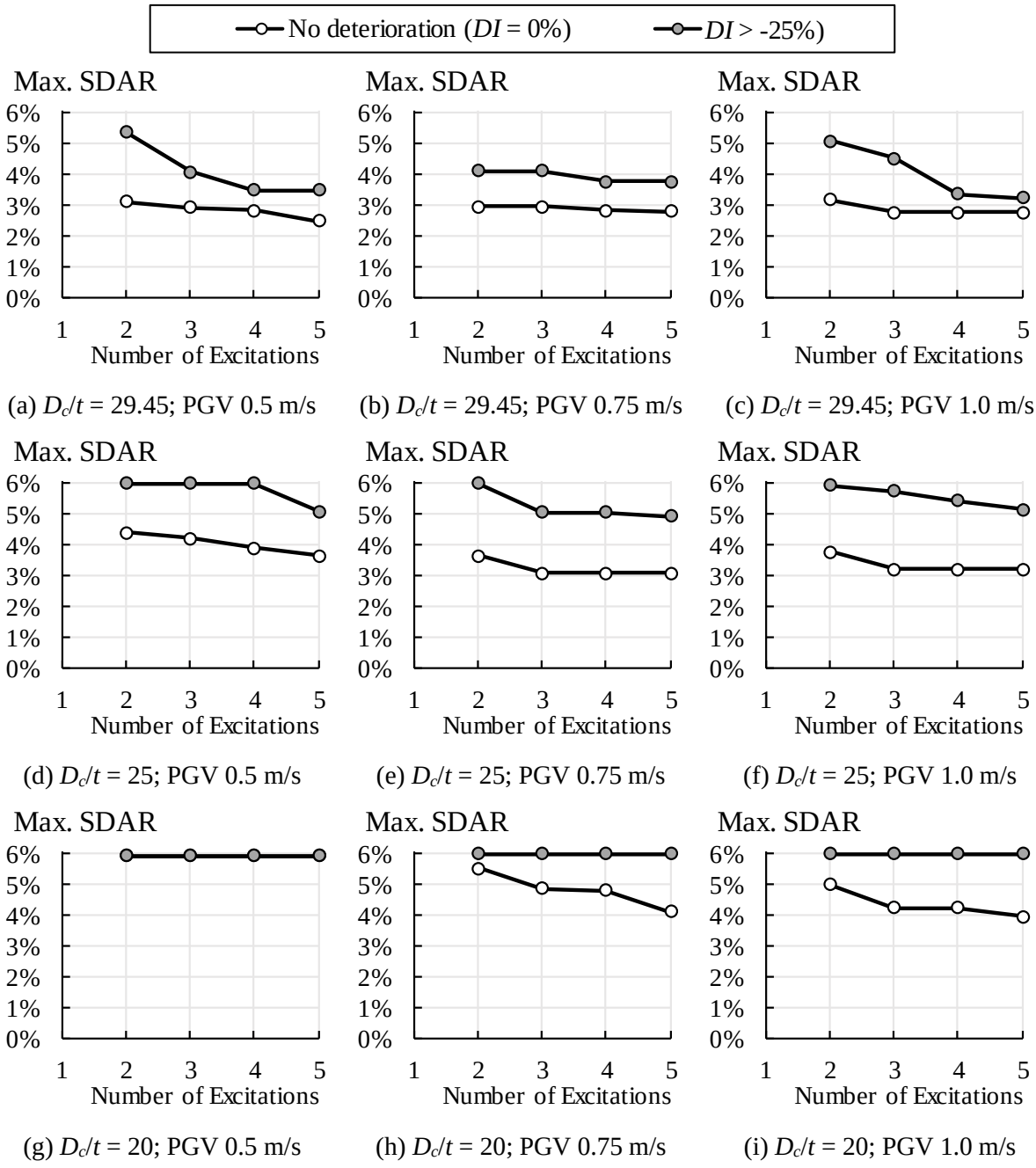

(a) D_c/t = 29.45; PGV 0.5 m/s (b) D_c/t = 29.45; PGV 0.75 m/s (c) D_c/t = 29.45; PGV 1.0 m/s

(d) D_c/t = 25; PGV 0.5 m/s (e) D_c/t = 25; PGV 0.75 m/s (f) D_c/t = 25; PGV 1.0 m/s

(g) D_c/t = 20; PGV 0.5 m/s (h) D_c/t = 20; PGV 0.75 m/s (i) D_c/t = 20; PGV 1.0 m/s

Figure J-1 Limitation of maximum story drift angle range ($SDAR_{max}$) under multiple earthquakes

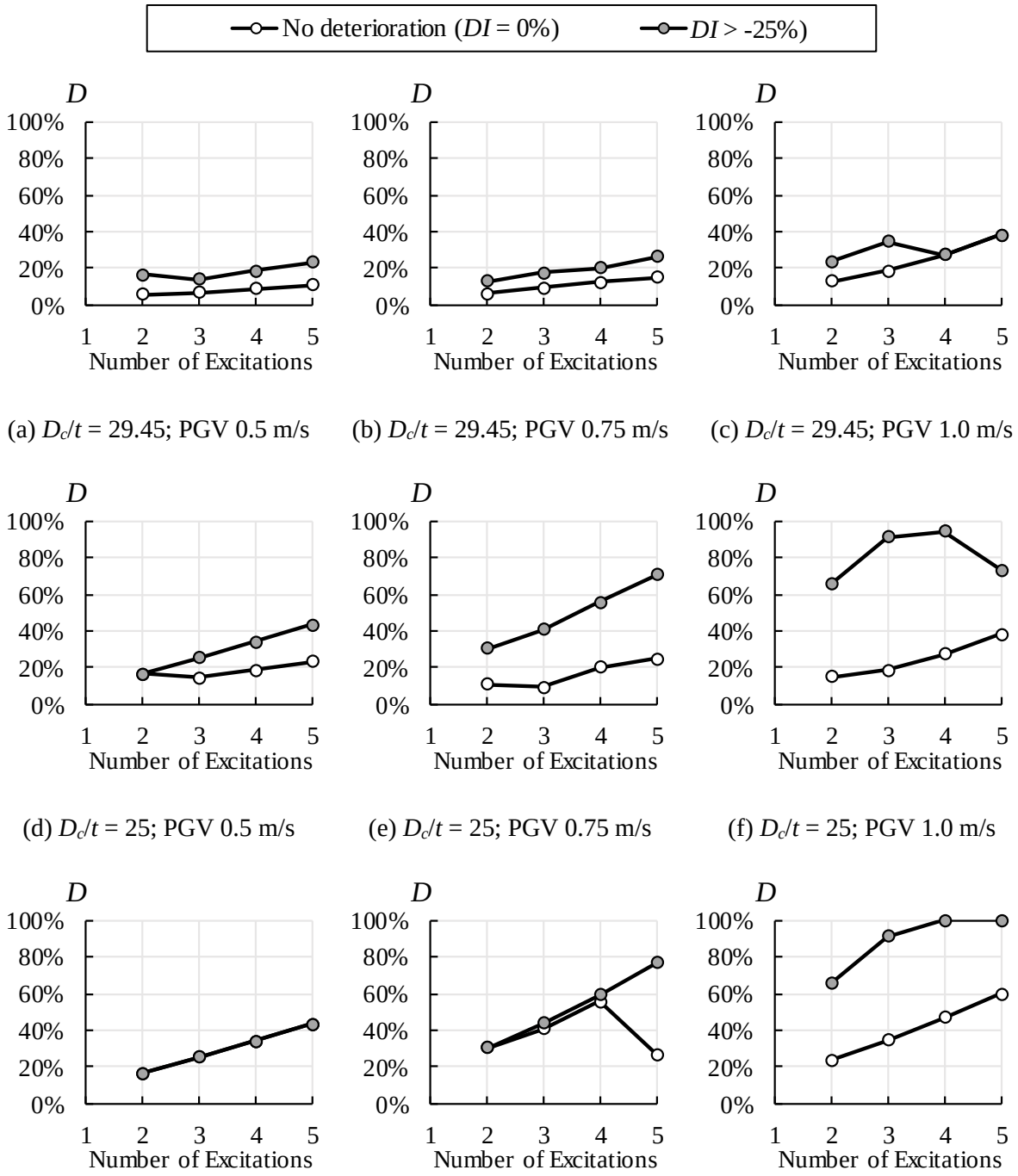

(a) D_c/t = 29.45; PGV 0.5 m/s (b) D_c/t = 29.45; PGV 0.75 m/s (c) D_c/t = 29.45; PGV 1.0 m/s

(d) D_c/t = 25; PGV 0.5 m/s (e) D_c/t = 25; PGV 0.75 m/s (f) D_c/t = 25; PGV 1.0 m/s

(g) D_c/t = 20; PGV 0.5 m/s (h) D_c/t = 20; PGV 0.75 m/s (i) D_c/t = 20; PGV 1.0 m/s

Figure J-2 Maximum cumulative damage of critical beam (D) for each limitation of $SDAR_{max}$

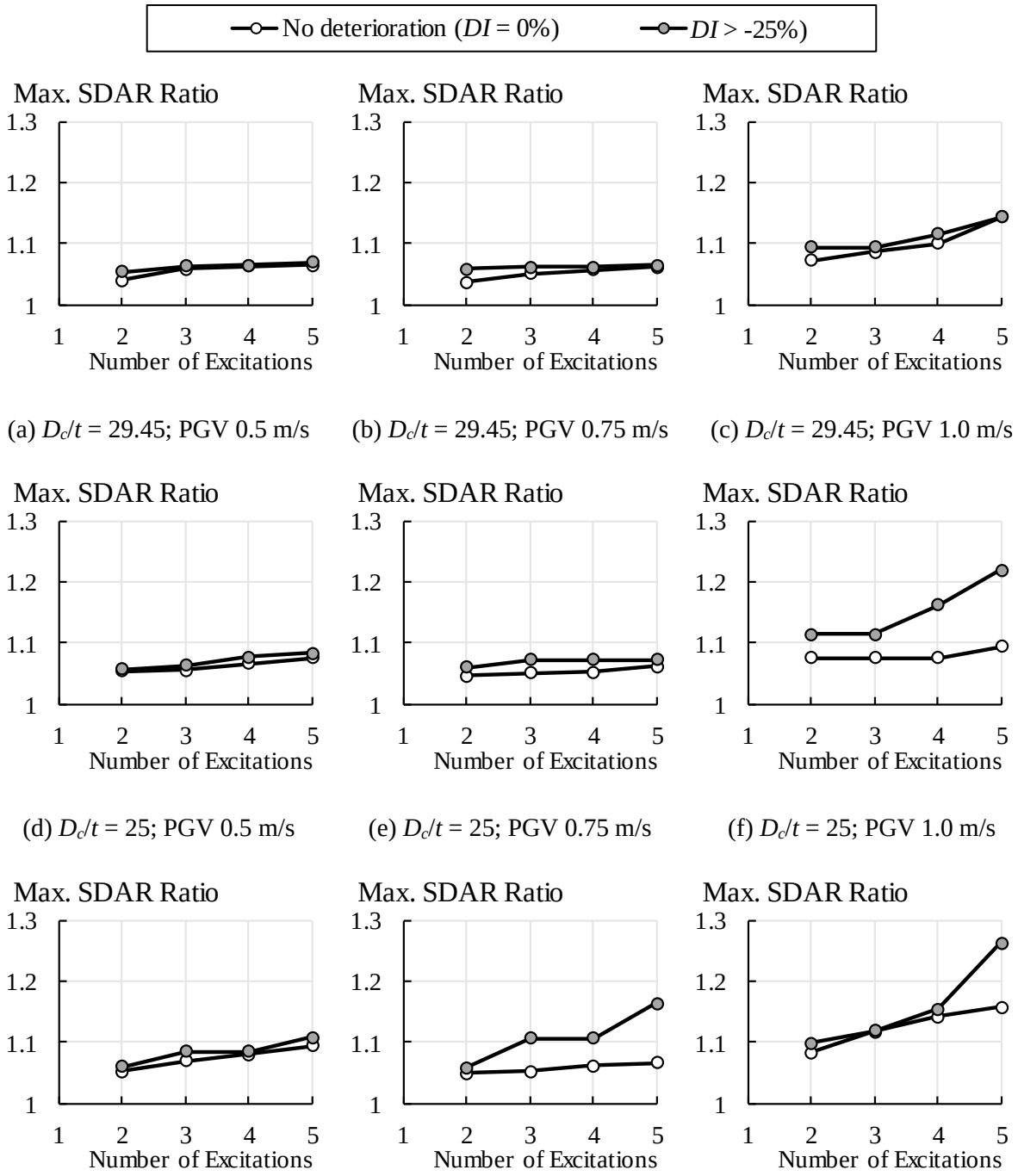

(a) D_c/t = 29.45; PGV 0.5 m/s (b) D_c/t = 29.45; PGV 0.75 m/s (c) D_c/t = 29.45; PGV 1.0 m/s

(d) D_c/t = 25; PGV 0.5 m/s (e) D_c/t = 25; PGV 0.75 m/s (f) D_c/t = 25; PGV 1.0 m/s

(g) D_c/t = 20; PGV 0.5 m/s (h) D_c/t = 20; PGV 0.75 m/s (i) D_c/t = 20; PGV 1.0 m/s

Figure J-3 Maximum increment ratio of $SDAR_{max}$ under multiple earthquakes

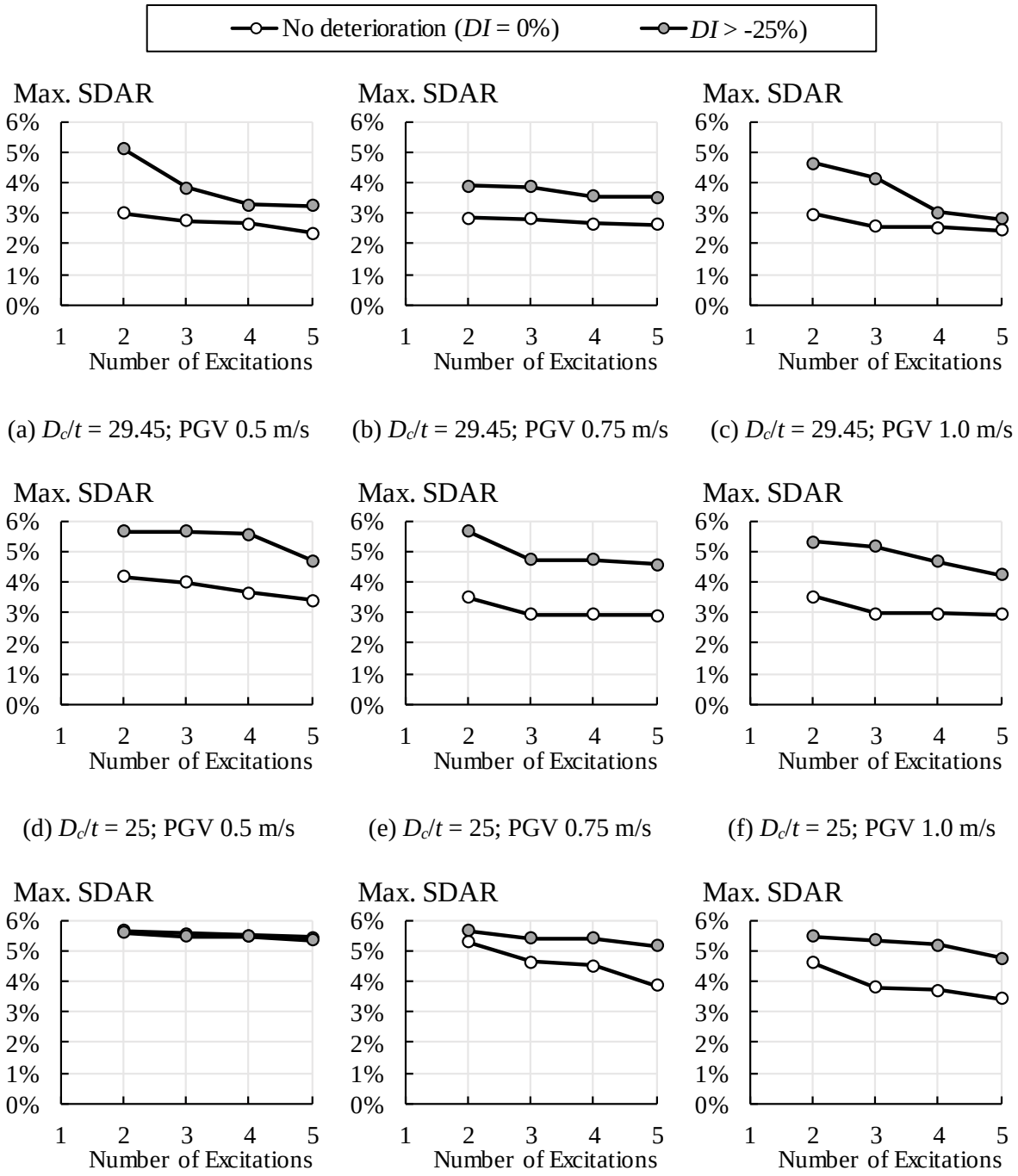

(a) D_c/t = 29.45; PGV 0.5 m/s (b) D_c/t = 29.45; PGV 0.75 m/s (c) D_c/t = 29.45; PGV 1.0 m/s

(d) D_c/t = 25; PGV 0.5 m/s (e) D_c/t = 25; PGV 0.75 m/s (f) D_c/t = 25; PGV 1.0 m/s

(g) D_c/t = 20; PGV 0.5 m/s (h) D_c/t = 20; PGV 0.75 m/s (i) D_c/t = 20; PGV 1.0 m/s

Figure J-4 Limitation of maximum story drift angle range ($SDAR_{max}$) at the 1st excitation